UNICA

UNIVERSITÀ
DEGLI STUDI
DI CAGLIARI

Ph.D. DEGREE IN
CHEMICAL SCIENCES and TECHNOLOGIES

Cycle XXXVII

TITLE OF THE Ph.D. THESIS

Development of novel reactive oxygen species (ROS)-modulating agents and carbonic anhydrase inhibitors for the treatment of Pancreatic Ductal Adenocarcinoma and other resistant cancers.

Scientific Disciplinary Sector(s)

CHEM-07/A

Ph.D. Student:	Federico Ladu
Supervisor	Mario Sechi
Co-Supervisor	-

Final exam. Academic Year 2023/2024

Thesis defense session: April 2025

Aknowledgements

This research project was made possible through the collaboration and participation of various individuals and institutions

My supervisor, Prof. Mario Sechi, who welcomed me into his "Drug Design and Nanomedicine" laboratory at the Department of Medicine, Surgery, and Pharmacy, University of Sassari, Italy, and who was responsible for the scientific aspects of my doctoral project. He provided me with all the necessary support to carry out the three-year research journey in the best possible way.

Prof. Nouri Neamati from the Department of Medicinal Chemistry, College of Pharmacy, University of Michigan, USA, who was responsible for the biological part of the project on ROS modulators.

Prof. Jean-Yves Winum from the University of Montpellier, CNRS, ENSCM, Montpellier, France, who welcomed me into his research group during my research period at the Institut des Biomolécules Max Mousseron and coordinated the scientific aspects of the project on multivalent carbonic anhydrase inhibitors.

Prof. Claudiu Supuran and Prof. Fabrizio Carta from the Neurofarba Department, University of Florence, Italy, who contributed to the scientific and biological aspects of the two projects on carbonic anhydrase inhibitors.

Prof. Claudia Crosio from the Department of Biomedical Sciences, University of Sassari, Italy, who was responsible for a section of the biological experimentation in the project on carbonic anhydrase inhibitors.

Prof. Wojciech Szlasa from the Department of Molecular and Cellular Biology, Wroclaw Medical University, who was responsible for holotomography and fluorescence detection experiments.

The research leading to these results has received funding fromAIRC under

IG 2021 – ID. 26211 – P.I. Sechi Mario" for Mario Sechi.

Table of contents

Sommario

Introduction 1

Chapter I - Cancer disease: from evolution to the treatment 7

1. General view 7

2. Global cancer statistics 10

3. Cancer treatment therapies 11

4. Classes of chemotherapeutics 13

5. The Hallmarks of cancer 16

6. Reactive Oxygen Species 17

6.1 Regulation of ROS 21

6.2 Role of reactive oxygen species in cancer 21

6.3 Cancer metastasis and ROS 25

7. Cell death 26

7.1 Autophagy 26

7.2 Necroptosis 26

7.3 Anoikis 27

7.4 Ferroptosis: a new ROS mediated cell death 27

7.4.1 Mechanisms of ferroptosis activation 28

7.4.1.1 Xc^- antiporter dysregulation 28

7.4.1.2 Inhibition of GPX4 29

7.4.1.3 Regulation of lipid metabolism pathway 29

7.4.1.4 Iron metabolism 30

7.4.1.5 P53-mediated ferroptosis 31

7.4.2 Ferroptosis as druggable pathway for diseases' therapy 32

7.4.2.1 Ferroptosis inductors 32

8. Pancreatic ductal adenocarcinoma 34

8.1 Pathogenesis 34

8.2 The PDAC genome 36

8.3 The PDAC metabolism 37

8.4 The PDAC stroma 37

8.5 The immunosuppressive microenviroment 38

8.6 Metastasis 39
8.7 PDAC treatment 40
Chapter II - Development of novel reactive oxygen species (ROS)-modulating agents 45
1. State of art 45
2. Rational of the PhD work 54
2.1 Preparation of the quinazoline-5,8-dione 55
2.2 Preparation of the quinoxaline-5,8-dione 56
2.3 Coupling reaction with the key synthons 56
2.4 The new set of QDs 57
2.5 Preparation of biotin/biotin-PEGylated QDs 58
2.6 Preparation of fluorescent QD-dye probes 59
2.7 Preparation of QD394 protected derivatives 60
2.8 X-Ray crystallography 61
2.9 Biological assays 62
2.10 Analysis for the fluorescent QD-dye probes 65
2.11 Binding studies of QDs with the enzyme GPX4 65
2.12 Surface plasmon resonance between QDs and the enzyme GPX4 67
3. Conclusions 68
4. Experimental part 70
4.1 General methods 70
4.2 Synthesis and characterization of the key synthons and the lateral chains 71
4.2.1 Synthesis of quinazoline-5,8-dione 71
4.2.2 Synthesis of quinoxaline-5,8-dione 75
4.2.3 Preparation of the biotin/biotin-PEGylated lateral chains 79
4.2.4 Preparation of the fluorescent dye-side chains 83
4.2.5 Preparation of the protected side chains 87
4.3 Syntheisis of the final compounds QD431-451 92
4.3.1 General procedure 92
4.3.2 Final compounds 94
Bibliography 117
Chapter III - Discovery and development of novel selective Carbonic Anhydrases Inhibitors (CAIs) 135
1. Carbonic anhydrase inhibitors: a general view 135
1.1 Human carbonic anhydrases 135
1.1.1 Catalytic mechanism of hCAs 137

1.1.2 Physiological functions of hCA isozymes[10] 138
1.1.3 Pathological functions of the hCA isozymes 139
1.2 CA inhibitors and mechanisms of action 140
Chapter IIIA- Development of a novel class of CAIs containing a trifluoro dihydroxy propanone pharmacophore 145
1 State of art 145
2 Molecular modelling 149
3 Rational of the PhD work 150
3.1 Repreparation of the novel class of trifluoro-hydroxy-propanone CA inhibitors 152
3.1.1 Chemistry 152
3.2 X-Ray crystallography 152
3.3 Biological assays 153
3.5 Holotomography 154
3.6 Fluorescence studies 156
4 Conclusions 157
5. Experimental section 158
5.1 Chemistry 158
5.1.1 General methods 158
5.1.2 General procedure for the preparation of N,N-dimethyl arene aldehyde hydrazones (3a-f)[32] 159
5.1.3 General procedure for the trifluoroacetylation of N,N-dimethyl-arene-aldehyde hydrazones (4a-f) 165
5.1.4 General procedure for the hydrolysis of trifluoroacetylated N,N-dimethyl hydrazones (TDP 1-6) 172
5.2 X-Ray crystallography of hCA II in complex with TBP4 178
5.2.1 Materials and methods 178
5.3 Biological assay 180
5.3.1 CA inhibition assay 180
Bibliography 183
1. General view 190
2. The multivalence inhibition approach 191
3. Multivalent carbonic anhydrase inhibition 192
4. Rational of the PhD work 193
4.1 Chemistry 194
4.1.1 Preparation of the azido-modified carbonic anhydrase inhibitors 195

4.1.2 Preparation of the single strand 12mer oligonucleotide 196
4.1.3 Incorporation of the CA inhibitors in the DNA oligonucleotide 200
4.2 Enzymatic inhibition assay 202
5. Conclusions 205
6. Experimental part 206
6.1 General methods 206
6.2 Synthesis and characterization of the CA inhibitors 207
6.3 Synthesis of oligonucleotide strands 210
6.3.1 General procedure A for solid supported synthesis 210
6.3.2 General procedure B for oligonucleotide supports cleavage and deprotection 210
6.3.3 Synthesis of modified sequences (ON-I-II-III-IV) 210
6.4 Synthesis of the final compounds (OCA1-8) 212
6.4.1 Preparation of the sulfonamide multivalent inhibitors 212
6.4.2 Preparation of the coumarin multivalent inhibitors 214
6.5 Characterizations 216
6.5.1 Oligonucleotide strands 216
6.5.2 Final compounds 218
Bibliography 222

Introduction

In the present PhD thesis, I report the results of a three-year research project in the context of the PhD course in Chemical Sciences and Technologies of the University of Cagliari, in collaboration with the department of Medicine, Surgery, and Pharmacy of the University of Sassari where I spent all my research period. I had the opportunity to work under the supervision of Prof. Mario Sechi, in the laboratory of Drug design and Nanomedicine within a research program focused on the identification and development of novel biologically active compounds as prototypes of novel anticancer drugs, in particular for the treatment of pancreatic ductal adenocarcinoma and other aggressive and resistant cancers.

In *Chapter 1*, I will dissect the cancer physiopathology, starting with its general features and examining the distinct characteristics which distinguish it from other diseases, also considering the impact in the World and providing a statistical overview about the new cases and deaths in the recent years. As for the peculiar features of cancer, in my PhD work I focused on the Reactive Oxygens Species and their dual role in both cancer development and treatment, and the ferroptosis death mechanism as a suitable approach for the development of novel anticancer agents. Moreover, I will discuss pancreatic ductal adenocarcinoma, starting from its pathogenesis to the therapies used nowadays.

In *Chapter 2*, I will discuss the study of a new class of ROS-modulators chemically related to the quinazoline-5,8-dione ring system, beginning from the state of the art, the work done in the past, to the new insights pursued in the PhD research period.

In the last *Chapter 3*, I report on the development of novel carbonic anhydrase inhibitors (CAI) for the treatment of cancer diseases. The first subchapter discusses the next step of a previous study on a new class of trifluoro-dihydroxy-propanone (TDP) derivatives as selective inhibitors of the human carbonic anhydrase isoform IX, with the potential to inhibit the proliferation of pancreatic tumor cells.

The second subchapter summarizes part of the work conducted during my six-month research in Montpellier, under the supervision of Prof. Jean-Yves Winum and his group ChemBioNac of the 'Institute des Biomolécules Max Mousseron'. It reports on the development of multivalent CAI as a new strategy to improve the potency and selectivity of this class of enzyme inhibitors.

CHAPTER I

CANCER DISEASE: FROM THE EVOLUTION TO THE TREATMENT

Chapter I - Cancer disease: from evolution to the treatment

1. General view

"Cancer is a disease in which some of the body's cells grow uncontrollably and spread to other parts of the body"[1]. This NCI definition is by now the most well know description of one of the three leading causes of death over the world, first in the very high-HDI countries and second in the mainly high-HDI countries.[2]

Although this term, along with and many other, conceptually aligns, the description remains a general overview of what cancer does and now it appears, rather that what it is and how it has evolved. Kenneth J. Pienta and others attempted to refine this old but consistent definition with a new one that more deeply explains the concept of cancer disease, which is "Cancer is a disease of uncontrolled proliferation by transformed cells subject to evolution by natural selection".[3]

This modern definition includes several aspects that can be compared with others nowadays, described below:

- **disease**: this term describes a state of disruption of the normal organism physiology and in this way even cancer, with its cells' growth, spread and disruption of tissues and normal body functions is obviously a disease. The conceptual upgrade comes from the fact that many definitions refer to cancer as a collection of diseases, because it arises in many different organs or with tissue-specific hits. In this case considering the convergent behavior of evolution of cancer through individuals, the concept of diseases is nonessential. In this context it is ever necessary to remember that the assignment of the characteristic of disease must stay distinguished from the definition of tumor albeit they are used interchangeably. In medical terminology tumor describes an abnormal growth of tissue that can be dangerous (malignant neoplasia) or not dangerous (benign neoplasia);
- **uncontrolled cell proliferation**: the term "*uncontrolled*" doesn't describe perfectly this characteristic of the cancer. Normally this term refers to processes which lack of regulation handling. At the tissue level, the uncontrollability of

cancer cells refers to their inability to be regulated by the normal mechanisms that maintain homeostasis, leading to potentially deleterious outcomes. In a typical scenario, deviation from normal biological behavior results in programmed cell death (apoptosis). The independence from normal cellular mechanisms does not make cancer free from limitations, which must instead be sought in environmental constraints for growth. Normal cells are maintained in a state of homeostasis in terms of number and density, allowing access to nutrients, necessary space, and limited exposure to toxic and harmful factors. Thus, cancerous proliferation is regulated by ecological parameters (including physical, chemical, and biological factors) that fall outside the normal biological behavior of homeostasis;

- **transformed cells**: transformation is a central feature of cancer formation, referring to the process by which normal cells acquire genetic and epigenetic modifications that lead them to become malignant. This term explains better the features of cancer cell with respect to the simple term “spreading”, because it includes all the intrinsic features of cancer cells, that are well described by Hanahan and Weinberg’s with the “Hallmarks of Cancer” [4]. In general, the risk factors that can induce the development of cancer are categorized into endogenous (genetic mutations, heredity, hormonal imbalances) and exogenous factors, which determined by environmental conditions (smoking, drugs, exposure to toxic substances, UV radiation, etc.);
- **evolution**: it refers to the change in heritable characteristics of a population over generations. Considering cancer in terms of cells as 'individuals' with altered genomes better conveys the idea that, although the human organism is a system composed of multiple levels of cellular coordination, from organs to tissues and down to individual cells that cooperate harmoniously, the concept of carcinogenesis can be considered as a process of individual speciation of a single cell as an entity that survives and can be selected independently from the tissue context in which it arises. Factors that drive evolution include genetic mutations, genetic drifts, gene flow and natural selection. Nevertheless, many of these mutations lead to cell death or, in some cases, the emergence of cancerous cells. In these instances, the mutated genes are referred as oncogenes, which are derived

from proto-oncogenes, which are thus involved in cell growth, proliferation, and migration;

- **natural selection**: it is the driving force of evolution that promotes adaptations, which are inherited to maximize fitness, defined as the difference between the birth rate and the death rate. Natural selection occurs through heritable variations and competition for survival, where the traits must significantly influence the success of the survival struggle. Since cancer possesses all of these characteristics, which allow its evolution, resistance, and adaptation, it is essential for this concept to be included in its modern definition.

2. Global cancer statistics

In 2022 approximately 20 million new cancer cases were diagnosed, and about 10 million people died from cancer worldwide **(Figure1A)**. According to projections based on aging and population growth, over 35 million new cancer cases are expected to occur by 2050, representing an increase of approximately 77%. In addition to this enormous problem, the greatest relative increase will take in lower HDI countries (HDI i.e. Human Development Index is a summary measurement of the human welfare considering several factors, **Figure 1B**) with a 142% predicted increase, probably because they are least resourced to manage additional burden.[2,5]

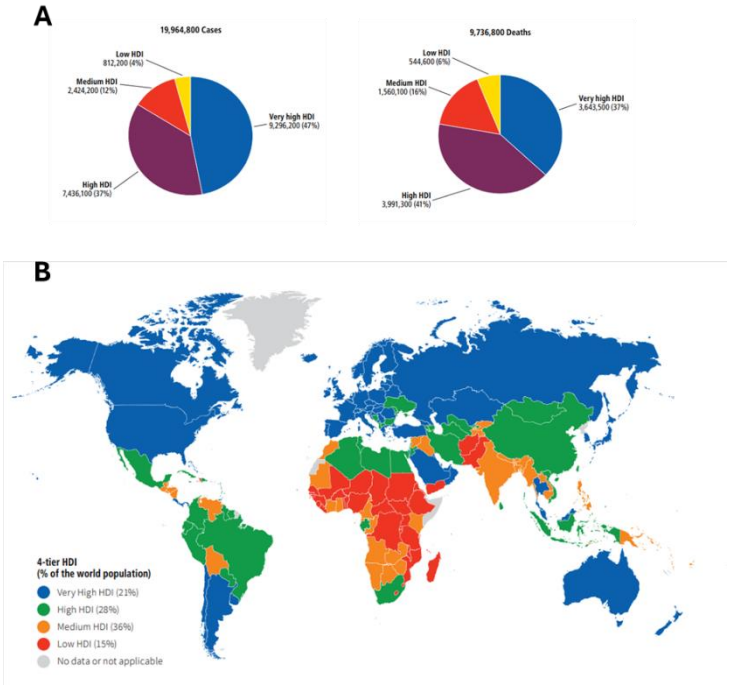


Figure 1. A) Estimated number of new cancer cases and deaths by Human Development Index (HDI);

B) Human Development INDEX (HDI), 2021. Source: [2]

In general, lung cancer is the most diagnosed neoplasia and the leading cause of cancer death worldwide. For males it is followed by prostate, colorectal and stomach for incidence and always the same for mortality. In females breast cancer overcomes lung cancer and ranks first both for incidence and mortality. **(Figure 2)**.[2]

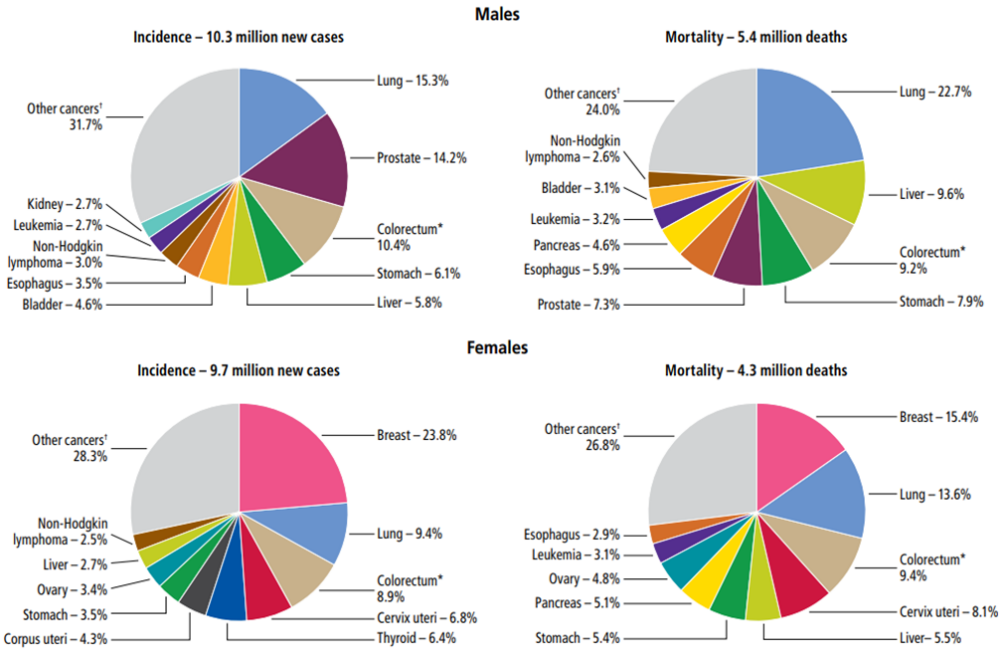


Figure 2. Distribution of cases and deaths for the most common cancers by sex, 2022. Source: [2]

3. Cancer treatment therapies

The scenario of cancer treatment has continuously changed over the decades. Starting from the period when surgery and radiotherapy were the only choice to effectively fight tumor growth, we are now in an epoch where these two, always pivotal methodologies, are supported or sometimes replaced by chemotherapy with its various particular categories (targeted therapy, immunotherapy, hormone therapy, photodynamic therapy[6] and new advanced cell and gene therapy).[7] (**Figure 3)**

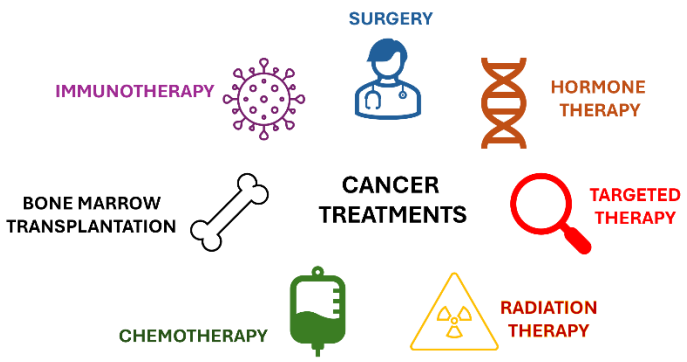


Figure 3. Cancer therapies

Cancer treatments are under the supervision of oncologists who construct the strategy of the treatment in relation of the cancer type, size and stage. The treatments include:

Surgery is effective in the treatment of localized primary tumor and associated regional lymphatics but in some cases is not sufficient to eradicate neoplasia completely because of subclinical or microscopic cancer cell remanences; in these cases the combination with other therapies is necessary.

Radiotherapy consists in the use of ionizing radiations that deliver a lethal dose to a defined tumor volume, damaging DNA and inducing intracellular mechanisms of programmed cell death. Its combination with surgery is effective and sometimes essential to eradicate cancer at microscopic level.[8]

Chemotherapy consists in the use of chemical substances for the treatment of a disease. The first role of chemicals for cancer therapy arises from the systemic use of cytotoxic compounds designed to kill or inhibit cell growth. The disadvantage of traditional chemotherapy agents is their inability to distinguish normal from cancer cells.[9] In addition to reduce or eliminate the tumor these treatments produce several unwanted side effects. From the first approach with chemotherapeutics in the1940s and the astonishing increase of knowledge in the last 20 years as regards the distinctive traits of cancer, especially with the introduction of the "Hallmarks of Cancer" by Hanahan and Weinberg,[4] chemotherapy is at the center of medicinal research. This important categorization of the distinctive features of cancer is object of current studies and research of new and more innovative drugs for preventing side effects and drug resistance, switching from systemic therapy to targeted chemotherapy, where a specific molecule is designed to selectively perform its effect toward cancer biological target.

4. Classes of chemotherapeutics

Although new cancer targets have been continuously identified and novel and innovative prototypes of drugs have been designed, increasing the panel of chemotherapeutic classes, it is possible to differentiate them in many big classes depending on the pharmacological activity.[9] **(Figure 4)**

- **DNA cross-linking agents:** the main target of these molecules is the dividing DNA, particularly electrophilic reactive sites which are readily attacked by DNA bases as N7 of guanine or others. They are more toxic in specific G1 or S phase of cell cycle where DNA is unwinding and exposes better nucleotides. Examples of subclasses are nitrogen mustards and Aziridine alkylators (Mechlorethamine HCl, Melphalan, Chlorambucil, Bendamustide, Cyclophosphamide, etc.), Nitrosoureas (Carmustide, Lomustide, Streptozocin, etc.), DNA methylators (Procarbazide HCl, Dacarbazide, etc.), Organoplatinum complexes (Cisplatin, Carboplatin, Oxaliplatin, etc.).
- **Antimetabolites:** this type of compounds act stopping the de-novo synthesis of DNA by inhibiting the formation of the nucleotides, mostly promoting the incorporation of false nucleotides into the growing of DNA strand. Many of them are categorized by the class of nucleotide synthesis they inhibit, as pyrimidine antagonists (Fluorouracil, Floxuridine, Capecitabine) and purine antagonists (Mercaptopurine, Thioguanine); other antimetabolites are implicated in the inhibition of other key metabolic pathways of DNA synthesis, as folate antagonists (Methotrexate, Pemetrexed and Pralatrexate), DNA polymerase and chain elongation inhibitors (Cytarabine, Gemcitabine, Fludarabine, etc.) and DNA methyltransferase inhibitors (Azacitidine, Decitabine and nelarabine).
- **Histone deacetylase inhibitors:** this class of compounds acts against histone proteins involved in regulating gene transcription, particularly by inhibiting the deacetylation of lysine residue. This is associated with an increase in the induction of antioncogene p21 and subsequent apoptosis.[10]
- **Immunomodulators:** this class acts augmenting circulating natural killer cells and increasing the signaling pathways to support immune homeostasis. Despite the first negative beginning in the history of chemo-agents, Thalidomide and its

derivatives have been raised their reputation about their immune regulation activity in many chemotherapeutic regimens.[11,12.] The new class of monoclonal antibodies (MoAbs) acts targeting tumor cell antigens and, after complexing, recruits endogenous immunomodulators and cell-destroying cytokines; some examples include Cetuximab, Trastuzumab, Gemtuzumab, etc.

- **Antibiotics:** antibiotic antineoplastics have broad activities, from inhibition of DNA replication enzymes to induction of rupture of point mutations in the DNA. Examples are the class of Anthracycline (Doxorubicin HCl, Epirubicin HCl, Valrubicin, etc.) which function as Topoisomerase IIα (TopIIα) poisons; other antibiotics as Bleomycin generates free radicals that cause DNA breaks and Mitomycin alkylates DNA with a mechanism similar to mustard antineoplastics.
- **Mitosis inhibitors:** in the mitotic process, microtubules play a crucial role ultimately allowing the formation of the mitotic spindle and the attachment to chromosomes, essential condition for cell division. Inhibition of dynamic changes in microtubular structure results in mitotic arrest and apoptosis. Two general classes have historically been used, Taxanes (Paclitaxel, Docetaxel, Cabazitaxel) and Vinca alkaloids (Vincristine, Vinblastine, Vinorelbine).
- **Topoisomerase poisons:** topoisomerases are enzymes that control the degree of DNA coiling by retaining the proper structure. Topoisomerase IIα (TopIIα) cleaves and relegates double stranded DNA during replication while Topoisomerase I (TopI) acts in the same way but cuts and relegates a single strand. Antineoplastic agents work simulating DNA cleavage but inhibiting the resealing activity of the enzyme, thus leading to DNA damage. Two classes can be mentioned with such activity, Camptothecins (Irinotecan, Topotecan) and Epipodophyllotoxins (Etoposide, Etoposide phosphate and Teniposide HCl).
- **Tyrosine kinase and related inhibitors:** protein tyrosine kinases (TKs) normally regulate cell proliferation, differentiation and survival but, when they are dysregulated, the evolution can accelerate cell signaling cascades and cellular growth, thus inducing tumors, blocking apoptotic processes and also conferring resistance from many chemotherapeutic drugs. Aberrations in the activity of protein tyrosine kinases are associated with several neoplastic disorders, and it has been estimated that more than 80% of human oncogenes and proto-oncogenes

direct the expression of these essential phosphorylating enzymes. Inhibitors of these enzymes act blocking the phosphorylation activity resulting in dysregulation of cancer cell activity and inducing cell death. The classes are extremely wide and continuously increasing, but some of these are well known for the historical contribution to cancer therapy and include Bcr-Abl inhibitors (Imatinib, Nilotinib and Dasatinib), EGFR and EGFR/HER2 inhibitors (Erlotinib, Gefitinib and Lapatinib), VEGFR inhibitors (Sunitinib, Sorafenib and Pazopanib), mTOR inhibitors (Temsirolimus, Everolimus).

- **Hormone therapy:** some tumors, such as estrogen-dependent breast cancer, endometrial cancer, prostate cancer etc., depend on the presence of sex hormones for their viability. In these neoplastic diseases, the use of steroids receptor antagonists, secretion inhibitors and synthesis inhibitors, alone or in combination, is a common approach. Some classes are Antiestrogens (Tamoxifen), Antiandrogens (Flutamide), Progestins (Megestrol), Aromatase inhib. (Exemestane) and Luteinizing hormone-releasing hormone agonists (Leuprolide).
- **Miscellaneous anticancer agents:** this class includes compounds with many therapeutic effects and a not completely understood mechanism. Examples are the proapoptotic Arsenic trioxide (As_2O_3), which showed inhibition of intracellular catalase and glutathione peroxidase as well as downregulation of the antiapoptotic protein Bcl-2 and the proteasome inhibitor Bortezomib.
-

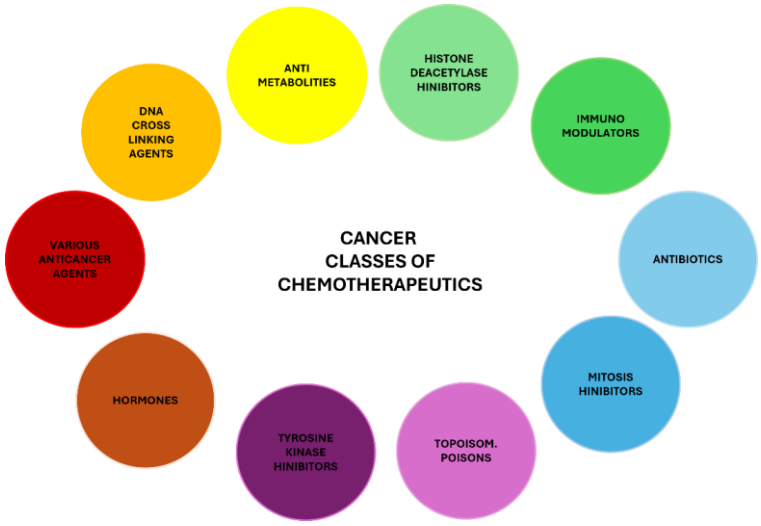


Figure 4. Classification of chemotherapeutics

5. The Hallmarks of cancer

Cancer research has undergone significant transformations, particularly with the rapid advancement of technology and the numerous studies aimed at understanding the biological mechanisms of cancer development, that previously appeared not comprehensible. With the proposal in 2000 by Hanahan and Weinberg of the so-called Hallmarks of Cancer[4] the fundamental change was precisely conceptual. Many scientific evidences indicated that tumorigenesis in humans is a multistep process reflecting genetic alterations that lead to the transformation of normal human cells into malignant derivatives. The major challenge was classifying these biological behaviors that drive the development of a cancerous cell.

The hallmarks constitute an organizing principle for rationalizing the complexities of neoplastic disease. They include sustaining proliferative signaling, evading growth suppressors, resisting cell death, enabling replicative immortality, inducing angiogenesis, and activating invasion and metastasis. In addition to these, four new features have been subsequently added, two enabling characteristics (i.e. genome instability and mutation and tumor promoting inflammation) that emphasize the importance of some occurrences for the acquisition of cancer capability and two emerging hallmarks (i.e. avoiding immune destruction and deregulating cellular energetics).[13] In the next decade, other new enabling characteristics were added to the core components of the hallmarks of cancer conceptualization, which include unlocking phenotypic plasticity, no mutational epigenetic reprogramming, polymorphic microbiomes and senescent cell.[14] **(Figure 5).** All of these fourteen cancer characteristics are combined with the widely appreciated integral role of tumor microenvironment (TME) in tumorigenesis and malignant progression.

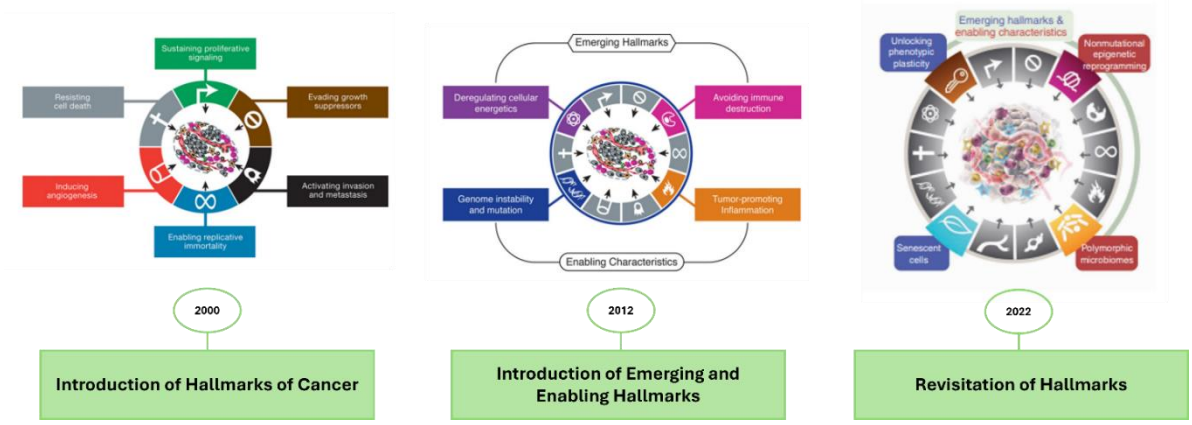


Figure 5. Timeline of the Hallmarks of Cancer

6. Reactive Oxygen Species

In the context of the hallmarks of cancer, an important factor is the contribution of Reactive Oxygen Species (ROS). Increased ROS levels along with deregulated redox homeostasis and increased antioxidant ability can be considered as a contributing factor to the concrete growth of cancer as well as a consequence of many hallmarks of cancer, so much that it could be located in the circle of the fundamental characteristics of cancer.

ROS encompasses a family of molecules, although the main characteristic is that they are short-lived molecules having unpaired electrons, formed by the partial reduction of molecular oxygen. They are oxygen containing derivatives comprised of highly unstable oxygen free radicals, for example, superoxide (O2 •⁻) and hydroxyl (OH•) which can be quickly converted into more stable, freely diffusible non-radical species including hydrogen peroxide (H_2O_2) and hypochlorous acid (HClO)[15]. These highly active radicals originate from both intrinsic and extrinsic sources. Intrinsic sources of ROS mostly include mitochondria, inflammatory cells, and several enzymatic cellular complexes; extrinsic sources of ROS include pro-oxidant environmental toxins, radiations and diverse chemical compounds, including alcohol, tobacco smoking, and certain drugs **(Figure 6)**.

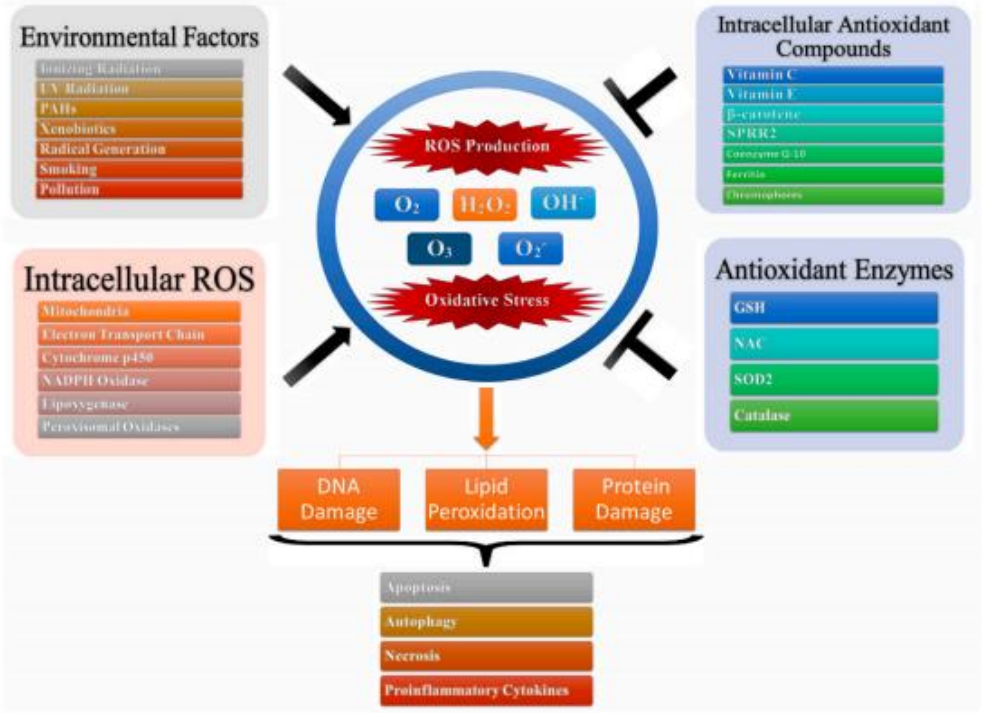


Figure 6. Oxidative stress and production of Reactive Oxygen Species. Intracellular ROS and environmental factors initiate ROS production leading to oxidative stress which in turn leads to DNA/lipid/protein degradation resulting in apoptosis, autophagy, necrosis and production of pro-inflammatory cytokines. Source: [16]

ROS are normal byproducts of a wide variety of cellular processes, including oxygen metabolism.[17] They have a dual role in cell metabolism: at low to moderate levels, ROS act as signal transducers to activate cell proliferation, migration, invasion, and angiogenesis. In contrast, elevated levels of ROS cause damage to proteins, nucleic acids, lipids, membranes and organelles, leading to cell death. The classic examples of organelles with localized ROS physiological generation include phagosomes within specialized cells of the immune system used for pathogen killing, and peroxisomes, which mediate catabolic oxidation reactions for energy metabolism. In addition to these canonical ROS sources three other significant sites in cells are mitochondria, the endoplasmic reticulum (ER) and cell membranes.

Mitochondria are one of the largest contributors to the endogenous source of ROS (mROS).[18] **(Figure 7)**. This organelle is responsible for generation of ATP through the oxidation of amino acids, glucose and lipids, culminating in the transfer of NADPH and $FADH_2$ to the electron transport chain (ETC). However, because of the imperfect process of the flow of electrons through the ETC, mitochondrial leakage of ROS is an inevitable

consequence of aerobic respiration. ROS generated from complex I and III of the ETC have been documented to have a role in cellular signaling. Most of the O_2 •⁻ generated in the mitochondria are dismutated to H_2O_2 by manganese superoxide dismutase (MnSOD) in the mitochondrial matrix[19]. H_2O_2 is a second messenger that is highly diffusible and has been shown to cross the mitochondrial membrane through specific members of the aquaporin family.[20]

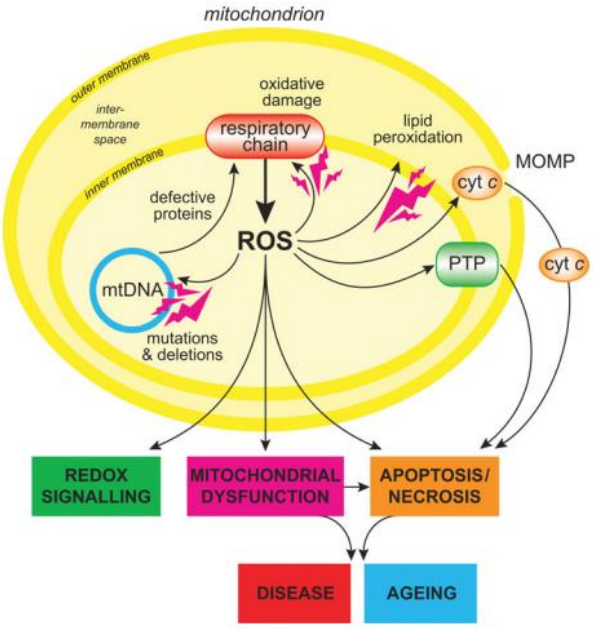


Figure 7. Overview of mitochondrial ROS production. Source: [19]

The primary source of ROS from the *Endoplasmic Reticulum* (ER) results from oxidative protein folding where secreted proteins often undergo disulfide bond formation as a post-translational modification as they fold in the ER lumen. The protein disulfide formation reactions are mostly initiated by the glycoprotein ER oxideructin 1 (Ero1) which triggers a two-electron oxidation of the thioredoxin protein disulfide isomerase (PDI).[21] In its oxidized disulfide form, PDI is then used to introduce disulfide bonds into protein targets through thiol-disulfide exchange. In addition to the oxidative folding machinery, the ER can also use an isoform of NADPH oxidase (Nox4) that primarily generates H_2O_2 from O_2 by a two-electron reduction.[22]

NADPH oxidases (NOXs) and dual oxidase (DUOX) are the first families of enzymes that generate ROS not as by-product, but as their primary function.[23] Nox proteins are classically known as important ROS producers for the phagocytic killing of pathogens during the immune response. The NOX family consists of 7 transmembrane protein isoforms, NOX1-5 and dual oxidase (DUOX) 1–2, which possess similarities in terms of structure and enzyme function but although their similarities, each of them is activated by specific mechanisms and regulatory subunits. NOXs transfer electrons across biological membranes to produce O_2 $\bullet^-$ and H_2O_2.[23]

In addition to O_2 $\bullet^-$ and H_2O_2, a number of other oxygen-containing free radicals are capable of causing oxidation of essential cell components: nitric oxide (NO), peroxynitrite ($ONOO^-$), lipid hydroperoxides (LOOH), alkoxyl radical ($RO\bullet^-$), peroxyl radical (OOH), nitrogen-centered radical and sulfate radical ($SO_4\bullet^-\cdot$) originating by other biological enzymes as cyclooxygenases (COXs), lipoxygenases, xanthine oxidases, nitric oxide synthases and cytochrome p450 enzymes.

6.1 Regulation of ROS

ROS homeostasis is essential for normal signaling and survival, preventing cells from damage. Detoxification if achieved in two ways, by non-enzymatic and enzymatic antioxidants **(Figure 8)**. Non-enzymatic molecules include glutathione, flavonoids, bilirubin, ferritin, coenzyme Q, L-carnitine, alpha lipoic acid, melatonin, vitamins, iron, Nfr2, selenium, N-acetyl cysteine (NAC) and many others. Enzymatic antioxidants include superoxide dismutase (SOD), superoxide reductase (SOR), catalase, glutathione peroxidase (GPX), glutathione reductase (GSR), peroxiredoxin (PRX) and thioredoxin (TRX).[16,24]

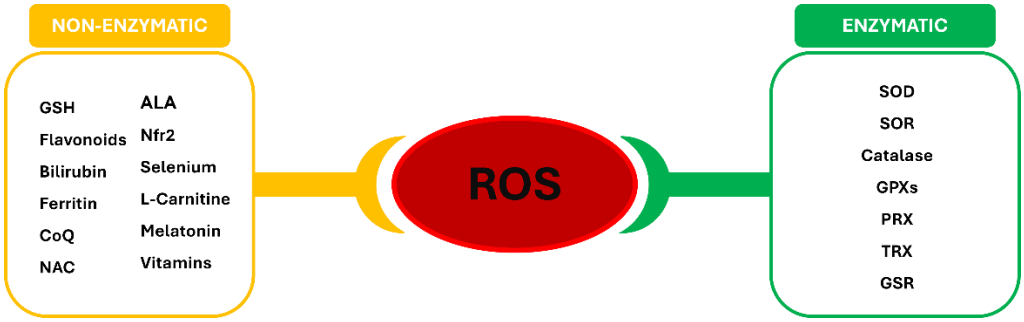


Figure 8. ROS scavenging mechanisms

6.2 Role of reactive oxygen species in cancer

The overproduction of ROS in cancer has been shown to induce a variety of biological effects such as enhanced cell proliferation, DNA damage and genetic instability, adaptation, cellular injury and cell death, autophagy and resistance to drugs.[25,26] The outcome is dependent on the genetic background of the cancer, the types of ROS involved (O2 $\bullet^{-}$, H_2O_2, etc.) and the levels and duration of ROS exposure.[26–29]

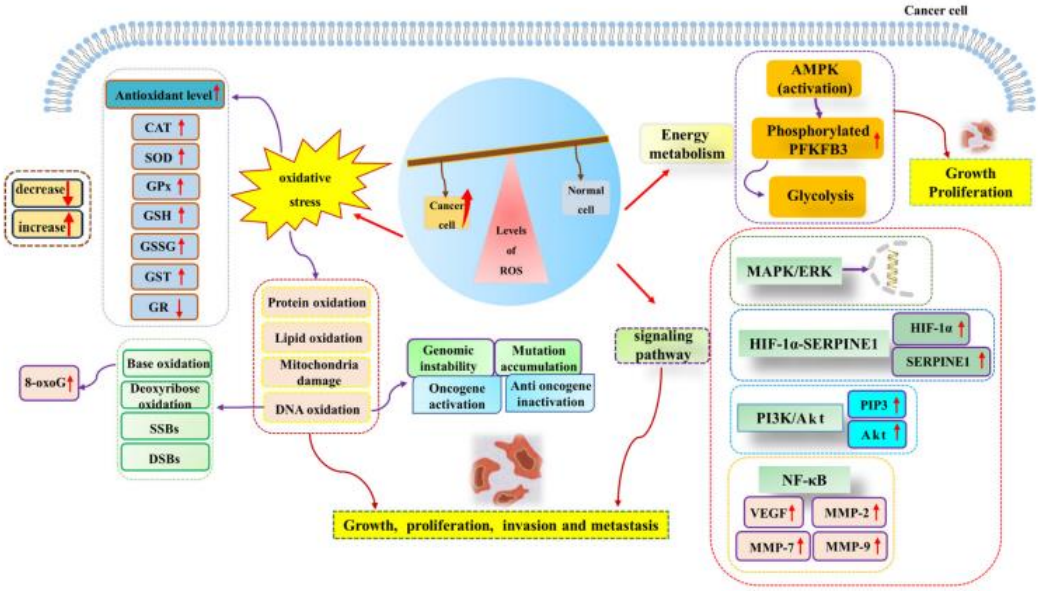


Figure 9. Schematic representation of ROS mediated cell signaling pathways and their biological effects. Source [30]

Enhanced cell proliferation and cell survival: an increase of ROS has been involved in cellular proliferation, increased cellular growth, cell survival and development of cancer through different biological pathways such as mitogen activated-protein kinase (MAPK)/extracellular-regulated kinase 1/2 (ERK1/2), phosphoinositide-3-kinase (PI3K)/Akt and protein kinase D (PKD) signaling pathways, negative regulation of phosphatases, PTEN and protein tyrosine phosphatase 1B (PTP1B), regulation of nuclear factor k−B (NF-kB) activating pathways, as well as mutations in transcription factors and tumor suppressor genes as Nrf2 and p53 **(Figure 9).**

Growth factors and K-Ras stimulated pathways have been shown to activate MAPK/ERK 1/2 in cancer and this has a role in the increased cellular proliferation.[31,32]

The Akt pathway has a function in cell survival through the phosphorylation and inactivation of its target proteins including pro-apoptotic Bad, Bax, Bim and Foxo transcription factors.[33–38]

PKD family of serine/threonine kinases consists of three members, PKD1-PKD3, which act as downstream of protein kinase C (PKC) and other signaling pathways. PKD signaling has been implicated in various human tumors including breast, pancreatic and prostate cancer and plays an important role in the detoxification from elevated ROS

production and stimulation of anti-apoptotic genes.[39–44] Inactivation of PTEN is found frequently in a variety of cancers including breast, endometrial cancers, glioblastomas, melanoma and prostate cancer.[45]

The transcription factor NF- B, has a role in proliferation, cell survival, regulation of the cell cycle and in the development of resistance to drug therapies.[46–48]

It is well established that p53 is lost or mutated in more than 50% of cancers, allowing for ROS accumulation and pro-tumorigenic signaling to occur.[49]

DNA damage and genetic instability: the overproduction of ROS is associated with an increase in DNA damage, and this may be important in terms of genetic instability. DNA damage causes oxidation of DNA, resulting in a variety of its alterations including deletions, insertions, base pair mutations and double strand breaks (dsbs) which are one of the most deleterious lesions.[50,51] Genomic instability has been suggested to be the major driving force of oncogenesis and can account for genetic diversity in many cancers.[52,53] For example mutagenic 8-oxo-7-hydro-2′-deoxyguanosine (8-oxodG) is considered one of major cause of spontaneous mutagenesis, because it induces guanine to thymine transversion through its capacity to pair with both cytosine and adenine.[54]

In the context of cancer initiation, an important target of mitochondrial ROS is mitochondrial DNA (mtDNA), as mutations in mtDNA seem to be capable of promoting tumorigenesis.[55,56] It encodes for example some components of the oxidative phosphorylation system (OXPHOS system) which is dysregulated in many cancer types. One reason for which mtDNA is more subject to mutation respect to nuclear DNA is the unprotection by histones, which limits the proofreading capacity and so ROS that is generated in the matrix can attack it.[57,58]

Adaptation: cells employ a variety of adaptation mechanisms in response to ROS and oxidative stress, for example with up-regulation of antioxidant system activity. Antioxidant enzyme systems in a cancer cell are regulated by the redox regulators including nuclear factor erythroid-2-related factor 2 (Nrf2), fork head homeobox type O family (FoxOs), ataxia telangiectasia mutated (ATM) and apurinic/apyrimidinic (AP) endonuclease1/redox factor-1 (APE1/Ref-1)

One particular adaptation of cancer cells is the modification of *cellular metabolism* **(Figure 10).** The uncontrolled growth leads to an accelerated formation of a tumor mass

that is accompanied in the first moment by increased formation of new vessels. ROS-dependent angiogenesis is initiated through cancer proliferation, which in turn increases the metabolic rate leading to the generation of high ROS levels.[59,60] At this first stage cancer cells maintain an aerobic respiration but when the cancer mass increases, the supply of nutrients and oxygen by new vasculature become difficult because of the hyperproduction of extracellular matrix and the stiffness of the tumor. In this case of hypoxia, cancer cells can modify their metabolism resulting in a variety of cell subtypes with different surviving modifications. Tumor cells adapt to hypoxia through a metabolic switch activating glucose metabolism, a phenomenon known as the Warburg effect and this contributes to an aggressive phenotype.[61,62] This switch in the glucose metabolism leads normally to reduction in oxygen consumption and ROS production, but many cancer cells maintain a substantial mitochondrial oxygen consumption and glycolysis despite the O_2 supply. The reason is not completely understood but many transcription factors are found to be modified. For example, hypoxia inducible factor-1 (HIF-1) is one of several transcription factors activated by hypoxia and ROS have been shown to mediate stabilization of HIF-1α in the signaling transduction pathways.[63–65]

In the mitochondrial matrix, non-specific ROS generation decreases during hypoxia and increases when cells are made hyperoxic.[66,67] However, release of ROS from complex III to the IMS increases paradoxically during hypoxia.[68,69] Although the specific mechanism has not been described, a likely source is the outer ubiquinone binding site (Qo-site) of complex III, in which lowered oxygen concentrations may prolong the lifetime of the semiquinone radical. This could enhance superoxide generation by augmenting the favoring conditions of its generation, even though the oxygen concentration is lower.[70]

The alteration of metabolism is accompanied by changing in other metabolic pathways that are interconnected between cytosol and organelles, as TCA cycle enzymes (e.g., α-ketoglutarate dehydrogenase, succinate dehydrogenase, fumarate hydratase and isocitrate dehydrogenase), ETC and OXPHOS enzymes, fatty acid oxidation (FAO), protein synthesis and one carbon metabolism.[71,72] In addition to altered metabolism, cancer cells also exhibit altered general functions, including transport, dynamics and response to oxidative stress. **(Figure 10)**

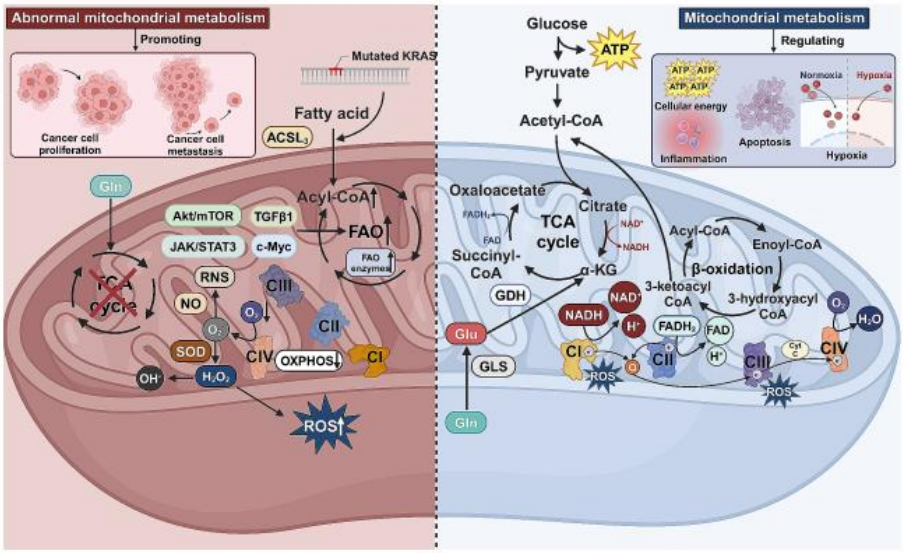


Figure 10. Mitochondrial metabolism and role in cellular energy dynamics and cancer development. Source: [73]

6.3 Cancer metastasis and ROS

Metastasis involves the spread of cancer cells from the primary tumor to the surrounding tissues and to distant organs, and it is the primary cause of morbidity and mortality.[74,75] It is a complex, multi-step process beginning with cancer cells in the primary tumor undergoing epithelial-mesenchymal transition (EMT, **Figure 11**). EMT is the process by which cells acquire plasticity and gain the properties of stem cells, in particular cells of a differentiated epithelial phenotype lose apicobasal polarity, become motile, and express markers characteristic of mesenchymal cells.[76,77] This leads to an invasive tumor epithelial phenotype characterized by detachment from and degradation of the basement membrane.[78] Several pieces of evidence have established a strong connection between EMT of epithelial cancer cells and ROS. For example TGF-β1 is well-established as one of the more prominent players of the induction of EMT.[79] For example TGF-β1 facilitate cell migration and invasion via the activation of NF-κB through the Rac1-NOXs-ROS-dependent mechanism.[80] Another important evidence is the acquisition of anoikic resistance of cancer cell mediated by ROS inducing activation of PI3K/Akt and ERK pathways[81] or by the upregulation of EGFR.[82,83]

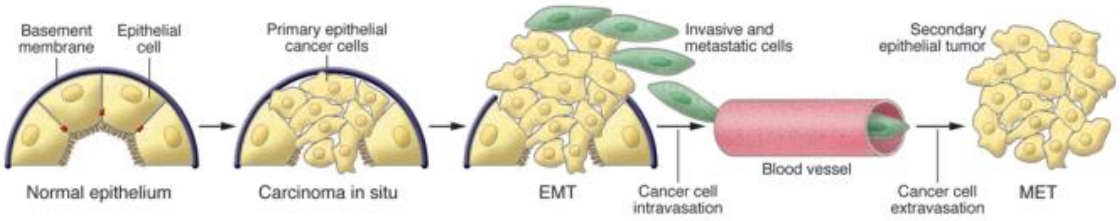


Figure 11. Progression from normal epithelium to invasive carcinoma through EMT. Source: [78]

7. Cell death

Excessive cellular levels of ROS cause damage to proteins, nucleic acids, lipids, membranes, and organelles, which can lead to activation of cell death processes such as apoptosis, autophagy, necroptosis, anoikis[30,84] and ferroptosis.[85] It has been already established the dual role of ROS in the cancer induction and regression since at higher levels respect to normal cell can induce proliferation and metastasis, but a disproportional increasing level can also damage and induce cell death in malignant cells. Apoptosis can be triggered by three main signaling pathways, upstream of caspase activation. These include an extrinsic pathway involving death receptors localized at the cell surface[86] or intrinsic pathways involving mitochondria or the ER.[87,88]

7.1 Autophagy

The process of autophagy, involving degradation of organelles and proteins range from prevention of infection to pathogen elimination to cell death and plays a crucial role in cellular processes which is associated with elevated ROS levels.[89] The tight interaction between ROS and autophagy is reflected in two ways, the induction by oxidative stress and the reduction of ROS by autophagy.[90]

7.2 Necroptosis

Necrosis was originally classified as an accidental form of cell death, where there was an explosive release of cellular contents following rupture of the cytoplasmic membrane.[91] Necroptosis emerged as a highly regulated process, likely dependent on cell type and tissue, but the intrinsic mechanisms is not clarified. The necroptosis activation is already verified in response to death receptors (e.g. TNF-R. Fas), Toll-receptors, viruses

and DNA damage.[92,93] In addition, ROS have been implicated in the induction and execution of cell death by necroptosis.[94]

7.3 Anoikis

Anoikis was first characterized by Frisch and Francis in 1994.[95] It is a cell death program where a cell dies when it becomes detached from the extracellular matrix (ECM), but in the case of cancer cells to undergo metastasis they need to inhibit anoikis[96] and ROS can take part to this mechanism.[81]

7.4 Ferroptosis: a new ROS mediated cell death

In addition to the well-known types of programmed cell death, one of these appeared interesting for its function in the biological activity of the normal cells, but particularly in the carcinogenesis process. In 2012 Dixon first proposed the concept of ferroptosis, an iron dependent cell death, characterized by the accumulation of lipid reactive oxygen species (LROS).[85] This new non-apoptotic cell death emerges from studies of RAS family small GTPases mutated in cancer cells where the treatment with two molecules, ERASTIN and RSL3 demonstrated new particular features different from apoptosis. (**Figure 12**) Ferroptosis is different from necrosis, apoptosis and autophagy in cell morphology and functions. Morphologically, ferroptosis mainly manifests shrinkage of mitochondria with increased membrane density and reduction in or vanishing of mitochondrial cristae, which is a different process from other modes of cell death. Biochemically there is an intracellular depletion of glutathione (GSH) and glutathione peroxidase 4 (GPX4), increased lipid peroxidation and iron homeostasis dysregulation.[85,97,98]

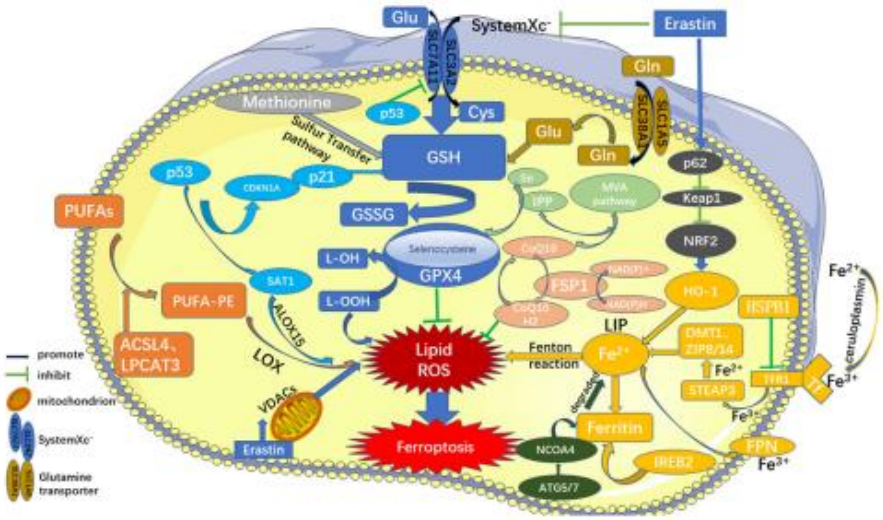


Figure 12. Regulatory pathways of ferroptosis. Source: [97]

A normal physiological function for ferroptosis as an adaptive and programmed form of cell death (e.g., during development) has not been established. Some degenerative pathologies appear to be caused by overwhelming the capacity to repair peroxidized lipids, resulting in cell death; emerging evidence also suggests that ferroptosis might serve a tumor suppressor function in removing cells. A large-scale characterization of ferroptosis sensitivity of cancer cell lines found that cancer cell lines have highly varied sensitivity to ferroptosis.[99]

7.4.1 Mechanisms of ferroptosis activation

7.4.1.1 Xc^- antiporter dysregulation

System Xc^- is a disulfide-linked heterodimer composed of SLC7A11 (xCT) and SLC3A2 (4F2hc and CD98hc) that exchange cystine and glutamate in and out of the cell at a ratio 1:1.[100] Cystine is than reduced to cysteine which is involved in the synthesis of glutathione (GSH). GSH takes part in the reduction of ROS and reactive nitrogen under the action of glutathione peroxidases (GPXs). The inhibition of the system Xc^- impairs the absorption of cystine and consequently the synthesis of GSH, affecting the activity of ROS scavenging; this ultimately increases the oxidative damage and induce ferroptosis.[85,99] Erastin inhibits Xc^- system by affinity with SLC7A5, reducing the uptake

of cystine. In cancer cells, inhibition of system Xc^- mediated cystine uptake by erastin, SAS or glutamate may be sufficient to initiate iron-dependent ferroptosis. Inhibition of system Xc^- is, however, not necessary; for example RSL3 and ML162, two direct GPX4 inhibitor does not inhibit cystine uptake and yet triggers an otherwise similar iron- and ROS-dependent ferroptotic death program.[101] **(Figure 12)**

7.4.1.2 Inhibition of GPX4

Among the many members of the GPX family, GPX4 plays a pivotal role in the ferroptotic process and is the key regulator of its occurrence, mainly by inhibiting the formation of lipid peroxides. This enzyme is directly dependent from Xc^- antiporter for the requirement of cystine to obtain GSH, required for its activity. GPX4 converts GSH into oxidized glutathione (GSSG) and reduces the cytotoxic lipid peroxides (L-OOH) to the corresponding alcohols (L-OH). RSL3, the first covalent ferroptosis inducer and other molecules as ML162 directly act on GPX4 and inhibit its activity, thus reducing the antioxidant capacity of cells and activating ferroptosis.[99,101,102] (**Figure 12**)

7.4.1.3 Regulation of lipid metabolism pathway

Lipid metabolism is closely related to ferroptosis. Indeed, the accumulation and the oxidation of specific lipids is connected with ferroptosis rather than generalized production of free radicals. Several studies have examined which lipids undergo peroxidation during ferroptosis. Lipidomic studies revealed that polyunsaturated-fatty-acid-containing phospholipids (PUFA-PLs) are the lipids most susceptible to peroxidation and drive the subsequent cell death.[103,104] (**Figure 12**)

Free polyunsaturated fatty acids (PUFAs) are substrates for synthesis of lipid signaling mediators, yet they must be esterified into membrane phospholipids. Lipid peroxidation is triggered by two essential mechanisms: [105]

- *the non – enzymatic pathway*: it is a free radical-driven chain reaction in which reactive oxygen species (ROS) initiate the oxidation of PUFAs. Fenton and Fenton-like reactions, which mainly involve the reaction between hydrogen peroxide (H_2O_2) and a transition metal such as free ferrous labile iron (Fe^{2+}), are

the main sources of hydroxyl radical formation that subsequently reacts with PUFA to form a lipid radical (L$^{\bullet}$), peroxyl radical (LOO$^{\bullet}$) and lipid hydroperoxides (LOOH) in a series of domino reactions;

- *the enzymatic pathway*: lipid peroxidation is mediated in a controlled manner primarily by the activity of the lipoxygenase (LOX) family. LOXs are nonheme iron-containing enzymes that catalyze the deoxygenation of free and esterified PUFAs to generate various lipid hydroperoxides.[106] There are also other well defined lipid peroxidation enzymes as cyclooxygenases (COXs)[107] and cytochrome p450 (CYPs).[108,109]

One reason that could explain the role of lipid peroxides in the process of ferroptosis is that membrane extensive oxidation and depletion of PUFAs might modify membrane fluidity and structure, and increase its permeability, eventually leading to a loss of integrity.[110] Anyway the exact mechanisms leading to ferroptotic cell death downstream of lipid peroxidation remain elusive.[111]

7.4.1.4 Iron metabolism

Iron is required in a variety of important biological processes including oxygen transport (as heme in hemoglobin), DNA biosynthesis (as a cofactor of ribonucleotide reductase), and ATP generation (as a cofactor for many proteins in the citric acid cycle and electron transport chain); therefore, cells must maintain a sufficient amount of iron. Fe^{2+} formed by intestinal absorption or erythrocyte degradation can be oxidized by ceruloplasmin to Fe^{3+}, which binds to transferrin (TF) to form TF-Fe^{3+}, which forms a complex through membrane protein TF receptor 1 (TFR1) to endocyte this complex[112]; Fe^{3+} is then reduced to Fe^{2+} by six transmembrane epithelial antigen of the prostate 3 (STEAP3), and Fe^{2+} is then stored in the unstable iron pool (LIP) and ferritin. Excess Fe^{2+} is oxidized to Fe^{3+} by ferroportin.[113] Abnormal distribution and content of iron in the body can affect the normal physiological processes. For example, iron is redox-active and can generate reactive oxygen species (ROS), leading to oxidative stress and initiation of signaling pathways crucial for cell survival and cell death. Changes in the iron pool plays a key role in the occurrence and development of ferroptosis. Free intracellular Fe^{2+} can

produce hydroxyl radicals or peroxide radicals under the action of the Fenton reaction[114], thus further oxidizing lipids.[104,115]

The specific role of iron in ferroptosis stays unclear. Ferroptosis cannot be explained by a simple increase in H_2O_2- dependent, iron-catalyzed ROS production, rather, the last results are most consistent with one or more iron-dependent enzymes functioning as part of the core oxidative lethal mechanism.[85] (**Figure 13**)

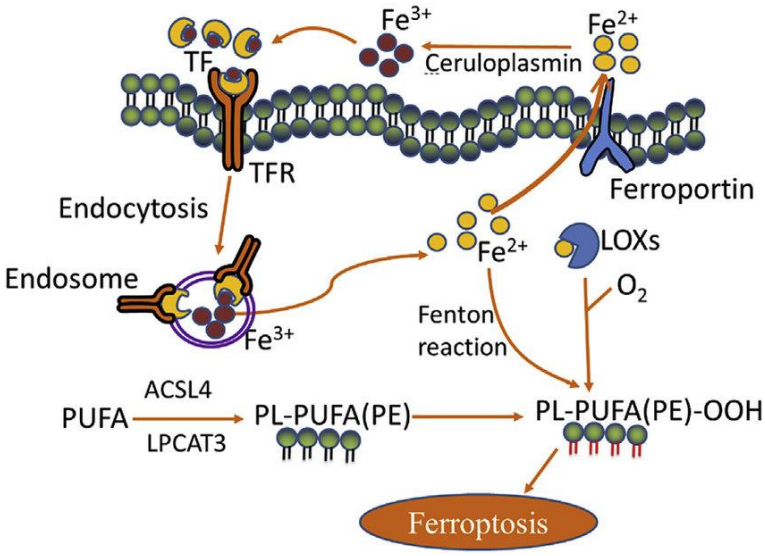


Figure 13. Iron metabolism and its role in the ferroptotic process. Source: [116]

7.4.1.5 P53-mediated ferroptosis

The guardian of the genome p53, encoded by the TP53 gene, is a crucial tumor suppressor that is mutated or inactivated in more than half of all human cancers. The p53 protein achieves its diverse cellular outcomes by canonical activity serving as a DNA-binding transcription factor that selectively modulates the expression of certain p53 transcriptional target genes and inducing cell-cycle arrest, senescence, or apoptosis. However, non-canonical functions of p53 such as controlling metabolism and redox state can also contribute to tumor suppression by regulating ferroptosis.[117–119] For example by transcriptional suppression of SLC7A11, a component of the cystine/glutamate antiporter, p53 inhibits cystine uptake and sensitizes cells to ferroptosis.[120] Conversely, depending on the p53 mutation status and cellular context, p53 can have either pro- or anti-ferroptotic functions in response to oxidative stress.[117,121]

7.4.2 Ferroptosis as druggable pathway for diseases' therapy

Ferroptosis is evidently a valuable mechanism for the potential treatment of various diseases. This pathway can be modulated in two ways: induction of ferroptosis can be used to eliminate malignant cells, while its inhibition can help prevent cell loss and tissue deterioration in degenerative diseases.[122–124]

In the context of anti-cancer therapy ferroptosis can be induced operating to many targets: the inhibition of the system Xc^- can affect the supplying of cystine, thus influencing the production of GSH, but also providing direct inhibition of some GSH synthesis enzymes.[125] GPX4 inhibition is one of the main processes either indirectly caused by the depletion of GSH (which is essential for its peroxidative activity) or directly by blocking its enzymatic activity.[99] Iron overload and subsequent increase of Fenton peroxidation can be altered by upregulation of iron import, export and storage.[113]

7.4.2.1 Ferroptosis inductors

Four classes of ferroptosis inductors (FINs) have been identified[111,126] :

- *class I FINs* acts by depriving cells of the amino acids cysteine and consequently reducing the amount of GSH, necessary for the ROS scavenging of GPX4 increasing the oxidative stress and ferroptosis. This result can be obtained by blocking the system Xc^-, and this effect is obtained with Erastin and its more potent and stable derivatives imidazole ketone (IKE) and piperazine[99] or with sulfasalazine and sorafenib. GSH synthesis can be prevented also by inhibition of glutamate-cysteine ligase (GCL) with buthionine sulfoxime[99,127] or by blocking the glutathione S-transferase by Artesunate;[128]
- *class II FINs* acts through direct inhibition of GPX4. [1S,3R]-RSL3 and ML162 covalently interact with GPX4 selenocysteine 46 in the active site but also in other allosteric sites as C66; although these compounds are useful for mechanistic studies, these are unfortunately not suitable for in vivo development;[129]
- *class III FINs* acts by indirect inhibition of GPX4 and depletion of mevalonate coenzyme Q10 (CoQ10), an important radical trapping agent. FIN56

is a dual ferroptosis inhibitor that depletes GPX4 and inhibits squalene synthase in distinct manner;[130]

- *class IV FINs* includes compounds that induce ferroptosis by increasing LIP or oxidizing iron. To date, $FINO_2$ is the only compound of this class used in vitro but not evaluated in vivo.[131]

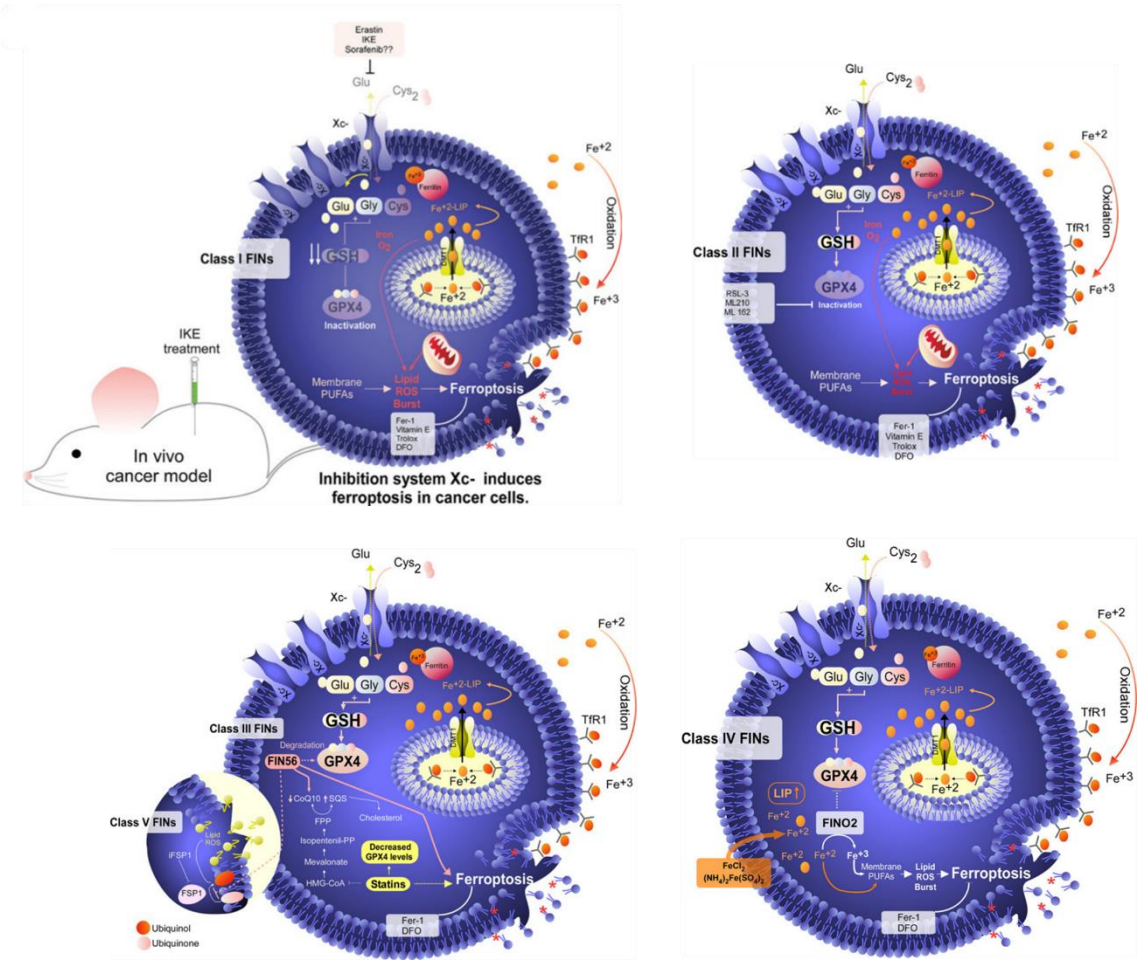


Figure 14. Illustration of the classes of ferroptosis inductors and their mechanism. Source: modified image from [126]

8. Pancreatic ductal adenocarcinoma

Pancreatic ductal adenocarcinoma (PDAC) is the sixth leading cause of cancer-related deaths, accounting for nearly 5% of all cancer-related fatalities worldwide. (**Figure 15A**) The projection of incidence in 2030 indicates that PDAC will become the second most prevalent cause of cancer-related death (**Figure 15B**).[132] With its high mortality rate (about 91%) and 5-year survival rate (10% to 12%) this disease is among the poorest in terms of prognosis.[2] The cause of high mortality rate of PDAC stems primarily from the lack of early diagnosis and ineffective treatment for advanced tumors. Therefore, a deeper understanding of cancer biology and its peculiarities is necessary to improve the diagnosis and the therapeutic strategies.

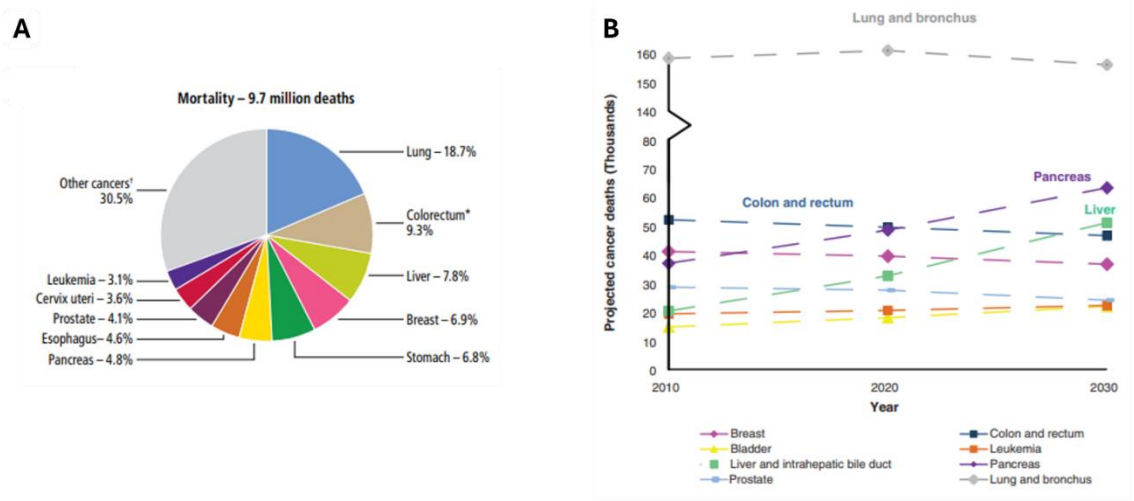


Figure 15. A) Distribution of deaths for the 10 most common cancers, 2022. B) Death projections of the top cancer cells to 2030. Source: [5,132]

8.1 Pathogenesis

The pancreas contains cells of exocrine (acinar), epithelial (ductal), and endocrine (α, β, δ, ε) type, among which acinar cells are well known for their high degree of plasticity that drives the regeneration and homeostasis. The pancreas, derived from the endodermal lineage, is composed of functionally distinct compartments that all originate from a common pool of progenitors. Exocrine acinar cells secrete digestive enzymes that are supplied to the gut through an elaborate ductal tree, and endocrine cells regulate blood

glucose through secretion of hormones, including insulin and glucagon from β and α cells, respectively. (**Figure 16**)

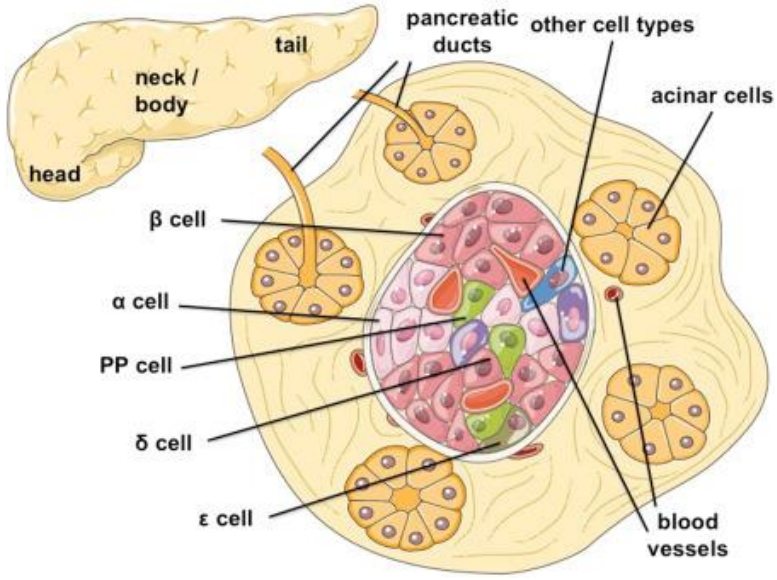


Figure 16. Illustration of the various cell types in pancreas. Source: [133]

In contrast to other organs, pancreas seems to lack of well defined stem cell compartment and acinar cells, with their high plasticity, drives pancreas homeostasis and regeneration[134] in a process called acinar-to-ductal metaplasia (ADM) (**Figure 17).**[135] During ADM, acinar cells dedifferentiate to a ductal-like morphology, losing their mature functional characteristics and adopting embryonic progenitor properties.[136] The metaplasia of pancreatic acinar cells manifests their ability to adapt to the genetic and environmental pressure they encounter, showing a crucial role in the post injury regeneration[134] but also as precursors that lead to the development of pancreatic intraepithelial neoplasia (PanIN) (**Figure 17**) which is a common precancerous lesion that precedes PDAC.[137,138]

From a general view PDAC presents as a poorly demarcated, firm white–yellow mass, with the surrounding nonmalignant pancreas typically showing atrophy, fibrosis, and dilated ducts due to the obstructive effects of expanding carcinoma. In the early disease the histology manifests several distinct type of precursor lesions such as pancreatic intraepithelial neoplasia (PanIN), formerly classified in low grade (PanIN1 and 2 type)

and high grade (PanIN3),[139] intraductal papillary mucinous neoplasm (IPMN) and mucinous cystic neoplasm (MCN).

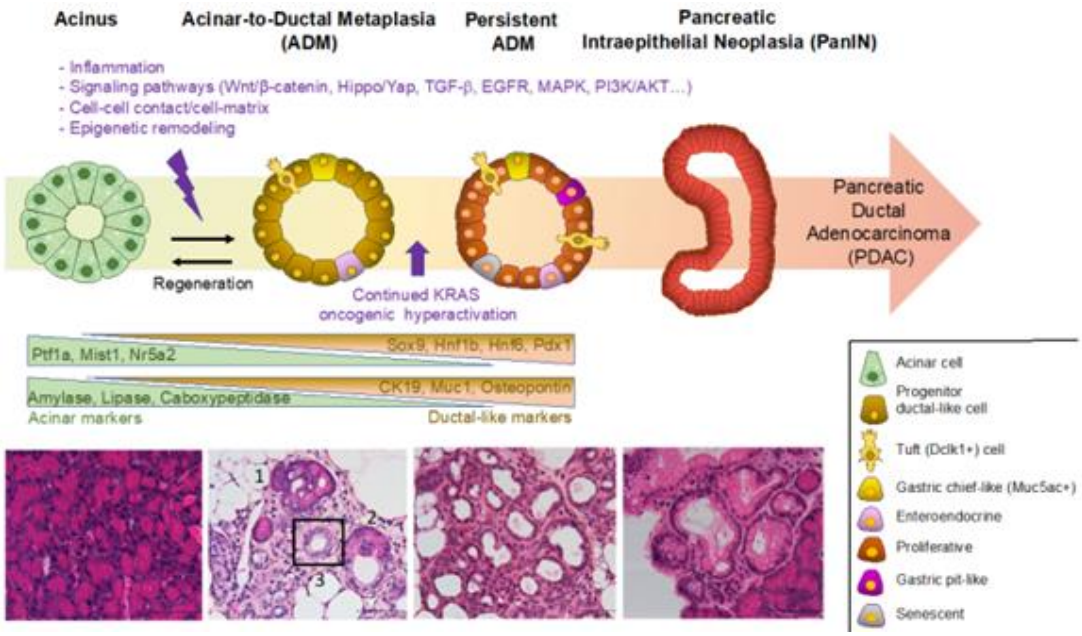


Figure 17. Model of acinar-to-ductal metaplasia (ADM) initiation to pancreatic intraepithelial neoplasia (PanIN). Source: [135]

8.2 The PDAC genome

PDAC, highlighting the disease's myriad mutations, gene expression changes, epigenetic alterations, chromosomal rearrangements, and copy number aberrations includes the oncogenic KRAS mutation and the frequent inactivation of TP53, SMAD4, and CDKN2A tumor suppressors.[140] The transcriptomic panorama of PDAC is not entirely governed by genetic alterations but also by integrated epigenetic regulatory circuits comprising chromatin-based mechanisms, such as DNA methylation and histone post-translational modification, as well as regulation by non-coding RNAs. In this regard, key tumor suppressor genes have been described to be repressed, and oncogenes upregulated due to epigenetic alterations in the tumor progression and metastasis.[141]

The prevalence of oncogenic KRAS mutation in PDAC ranges from 88% to 100%[142] that leads to frequent alteration of embryonic signaling pathways as transforming growth factor β (TGFβ), Notch, Hedgehog (Hh), and Wnt–β-catenin signalling[143] and the major

downstream effectors that include RAF/MEK/MAPK, PI3K/PTEN/AKT, and RAL-GDS pathways.[144]

8.3 The PDAC metabolism

In the case of PDAC, alterations in metabolic programs may be particularly important for the growth and survival of cancer cells given nutrients and oxygen-poor tumor microenvironment, perhaps due to dense stroma and hypo vascularization. Examples of the classic features modifications of tumor metabolism is enhanced glycolysis and conversion of glucose into lactate even when oxygen is available for OXPHOS, a phenomena known as Warburg effect[145] which is also observed in PDAC.[146] The increased glucose uptake is possible by up-regulation of multiple glycolysis enzymes including glucose transporter type 1 (GLUT1), hexokinase ½ (HK1/2), phosphofructokinase 1 (PFK1) and lactate dehydrogenase A (LDHA). Another function of oncogene KRAS in PDAC is to reprogram the use of glycolysis intermediates, especially through the pentose phosphate pathway (PPP),[147] important to provide macromolecules as NADPH, that is essential for ROS scavenging. PDAC also uses an alternative metabolism pathway for the maintenance of redox homeostasis, through the use of glutamine, which is converted in oxalacetate and combined to produce NADPH.[144]

8.4 The PDAC stroma

The PDAC stroma is composed of myofibroblasts, suppressor immune cells such as MDSCs, regulatory T (Treg) cells, tumor-associated macrophages (TAMs), and acellular components such as collagen, cytokines, and soluble growth factors. (**Figure 18**) All these components contribute to the initiation, progression, metastasis, immune infiltration, and drug resistance.

The desmoplastic stroma can constitute up to 90% of the tumor volume and is commonly considered to originate from cancer-associated fibroblasts (CAFs) with distinct subtypes.[148] Pancreatic stellate cells (PSCs) are the predominant fibroblasts present in the PDAC stroma that in healthy situation secrete matrix metalloproteinases (MMPs) and acts as lipid-storing cells. In contrast, upon pancreatic injury such pancreatitis or PDAC, cells

lose their cytoplasmic lipid storage, increase ECM production, acquire a myofibroblast-like phenotype, leading to the classical observed fibrosis.[144] In this environment the Hedgehog dysregulated pathway plays an important role driving CAFs to produce pro-tumorigenic factors and increase cancer angiogenesis by paracrine signals.[143]

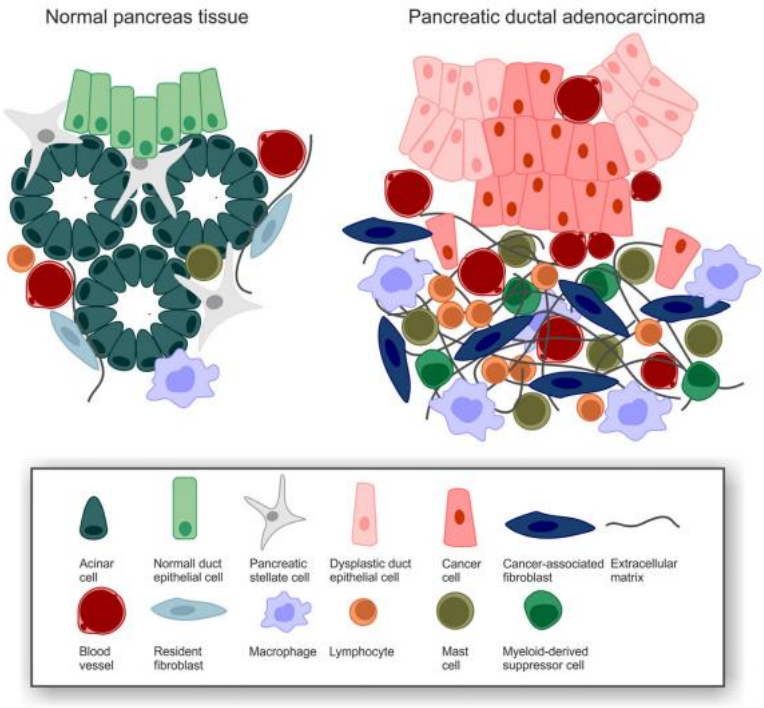


Figure 18. Illustration of PDAC desmoplasia. Source: [148]

8.5 The immunosuppressive microenviroment

In the PDAC microenvironment, the process of inflammation plays a crucial role for cancer progression. Nonetheless many studies have associated pancreatitis with risk of the development of pancreatic cancer.[149,150] The multi immunocompetent of the PDAC microenvironment acts to create a barrier for the migration and infiltration of T-cells avoiding their cytotoxic activity; for example, macrophages that are recruited, adopt an immunosuppressive state, block CD4+ T cell, entry into the PDAC microenvironment and support PDAC progression. On the cytokine level, the PDAC microenvironment represents a comparable degree of complexity. Nevertheless, the dominating cytokines seem to be transforming growth factor beta (TGF-β), interleukin (IL-) 6, IL-8 and many

others that have a role of immunosuppressive, proliferation, angiogenesis, invasion and migration.[144]

8.6 Metastasis

Another nasty trait of PDAC is its early progression to metastatic disease and unfortunately the lack of rapid diagnosis makes the treatment more difficult. One metastatic mechanism seems to be determinant in PDAC as other cancer types, the Epithelial to mesenchymal transition (EMT)[138,151] **(Figure 19**), which is also considered a Hallmarks of Cancer.[13] EMT is a biologic process that allows an epithelial cell, which normally interacts with basement membrane via its basal surface, to undergo multiple biochemical changes that enable it to assume a mesenchymal cell phenotype. Such phenotype acquires enhanced migratory capacity, invasiveness, elevated resistance to apoptosis, and greatly increased production of ECM components.[78] Once tumor cells invade through the tumor stroma, they have the capacity to disseminate in circulation and colonize distant organs, the latter influenced by the pre-metastatic niche and organotropism.

The transition from epithelial to mesenchymal cells is not irreversible, as several rounds of EMT and MET (mesenchymal to epithelial transition) are necessary for the final differentiation of specialized cell types and the acquisition of the complex three-dimensional structure of internal organs; this is an important dual interconversion necessary for metastasis cell to disseminate and create a new core of cancer neoplasia in other organs.[76,77,138] Activation of EMT might be triggered by various signaling pathways depending on the tumor microenvironment. Indeed, tumor-associated stroma can increase the expression of EMT-transcription factors (EMT-TFs). Several signaling pathways are included, as transforming growth factor β (TGF-β), bone morphogenic protein (BMP), Notch, Wnt/βcatenin, sonic hedgehog, epidermal growth factor (EGF), fibroblast growth factor (FGF), and platelet-derived growth factor (PDGF). In cancer cells, EMT can be activated through different stimuli. Marcucci et al. have identified five main classes of stimuli: mechanical stress, low pH and hypoxia, innate and adaptative immune responses, altered ECM and treatment with anti-tumor drugs.[152] PDAC is well known for its desmoplastic stroma with high presence of CAFs that takes part in the EMT transition which is present already in the early stage of tumorigenesis.[138] **(Figure 19**)

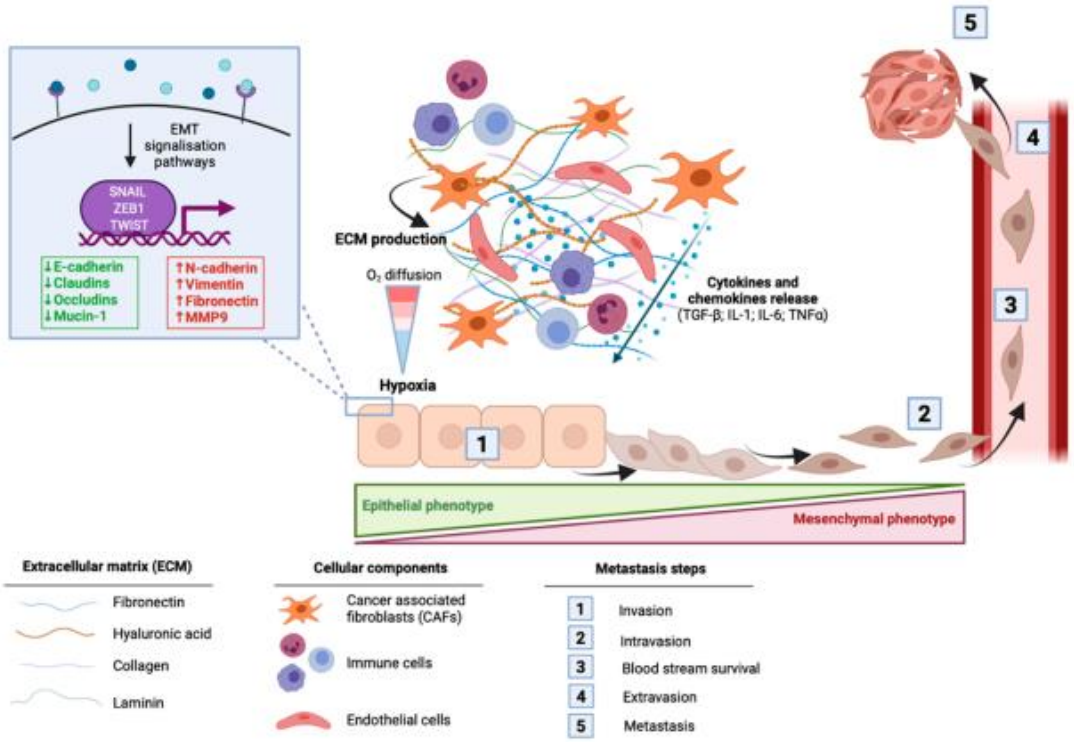


Figure 19. Impact of the tumor microenvironment of pancreatic ductal adenocarcinoma (PDAC) in the activation of epithelial to mesenchymal transition (EMT) and metastasis. Source: [151]

8.7 PDAC treatment

The problem of late diagnosis makes PDAC difficult to manage with the several weapons available to the therapists and the efficacy and outcome of treatment are largely determined by the stage of disease. Surgical resection accompanied by chemotherapy is the only curative choice but only for 10-20% of PDAC patients, because the remaining 80-90% show advanced and non-resectable stages, including metastasis and often resistance to treatment.[148] Radio(chemo)therapy has been rather infrequently adopted for the treatment of PDAC, since the majority of patients suffer from disseminated stages in which local treatment procedures are of secondary importance.[153] Apart from its potential to induce tumor cell death, radiotherapy could be useful to recondition the tumor microenvironment and to stimulate systemic anti-tumor immune responses (abscopal effects of radiotherapy).[154,155]

Patients with locally advanced or metastatic PDAC are generally considered non-curative and managed with palliative intent. Systemic chemotherapy is commonly employed as first-line treatment in patients with non-resectable or borderline-resectable tumors. It can be used as an adjunct to other therapies (surgery or radiotherapy) in order to maximize the effect (adjuvant or augmented therapy) or as pre-treatment (neoadjuvant). (**Figure 20**) Gemcitabine, Irinotecan, Erlotinib, 5-Fluorouracil, Epirubicin, Oxaliplatin, Paclitaxel and Docetaxel are some of the drugs used in monotherapy, but also in combination (FOLFIRINOX, Gem-nabP, FOLFOX, etc.) to reduce the intrinsic toxicity of these chemicals and also improve the therapy efficacy, considering the intrinsic resistance of the PDAC.[148,156]

Study	Design	Local stage	Chemotherapy	n	Resectability	R0 rate	Median OS (months)
McKenzie 2013	Phase 2 trial	Res	Gem/nP	25	80.0%	95%	NA
O'Reilly 2014	Phase 2 trial	Res	Gem/oxaliplatin	38	71.0%	74%	27.2
Sliesoraitis 2014	Phase 2 trial	Res/BR	Gem/nP vs surgery	32 (10 vs 22)	80% vs 100%	60% vs 77%	NA
Ielpo 2016	Phase 2 trial	Res/BR	Gem/nP	25	68.0%	100%	21
Katz 2016	Phase 1/2 trial	BR	mFOLFIRINOX	22	68.0%	93%	21.7
Okada 2017	Phase 1 trial	BR	Gem/nP	10	80.0%	70%	NA
Tsai 2018	Phase 2 trial	Res/BR	5-FU or gemcitabine-based chemotherapy, depending on molecular profiling	130	82.0%	81%	38
Reni 2018	Phase 2/3 trial	BR/LA	Gem/nP vs Gem/nP/cis/cap	54 (28 vs 26)	32% vs 31%		NA
Murphy 2018	Phase 2 trial	BR	FOLFIRINOX + CRT	48	66.6%	97%	37.7
De Marsh 2018	Phase 2 trial	Res	FOLFIRINOX	21	81.0%	94%	34
Wei 2019	Phase 2 trial	Res	Gem/erlotinib	114	73.0%	81%	21.3
Barbour 2020	Phase 2 trial	Res	Gem/nP	42	71.4%	86%	23.5
Sohal 2020	Phase 2 trial	Res	FOLFIRINOX vs Gem/nP	55 vs 47	73% vs 70%	85% vs 85%	22.4 vs 23.6

Abbreviations: Gem = gemcitabine, nP = nab-paclitaxel, CRT = chemoradiation therapy, OS = overall survival, Res: resectable, BR: borderline resectable.

Figure 20. Recent trials on neoadjuvant chemotherapy, resectability and outcomes. Source: [156]

CHAPTER II

DEVELOPMENT OF NOVEL REACTIVE OXYGEN SPECIES (ROS)-MODULATING AGENTS

Chapter II - Development of novel reactive oxygen species (ROS)-modulating agents

1. State of art

Considering the dual role of ROS in cancer development, both as tumor-specific factors for the malignant progression and as contributor to toxicity at high levels[27,157], it is well established that the efficacy of many anticancer therapies, including chemotherapy and radiotherapy, largely depends on their ability to induce ROS accumulation and evoke cell toxicity and death.[30] In this context, the manipulation of REDOX homeostasis in cancer cells including PDAC could be a promising strategy to improve the efficacy of therapies and overcome drug resistance. Despite their adaptability to high ROS levels, cancer cells are more susceptible to exogenously induced ROS-mediated cell death. Increasing the oxidative stress could overwhelm their adaptive capacity and promote cell death, while sparing healthy cells, which would be able to counteract the oxidative insult by normal scavenging mechanisms.[158] (**Figure 21**)

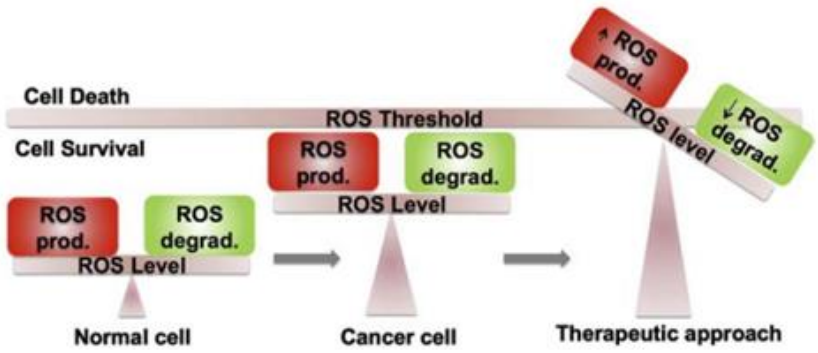


Figure 21. Rationale for ROS-mediated cancer therapy. Normal cells mantain homeostasis by balancing ROS generation and scavenging. Many cancer types exhibit elevated oxidative stress which promote tumor initiation, progression and metastasis while also triggering adaptive responses to increased ROS levels. However, their inherently higher basal ROS levels make cancer cells more susceptible to exogenously induced ROS-mediated cell death, a vulnerability that can be exploited as a therapeutic strategy. Source: [159]

My PhD research work is a direct continuation of a decade-long project developed in the "Drug Design and Nanomedicine" laboratory, coordinated by Prof. Mario Sechi at the

University of Sassari, in collaboration with Prof. Nouri Neamati at the University of Michigan. This project was planned to develop new chemotherapeutic prototypes for the treatment of PDAC and other resistant cancer types. The rational aimed on the observation that PDAC and other cancer typologies exhibit dysregulated intracellular ROS levels, which which can be exploited as a therapeutic strategy. By using ROS-inducing chemotherapeutics, these cancer cells can be driven to undergo ROS-mediated cell death.

In an initial study aimed at discovering new compounds that alter cellular energetics, a new class of quinazoline-5,8-dione (QDs)-based compounds was identified through a laboratory screening of approximately 1,000 drug-like small molecule and demonstrated a significant increase in cellular oxygen consumption[159] (**Figure 22A).** After structural optimization of this novel chemotype, QD232 or Sarkostat showed increased cytotoxicity and inhibition of cancer cell proliferation by MTT assay in different cancer cell lines (BxPC-3, MIA PaCa-2 and PANC-1). Furthermore, the oxygen consumption rate analysis (OCR) and other related experiments confirmed the increased level of ROS production of cancer cells treated with QDs (**Figure 22B)**. Western blot assay showed induction of p-Akt by QDs and subsequently downstream activation of FoXO3a by phosphorylation and inactivation, reducing expression of its target enzyme MnSOD (ROS scavenger), thus confirming the dysregulation of ROS production in mitochondria and cytoplasm (**Figure 22C)**. Increased ROS generation by Sarkostat resulted in immediate and sustained activation of stress kinases' pathways (p38, JNK) that were implicated in induction of cell death.[160–164]

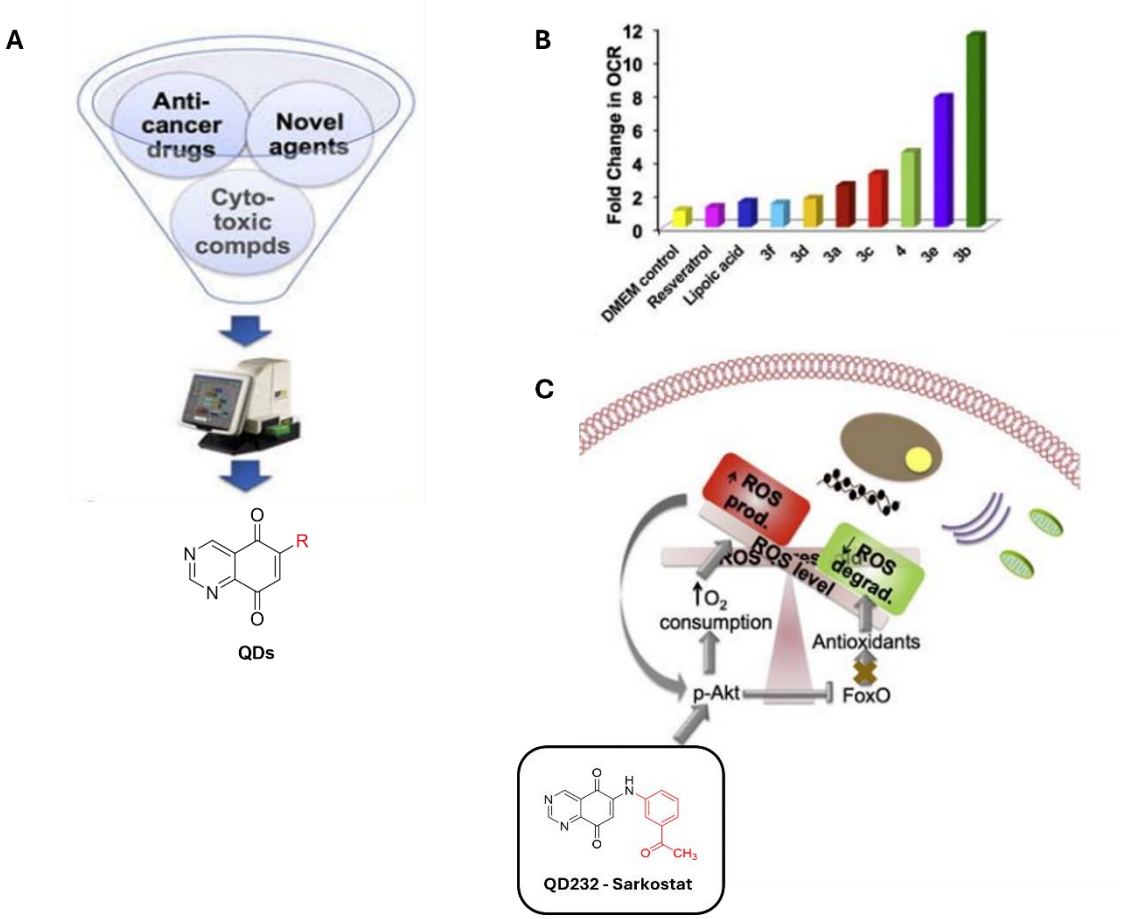


Figure 22. A) Quinazoline-5,8-dione prototype was identified by a medium throughput screening of an in-house database using XF24 Flux Analyzer. B) Fold change increase in OCR was most significant for compound QD232. C) QD232 induces ROS-mediated cell death in cancer cells. Treatment with QD232 resulted in Akt-directed increase in cellular oxygen consumption, ROS production and decreased antioxidants' expression (MnSOD and catalase). Finally, increased cellular ROS resulted in activation of stress kinases and induction of cell death in cancer cells. Source: image modified from [159]

Later mechanistic studies on Sarkostat were performed to obtain more information about its cytotoxicity and ROS modulation in PDAC.[165] Pancreatic cancer has numerous mutations in genes that modify the normal signal transduction pathways. One of these, Src Kinase is overactivated and several studies have successfully validated Src and its phosphorylated form (pSrc) as novel biomarkers for pancreatic cancer.

The effort to develop new treatments for pancreatic cancer led to the evaluation of Dasatinib, a potent Src inhibitor that showed inhibition of migration and invasion resulting in tumor growth reduction in vivo. Nevertheless, Dasatinib also induced resistance because of the lack of inhibition of signaling via the STAT3 and MAPK

pathways.[166] STAT3 reactivation following Src inhibition occur in several forms of cancer resulting in resistance to Src inhibitors.[167]

Treatment of pancreatic cancer cells with Sarkostat showed decrease of tumor growth without significant toxicity in healthy cells (**Figure 23 A, B)**. Sarkostat showed inactivation of Src, FAK and STAT3 in different manners. (**Figure 23 C**)
Treatment of MIA PaCa-2 and PANC-1 cells with Sarkostat decreased the activating phosphorylation of FAK and Src in their activating and inactivating phosphorylation sites in concentration and time dependent time. Since Src protein family promotes the activation of target proteins as paxillin and p130 which are important for cell migration, cell were treated also for these two protein showing their inactivation, suggesting inhibition of cell migration (**Figure 23 C, D**).

The Src/FAK complex governs cell cycle progression by regulating several downstream targets.[168] So the dysregulation of these two factors by Sarkostat supports the arrest of cell cycle. Sarkostat caused cell death decreasing Bcl-2 (survival protein) and increasing expression of pro-apoptotic protein Bax without abnormalities in normal tissue samples.

As regards STAT3, the lack of its inhibition by phosphorylation (p-STAT3) is one of the reasons for resistance to Dasatinib therapy.[166] STAT3 is a transcription factor regulated by Src cascade and its activation by phosphorylation leads to increased cell proliferation, angiogenesis and tumor growth in vivo.[169] Tumor cells treated with Sarkostat showed a clear decrease in p-STAT3 and subsequent increased apoptosis, decreased proliferation, and decreased tumor size. In MIA PaCa-2 cells STAT3 is activated even in the absence of Src and interestingly Sarkostat was able to decrease STAT3 phosphorylation in Src knocked down MIA PaCa-2 pancreatic cells, but not in the presence of antioxidants. This behavior suggested a possible other pathway of STAT3 ROS-dependent inactivation.

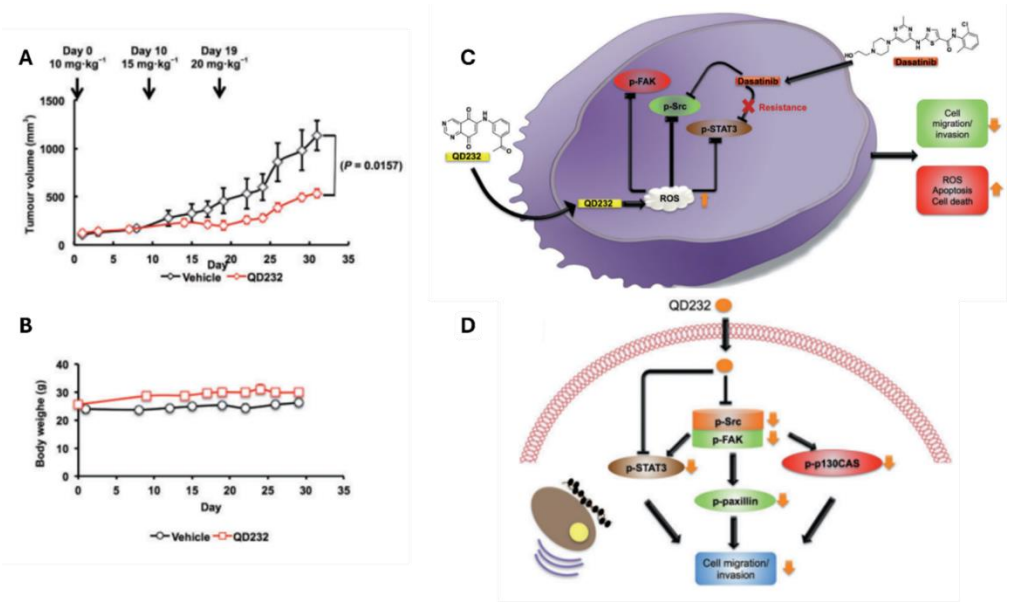


Figure 23. QD232 suppresses tumor growth in a mouse xenograft model of pancreatic cancer A) The plot shows the tumor volumes (means ± SD) among the treatment groups over the course of the experiment. B) Treatment with QD232 does not result in loss in body weight. C) Proposed mechanism of action of QD232. D) Schematic representation of the effects of QD232 on selected cell-signaling pathways. Source: image modified from [165]

In a 2018 study, Sechi and coll. conducted a hit-to-lead optimization of Sarkostat (QD232) by modifying the side chain of the quinazoline-5,8-dione ring system and applying different substitutions on the phenyl ring to explore lipophilicity and steric effects.[170] (**Figure 24**)

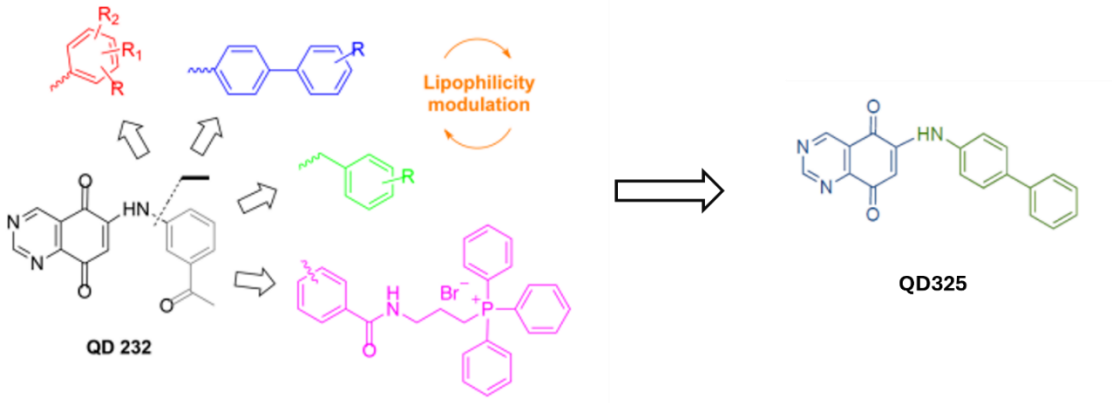


Figure 24. Lead optimization from QD232 to QD325. Source: image modified from [170]

From this new set of derivatives, QD325 showed the most potent redox modulation, inducing substantial reactive oxygen species in PDAC. In terms of antiproliferative activity in pancreatic cancer cells, QD325 was found to be the most potent analogue with IC50 values <1 μM in all three PDAC cell lines (MIA PaCa-2, Panc-1, and BxPC-3) and gemcitabine resistant MIA PaCa-2 cell line (**Figure 25A**). The increased ROS production of QDs well correlated with improved cytotoxic profile (**Figure 25B**)

A

ID	IC $_{50}$ (μM)[a]		
	MIA PaCa-2	MIA PaCa-2-GR	HPDE
232	2.3 ± 0.2	3.6 ± 0.6	4.5 ± 0.6
325	0.9 ± 0.2	1.0 ± 0.3	2.7 ± 0.3
326	1.5 ± 0.1	2.0 ± 0.1	3.2 ± 0.4
340	15.3 ± 2.5	17.7 ± 1.8	18.3 ± 2.1
359	16.3 ± 3.5	16.2 ± 1.9	24.3 ± 1.2
gemcitabine	0.11 ± 0.07	3.3 ± 0.6	0.14 ± 0.05

[a]Data is presented as mean ± SD from three independent experiments.

B

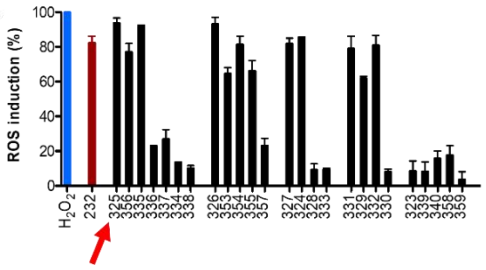


Figure 25. A) Cytotoxicity of QD compounds in Gemcitabine resistant MIA PaCa-2 cells and normal pancreatic cells by MTT assay. B) QD compounds correlation with ROS induction. Image modified from [170]

To better elucidate the mechanism of QDs, transcriptomic studies were done using RNA Bru-Seq technique. Bru-Seq analysis captures nascent RNA and provides information on the current transcription genome-wide without interference by pre-existing RNA. The results showed increased synthesis of NQO1 and HMOX1 RNAs after treatment with QD325 in a dose-dependent manner. NQO1 (which encodes the NAD(P)H quinone oxidoreductase1) and HMOX1 (which encodes for heme oxygenase) are two target genes of NRF2 transcription factor that is rapidly activated in response to oxidative stress.

Transcription of the two stress-responsive genes DDIT3 and HSPA5 is significantly increased by Sarkostat or QD325 treatment in a dose-dependent manner. DDIT3 gene products CHOP which promotes apoptosis by induction of transcription of pro-apoptotic genes PUMA and BIM. HSPA5 encodes the activation of GRP78 an inhibitory factor of IRE-a1, one of the three pathways of UPR (unfolded protein response). Deregulation of the expression of mitochondrial genes can lead to interruption of the oxidative phosphorylation pathway, resulting in the accumulation of ROS. Bru-seq data showed that QDs inhibited the transcription of mtDNA for these essential genes for mitochondrial oxidative phosphorylation (**Figure 26).**

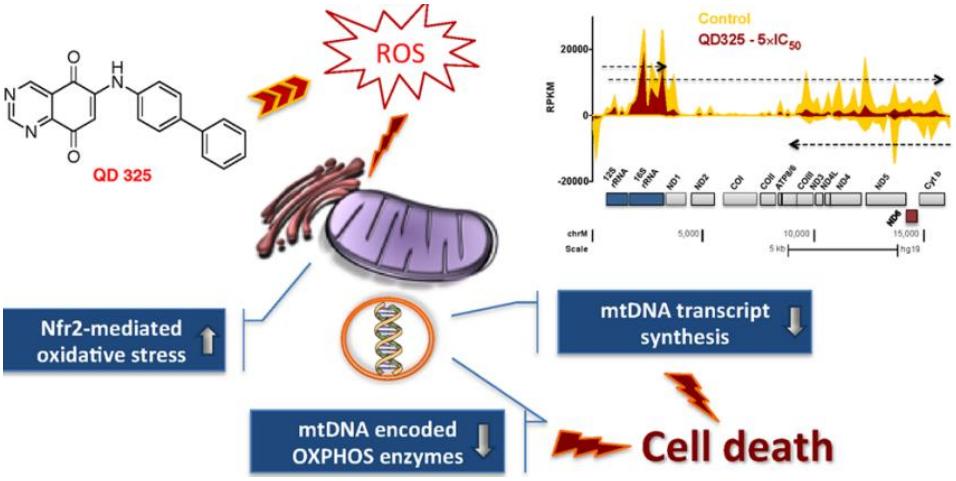
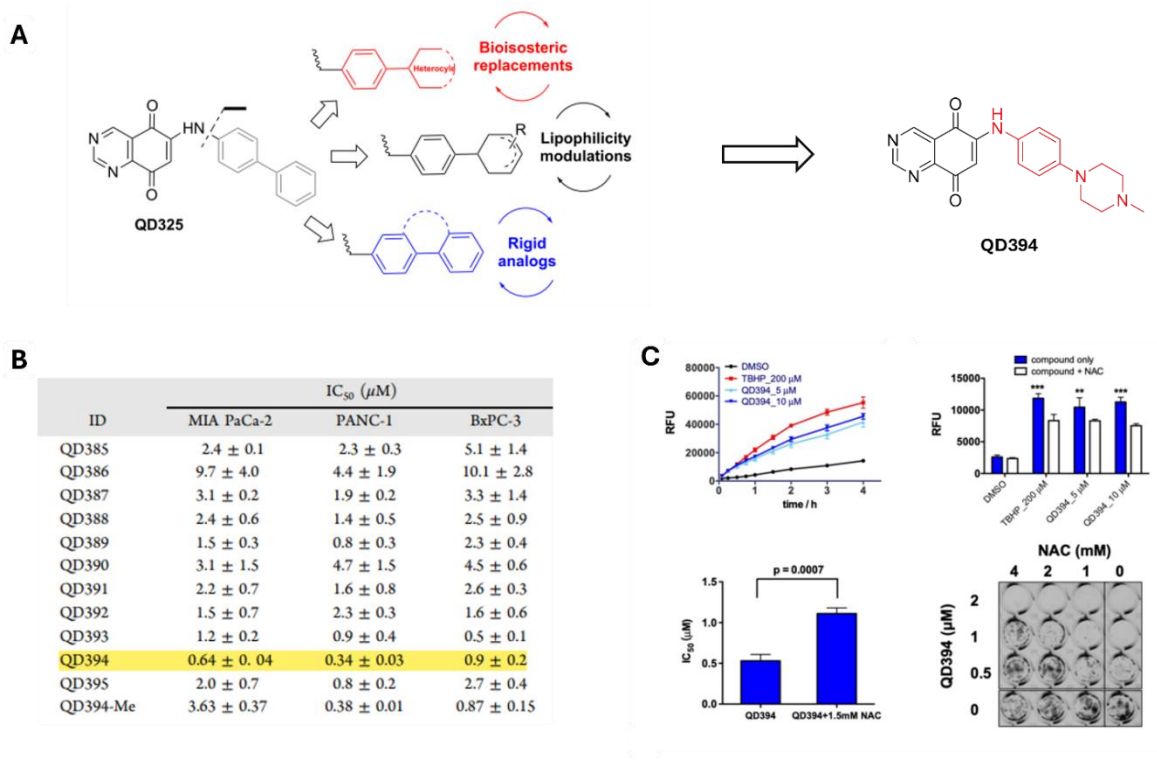


Figure 26. Treatment with QD325 shows inhibition of nascent mitochondrial RNA synthesis and promotion of ROS production. Source: [170]

The next step of the structural optimization campaign was performed to identify compounds able to induce maximum ROS production.[171] (**Figure 27A**). The N-methyl-piperazine analogue QD394 showed the best profile (**Figure 27B**) and was selected for further mechanistic studies. QD394 induced the highest level of intracellular ROS (**Figure 27C**), and Bru-seq experiments confirmed a similar mechanism of action with QD325. QD394 showed dysregulation of STAT3 signaling and increasing phosphorylation of H2AX, a DNA damage biomarker. Further proteomics analysis performed to measure the changes caused by QD394 showed reduced expression of proteins involved in mitochondrial RNA catabolic processes and showed synergic effect in the colony formation assay of both MIA PaCa-2 and PANC31 cells with other cytotoxic agents. Interestingly, the cells treatment with Napabucasin (a STAT3 and stemness inhibitor) and QD394 separately showed opposite effect when combined with necrostatin-1 (necroptosis inhibitor). Indeed, only cells treated with Napabucasin/Necropstatin-1 showed cell death inhibition confirming a different mechanism of cell death between QDs and Napabucasin.



ID	IC_{50} (μM) MIA PaCa-2	PANC-1	BxPC-3
QD385	2.4 ± 0.1	2.3 ± 0.3	5.1 ± 1.4
QD386	9.7 ± 4.0	4.4 ± 1.9	10.1 ± 2.8
QD387	3.1 ± 0.2	1.9 ± 0.2	3.3 ± 1.4
QD388	2.4 ± 0.6	1.4 ± 0.5	2.5 ± 0.9
QD389	1.5 ± 0.3	0.8 ± 0.3	2.3 ± 0.4
QD390	3.1 ± 1.5	4.7 ± 1.5	4.5 ± 0.6
QD391	2.2 ± 0.7	1.6 ± 0.8	2.6 ± 0.3
QD392	1.5 ± 0.7	2.3 ± 0.3	1.6 ± 0.6
QD393	1.2 ± 0.2	0.9 ± 0.4	0.5 ± 0.1
QD394	0.64 ± 0. 04	0.34 ± 0.03	0.9 ± 0.2
QD395	2.0 ± 0.7	0.8 ± 0.2	2.7 ± 0.4
QD394-Me	3.63 ± 0.37	0.38 ± 0.01	0.87 ± 0.15

Figure 27. A) Lead optimization of QD235 to QD394. B) Cytotoxicity of QD Compounds in MIA PaCa-2, PANC-1, and BxPC-3 Pancreatic Cancer Cell Lines. C) UP: Some plots indicating the generation of cellular ROS by QD394 and the reduction of ROS by co-treatment with NAC. DOWN: MTT assay and colony formation assay show the reduction of cytotoxicity by treatment of cell lines with QD94 and NAC. Source: image modified from [171]

The stability of QD394 in the liver microsomes and plasma were performed, but half-life of 60 minutes and 6 minutes, for liver microsomes and plasma, respectively, indicated a poor metabolic stability. After determination of possible metabolites of QD394, a new 6-position protected derivative QD394-Me synthesized and tested, resulting in improved plasma stability [171].

On the other hand, pancreatic cancer cells showed increased survival when treated with QDs and glutathione (GSH) confirming ROS-mediated cell death mechanism. Further investigations on the role of GSH in the mechanism of QDs induced cell death shared decreasing of GSH/GSSG ratio instead of direct decrease of total GSH level (**Figure 28 A, B**). In this scenario ferroptosis, which is a ROS induced cell death but with different peculiar characteristics, was suggested as a potential mechanism of action for QDs (**Figure 28 C**),.[85] The measurement of increasing intracellular lipid ROS and the rescue in combination with deferoxamine and deferasirox (iron chelators) in the QD394 and 394-

Me treated tumor cells indicated the role of ferroptosis as the mechanism of action of QDs derivatives. Further studies using cellular thermal shift assay (CETSA) to detect interaction between QD models (i.e. QD394 394-Me) with GPX4, an important central mediator in ferroptosis, indicated a destabilization of GPX4 protein, and corroborated their possible role in the inhibition of the enzyme (**Figure 28 A, B**).

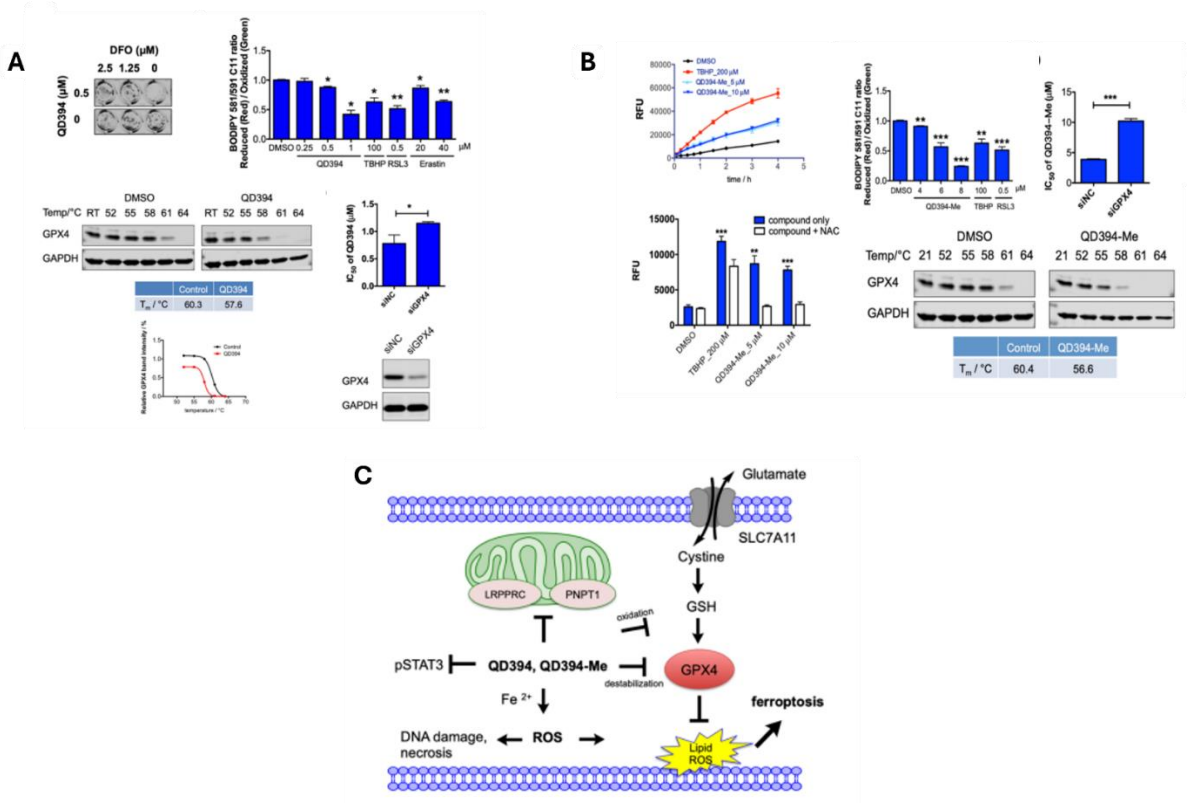


Figure 28. A) UP LEFT: QD394 inhibition of colony formation assay after treatment with DFO; UP RIGHT: induction of lipid peroxidation similar to THBP, RSL3 and Erastin; DOWN: the potential interaction between QD394 and GPX4 was determined by the cellular thermal assay. B) LEFT: QD394-Me increased cellular ROS level and NAC reduced ROS after treatment; RIGHT: QD394-Me increased level of lipid peroxidation, cytotoxicity was reduced in GPX4-knockout MIA-PaCA-2 cells. siNC: samples treated with scamble siRNA, siGPX4: samples treated with GPX4 siRNA; the potential interaction between QD394-Me and GPX4 was determined by the cellular thermal shift assay. Source: image modified from [171]

2. Rational of the PhD work

QD394 demonstrated significant therapeutic potential in several cancer types at an advanced preclinical stage; however, improving its pharmacokinetic properties, along with achieving more consistent efficacy, was necessary. One of the objectives of this PhD project was to explore new strategies to enhance the pharmacological profile of QDs in order to obtain further preclinical data. In this context, using the key synthon (1) and the lead compound QD394 as a platform for the new modifications, several approaches to develop a new set of congeners were considered. (**Figure 29**).

Specifically, the modification of the side chain at position 6 of the quinazoline-5,8-dione was designed to elucidate its contribution to the activity in terms of chemical characteristics, including solubility, steric hindrance, and electronic properties. The introduction of a biotin/biotin-PEGylated side chain was considered to improve the lipophilicity/hydrophilicity balance of the QDs. On the other hand, a bioisosteric replacement of the quinazoline-5,8-dione heteroaromatic platform with quinoxaline-5,8-dione was proposed to assess the contribution of a different heterocycle to the activity of the QD compounds.

Previous metabolomic study[171] indicated several metabolic modifications, both at position 7 on the quinazoline-5,8-dione backbone and at various sites on the side chain, which could impact the stability and half-life of the QDs in plasma. Therefore, blocking potential metabolic sites on the aromatic and aliphatic rings seemed a suitable strategy to create protected derivatives of QD394 for further biological studies.

Since cancer cells pretreated with QDs exhibited increased ROS production in both the cytoplasm and mitochondrial compartments, a set of chimeric QD-probes linked to fluorescent dyes was designed to gather information about their cellular localization. Furthermore, keeping in mind the possible role of QDs in the activation of ferroptosis and the role in the dysregulation of the central enzyme GPX4[171], several biological assays, specifically designed to obtain further detailed information, were planned.

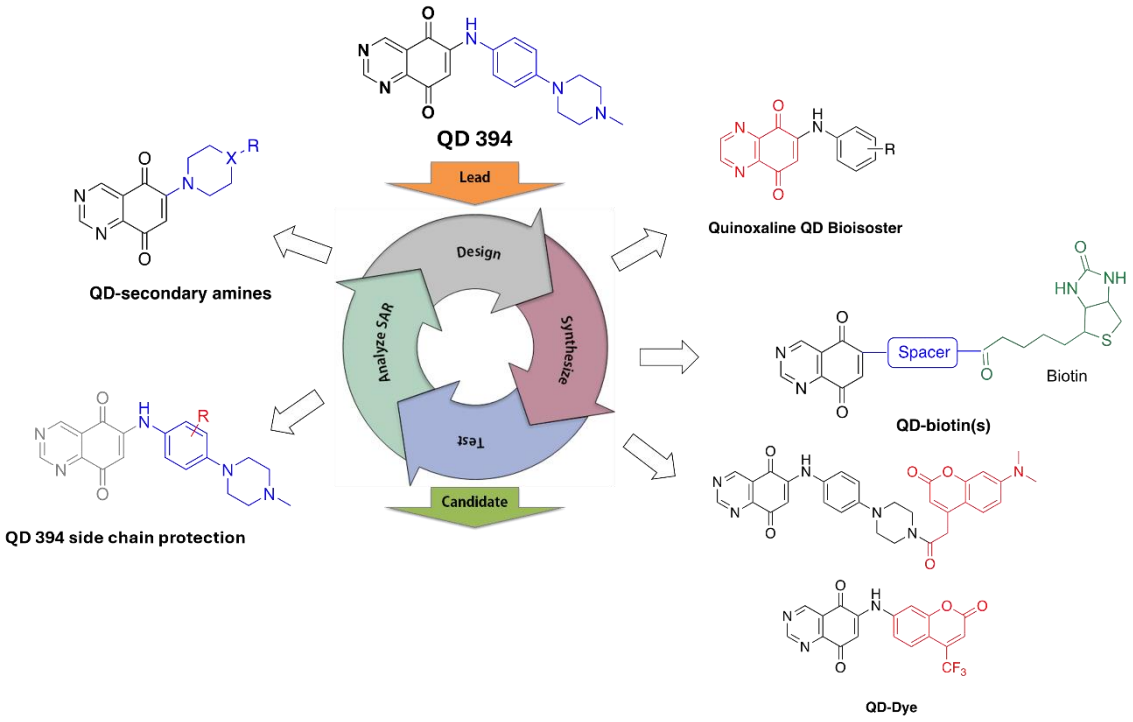
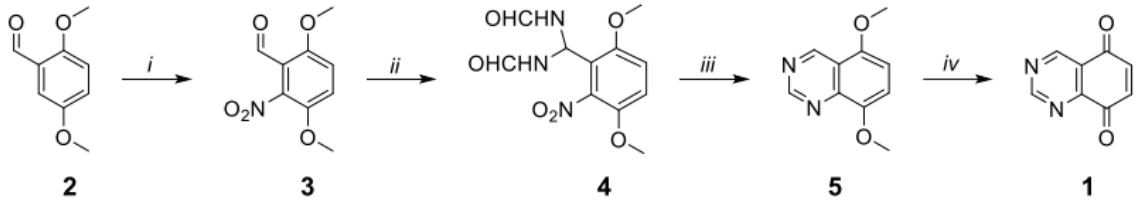


Figure 29. Lead optimization strategies proposed for QD in the PhD project.

2.1 Preparation of the quinazoline-5,8-dione

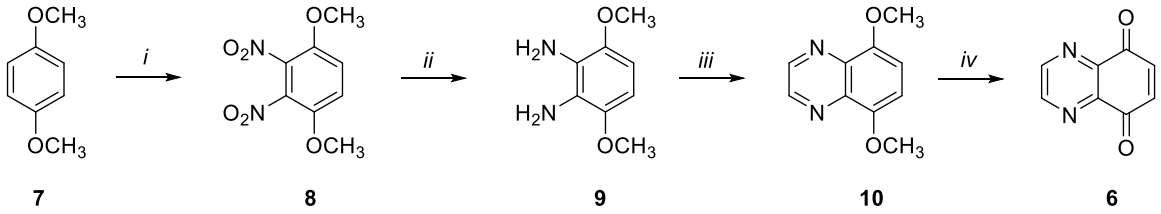
The key synthon quinazoline-5,8-dione **1** is the heterocyclic platform for the preparation of all the designed derivatives. **1** was prepared by using a previously optimized synthetic approach [170], where the 2,5-dimethoxybenzaldehyde **2** was reacted with fuming nitric acid and acetic anhydride, followed by isomeric separation with flash chromatography, to give the nitroderivate **3**. The latter was then converted in the bis-formamide derivative **4** using gaseous hydrochloric acid and formamide, with subsequent reduction of the nitro group to amine with zinc in acetic acid, followed by immediate cyclization to the quinazoline **5**. Finally, **5** was then converted to the desired synthon **1** using cerium ammonium nitrate (**Scheme 1**).



Scheme 1. Synthetic scheme for the preparation of quinazoline-5,8-dione. Reagents and conditions: (i) conc. HNO_3, $(CH_3CO)_2O$, 0 °C, 1.5 h; (ii) H_2NCHO, HCl(g) from 40 to 80 °C, 1 h; (iii) glacial CH_3COOH, Zn, 0°C for 2 h, rt for 4 h; (iv) $(NH_4)_2Ce(NO_3)_6$, CH_3CN/H_2O, 0 °C, 20 min

2.2 Preparation of the quinoxaline-5,8-dione

The preparation of the bioisosterically substituted heteroaromatic synthon **6** was designed introducing some modification to the quinazoline-related synthetic route. Starting from the para-dimethoxy benzene derivative **7**, a vicinal bis-nitration was carried out using fumic nitric acid, which gave the 1,2 and the 1,4 dinitro isomers. After separation, the isomer **8** was converted to the diamine **9** by tin/hydrochloric acid, and subsequently cyclized to the dimethoxy-quinoxaline **10** using glyoxal and sodium bisulfite. **10** was then converted to diketone **6** using cerium ammonium nitrate. (**Scheme 2**)



Scheme 2. Synthetic scheme for the preparation of quinoxaline-5,8-dione. Reagents and conditions: (i) conc. HNO_3, 0 °C 1.5 h, r.t 1 h, 90 °C 1 h; (ii) HCl conc., tin, reflux, 3 h; (iii) NaHSO3, glyoxal 40%, 75 °C, 3h (iv) $(NH_4)_2Ce(NO_3)_6$, CH_3CN/H_2O, 0 °C, 20 min.

2.3 Coupling reaction with the key synthons

The coupling reaction for all the proposed side chains was carried out using cerium chloride heptahydrate as a catalyst to facilitate a selective Michael-like addition at position 6 of the heteroaromatic platform, specifically in the quinazoline-5,8-dione scaffold. This approach ensured regioselectivity and allowed for efficient

functionalization while maintaining the core structure necessary for biological activity. (**Figure 30 A**). Mechanistically, the explanation of regioselectivity can be attributed to the formation of complex by nitrogen in first position and the carbonyl group in position 8 of the key synthon (in the case of quinazoline-1,4-dione ring) with cerium ion, which increases the reactivity as Michael acceptor for the nucleophilic attack by the amines **(Figure 30 B**)

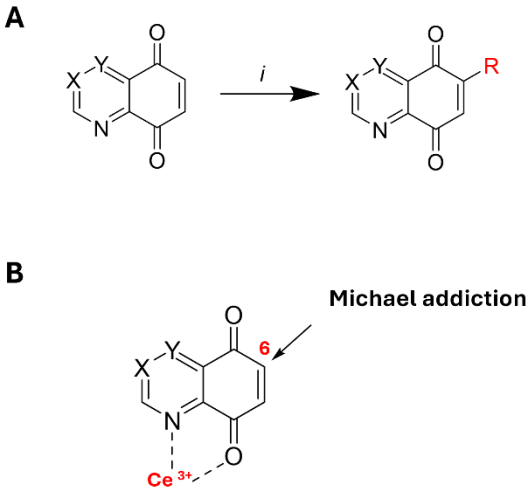


Figure 30. A) Scheme of the final coupling reaction for the obtainment of QDs (X= C or N , Y= N or C). Reagents and conditions: $CeCl_3 \cdot 7H_2O$, amine/aniline side chain, abs EtOH, r.t, 3 h. B) Cerium (III) coordinates with nitrogen in position 1 and oxygen in position 8 withdrawing the electron density in the position 6 and favoring the regioselective Michael addiction of the side chain.

2.4 The new set of QDs

To modulate the physicochemical properties of QDs, a new set of compounds was designed and synthesized, focusing on modifications to the lateral chain of the quinazoline-5,8-dione scaffold. These modifications explored variations in chemical topology, steric hindrance, and polarity. In particular, the introduction of aliphatic lateral chains was evaluated to assess the impact of the aromatic portion on the overall properties and activity of the compounds. The choice to replace the aromatic portion with an aliphatic nucleus bearing a piperazine or piperidine moiety was driven by the intent to retain aminic properties, which are commonly found in many drug compounds[172,173], while also exploring the impact of chemical property modifications between aromatic and aliphatic structures. To further investigate the chemical properties, the introduction of

aromatic and heteroaromatic moieties linked to the aliphatic amine was also explored (Figure 31). All the selected side chains were commercially available and directly used in the coupling reaction. (**Figure 30 A**)

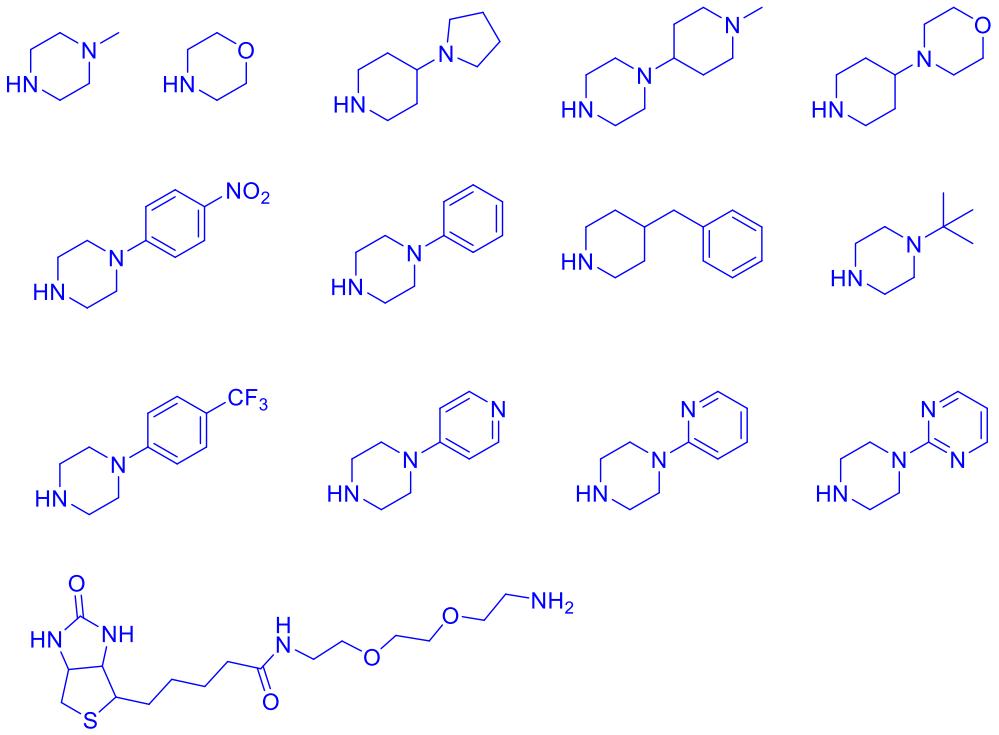
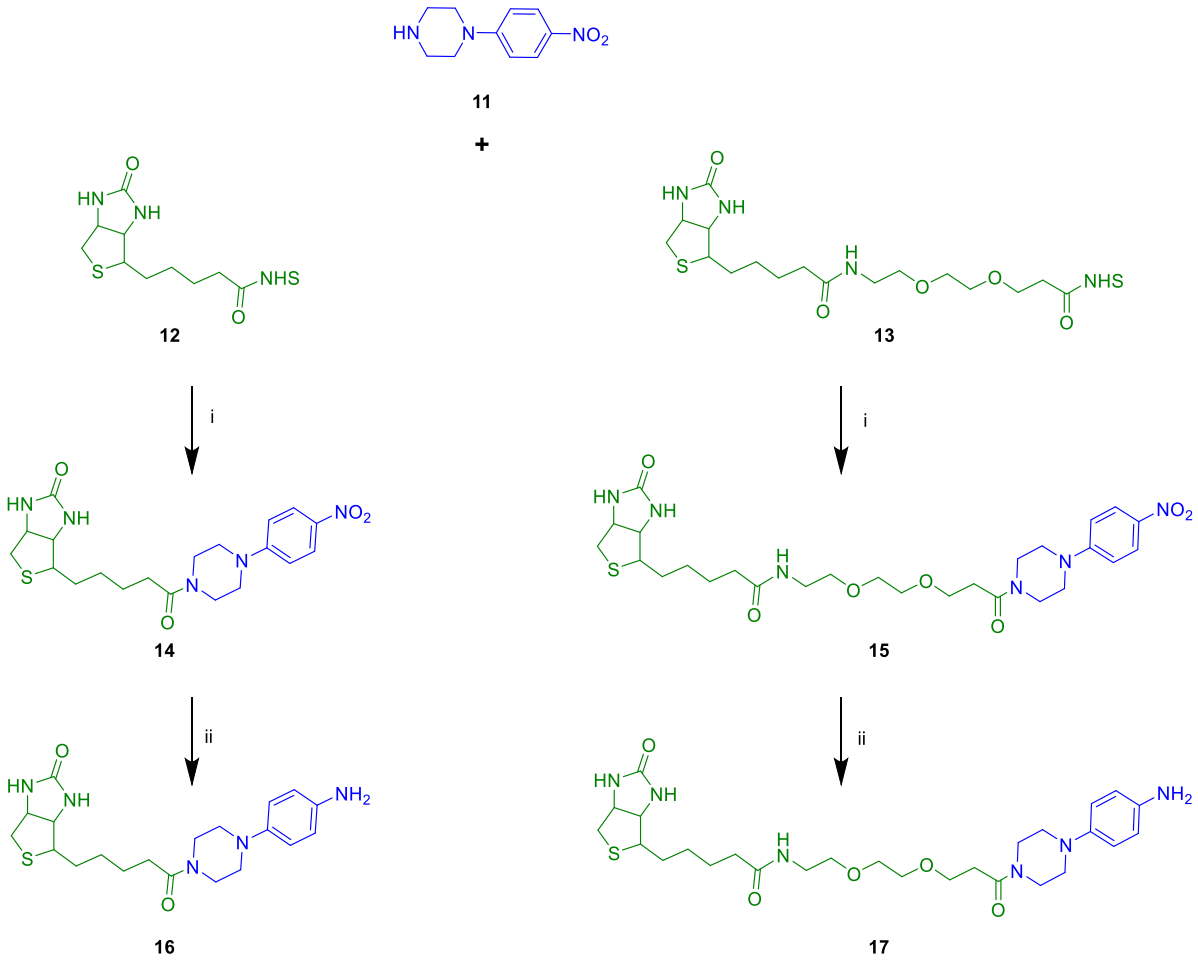


Figure 31. List of side chain proposed for the preparation of the new series of QDs.

2.5 Preparation of biotin/biotin-PEGylated QDs

The two pegylated lateral chains were obtained by following the same synthetic plan (**Scheme 3**). Operatively, amines **16** and **17** were prepared in two steps by coupling the 1-(4-nitrophenyl)piperazine **11** with activated biotin NHS in the presence of DIPEA to obtain the derivatives **12** and **13**, which were isolated in the first step. Then, reduction of **12** and **13** with ammonium formate and Pd/C afforded the anilines **14** and **15**, which were coupled to **1** using the previously mentioned procedure (**Figure 30 A**). The derivative QD444 (bearing the only biotin-PEG side chain) was prepared by coupling the synthon **1** with the biotin-PEG-amine linker (**Figure 31**) using the same regio-selective procedure (**Figure 30 A**)



Scheme 3. Synthetic scheme for the preparation of the biotin/biotin-PEGylated side chains. Reagents and conditions: (i) DIPEA, CH_3CN, 5 h, rt; (ii) $HCOONH_4$, 10% Pd-C, MeOH anh, r.t, 2 h

2.6 Preparation of fluorescent QD-dye probes

To detect the QDs in the cellular compartment we planned to prepare two QDs fluorescent probes by linking **1** with appropriate coumarin-based side chains, which were previously used as probes for fluorescent detecting analysis.[174] The 7-dimethylamino coumarin derivative **18** was synthesized from the diethylaminophenol **19** and diethoxy-3-oxopentanoate **20** in the presence of zinc chloride. The resulting coumarin ester **2**1 was then hydrolyzed to the corresponding acid **22** using lithium hydroxide. This acid was subsequently used in a coupling reaction with nitrophenyl-piperazine **11** in the presence of EDC and hydrated HOBt. The resulting nitro derivative **23** was reduced to the corresponding aniline using 10% Pd/C, and the final compound was obtained by coupling

with key synthon **1**. The same reaction (**30 A)** was used for the direct coupling of the trifluoro coumarin derivative **31** (Figure **32 B**)

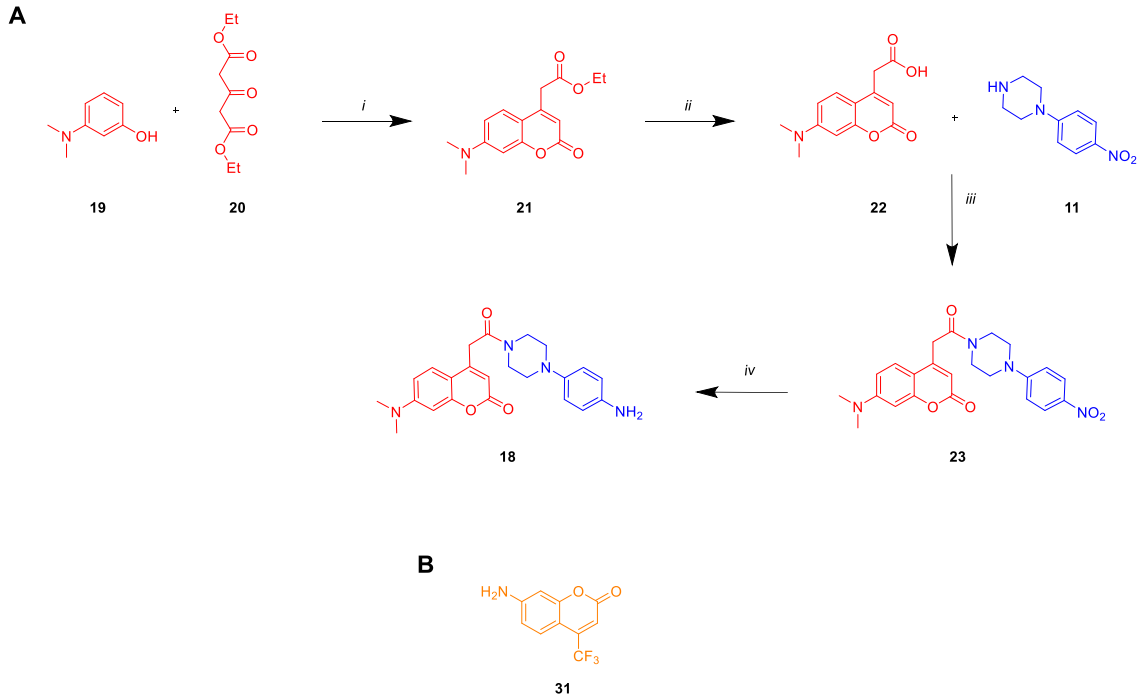
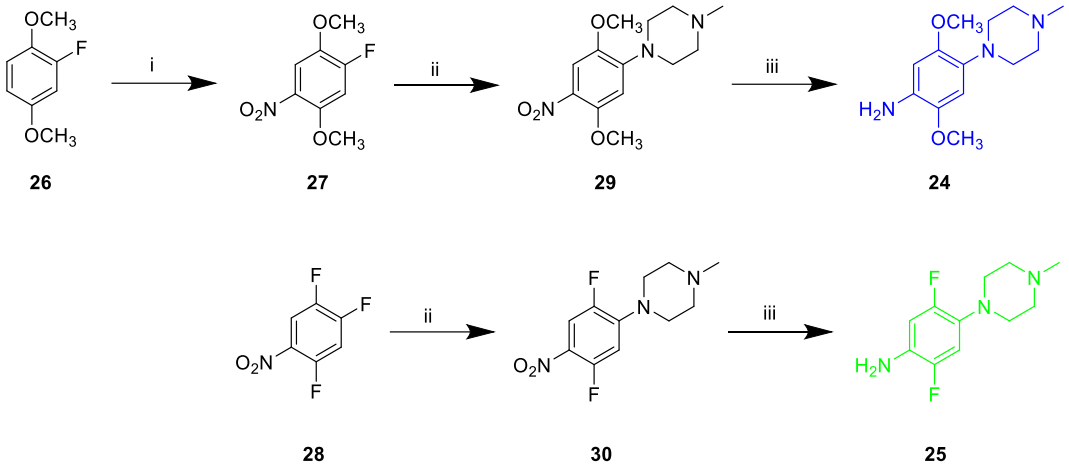


Figure 32. A) Synthetic scheme for the preparation of the fluorescent QD394 side chain. Reagents and conditions: (*i*) $ZnCl_2 \cdot H_2O$, abs EtOH, reflux, 24 h; (*ii*) $LiOH \cdot H_2O$, THF/H_2O, r.t, 3 h; (*iii*) EDC, HOBt hyd, DMF anh, N_2, r.t, 5 h; (*iv*) $HCOONH_4$, 10% Pd-C, MeOH anh, r.t, 3 h. B) The trifluoro-coumarin derivative 31 used directly to obtain the QD-dye probe QD445

2.7 Preparation of QD394 protected derivatives

Concerning the preparation of the derivatives designed to prevent metabolic inactivation (**24-25**), a suitable retrosynthetic approach was planned (**Scheme 4**). The appropriately substituted para-fluoronitrobenzenes (**27** and **28**) were used to connect the N-methyl piperazine in the presence of sodium carbonate, yielding the desired intermediates in good yield. Specifically, the nitro derivative **27** was synthesized from the dimethoxy-fluoro precursor **26** using fuming nitric acid, while the nitro derivative **28** was commercially available. These nitro derivatives were then reduced to the corresponding anilines (**29**-**30**) using ammonium formate and Pd/C, followed by coupling to synthon 1 using the previously established procedure (**Figure 30A**).



Scheme 4. Synthetic scheme for the preparation of the protected QD394-based side chains. Reagents and conditions: (i) conc. HNO_3, 0 °C, 10 min.; (ii) K_2CO_3, DMF anh, rt, 2 h; (iii) $HCOONH_4$, 10% Pd-C, MeOH anh, r.t, 2 h.

2.8 X-Ray crystallography

To confirm the regioselectivity of the coupling reaction in which Cerium (III) was used, we extended the study to other secondary amines. The piperazine derivative QD431 was selected as a model compound for X-ray analysis. Crystallographic results confirmed the occurrence of the Michael addition at position 6 of the quinazoline-5,8-dione ring system (**Figure 33**

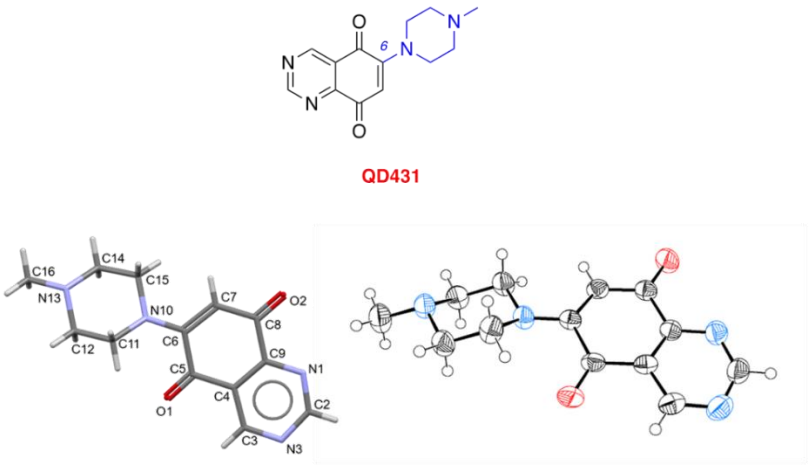
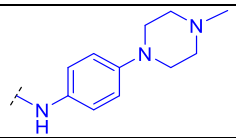
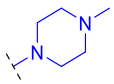
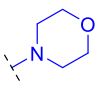
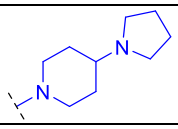
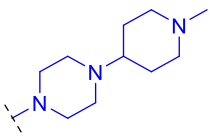
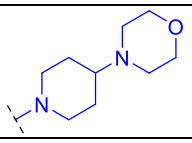


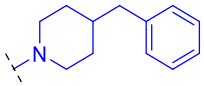
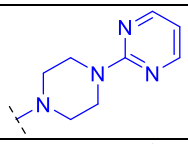
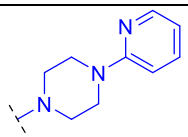
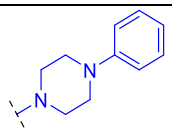
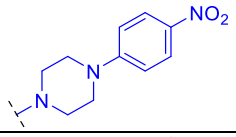
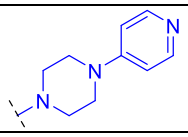
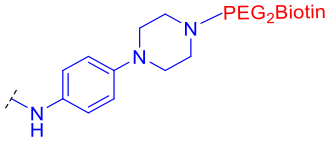
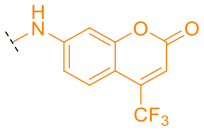
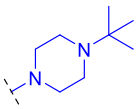
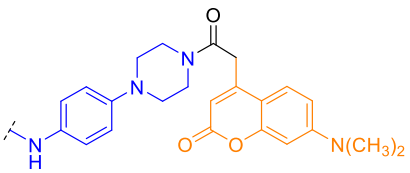
Figure 33. Structure representation of the X-ray crystallography analysis for QD431

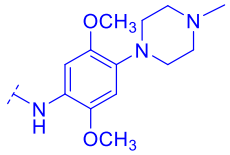
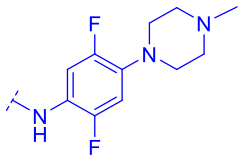
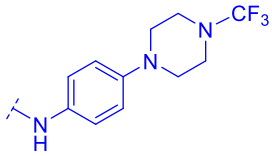
2.9 Biological assays

The new series of compounds QD431-451 were tested for their cytotoxicity against two pancreatic tumor cell lines (MIA PaCa-2 and Panc-1) as well as for resistant cell lines of colon cancer (HCT116) and uveal melanoma (MP41) (**Table 1**). The results showed an interesting activity of the new QD series against almost all the cancer cell lines with an overall antiproliferative effect in the submicromolar range. However, the lead QD394 and the QD449 derivative were the most potent compounds. Interestingly, the biotinylated QDs exhibited minimal cytotoxic activity across all tumor cell lines. Parallel solubility experiments revealed a significant increase in hydrophilicity, suggesting a potential correlation between the two findings. It is hypothesized that the enhanced solubility may have led to reduced cellular uptake of the QDs, thereby diminishing their cytotoxic effects.

Table 1. Cytotoxicity of QDs in pancreatic cancer cell lines (MIA PaCa-2, PANC-1), colon cancer (HCT116) and uveal melanoma (MP41)

IC50 (µM)					
QDs	**R**	**MIA PaCa-2**	**HCT116**	**PANC1**	**MP41**
394		0.6±0.2	0.4 ± 0.06	0.3 ±0.1	1.57±0.02
431		6.7 ±1.5	1.4 ± 0.5	0.7 ± 0.3	-
432		>10	2.0 ± 1.3	1.0 ± 0.5	-
433		>10	3.7 ± 1.2	1.3 ± 0.3	-
434		>10	>10	4.4 ± 1.7	-
435		>10	3.7 ± 1.1	1.4 ± 0.5	-

436		3.9 ±1.1	0.9 ± 0.4	1.0 ± 0.9	-
437		8.9 ±1.0	2.8 ± 0.4	1.0 ± 0.3	3.63±0.3
438		9.0 ±0.8	2.7 ± 0.9	0.6 ± 0.2	4.44±0.4
439		7.8±0.6	1.3 ± 0.4	0.4 ± 0.2	2.60±0.31
440		>10	1.5 ± 0.2	0.5 ± 0.2	3.35±0.12
441		>10	>10	4.0 ± 0.7	>10
442		>10	5.4 ± 1.1	6.3 ± 4.5	>10
443		>10	3.7 ± 1.0	4.5 ± 1.6	>10
444		>10	>10	5.7 ± 1.4	>10
445		6.14.1	6.8 ± 1.0	4.2 ± 2.1	-
446		1.9±0.4	1.0 ± 0.4	0.5 ±0.06	-
447		>10	4.7 ± 3.7	6.3 ± 4.3	-

448 (Quinoxaline -5,8-dione)		>10	1.5 ± 0.3	0.6 ± 0.2	-
449		0.5±0.06	0.4 ± 0.1	0.4 ± 0.1	-
450		1.3±0.4	0.9 ± 0.2	0.3 ± 0.1	-
451		1.5±0.1	0.5 ± 0.06	0.4 ±0.06	-

Interestingly, QD449 exhibited antiproliferative activity comparable to that of the lead compound QD394 across all tested cell lines (Table 1). Consequently, it was selected for further cytotoxic studies on additional cancer cell types. Notably, QD449 demonstrated strong activity against various osteosarcoma cell lines (**Table 2**).

Table 2. Cytotoxicity of QD449 in different osteosarcoma cell lines

Compound	IC50 (µM) KHOS/NP	IC50 (µM) 143B	IC50 (µM) SaOS	IC50 (µM) SJSA1
QD449	0.31	0.22	0.39	0.31

Pharmacokinetic studies using QD449 are ongoing to evaluate the influence of derivatization in enhancing metabolic stability.

2.10 Analysis for the fluorescent QD-dye probes

The QD derivatives specifically designed for the fluorescent detection (QD445, QD447) were analyzed with a Keyence BZX800 Fluorescence Microscope in osteosarcoma cell lines (143B). However, the newly developed dyes exhibited weak fluorescence, as observed in the detection images of the osteosarcoma cell lines used for analysis (Figure 34). Consequently, further studies are underway to better characterize the properties of these probes, including the potential development of novel derivatives with enhanced fluorescence characteristics.

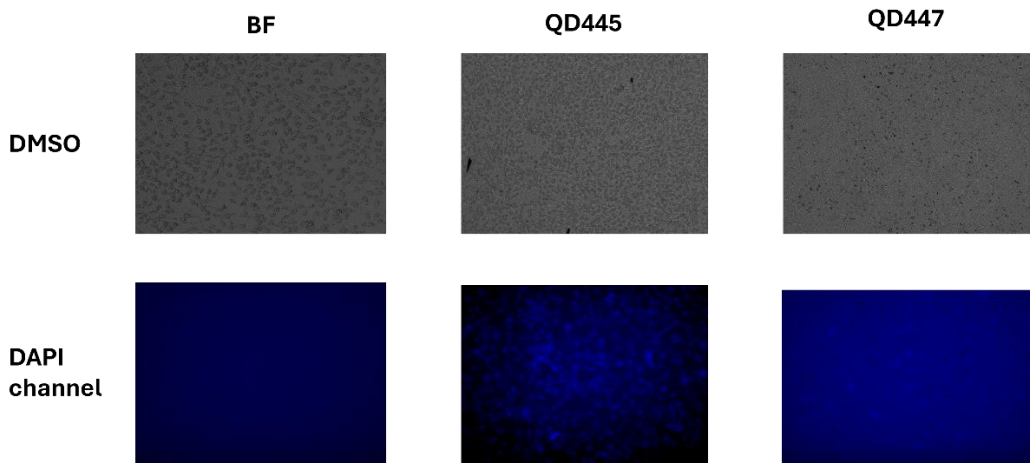


Figure 34. Fluoresce detection image of B164 osteosarcoma cells treated with 100 µM of QD445 and QD447, after 1h of incubation.

2.11 Binding studies of QDs with the enzyme GPX4

Previously, the Cellular Thermal Shift Assay (CETSA) was employed to investigate the potential interaction between QD model compounds and the GPX4 enzyme. In a new experiment, a shift in the melting temperature of GPX4 was observed upon interaction with QD449 (**Figure 35)**, indicating protein destabilization. These findings further support previous observations, reinforcing the hypothesis of a direct interaction between QD derivatives and GPX4.

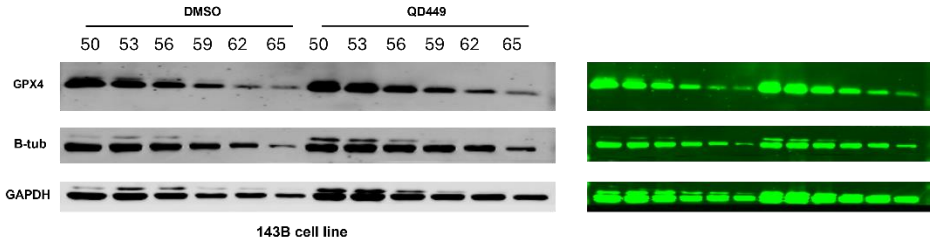


Figure 35. Cellular Thermal Shift Assay for GPX4 in 143B osteosarcoma cell line. QD449 reduced the melting point of GPX4.

2.12 Surface plasmon resonance between QDs and the enzyme GPX4

In previous studies, QD394 was shown to destabilize GPX4 in a cellular thermal shift assay (CETSA), suggesting a potential interaction between the compound and the enzyme.[171] CETSA measures changes in the thermal stability of a protein upon ligand binding, which is typically indicative of a putative interaction. To further investigate the binding ability of QDs to GPX4, Surface Plasmon Resonance (SPR) was employed. This optical technique enables real-time analysis of molecular interactions by detecting variations in laser light reflection (**Figure 36A**). SPR analysis of the two model compounds, QD394 and QD431 (**Figure 36B, C**), which were selected as representative ligands for the aniline- and piperazine-based QD derivatives, respectively, revealed a significant variation in resonance units (RU), confirming their interaction with the enzyme. The binding profile indicated a non-covalent interaction, as evidenced by a gradual reduction in RU over time, suggesting a time-dependent dissociation between the molecule and the protein.

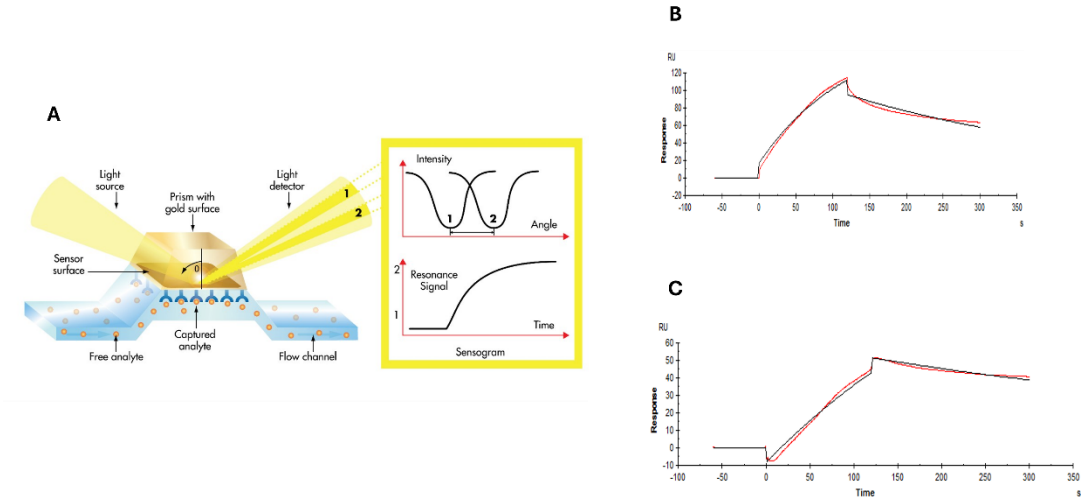


Figure 36. A) Graphical representation of the SPR analysis. B) Plot of resonance units (RU) in real time of the SPR analysis of QD394 with GPX4. C) Plot of resonance units (RU) in real time of the SPR analysis of QD431 with GPX4. Both assays showed the noncovalent interaction of QDs with the enzyme, deducible from the reduction of response of the analyzer after 120 seconds, thus indicating the decreasing of interaction between the QDs and the protein.

3. Conclusions

QD compounds induce oxidative stress and modulate the cellular production of reactive oxygen species (ROS), disrupting normal signaling pathways involved in the cell cycle and triggering cell death in resistant tumor cell lines. The exploration of new side chains with diverse chemical properties, such as the piperazine-like series, further expanded our panel of active compounds, reinforcing the antiproliferative potential of quinazoline-5,8-dione-based derivatives.

The introduction of biotinylated linkers, designed to modulate the solubility characteristics of QD derivatives, resulted in a reduction of their antiproliferative activity. This suggests that the increased water solubility came at the expense of cellular membrane uptake in tumor cells. Meanwhile, bioisosterical modification on the nucleic platform from quinazoline to quinoxaline-5,8-dione in the QD448 derivative preserved its antiproliferative activity, maintaining levels comparable to other analogues. This suggests a potential role of the heterocyclic platform in the cytotoxic mechanism.

Moreover, protection of the aromatic portion of the side chain in the lead compound yielded derivatives with antiproliferative activity comparable to QD394, indicating that the introduction of different substituents does not alter the activity. Furthermore, the development of QD-dye derivatives, designed to investigate the intracellular localization of the compounds, exhibited weak fluorescence, prompting further experiments to obtain additional insights.

Previous studies have reinforced the hypothesis that the antiproliferative mechanism of QDs is ROS-dependent and involves ferroptosis activation, particularly through GPX4 inactivation. In this PhD project, we further confirmed the interaction of this new class of compounds, including the protected derivatives, with GPX4 using cellular thermal shift assays and surface plasmon resonance. Given the crucial role of GPX4 in ferroptosis induction, these findings strengthen the rationale for continued exploration and optimization of this compound class. Our goal is to achieve an optimal balance between pharmacokinetic and pharmacodynamic properties, ultimately paving the way for preclinical and clinical studies targeting pancreatic tumors and other resistant cancer types.

4. Experimental part

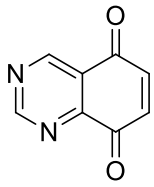
4.1 General methods

Unless otherwise noted, all solvents, including anhydrous solvents and chemicals, were purchased from Aldrich Co. and/or Alfa Aesar, and used without further purification. All reactions involving air- or moisture-sensitive compounds were performed under a nitrogen atmosphere using oven-dried glassware and syringes to transfer solutions. Silica gel thin-layer chromatography (TLC) sheets for Merck silica gel F-254 plates (silica gel precoated aluminum sheets with fluorescent indicator at 254 nm) were used for TLC. Melting points (m.p.) were determined using an Electrothermal melting point or a Köfler apparatus and are uncorrected. Proton nuclear magnetic resonance (^{1}H NMR) spectra were recorded in $CDCl_3$ or DMSO-d_6 on 400 MHz Bruker Avance III nanobay. Chemical shifts (δ) are reported in parts per million (ppm) downfield from tetramethylsilane (TMS), used as internal standard. Splitting patterns are designated as follows: broad singlet (bs), singlet (s), doublet (d), triplet (t), quartet (q), septet (sep), and multiplet (m). Mass spectra were obtained on a triple-quadrupole QqQ Varian 310-MS mass spectrometer, or a MALDI micro-MX (Waters, Micromass) equipped with a reflection analyser. Elemental analyses were performed on a Perkin-Elmer Elemental Analyzer 2400-CHN and were within ±0.4% of the theoretical values.

4.2 Synthesis and characterization of the key synthons and the lateral chains

4.2.1 Synthesis of quinazoline-5,8-dione

Synthesis of quinazoline-5,8-dione [1]



A solution of cerium ammonium nitrate $(NH4)_2[Ce\ (NO_3)_2$ (2.7 g, 4.9 mmol) in acetonitrile (CH_3CN, 9 mL) and water (1 mL) was dropped continuously in a stirred solution of 5,8-dimethoxyquinazoline (**5**, 0.35 g, 1.8 mmol), CH_3CN (7 mL) and water (3 mL), in ice bath. After 20 min, the solution was poured in ice (10 mL) and extracted with dichloromethane; the organic phase was then washed with water, dried with Na_2SO_4 and reduced under pressure. The resulting solid was tritured with petroleum ether to obtain a dark powder.

Yield: 70%.

Rf: 0.44 (methanol / dichloromethane = 0.5: 9.5).

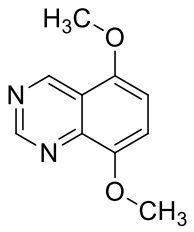
Mp: > 320 °C.

^{1}H-NMR (DMSO-d$_6$): δ 9.68 (s, 1H), 9.43 (s, 1H), 7.29-7.27 (d, 1H), 7.19-7.17 (d, 1H).

^{13}C-NMR MHz (DMSO-d$_6$): δ 162.08, 156.27, 139.46, 137.74.

MS: m/z 160 (M^+).

Synthesis of 5,8-dimethoxyquinazoline [5]



Zinc powder (8.2 g, 65.4 mmol) was added to a solution of glacial acetic acid (11.6 mL, 202.11 mmol), ice (32.9 g) and *N*,*N'*-[(3,6-dimethoxy-2-nitrophenyl)methylen]diformamide (**4**, 2.5 g, 8.8 mmol). The mixture was stirred for 2 hr in ice bath and then 4 hr at room temperature. After that the solution was filtered and dropped in a solution of NaOH 50% (50 mL). The appeared yellow suspension was let in the solution for 1 hr and then filtered to obtain a yellow solid which was then solubilized in ethyl acetate and stirred for 20 min. After filtration, the organic phase was reduced to obtain a pale-yellow pure powder.

Yield: 80%.

Rf: 0.44 (methanol / dichloromethane = 0.5 : 9.5).

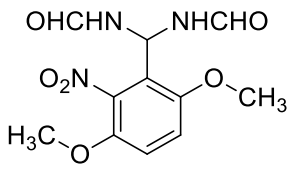
Mp: 76-77 °C.

^{1}H-NMR (DMSO-d$_6$): δ 9.64 (s, 1H), 9.28 (s, 1H), 7.40-7.38 (d, 1H), 7.11-7.09 (d, 1H), 3.98 (s, 3H), 3.94 (s, 3H).

^{13}C-NMR (DMSO-d$_6$): δ 154.88, 154.49, 148.35, 148.02, 141.60, 117.16, 113.59, 106.14, 56.11.

MS: m/z 190 (M^+).

Synthesis of *N*,*N'*-[(3,6-dimethoxy-2-nitrophenyl)methylen]diformamide [4]



To a solution of 3,6-dimethoxy-2-nitrobenzaldehyde (**3**, 6 g, 28 mmol) in formamide (NH_2COH, 90 mL) at 40 °C, gaseous HCl was insufflated inside until the temperature reached 85 °C (in 1 hr). After that gaseous HCl was removed and the solution let to cool to room temperature, then poured into ice/water. The solid was filtered, triturated with petroleum ether and ethyl acetate 1/1 to give yellow powder.

Yield: 87%.

Rf: 0.26 (methanol / dichloromethane = 0.5: 9.5).

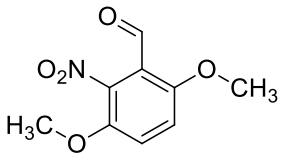
Mp: 255-256 °C.

^{1}H-NMR (DMSO-d$_6$): δ 8.68-8.66 (d, 2H), 7.92 (s, 2H), 7.28 (s, 2H), 6.79-6.75 (t, 1H), 3.87-3.82 (m, 6H).

^{13}C-NMR (DMSO-d$_6$): δ 163.80, 160.16, 150.77, 143.64, 139.60, 119.59, 114.32, 113.94, 57.02, 56.64, 48.51.

MS: m/z 283 (M^+)

Synthesis of 3,6-dimethoxy-2-nitrobenzaldehyde [3]



2,5-dimethoxybenzaldehyde (**2**, 18 g, 130.3 mmol) was poured in a solution of conc. nitric acid (28 mL)) and acetic anhydride (28 mL) and let under stirring for 1.5 hr at 0°C. The mixture was then poured into ice/water and filtered to obtain a yellow solid. The solid was a mixture of the two isomers 2-nitro- and 4-nitrodimethoxybenzaldehyde in a rate of 3/1, so the isomers were isolated using flash chromatography (eluents: petroleum ether / ethyl acetate = 6 / 4) to obtain the desired compound.

Yield: 54%.

Rf: 0.26 (petroleum ether / ethyl acetate = 6 : 4).

Mp: 151-152 °C.

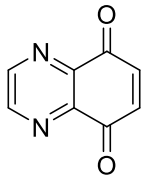
^{1}H-NMR (DMSO-d$_6$): δ 10.26 (s, 1H), 7.71-7.69 (d, 1H), 7.50-7.48 (d, 1H), 3.96 (s, 3H), 3.87 (s, 3H).

^{13}C-NMR (DMSO-d$_6$): δ 186.69, 166.22, 154.21, 153.42, 148.42, 123.72, 121.71, 116.48, 57.14.

MS: m/z 211 (M^+).

4.2.2 Synthesis of quinoxaline-5,8-dione

Synthesis of quinoxaline-5,8-dione [6]



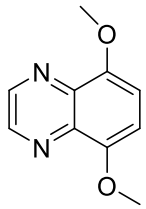
To a stirred solution of 5,8-dimethoxyquinoxaline (**10**, 0.515 g, 2.70 mmol) in (1:1) acetonitrile/water (12 ml), a solution of ceric ammonium nitrate (2.5 eq, 3.711 g, 6.77 mmol) in (20:1) acetonitrile/water (20 ml) was added dropwise. The reaction mixture was stirred for 20 min at room temperature, poured in ice/water and extracted (5-6 times) with dichloromethane. The combined organic layers were washed (4-5 times) with water, dried over anhydrous Na_2SO_4 and concentrated to dryness to obtain an orange powder, used for the next step without further purification.

Yield: 29.00%.

Rf:0.60 (dichloromethane / methanol = 9.5:0.5).

^{1}H-NMR 400MHz ($CDCl_3$): δ 9.08 (s, 2H); 7.27 (s, 2H).

Synthesis of 5,8-dimethoxyquinoxaline [10]



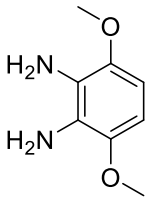
Sodium bisulfite (4 eq, 1.49 g, 14.27 mmol) and glyoxal solution 40 % in water (10.27 eq, 4.2 ml, 36.62 mmol) were respectively added in water (16 ml) at 55 °C, with stirring. The obtained solution was heated up to 75 °C and 3,6-dimethoxybenzene-1,2-diamine (**9**, 1 eq, 0.6 g, 3.57 mmol), previously solubilized in acetonitrile (2 ml), was added dropwise to obtain a mixture that was stirred at 75 °C for 3h. After stirring, the mixture was warmed at room temperature and filtered; the resulting solution was alkalized with NaOH 2N and extracted (5-6 times) with dichloromethane. The combined organic layers were washed (3 times) with water, dried over anhydrous Na_2SO_4 and concentrated to dryness to obtain a brown/orange sticky solid, used for the next step without further purification.

Yield: 40.26%.

Rf: 0.22 (ethyl acetate / petroleum ether = 9:1).

^{1}H-NMR 400MHz ($CDCl_3$): δ 8.89 (s, 2H); 7.03 (s, 2H); 4.06 (s, 6H)

Synthesis of 3,6-dimethoxybenzene-1,2-diamine [9]



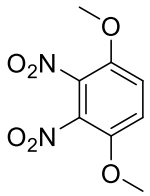
To a stirred mixture of granular Tin (5.8 eq, 2.41g, 20.33 mmol) in conc. HCl (33.55 eq, 9.6 ml, 117.62 mmol), 1,4-dimethoxy-2,3-dinitrobenzene (**8**, 1 eq, 0.8 g, 3.50 mmol) was added portion wise. The resulting mixture was stirred at reflux for 3 h and a white precipitate is formed. The white solid was filtered and solubilized in water. The solution obtained was alkalized with NaOH 2N and extracted (5-6 times) with dichloromethane. The combined organic layers were washed (3 times) with water, dried over anhydrous Na_2SO_4 and concentrated to dryness to obtain a brown solid.

Yield: 81.49%.

Rf: 0.56 (ethyl acetate / petroleum ether = 5:5).

^{1}H-NMR 400MHz ($CDCl_3$): δ 6.30 (s, 2H); 3.79 (s, 6H); 3.35 (s, 2H).

Synthesis of 1,4-dimethoxy-2,3-dinitrobenzene [8]



1,4-dimethoxybenzene (**7**, 2.0 g, 14.47 mmol) was added to conc. HNO_3 (20.53 eq, 19 ml, 297.03 mmol) in ice bath, for 30 minutes, with stirring. After 1 h in ice bath and another 1 h at room temperature, the yellow mixture was heated up to 90 °C and stirred for another 1 h. The resulting mixture was warmed at room temperature and poured into ice/water, to give a yellow precipitate that was filtered and dried in air. The obtained crude product was then purified by flash chromatography on silica gel using ethyl acetate/petroleum ether (5:5) to give first the regioisomer 1,4-dimethoxy-2,5-dinitrobenzene, and then (by further elution with only ethyl acetate) the desired compound 1,4-dimethoxy-2,3-dinitrobenzene as a yellow powder.

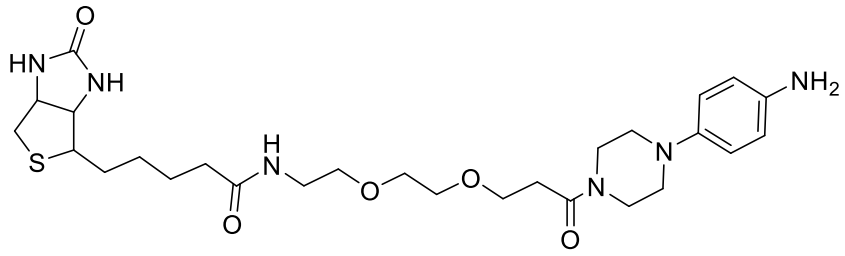
Yield: 74 %.

Rf: 0.40 (ethyl acetate / petroleum ether = 5:5).

^{1}H-NMR 400MHz ($CDCl_3$): δ 7.20 (s, 2H); 3.93 (s, 6H).

4.2.3 Preparation of the biotin/biotin-PEGylated lateral chains

N-(2-(2-(3-(4-(4-aminophenyl)piperidin-1-yl)-3-oxopropoxy)ethoxy)ethyl)-5-(2-oxohexahydro-1H-thieno[3,4-d]imidazol-4-yl)pentanamide [17]



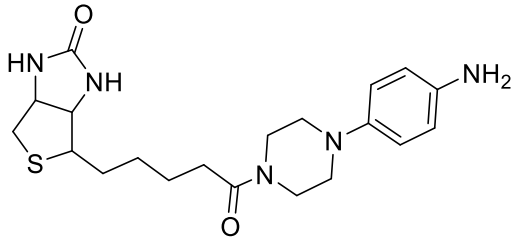
To a solution N-(2-(2-(3-(4-(4-nitrophenyl)piperidin-1-yl)-3-oxopropoxy)ethoxy)ethyl)-5-(2-oxohexahydro-1H-thieno[3,4-d]imidazol-4-yl)pentanamide (0,550 g, 0,9279 mmol) and Pd/C 10% (0.8255g, 0,7757 mmol) in anhydrous methanol (6 mL), NH_4HCO_2 (0.5851 g, 9,279 mmol) was added. The solution was stirred for 2 h at room temperature. The mixture was then filtered with celite and the solvent evaporated to obtain a dark purple solid.

Yield: 50 %.

Rf : 0.51 (dichloromethane / methanol = 9:1)

^{1}H-NMR 400MHz (DMSO-d$_6$): δ 6.71-6.69 (d, 2H), 6.51-6.49 (d, 2H), 6.41 (s, 1H), 6.35 (s, 1H), 4.32-4.11 (m, 2H), 3.66-3.5 (m, 12H), 3.4 (m, 4H), 3.19-2.61 (m, 5H) 2.8 (m, 4H), 2.08-2.05 (t, 1H), 1.61-1.13 (m, 6H)

Synthesis of 4-(5-(4-(4-aminophenyl)piperazin-1-yl)-5-oxopentyl)tetrahydro-1H-thieno[3,4-d]imidazol-2(3H)-one [16]



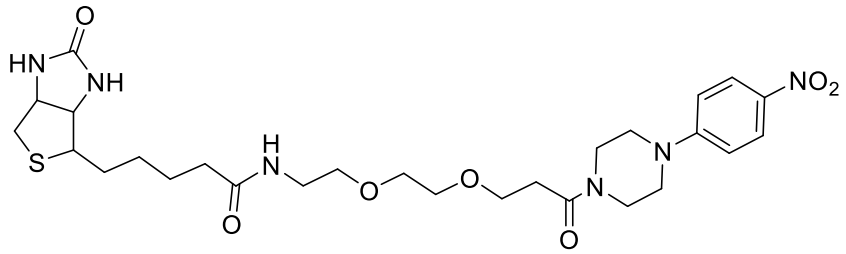
To a solution of 4-(5-(4-(4-nitrophenyl)piperazin-1-yl)-5-oxopentyl)tetrahydro-1H-thieno[3,4-d]imidazol-2(3H)-one (**14**, 0,370 g, 0,86 mmol) and Pd/C 10% (0,076 g, 0,718 mmol)) in anhydrous methanol (6 mL), NH_4HCO_2 (0,542 g, 8,6 mmol)) was added. The solution was stirred for 2 hr at room temperature. The mixture was then filtered with celite and the solvent evaporated to obtain a dark purple solid.

Yield :50%.

Rf: 0,56 (dichloromethane / methanol = 9:1)

^{1}H-NMR 400MHz (DMSO-d_6): δ 6.71-6.69 (d, 2H), 6.51-6.48 (d, 2H), 6.43 (s, 1H), 6.35 (s, 1H), 4.32-4.13 (m, 2H), 3.55 (s, 4H), 2.9-2.55 (m, 2H), 2.81 (t, 4H), 1.63-1.35 (m, 8H).

Synthesis of N-(2-(2-(3-(4-(4-nitrophenyl)piperidin-1-yl)-3-oxopropoxy)ethoxy)ethyl)-5-(2-oxohexahydro-1H-thieno[3,4-d]imidazol-4-yl)pentanamide [15]



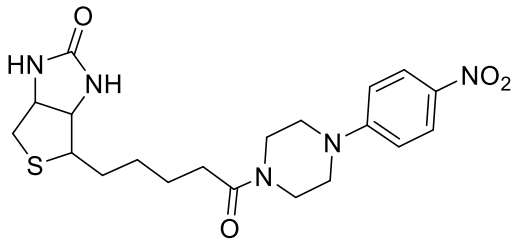
Biotin-PEG2-NHS (10, 0.500g, 0.9988 mmol) and 4-nitrophenylpiperazine (0.2587g, 1.248 mmol) were solubilized in ACN (10 ml)) and subsequently DIPEA (0.1946 g, 1.5061 mmol) was added dropwise to let the solution stirring for 5 hr under N_2. The mixture was reduced under pressure to obtain a sticked yellow solid. The compound was mixed with water and extracted with DCM. The organic phase was then washed with water, dried over anhydrous Na_2SO_4, and concentrated to dryness yielding the desired compound

Yield: 89%.

Rf: 0,68 (dichloromethane / methanol = 9:1)

^{1}H-NMR 400MHz (DMSO-d$_6$): δ 8,03-8,09 (d, 2H), 7,02-6,99 (d, 2H), 6.40 (s, 1H), 6.35 (s, 1H), 4.32-4.11 (m, 2H), 3.66-3.5 (m, 12H), 3.4 (m, 4H), 3.19-2.61 (m, 5H) 2.8 (m, 4H), 2.08-2.05 (t, 1H), 1.61-1.13 (m, 6H).

4-(5-(4-(4-nitrophenyl)piperazin-1-yl)-5-oxopentyl)tetrahydro-1H-thieno[3,4-d]imidazol-2(3H)-one [14]



Biotin-NHS (0,350g, 1,025mmol) and 4-nitrophenylpiperazine (0,167g, 0,8 mmol) were solubilized in ACN (8mL) and subsequently DIPEA (0,140 g, 1,088 mmol) was added dropwise. The solution was stirred for 5 h under N_2. The mixture was reduced under pressure and the resulted solid solubilized in DCM, washed with water, dried over anhydrous Na2SO4, and concentrated to dryness yielding the desired compound.

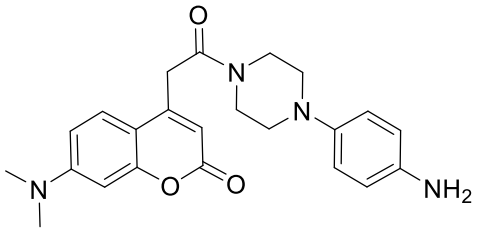
Yield: 89 %.

Rf: 0.77 (dichloromethane / methanol = 9:1).

^{1}H-NMR 400MHz (DMSO-d_6): δ 8.09-8.07 (d, 2H), 7.03-7.01 (d, 2H), 6.43 (s, 1H), 6.36 (s, 1H), 4.32-4.14 (m, 2H), 3.32 (m, 4H), 2.75 (t, 4H), 2.81-2.55 (m, 2H), 1.64-1.37 (m, 8H).

4.2.4 Preparation of the fluorescent dye-side chains

Synthesis of 4-(2-(4-(4-aminophenyl)piperazin-1-yl)-2-oxoethyl)-7-(dimethylamino)-2H-chromen-2-one [18]



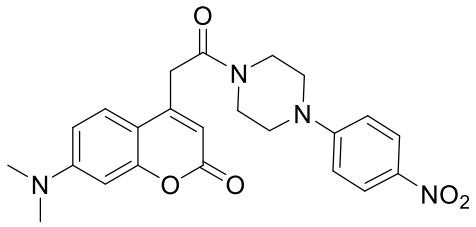
The nitro derivative (**24**, 0.3g, 0.687 mmol) was solubilized in anhydrous methanol and Pd/C 10% was added (0.146g, 0.137 mmol, 0.137 mmol). Then ammonium formate (0.195g, 3.09 mmol) was added in one pot and let in N2 atmosphere under vigorous stirring for 2 hr at room temperature. The mixture was filtered with celite pad and washed with methanol. The organic phase was reduced to obtain a green solid which was then triturated with petroleum ether and diethyl ether.

Yield: 90%

Rf: 0.6 (chloroform / methanol = 9.5:0.5).

^{1}H-NMR 400MHz ($CDCl_3$): δ 7.45 (d, 1H), 6.70 (d, 2H), 6.65 (d, 2H), 6.62 (m, 1H), 6.51 (d, 1H), 6.00 (s, 1H), 3.80 (s, 4H), 3.6 (m, 2H), 3.05 (s, 6H), 3.00 (m, 4H).

Synthesis of 7-(dimethylamino)-4-(2-(4-(4-nitrophenyl)piperazin-1-yl)-2-oxoethyl)-2H-chromen-2-one [24]



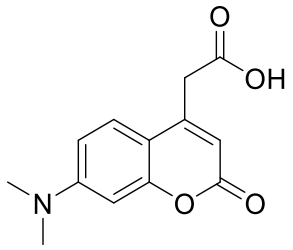
The 7-dimethylamino-coumarin-acetic acid (**22**, 0.8g, 3.24 mmol) was dissolved in anhydrous DMF (50mL) and HOBt (1g, 6.48 mmol), EDC (1g, 6.48 mmol) and TEA (0.656g, 6.48 mmol) were added sequentially. After 10 min, 1-(4-nitropneyl)piperazine (0.671g, 3.24 mmol) in DMF was added and the reaction let under stirring overnight at room temperature. The DMF was removed under pressure and the obtained oil was dissolved in dichloromethane, washed with citric acid 15%, saturated NaHCO3 and water (3 times with each solution) and finally dried with Na2SO4 and filtered. After evaporation, the solid was purified by flash chromatography using petroleum ether/ethyl acetate 5 / 5.

Yield: 54.30% (chloroform / methanol = 9.5:0.5)

Rf: 0.81

^{1}H-NMR 400MHz (DMSO-d$_6$): δ 8.09 (d, 2H), 7.5 (dd, 1H), 7.03 (d, 2H), 6.73 (m, 1H), 6.56 (m, 1H), 6.96 (s, 1H), 3.97 (s, 2H), 3.6 (m, 8H), 3.02 (s, 6H).

Synthesis of 2-(7-(dimethylamino)-2-oxo-2H-chromen-4-yl)acetic acid [22]



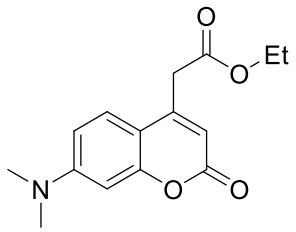
The Dye-ester derivative (**21**, 0.7g, 2.6 mmol) was dissolved in anhydrous THF (14 mL). LiOH monohydrate (0.218g, 5.2 mmol) was dissolved with H2O (20 mL), poured into the reaction mixture and let under stirring for 2hr at room temperature. The solution was diluted with H_2O, washed with diethyl ether and acidified to pH 2 with HCl under ice bath, to obtain a brown solid which was filtered.

Yield: 64%

Rf: 0.11 (petroleum ether / ethyl acetate = 5:5)

^{1}H-NMR 400MHz (DMSO–d_6): δ 7.46 (d, 1H), 6.73 (d, 1H), 6.56 (s, 1H), 6.05 (s, 1H), 3.78 (s, 2H), 3.37 (bs, 1H - OH), 3.02 (s, 6H).

Synthesis of ethyl 2-(7-(dimethylamino)-2-oxo-2H-chromen-4-yl)acetate [21]



3-(dimethylamino)phenol (0.411g, 3 mmol) and diethyl 3-oxopentanedioate (0.667g, 3.3 mmol) were mixed in anhydrous methanol and $ZnCl_2$ (0.49g, 3.6 mmol) was added. The solution was let under stirring at reflux overnight. After that the solution was poured into ice-water under stirring and a dark amorphous solid precipitate. The solid was then washed with cold ethanol to obtain a dark purple solid.

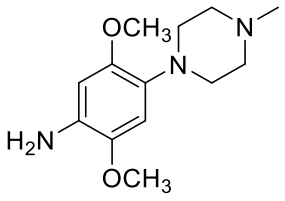
Yield: 38%

Rf: 0.61 (petroleum ether / ethyl acetate = 5:5)

^{1}H-NMR 400MHz ($CDCl_3$): δ 7.40 (d, 1H), 6.63 (d, 1H), 6.52 (s, 1H), 6.05 (s, 1H), 4.18 (q, 2H), 3.67 (s, 2H), 3.071 (s, 6H), 1.25 (t, 3H).

4.2.5 Preparation of the protected side chains

Synthesis of 2,5-dimethoxy-4-(4-methylpiperazin-1-yl)aniline [24]



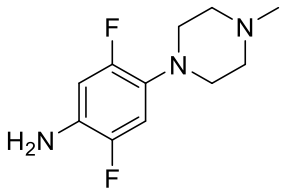
Pd/C 10% (0,453 g, 0,426 mmol) was poured in anhydrous methanol (10 mL) in N_2 atmosphere. Then 1-(2,5-dimethoxy-4-nitrophenyl)-4-methylpiperazine (**29**, 0,600 g, 2,13 mmol) was added and stirred for 5 min. NH_4HCO_2 (0,672 g, 10,65 mmol) was added in one pot and the mixture stirred at r.t for 2 hr. The mixture was filtered with celite and the filter washed with a solution of Dichloromethane / Methanol (9:1). The solvent was evaporated to obtain a dark blue solid which was used without further purification.

Yield: 56%

Rf: 0.50 (dichloromethane / methanol = 9.5:0.5)

^{1}H-NMR 400MHz ($CDCl_3$): δ 6.56 (s, 1H), 6.34 (s, 1H), 3.80 (s, 3H), 3.78 (s, 3H), 3.60 (bs, 2H), 3.02 (bs, 4H), 2.61 (bs, 4H), 2.35 8s, 3H).

Synthesis of 2,5-difluoro-4-(4-methylpiperazin-1-yl)aniline [25]



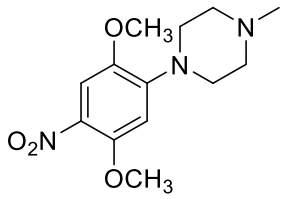
Pd/C 10% (0,496 g, 0,466 mmol) was poured in anhydrous methanol (10 mL) in N_2 atmosphere. Then 1-(2,5-dimethoxy-4-nitrophenyl)-4-methylpiperazine (**30**, 0,600 g, 2,33 mmol) and anhydrous dichloromethane (5 mL) were added and stirred for 5 min. NH_4HCO_2 (0,734 g, 11,65 mmol) was added in one pot and the mixture stirred at r.t for 2 hr. The mixture was filtered with celite and the filter washed with a solution of dichloromethane / methanol (9:1). The solvent was evaporated to obtain a red solid which was used without further purification.

Yield: 61%

Rf: 0.33 (dichloromethane / methanol = 9.5:0.5)

^{1}H-NMR 400MHz ($CDCl_3$): δ 6.70 – 6.65 (m, 1H), 6.53 – 6.48 (m, 1H), 3.55 (bs, 2H), 2.97 (t, 4H), 2.58 (t, 4H), 2.34 (s, 3H).

Synthesis of 1-(2,5-dimethoxy-4-nitrophenyl)-4-methylpiperazine [29]



K_2CO_3 (0,495 g, 3,58 mmol) was added a solution of N-methylpiperazine (0,358 g, 3,58 mmol) in anhydrous DMF (10 mL) and stirred for 5 min. Subsequently 1-fluoro-2,5-dimethoxy-4-nitrobenzene (**27**, 0,600 g, 2,98 mmol) was added portion wise and stirred at r.t for 24 h. The mixture was poured into ice/water and extracted with ethyl acetate, washed with water and brine and dried over anhydrous Na_2SO_4. The organic phase was concentrated to dryness and triturated with petroleum ether and diethyl ether to obtain the desired compound as yellow solid.

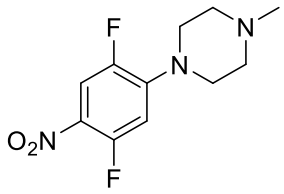
Yield: 79%

Rf: 0.5 (chloroform / methanol = 9.5:0.5).

^{1}H-NMR 400MHz ($CDCl_3$): δ 6.48 (s, 1H), 3.94 (s, 3H), 3.90 (s, 3H), 3.28 (m, 4H), 3.61 (m, 4H), 2.37 (s, 3H)

.

Synthesis 1-(2,5-difluoro-4-nitrophenyl)-4-methylpiperazine [30]



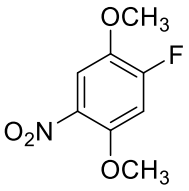
K_2CO_3 (0,936 g, 6,77 mmol) was added to the solution of N-methylpiperazine (0,678 g, 6,77 mmol) in anhydrous DMF (10 mL) and stirred for 5 min. Subsequently 1,2,4-trifluoro-5-nitrobenzene (**28**, 1 g, 5,65 mmol) was added portion wise and stirred at r.t for 24 h. The mixture was poured into ice/water and the precipitate filtered, solubilized in chloroform, washed with water and brine and dried over anhydrous Na_2SO_4. The organic phase was concentrated to dryness to obtain the desired compound as yellow solid.

Yield: 65%

Rf: 0.62 (chloroform / methanol = 9.5:0.5).

^{1}H-NMR 400MHz ($CDCl_3$): δ 7.84-7.79 (m, 1H), 6.66-6.61 (m, 1H), 3.35 (t, 4H), 5.58 (t, 4H), 2.36 (s, 3H).

Synthesis of 1-fluoro-2,5-dimethoxy-4-nitrobenzene [27]



2-fluoro-1,4-dimethoxybenzene (**26**, 1 g, 6,4 mmol) was slowly added to concentrated HNO_3 (9 mL) at 0 °C and stirred for 10 min. Subsequently ice/water (37g) was added and stirred for other 30 min. The mixture was filtered to obtain a yellow solid that was then purified by flash chromatography on silica gel using petroleum ether/ ethyl acetate (5:5) to the desired compound.

Yield: 59%

Rf: 0.57 (petroleum ether / ethyl acetate = 8:2).

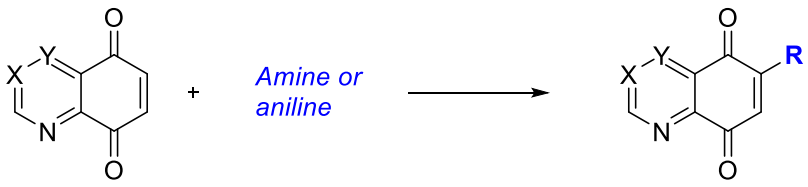
^{1}H-NMR 400MHz ($CDCl_3$): δ 7.62 (d, 1H), 6.88 (d, 1H), 3.93-3.91 (d, 6H)

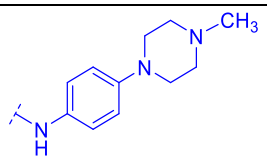
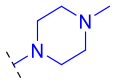
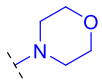
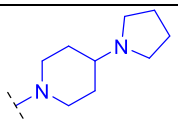
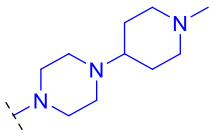
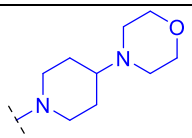
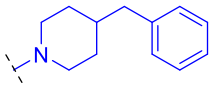
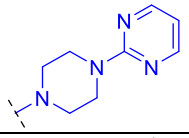
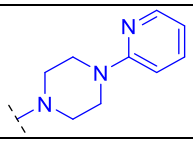
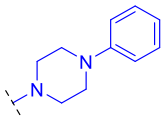
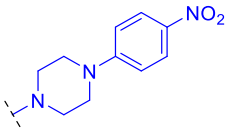
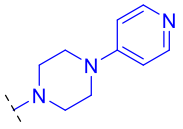
4.3 Syntheisis of the final compounds QD431-451

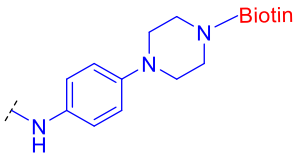
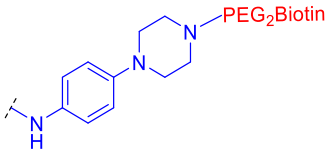
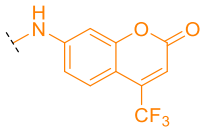
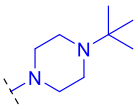
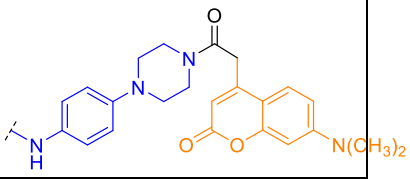
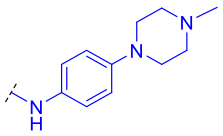
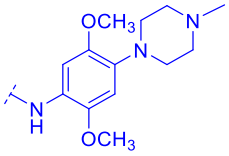
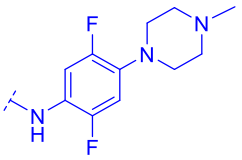
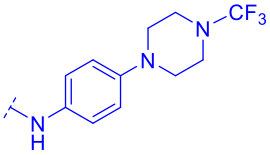
4.3.1 General procedure

To a solution of quinazoline-5,8-dione [1] or quinoxaline-5,8-dione [6] (1.2 mmol) and Cerium ammonium nitrate heptahydrate ($CeCl_3$ $7H_2O$) (1 eq, 1.2 mmol) in absolute ethanol (20 mL), the appropriate amine was added and the solution let under stirring under N_2 for 2-4 hr at room temperature. After that, the solution was reduced under pressure and extracted with dichloromethane, washed with water, dried with Na_2SO_4 and reduced under pressure to obtain the desired compound which was then purified by flash chromatography. In some cases, the reaction mixture was reduced under pressure and immediately purified by flash chromatography instead of using extraction, depending of the purity and or the difficulty to extract.

Scheme 1

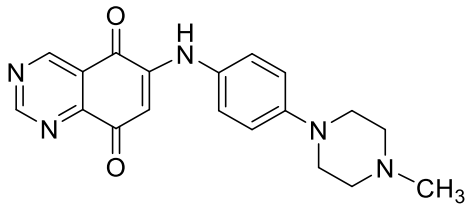


QDs	R
394	
431	
432	
433	
434	
435	
436	
437	
438	
439	
440	
441	

442	
443	
444	—PEG_2Biotin
445	
446	
447	
448 (Quinoxaline-5,8-dione)	
449	
450	
451	

4.3.2 Final compounds

Preparation of 6-[4-(4-metilpiperazin-1-il)anilino]chinazolin-5,8-dione (QD394)



The compound was purified by flash chromatography (dichloromethane / methanol - 9.5 / 0.5) to give a dark purple powder.

Yield: 70%.

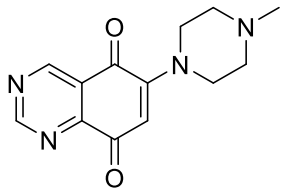
Rf: 0.30 (dichloromethane / methanol = 9.5:0.5)

Mp: 204-205 °C

^{1}H-NMR (DMSO-d$_6$): δ 9.60 (s, 1H), 9.46 (s, 1H), 9.39 (s, 1H), 7.24-7.22 (d, 1H), 7.04-7.01 (d, 1H), 6.13 (s, 1H), 3.18 (m, 4H), 2.47 (m, 4H), 2.23 (s, 3H)

MS: m/z 349 (M^+)

Synthesis of 6-(4-methylpiperazin-1-yl)quinazoline-5,8-dione (QD431)



The compound was purified by flash chromatography (dichloromethane / methanol - 9.5 / 0.5) to give a dark red powder.

Yield: 61%.

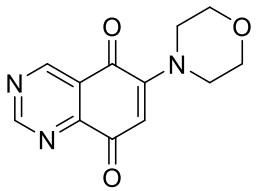
Rf: 0.29 (dichloromethane / methanol = 9.5:0.5).

Mp: 153.2 °C

^{1}H-NMR 400MHz ($CDCl_3$): δ 9.59 (s, 1H), 9.38 (s, 1H), 6.28 (s, 1H), 3.66 (t, 4H), 2.59 (t, 4H), 2.34 (s, 3H)

^{13}C-NMR 400 MHz (CDCl3): δ 181.45, 180.21, 162.94, 156.71, 153.39, 152.09, 125.19, 111.76, 54.55, 48.95, 45.87.

Synthesis of 6-morpholinoquinazoline-5,8-dione (QD432)



The compound was purified by flash chromatography (dichloromethane / methanol - 9.5 / 0.5) to give a dark powder.

Yield: 43%,

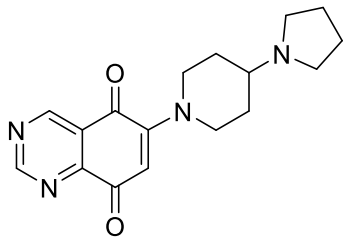
Rf: 0.52 (dichloromethane / methanol = 9.5:0.5).

Mp: 160 °C

^{1}H-NMR 400MHz ($CDCl_3$): δ 9.60 (s, 1H), 9.40 (s, 1H), 6.27 (s, 1H), 3.88 (t, 4H), 3.64 (t, 4H)

^{13}C-NMR 400 MHz ($CDCl_3$): δ 181.31, 180.36, 163.00, 156.81, 153.22, 152.02, 125.10, 111.92, 66.33, 49.16.

Synthesis of 6-(4-(pyrrolidin-1-yl)piperidin-1-yl)quinazoline-5,8-dione (QD433)



The compound was purified by flash chromatography (dichloromethane / methanol – 9 / 1) to give a dark powder.

Yield: 27%.

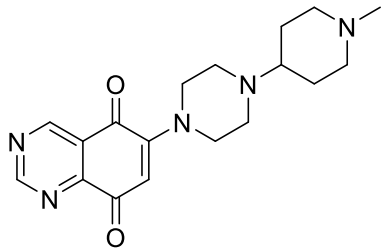
Rf: 0.60 (dichloromethane / methanol = 9:1).

Mp: 130 °C

^{1}H-NMR 400MHz ($CDCl_3$): δ 9.58 (s, 1H), 9.37 (s, 1H), 6.29 (s, 1H), 3.22 (t, 4H), 2.63 (s, 4H), 1.84 (m, 8H)

^{13}C-NMR 400 MHz ($CDCl_3$): δ 181.53, 180.09, 162.89, 156.65, 153.58, 151.97, 125.22, 111.06, 60.50, 51.45, 47.89, 31.92, 23.30

Synthesis of 6-(4-(1-methylpiperidin-4-yl)piperazin-1-yl)quinazoline-5,8-dione (QD434)



The compound was purified by flash chromatography (dichloromethane / methanol - 9 / 1) to give a dark powder.

Yield: 19%

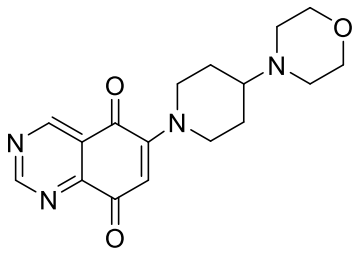
Rf: 0.56 (dichloromethane / methanol = 9:1).

Mp: 255 °C

^{1}H-NMR 400MHz ($CDCl_3$): δ 9.58 (s, 1H), 9.37 (s, 1H), 6.26 (s, 1H), 3.65 (s, 4H), 2.90 (m, 2H), 2.74 (m, 4H), 2.31 (s, 3H), 1.86-1.43 (m, 7H)

^{13}C-NMR 400MHz ($CDCl_3$): δ 181.48, 180.14, 162.90, 156.68, 154.50, 153.44, 152.83, 152.03, 125.19, 111.45, 61.28, 55.17, 49.92, 49.00, 46.03, 28.06.

6-(4-morpholinopiperidin-1-yl)quinazoline-5,8-dione (QD435)



The compound was purified by flash chromatography (dichloromethane / methanol – 9.5 / 0.5) to give a dark powder.

Yield: 29.3 %

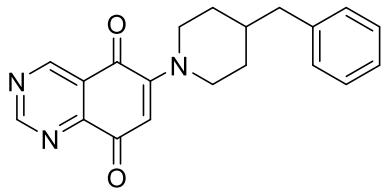
Rf: 0.12 (dichloromethane / methanol = 9.5:0.5).

Mp: 171 °C

^{1}H-NMR 400MHz ($CDCl_3$): δ 9.59 (s, 1H), 9.37(s, 1H), 6.29 (s, 1H), 4.19-4.16 (m, 2H), 3.73 (s, 4H), 3.13 (t, 2H), 2.57 (s, 5H), 2.02 (m, 2H), 1.71 (m, 2H)

^{13}C-NMR 400 MHz ($CDCl_3$): δ 181.52, 180.10, 162.94, 156.67, 153.52, 151.94, 125.19, 111.27, 67.15, 60.98, 49.84, 48.47, 28.26

6-(4-benzylpiperidin-1-yl)quinazoline-5,8-dione (QD436)



The compound was purified by flash chromatography (dichloromethane / methanol – 9.5 / 0.5) to give a dark powder.

Yield: 10%.

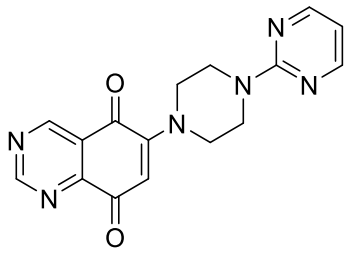
Rf: 0.70 (dichloromethane / methanol = 9.5:0.5).

Mp: 160 °C

^{1}H-NMR 400MHz ($CDCl_3$): δ 9.57 (s, 1H), 9.35 (s, 1H), 7.32-7.14 (m, 5H), 6.27 (s, 1H), 4.16 (s, 2H), 3.04 (t, 2H), 2.61 (d, 2H), 1.97-1.78 (m, 3H), 1.44 (qd, 2H)

^{13}C-NMR 400 MHz ($CDCl_3$): δ 181.61, 179.99, 162.87, 156.59, 153.63, 152.19, 139.52, 129.04, 128.56, 126.48, 125.26, 110.93, 49.86, 42.72, 37.85, 32.00.

6-(4-(pyrimidin-2-yl)piperazin-1-yl)quinazoline-5,8-dione DR 79 (QD437)



The compound was purified by flash chromatography (dichloromethane / methanol – 9.5 / 0.5) to give a dark powder.

Yield: 61%.

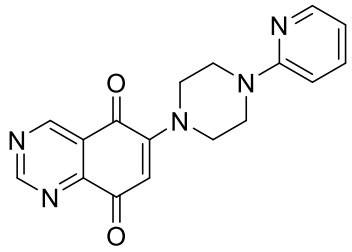
Rf: 0.28 (dichloromethane / methanol = 9.5:0.5).

Mp: 208 °C

^{1}H-NMR 400 MHz ($CDCl_3$): δ 9.61 (s, 1H), 9.42 (s, 1H), 8.36 (d, 2H), 6.53 (t, 1H), 6.29 (s, 1H), 4.05 (t, 4H), 3.79 (q, 4H)

^{13}C-NMR 400 MHz ($CDCl_3$): δ 181.44, 180.09, 163.03, 161.23, 157.86, 156.77, 153.41, 151.78, 125.19, 111.27, 110.79, 48.58, 42.49

6-(4-(pyridin-2-yl)piperazin-1-yl)quinazoline-5,8-dione (QD438)



The compound was purified by flash chromatography (dichloromethane / methanol – 9.5 / 0.5) to give a dark powder.

Yield:31%.

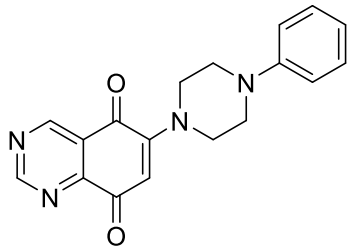
Rf: 0.30 (dichloromethane / methanol = 9.5:0.5).

Mp: 247.5°C

^{1}H-NMR 400 MHz ($CDCl_3$): δ 9.60 (s, 1H), 9.41 (s, 1H), 8.22 (s, 1H), 7.55 (t, 1H), 6.61-6.63 (d, 2H), 6.28 (s, 1H), 3.82 (q, 8H)

^{13}C-NMR 400 MHz ($CDCl_3$): δ 181.45, 180.03, 163.01, 158.42, 156.74, 153.43, 151.58, 148.07, 137.79, 125.05, 114.00, 110.87, 106.75, 48.40, 44.19, 29.69

6-(4-phenylpiperazin-1-yl)quinazoline-5,8-dione (QD439)



The compound was purified by flash chromatography (dichloromethane / methanol – 9.5 / 0.5) to give a dark powder.

Yield: 34%.

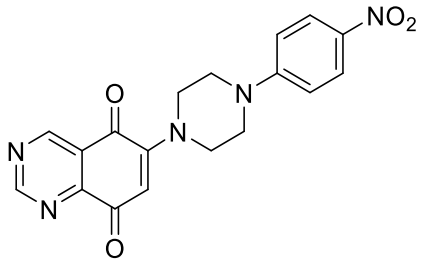
Rf: 0.62 (dichloromethane / methanol = 9.5:0.5).

Mp: 205 °C

^{1}H-NMR 400 MHz ($CDCl_3$): δ 9.60 (s, 1H), 9.41 (s, 1H), 7.27 (s, 2H), 6.95 (s, 3H), 6.31 (s, 1H), 3.83 (s, 4H), 3.40 (s, 4H)

^{13}C-NMR 400 MHz ($CDCl_3$): δ 181.43, 180.20, 163.01, 156.78, 153.38, 151.78, 150.24, 129.38, 125.11, 120.56, 116.06, 111.54, 48.79

6-(4-(4-nitrophenyl)piperazin-1-yl)quinazoline-5,8-dione (QD440)



The compound was purified by flash chromatography (dichloromethane / methanol – 9.5 / 0.5) to give a red powder.

Yield: 15%.

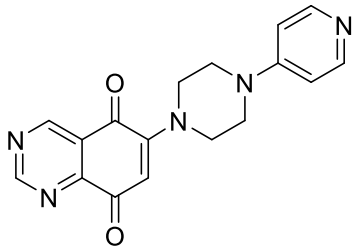
Rf: 0.54 (dichloromethane / methanol = 9.5:0.5).

Mp: 223 °C

^{1}H-NMR 400MHz (DMSO-d$_6$): δ 9.57 (s, 1H), 9.32 (s, 1H), 8.09 (d, 2H), 6.95 (d, 2H), 6.15 (s, 1H), 3.89 (m, 4H), 3.73 (m, 4H)

^{13}C-NMR 400 MHz (DMSO-d$_6$): δ 181.17, 179.14, 162.05, 156.02, 153.80, 152.95, 152.22, 136.61, 125.78, 111.57, 107.83, 47.08, 44.64.

6-(4-(pyridin-4-yl)piperazin-1-yl)quinazoline-5,8-dione (QD441)



The compound was purified by flash chromatography (dichloromethane / methanol - 9 / 1) to give a dark powder.

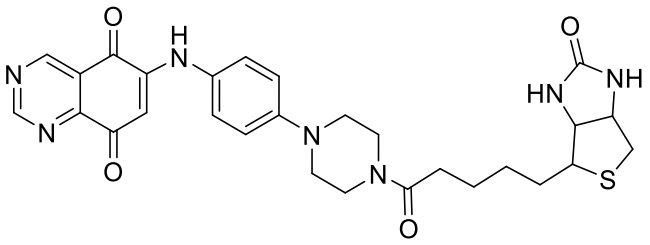
Yield: 15%.

Rf: 0.14 (dichloromethane / methanol = 9 :1).

Mp: 258 °C

^{1}H-NMR 400MHz (DMSO-d$_6$): δ 9.63 (s, 1H), 9.38 (s, 1H), 8.24 (d, 2H), 6.85 (d, 2H), 6.25 (s, 1H), 3.89 (m, 4H), 3.63 (m, 4H)

Synthesis of 6-((4-(4-(5-(2-oxohexahydro-1H-thieno[3,4-d]imidazol-4-yl)pentanoyl)piperazin-1-yl)phenyl)amino)quinazoline-5,8-dione (QD 442)



The compound was purified by flash chromatography (dichloromethane / methanol – 9.5 / 0.5) to give a purple-blue powder.

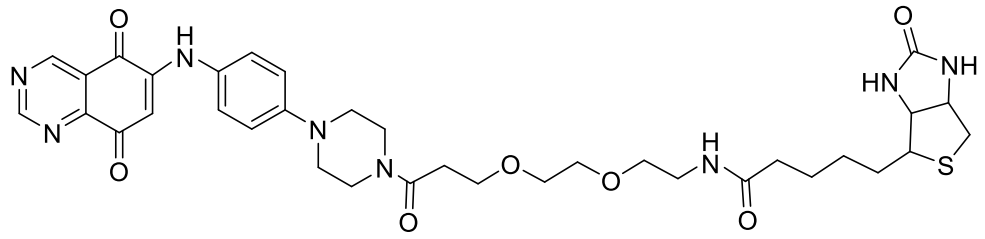
Yield: 15%.

Rf: 0.38 (dichloromethane / methanol = 9: 1).

^{1}H-NMR 400MHz (DMSO-d_6): δ 9.59(s, 1H), 9.38 (s, 1H), 7.26-7.42 (d, 2H), 7.06-7.04 (d, 2H), 6.44 (s, 1H), 6.36 (s, 1H), 6.13 (s, 1H), 4.33-4.13 (m, 2H), 3.61-3.55 (m, 4H), 2.85 (m, 4H), 2.85-2.57 (m, 2H), 1.65-0.8 (m, 8H)

^{13}C-NMR 400 MHz ($CDCl_3$): δ 180.60, 179.42, 170.67, 162.69, 162.58, 155.54, 154.02, 148.73, 146.52, 128.65, 125.00, 124.10, 116.11, 102.69, 69.74, 61.02, 60.14, 59.16, 55.43, 44.65, 32.04, 28.47, 24,80

Synthesis of N-(2-(2-(3-(4-(4-((5,8-dioxo-5,8-dihydroquinazolin-6-yl)amino)phenyl)piperazin-1-yl)-3-oxopropoxy)ethoxy)ethyl)-5-(2-oxohexahydro-1H-thieno[3,4-d]imidazol-4-yl)pentanamide (QD443)



The compound was purified by flash chromatography (dichloromethane / methanol – 9.5 / 0.5) to give a purple-blue powder.

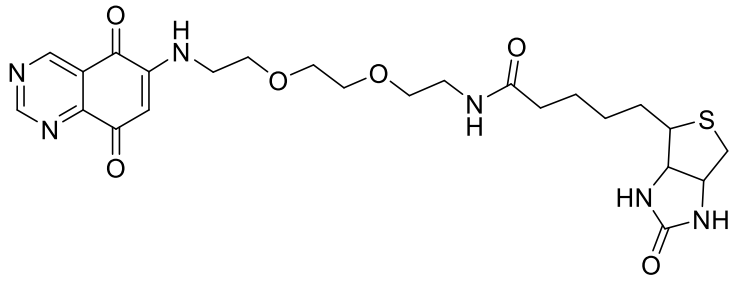
Yield: 10,61%.

Rf: 0,45 (dichloromethane / methanol = 9: 1).

Mp: 80 °C.

^{1}H-NMR 400MHz (DMSO-d$_6$): δ 9.59 (s, 1H), 9.38 (s, 1H), 7.82 (m, 1H), 7.26- 7.24 (d, 2H), 7.06-7.03 (d, 2H), 6.4 (s, 1H), 6.34 (s, 1H), 6.13 (s, 1H), 4.15-4.11 (m, 2H), 3.65-3.50 (m, 12H), 3.19-2.61 (m, 5H), 2,8 (m, 8H), 2.08-2.05 (t, 1H), 1.61-1.13 (m, 6H)

Synthesis of N-(2-(2-(2-((5,8-dioxo-5,8-dihydroquinazolin-6-yl)amino)ethoxy)ethoxy)ethyl)-5-(2-oxohexahydro-1H-thieno[3,4-d]imidazol-4-yl)pentanamide (QD444)



After the extraction procedure, the inorganic residue was separated by vacuum filtration and the aqueous solution evaporated. The solid was then triturated with petroleum ether.

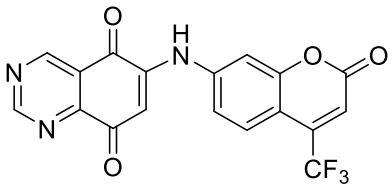
Yield: 10,61%.

Rf: 0,45 (dichloromethane / methanol = 9 :1).

^{1}H-NMR 400MHz (DMSO-d$_6$): δ 9.59 (s, 1H), 9.38 (s, 1H), 7.82 (m, 1H), 6.4 (s, 1H), 6.34 (s, 1H), 6.13 (s, 1H), 4.15-4.11 (m, 2H), 3.65-3.50 (m, 12H), 3.19-2.61 (m, 5H), 2.08-2.05 (t, 1H), 1.61-1.13 (m, 6H)

^{13}C-NMR 400 MHz (DMSO-d$_6$): δ 182.46, 178.51, 172.41, 162.78, 162.17, 159.25, 156.03, 152.59, 124.15, 111.45, 69.59, 69.34, 69.03, 66.54, 65.61, 61.04, 59.20, 55.38, 35.06, 2814, 27.98, 25.21, 13.73.

Synthesis of 6-((2-oxo-4-(trifluoromethyl)-2H-chromen-7-yl)amino)quinazoline-5,8-dione (QD445)



The compound was purified by flash chromatography (petroleum ether / ethyl acetate – 6 / 4) to give a red powder.

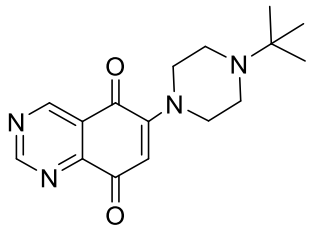
Yield: 10%

Rf: 0.1 (petroleum ether / ethyl acetate = 6:4).

^{1}H-NMR 400MHz (DMSO-d$_6$): δ 9.86 (s, 1H), 9.65 (s, 1H), 9.46 (S, 1H), 7.78 (m, 1H), 7.57 (s, 2H), 7.00 (s, 1H), 6.66 (s, 1H).

^{19}F NMR 400 MHz (DMSO-d$_6$): δ -64.60 (s, 3, CF_3).

Synthesis of f6-(4-(tert-butyl)piperazin-1-yl)quinazoline-5,8-dione (QD446)



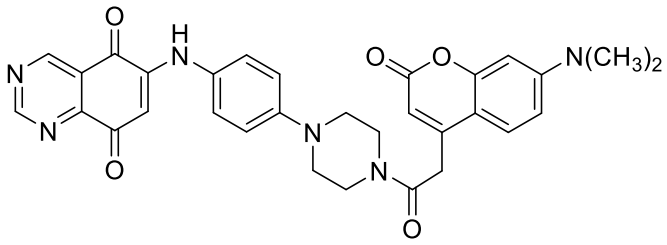
The compound was purified by flash chromatography (dichloromethane / methanol – 9.5 / 0.5) to give a dark powder.

Yield: 10.6%.

Rf: 0.51 (dichloromethane / methanol = 9.5:0.5).

^{1}H-NMR 400 MHz ($CDCl_3$): δ 9.60 (s, 1H), 9.40 (s, 1H), 6.26 (s, 1H), 3.66 (s, 4H), 2.77 (s, 4H), 1.12 (s, 9H)

Synthesis of 6-((4-(4-(2-(7-(dimethylamino)-2-oxo-2H-chromen-4-yl)acetyl)piperazin-1-yl)phenyl)amino)quinazoline-5,8-dione (QD447)



The compound was purified by flash chromatography (dichloromethane / methanol – 9.5 / 0.5) to give a dark powder.

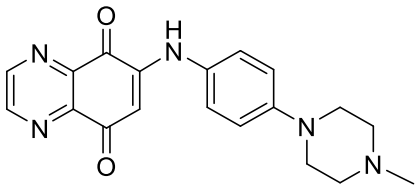
Yield: 28%

Rf: 0.55 (dichloromethane / methanol = 9.5:0.5).

^{1}H-NMR 400MHz ($CDCl_3$): δ 9.61 (s, 1H), 9.40 (s, 1H), 7.46 (d, 2H), 7.27 (d, 1H), 7.07 (d, 2H), 6.73 (m, 1H), 6.5 (m, 1H), 6.15 (s, 1H), 5.99 (s, 1H) 3.98 (s, 2H), 3.6 (m, 4H), 3.25 (s, 4H), 3.00 (m, 6H).

^{13}C-NMR 400 MHz ($CDCl_3$): δ 180.61 ,179.33, 166.94, 166.80, 162.60 , 160.67, 155.54, 155.27 152.75, 151.80, 148.61, 146.48, 142.70, 141.95, 126.30, 125.00, 118.57, 116.11, 114.69, 109.20, 109.01 108.46, 97.33, 79.12, 48.15, 45.04, 36.30.

Synthesis of 6-((4-(4-methylpiperazin-1-yl)phenyl)amino)-4a,8a-dihydroquinoxaline-5,8-dione (QD448)



The compound was purified by flash chromatography, using chloroform / methanol - 9.5 / 0.5), to obtain a violet powder.

Yield: 13%.

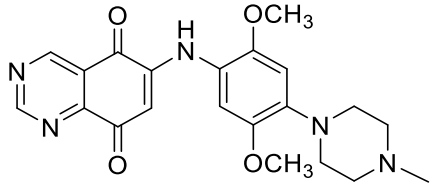
Rf: 0.25 (dichloromethane / methanol = 9.5:0.5).

Mp: 185-186 °C.

^{1}H-NMR 400MHz ($CDCl_3$): δ 9.01 (d, 1H), 8.94-8.93 (d, 1H), 7.65 (s, 1H), 7.20-7.18 (d, 2H), 6.97-6.95 (d, 2H), 6.52 (s, 1H); 3.26-3.24 (t, 4H), 2.61-2.58 (t, 4H), 2.37 (s, 3H).

^{13}C-NMR 400MHz ($CDCl_3$): δ 180.43 149.85, 147.38, 145.77, 142.90, 127.70, 124.50; 116.51, 103.32, 76.72, 54.88, 48.67, 46.10.

Synthesis of 6-((2,5-dimethoxy-4-(4-methylpiperazin-1-yl)phenyl)amino)quinazoline-5,8-dione (QD449)



The compound was purified by flash chromatography (dichloromethane / methanol – 9.5 / 0.5) to give a dark powder.

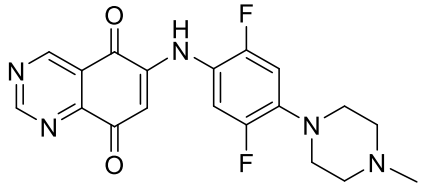
Yield: 42%.

Rf: 0.43 (dichloromethane / methanol = 9.5: 0.5)

^{1}H-NMR 400MHz ($CDCl_3$): δ 9.65 (s, 1H), 9.47 (s, 1H), 7.87 (s, 1H), 6.90 (s, 1H), 6.60 (s, 1H), 6.56 (s, 1H) 3.88 (s, 3H), 3.85(s, 3H), 3.15 (bs, 4H), 2.64 (bs, 4H), 2.38 (s, 3H)

^{13}C-NMR 400 MHz ($CDCl_3$): δ 180.72, 180.05, 163.61, 156.24, 154.64, 146.56, 146.17, 143.80, 140.68, 123.42, 118.87, 107.07, 104.36, 103.04, 56.44, 56.27, 55.41, 50.43, 46.13.

Synthesis of 6-((2,5-difluoro-4-(4-methylpiperazin-1-yl)phenyl)amino)quinoxaline-5,8-dione (QD450)



The compound was purified by flash chromatography (dichloromethane / methanol – 9.5 / 0.5) to give a dark powder.

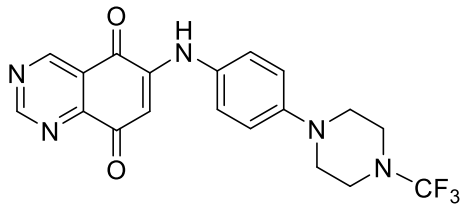
Yield: 23.5%.

Rf: 0.41 (dichloromethane / methanol = 9.5:0.5)

^{1}H-NMR 400MHz ($CDCl_3$): δ 9.66 (s, 1H), 9.50 (s, 1H), 7.40 (bs, 1H), 7.11-7.06 (m, 1H), 6.81-6.76 (m, 1H), 6.39 (s, 1H), 3,16 (s, 4H), 2,61 (s, 4H) 2.37 (s, 3H)

^{13}C-NMR 400 MHz ($CDCl_3$): δ 180.42, 180.19, 163.70, 156.40, 154.18, 149.60, 144.47, 123.33, 112.40, 106.92, 105.63, 54.83, 50.05, 46.07.

Synthesis of 6-((4-(4-(trifluoromethyl)piperazin-1-yl)phenyl)amino)quinoxaline-5,8-dione (QD451)



The compound was purified by flash chromatography (dichloromethane / methanol – 9.5 / 0.5) to give a dark powder.

Resa: 39%.

Rf: 1.45 (dichloromethane / methanol = 9.5:0.5).

^{1}H-NMR 400MHz ($CDCl_3$): δ 9.62 (s, 1H), 9.42 (s, 1H), 7.54 (d, 2H), 6.93 (d, 2H); 6.30 (s, 1H), 3.86 (t,4H), 3.54 (t,4H)

^{13}C-NMR 400 MHz ($CDCl_3$): δ 181.38, 180.19, 163.09, 156.82, 151.49, 126.67, 125.03, 121.49, 114.23, 111.41, 48.32, 47.12, 39.71.

Bibliography

(1) *National Cancer Institute - What is a Cancer*.

(2) Cao, W.; Qin, K.; Li, F.; Chen, W. Comparative Study of Cancer Profiles between 2020 and 2022 Using Global Cancer Statistics (GLOBOCAN). *Journal of the National Cancer Center* **2024**, *4* (2), 128–134. https://doi.org/10.1016/j.jncc.2024.05.001.

(3) Brown, J. S.; Amend, S. R.; Austin, R. H.; Gatenby, R. A.; Hammarlund, E. U.; Pienta, K. J. Updating the Definition of Cancer. *Molecular Cancer Research* **2023**, *21* (11), 1142–1147. https://doi.org/10.1158/1541-7786.MCR-23-0411.

(4) Hanahan, D.; Weinberg, R. A. The Hallmarks of Cancer. *Cell* **2000**, *100* (1), 57–70. https://doi.org/10.1016/S0092-8674(00)81683-9.

(5) Bray, F.; Laversanne, M.; Sung, H.; Ferlay, J.; Siegel, R. L.; Soerjomataram, I.; Jemal, A. Global Cancer Statistics 2022: GLOBOCAN Estimates of Incidence and Mortality Worldwide for 36 Cancers in 185 Countries. *CA Cancer J Clin* **2024**, *74* (3), 229–263. https://doi.org/10.3322/caac.21834.

(6) Alam, A. Chemotherapy Treatment and Strategy Schemes: A Review. *Open Access J Toxicol* **2018**, *2* (5). https://doi.org/10.19080/OAJT.2018.02.555600.

(7) Liu, J.; Pandya, P.; Afshar, S. Therapeutic Advances in Oncology. *Int J Mol Sci* **2021**, *22* (4), 2008. https://doi.org/10.3390/ijms22042008.

(8) Hosseinzadeh, E.; Banaee, N.; Nedaie, H. A. Cancer and Treatment Modalities. *Curr Cancer Ther Rev* **2017**, *13* (1). https://doi.org/10.2174/1573394713666170531081818.

(9) Lemke L., T.; Williams, A. D.; F., V.; PhD F. Roche; Zito, S. W. *Foye's Principles of Medicinal Chemistry*, 7th International.; Lippincott Williams and Wilkins, 2012.

(10) Radhakrishnan, V.; Song, Y.-S.; Thiruvengadam, D. Romidepsin (Depsipeptide) Induced Cell Cycle Arrest, Apoptosis and Histone Hyperacetylation in Lung Carcinoma Cells (A549) Are Associated with Increase in P21 and Hypophosphorylated Retinoblastoma Proteins Expression. *Biomedicine & Pharmacotherapy* **2008**, *62* (2), 85–93. https://doi.org/10.1016/j.biopha.2007.06.002.

(11) De Keersmaecker, B.; Fostier, K.; Corthals, J.; Wilgenhof, S.; Heirman, C.; Aerts, J. L.; Thielemans, K.; Schots, R. Immunomodulatory Drugs Improve the Immune Environment for Dendritic Cell-Based Immunotherapy in Multiple Myeloma Patients after Autologous Stem Cell Transplantation. *Cancer Immunology, Immunotherapy* **2014**, *63* (10), 1023–1036. https://doi.org/10.1007/s00262-014-1571-6.

(12) Busch, A.; Zeh, D.; Janzen, V.; Mügge, L.-O.; Wolf, D.; Fingerhut, L.; Hahn-Ast, C.; Maurer, O.; Brossart, P.; von Lilienfeld-Toal, M. Treatment with Lenalidomide Induces Immunoactivating and Counter-Regulatory Immunosuppressive Changes in Myeloma Patients. *Clin Exp Immunol* **2014**, *177* (2), 439–453. https://doi.org/10.1111/cei.12343.

(13) Hanahan, D.; Weinberg, R. A. Hallmarks of Cancer: The Next Generation. *Cell* **2011**, *144* (5), 646–674. https://doi.org/10.1016/j.cell.2011.02.013.

(14) Hanahan, D. Hallmarks of Cancer: New Dimensions. *Cancer Discov* **2022**, *12* (1), 31–46. https://doi.org/10.1158/2159-8290.CD-21-1059.

(15) Dickinson, B. C.; Chang, C. J. Chemistry and Biology of Reactive Oxygen Species in Signaling or Stress Responses. *Nat Chem Biol* **2011**, *7* (8), 504–511. https://doi.org/10.1038/nchembio.607.

(16) Aggarwal, V.; Tuli, H.; Varol, A.; Thakral, F.; Yerer, M.; Sak, K.; Varol, M.; Jain, A.; Khan, Md.; Sethi, G. Role of Reactive Oxygen Species in Cancer Progression: Molecular Mechanisms and Recent Advancements. *Biomolecules* **2019**, *9* (11), 735. https://doi.org/10.3390/biom9110735.

(17) Sena, L. A.; Chandel, N. S. Physiological Roles of Mitochondrial Reactive Oxygen Species. *Mol Cell* **2012**, *48* (2), 158–167. https://doi.org/10.1016/j.molcel.2012.09.025.

(18) Idelchik, M. del P. S.; Begley, U.; Begley, T. J.; Melendez, J. A. Mitochondrial ROS Control of Cancer. *Semin Cancer Biol* **2017**, *47*, 57–66. https://doi.org/10.1016/j.semcancer.2017.04.005.

(19) Murphy, M. P. How Mitochondria Produce Reactive Oxygen Species. *Biochemical Journal* **2009**, *417* (1), 1–13. https://doi.org/10.1042/BJ20081386.

(20) Bienert, G. P.; Møller, A. L. B.; Kristiansen, K. A.; Schulz, A.; Møller, I. M.; Schjoerring, J. K.; Jahn, T. P. Specific Aquaporins Facilitate the Diffusion of Hydrogen Peroxide across Membranes. *Journal of Biological Chemistry* **2007**, *282* (2), 1183–1192. https://doi.org/10.1074/jbc.M603761200.

(21) Einav Gross, C. S. S. N. H. E. V. M. B. C. A. K. C. T. and D. F. Generating Disulfides Enzymatically: Reaction Products and Electron Acceptors of the Endoplasmic Reticulum Thiol Oxidase Ero1p. *Pro. Natl. Acad. Sci. USA* **2006**, *3*, 299–304.

(22) Chen, K.; Kirber, M. T.; Xiao, H.; Yang, Y.; Keaney, J. F. Regulation of ROS Signal Transduction by NADPH Oxidase 4 Localization. *J Cell Biol* **2008**, *181* (7), 1129–1139. https://doi.org/10.1083/jcb.200709049.

(23) Bedard, K.; Krause, K.-H. The NOX Family of ROS-Generating NADPH Oxidases: Physiology and Pathophysiology. *Physiol Rev* **2007**, *87* (1), 245–313. https://doi.org/10.1152/physrev.00044.2005.

(24) Reczek, C. R.; Chandel, N. S. ROS-Dependent Signal Transduction. *Curr Opin Cell Biol* **2015**, *33*, 8–13. https://doi.org/10.1016/j.ceb.2014.09.010.

(25) Nakamura, H.; Takada, K. Reactive Oxygen Species in Cancer: Current Findings and Future Directions. *Cancer Sci* **2021**, *112* (10), 3945–3952. https://doi.org/10.1111/cas.15068.

(26) Saikolappan, S.; Kumar, B.; Shishodia, G.; Koul, S.; Koul, H. K. Reactive Oxygen Species and Cancer: A Complex Interaction. *Cancer Lett* **2019**, *452*, 132–143. https://doi.org/10.1016/j.canlet.2019.03.020.

(27) Moloney, J. N.; Cotter, T. G. ROS Signalling in the Biology of Cancer. *Semin Cell Dev Biol* **2018**, *80*, 50–64. https://doi.org/10.1016/j.semcdb.2017.05.023.

(28) Sabharwal, S. S.; Schumacker, P. T. Mitochondrial ROS in Cancer: Initiators, Amplifiers or an Achilles' Heel? *Nat Rev Cancer* **2014**, *14* (11), 709–721. https://doi.org/10.1038/nrc3803.

(29) Porporato, P. E.; Filigheddu, N.; Pedro, J. M. B.-S.; Kroemer, G.; Galluzzi, L. Mitochondrial Metabolism and Cancer. *Cell Res* **2018**, *28* (3), 265–280. https://doi.org/10.1038/cr.2017.155.

(30) Zhao, Y.; Ye, X.; Xiong, Z.; Ihsan, A.; Ares, I.; Martínez, M.; Lopez-Torres, B.; Martínez-Larrañaga, M.-R.; Anadón, A.; Wang, X.; Martínez, M.-A. Cancer Metabolism: The Role of ROS in DNA Damage and Induction of Apoptosis in Cancer Cells. *Metabolites* **2023**, *13* (7), 796. https://doi.org/10.3390/metabo13070796.

(31) Khavari, T. A.; Rinn, J. L. Ras/Erk MAPK Signaling in Epidermal Homeostasis and Neoplasia. *Cell Cycle* **2007**, *6* (23), 2928–2931. https://doi.org/10.4161/cc.6.23.4998.

(32) Roberts, P. J.; Der, C. J. Targeting the Raf-MEK-ERK Mitogen-Activated Protein Kinase Cascade for the Treatment of Cancer. *Oncogene* **2007**, *26* (22), 3291–3310. https://doi.org/10.1038/sj.onc.1210422.

(33) Brunet, A.; Bonni, A.; Zigmond, M. J.; Lin, M. Z.; Juo, P.; Hu, L. S.; Anderson, M. J.; Arden, K. C.; Blenis, J.; Greenberg, M. E. Akt Promotes Cell Survival by Phosphorylating and Inhibiting a Forkhead Transcription Factor. *Cell* **1999**, *96* (6), 857–868. https://doi.org/10.1016/S0092-8674(00)80595-4.

(34) Kawamura, N.; Kugimiya, F.; Oshima, Y.; Ohba, S.; Ikeda, T.; Saito, T.; Shinoda, Y.; Kawasaki, Y.; Ogata, N.; Hoshi, K.; Akiyama, T.; Chen, W. S.; Hay, N.; Tobe, K.; Kadowaki, T.; Azuma, Y.; Tanaka, S.; Nakamura, K.; Chung, U.; Kawaguchi, H. Akt1 in Osteoblasts and Osteoclasts Controls Bone Remodeling. *PLoS One* **2007**, *2* (10), e1058. https://doi.org/10.1371/journal.pone.0001058.

(35) Limaye, V.; Li, X.; Hahn, C.; Xia, P.; Berndt, M. C.; Vadas, M. A.; Gamble, J. R. Sphingosine Kinase-1 Enhances Endothelial Cell Survival through a PECAM-1–Dependent Activation of PI-3K/Akt and Regulation of Bcl-2 Family Members. *Blood* **2005**, *105* (8), 3169–3177. https://doi.org/10.1182/blood-2004-02-0452.

(36) Pastorino, J. G.; Tafani, M.; Farber, J. L. Tumor Necrosis Factor Induces Phosphorylation and Translocation of BAD through a Phosphatidylinositide-3-OH Kinase-Dependent Pathway. *Journal of Biological Chemistry* **1999**, *274* (27), 19411–19416. https://doi.org/10.1074/jbc.274.27.19411.

(37) Qi, X.-J.; Wildey, G. M.; Howe, P. H. Evidence That Ser87 of BimEL Is Phosphorylated by Akt and Regulates BimEL Apoptotic Function. *Journal of Biological Chemistry* **2006**, *281* (2), 813–823. https://doi.org/10.1074/jbc.M505546200.

(38) Xin, M.; Deng, X. Nicotine Inactivation of the Proapoptotic Function of Bax through Phosphorylation. *Journal of Biological Chemistry* **2005**, *280* (11), 10781–10789. https://doi.org/10.1074/jbc.M500084200.

(39) Eiseler, T.; Döppler, H.; Yan, I. K.; Goodison, S.; Storz, P. Protein Kinase D1 Regulates Matrix Metalloproteinase Expression and Inhibits Breast Cancer Cell Invasion. *Breast Cancer Research* **2009**, *11* (1), R13. https://doi.org/10.1186/bcr2232.

(40) Song, J.; Li, J.; Lulla, A.; Evers, B. M.; Chung, D. H. Protein Kinase D Protects against Oxidative Stress-Induced Intestinal Epithelial Cell Injury via Rho/ROK/PKC-δ Pathway Activation. *American Journal of Physiology-Cell Physiology* **2006**, *290* (6), C1469–C1476. https://doi.org/10.1152/ajpcell.00486.2005.

(41) Storz, P. Protein Kinase D Mediates a Stress-Induced NF-KappaB Activation and Survival Pathway. *EMBO J* **2003**, *22* (1), 109–120. https://doi.org/10.1093/emboj/cdg009.

(42) Storz, P.; Toker, A. NF-KB Signaling: An ALternate Pathway for Oxidate Stress Responses. *Cell Cycle* **2003**, *2* (1), 9–10. https://doi.org/10.4161/cc.2.1.234.

(43) Storz, P.; Döppler, H.; Toker, A. Protein Kinase Cdelta Selectively Regulates Protein Kinase D-Dependent Activation of NF-KappaB in Oxidative Stress Signaling. *Mol Cell Biol* **2004**, *24* (7), 2614–2626. https://doi.org/10.1128/MCB.24.7.2614-2626.2004.

(44) Storz, P.; Döppler, H.; Toker, A. Protein Kinase D Mediates Mitochondrion-to-Nucleus Signaling and Detoxification from Mitochondrial Reactive Oxygen Species. *Mol Cell Biol* **2005**, *25* (19), 8520–8530. https://doi.org/10.1128/MCB.25.19.8520-8530.2005.

(45) Wu, H.; Goel, V.; Haluska, F. G. PTEN Signaling Pathways in Melanoma. *Oncogene* **2003**, *22* (20), 3113–3122. https://doi.org/10.1038/sj.onc.1206451.

(46) Ahmed, K. M.; Cao, N.; Li, J. J. HER-2 and NF-KappaB as the Targets for Therapy-Resistant Breast Cancer. *Anticancer Res* **2006**, *26* (6B), 4235–4243.

(47) Bourguignon, L. Y. W.; Xia, W.; Wong, G. Hyaluronan-Mediated CD44 Interaction with P300 and SIRT1 Regulates β-Catenin Signaling and NFκB-Specific Transcription Activity Leading to MDR1 and Bcl-XL Gene Expression and Chemoresistance in Breast Tumor Cells. *Journal of Biological Chemistry* **2009**, *284* (5), 2657–2671. https://doi.org/10.1074/jbc.M806708200.

(48) Duffey, D. C.; Crowl-Bancroft, C. V; Chen, Z.; Ondrey, F. G.; Nejad-Sattari, M.; Dong, G.; Van Waes, C. Inhibition of Transcription Factor Nuclear Factor-KB by a Mutant Inhibitor-KBα Attenuates Resistance of Human Head and Neck Squamous Cell Carcinoma to TNF-α Caspase-Mediated Cell Death. *Br J Cancer* **2000**, *83* (10), 1367–1374. https://doi.org/10.1054/bjoc.2000.1423.

(49) Levine, A. J.; Oren, M. The First 30 Years of P53: Growing Ever More Complex. *Nat Rev Cancer* **2009**, *9* (10), 749–758. https://doi.org/10.1038/nrc2723.

(50) Karanjawala, Z. E.; Murphy, N.; Hinton, D. R.; Hsieh, C.-L.; Lieber, M. R. Oxygen Metabolism Causes Chromosome Breaks and Is Associated with the Neuronal Apoptosis Observed in DNA Double-Strand Break Repair Mutants. *Current Biology* **2002**, *12* (5), 397–402. https://doi.org/10.1016/S0960-9822(02)00684-X.

(51) Cooke, M. S.; Evans, M. D.; Dizdaroglu, M.; Lunec, J. Oxidative DNA Damage: Mechanisms, Mutation, and Disease. *The FASEB Journal* **2003**, *17* (10), 1195–1214. https://doi.org/10.1096/fj.02-0752rev.

(52) Loeb, L. A.; Loeb, K. R.; Anderson, J. P. Multiple Mutations and Cancer. *Proceedings of the National Academy of Sciences* **2003**, *100* (3), 776–781. https://doi.org/10.1073/pnas.0334858100.

(53) Sieber, O. M.; Heinimann, K.; Tomlinson, I. P. M. Genomic Instability — the Engine of Tumorigenesis? *Nat Rev Cancer* **2003**, *3* (9), 701–708. https://doi.org/10.1038/nrc1170.

(54) Shibutani, S.; Takeshita, M.; Grollman, A. P. Insertion of Specific Bases during DNA Synthesis Past the Oxidation-Damaged Base 8-OxodG. *Nature* **1991**, *349* (6308), 431–434. https://doi.org/10.1038/349431a0.

(55) Brandon, M.; Baldi, P.; Wallace, D. C. Mitochondrial Mutations in Cancer. *Oncogene* **2006**, *25* (34), 4647–4662. https://doi.org/10.1038/sj.onc.1209607.

(56) Ishikawa, K.; Takenaga, K.; Akimoto, M.; Koshikawa, N.; Yamaguchi, A.; Imanishi, H.; Nakada, K.; Honma, Y.; Hayashi, J.-I. ROS-Generating Mitochondrial DNA Mutations Can Regulate Tumor Cell Metastasis. *Science (1979)* **2008**, *320* (5876), 661–664. https://doi.org/10.1126/science.1156906.

(57) Alexeyev, M.; Shokolenko, I.; Wilson, G.; LeDoux, S. The Maintenance of Mitochondrial DNA Integrity--Critical Analysis and Update. *Cold Spring Harb Perspect Biol* **2013**, *5* (5), a012641–a012641. https://doi.org/10.1101/cshperspect.a012641.

(58) Larsen, N. B.; Rasmussen, M.; Rasmussen, L. J. Nuclear and Mitochondrial DNA Repair: Similar Pathways? *Mitochondrion* **2005**, *5* (2), 89–108. https://doi.org/10.1016/j.mito.2005.02.002.

(59) de Sá Junior, P. L.; Câmara, D. A. D.; Porcacchia, A. S.; Fonseca, P. M. M.; Jorge, S. D.; Araldi, R. P.; Ferreira, A. K. The Roles of ROS in Cancer Heterogeneity and Therapy. *Oxid Med Cell Longev* **2017**, *2017* (1). https://doi.org/10.1155/2017/2467940.

(60) Schito, L. Hypoxia-Dependent Angiogenesis and Lymphangiogenesis in Cancer; 2019; pp 71–85. https://doi.org/10.1007/978-3-030-12734-3_5.

(61) Dang, C. V; Semenza, G. L. Oncogenic Alterations of Metabolism. *Trends Biochem Sci* **1999**, *24* (2), 68–72. https://doi.org/10.1016/S0968-0004(98)01344-9.

(62) Harris, A. L. Hypoxia — a Key Regulatory Factor in Tumour Growth. *Nat Rev Cancer* **2002**, *2* (1), 38–47. https://doi.org/10.1038/nrc704.

(63) Chandel, N. S.; McClintock, D. S.; Feliciano, C. E.; Wood, T. M.; Melendez, J. A.; Rodriguez, A. M.; Schumacker, P. T. Reactive Oxygen Species Generated at Mitochondrial Complex III Stabilize Hypoxia-Inducible Factor-1α during Hypoxia. *Journal of Biological Chemistry* **2000**, *275* (33), 25130–25138. https://doi.org/10.1074/jbc.M001914200.

(64) Schroedl, C.; McClintock, D. S.; Budinger, G. R. S.; Chandel, N. S. Hypoxic but Not Anoxic Stabilization of HIF-1α Requires Mitochondrial Reactive Oxygen Species. *American*

Journal of Physiology-Lung Cellular and Molecular Physiology **2002**, *283* (5), L922–L931. https://doi.org/10.1152/ajplung.00014.2002.

(65) Park, J.-H.; Kim, T.-Y.; Jong, H.-S.; Kim, T. Y.; Chun, Y.-S.; Park, J.-W.; Lee, C.-T.; Jung, H. C.; Kim, N. K.; Bang, Y.-J. Gastric Epithelial Reactive Oxygen Species Prevent Normoxic Degradation of Hypoxia-Inducible Factor-1alpha in Gastric Cancer Cells. *Clin Cancer Res* **2003**, *9* (1), 433–440.

(66) Waypa, G. B.; Marks, J. D.; Guzy, R. D.; Mungai, P. T.; Schriewer, J. M.; Dokic, D.; Ball, M. K.; Schumacker, P. T. Superoxide Generated at Mitochondrial Complex III Triggers Acute Responses to Hypoxia in the Pulmonary Circulation. *Am J Respir Crit Care Med* **2013**, *187* (4), 424–432. https://doi.org/10.1164/rccm.201207-1294OC.

(67) Farrow, K. N.; Lee, K. J.; Perez, M.; Schriewer, J. M.; Wedgwood, S.; Lakshminrusimha, S.; Smith, C. L.; Steinhorn, R. H.; Schumacker, P. T. Brief Hyperoxia Increases Mitochondrial Oxidation and Increases Phosphodiesterase 5 Activity in Fetal Pulmonary Artery Smooth Muscle Cells. *Antioxid Redox Signal* **2012**, *17* (3), 460–470. https://doi.org/10.1089/ars.2011.4184.

(68) Waypa, G. B.; Marks, J. D.; Guzy, R.; Mungai, P. T.; Schriewer, J.; Dokic, D.; Schumacker, P. T. Hypoxia Triggers Subcellular Compartmental Redox Signaling in Vascular Smooth Muscle Cells. *Circ Res* **2010**, *106* (3), 526–535. https://doi.org/10.1161/CIRCRESAHA.109.206334.

(69) Chandel, N. S.; Maltepe, E.; Goldwasser, E.; Mathieu, C. E.; Simon, M. C.; Schumacker, P. T. Mitochondrial Reactive Oxygen Species Trigger Hypoxia-Induced Transcription. *Proceedings of the National Academy of Sciences* **1998**, *95* (20), 11715–11720. https://doi.org/10.1073/pnas.95.20.11715.

(70) Guzy, R. D.; Schumacker, P. T. Oxygen Sensing by Mitochondria at Complex III: The Paradox of Increased Reactive Oxygen Species during Hypoxia. *Exp Physiol* **2006**, *91* (5), 807–819. https://doi.org/10.1113/expphysiol.2006.033506.

(71) Sainero-Alcolado, L.; Liaño-Pons, J.; Ruiz-Pérez, M. V.; Arsenian-Henriksson, M. Targeting Mitochondrial Metabolism for Precision Medicine in Cancer. *Cell Death Differ* **2022**, *29* (7), 1304–1317. https://doi.org/10.1038/s41418-022-01022-y.

(72) Ducker, G. S.; Rabinowitz, J. D. One-Carbon Metabolism in Health and Disease. *Cell Metab* **2017**, *25* (1), 27–42. https://doi.org/10.1016/j.cmet.2016.08.009.

(73) Lin, P.; Lu, Y.; Zheng, J.; Lin, Y.; Zhao, X.; Cui, L. Strategic Disruption of Cancer's Powerhouse: Precise Nanomedicine Targeting of Mitochondrial Metabolism. *J Nanobiotechnology* **2024**, *22* (1), 318. https://doi.org/10.1186/s12951-024-02585-3.

(74) Liao, Z.; Chua, D.; Tan, N. S. Reactive Oxygen Species: A Volatile Driver of Field Cancerization and Metastasis. *Mol Cancer* **2019**, *18* (1), 65. https://doi.org/10.1186/s12943-019-0961-y.

(75) Seyfried, T. N.; Huysentruyt, L. C. On the Origin of Cancer Metastasis. *Crit Rev Oncog* **2013**, *18* (1–2), 43–73. https://doi.org/10.1615/CritRevOncog.v18.i1-2.40.

(76) Thiery, J. P.; Acloque, H.; Huang, R. Y. J.; Nieto, M. A. Epithelial-Mesenchymal Transitions in Development and Disease. *Cell* **2009**, *139* (5), 871–890. https://doi.org/10.1016/j.cell.2009.11.007.

(77) Bakir, B.; Chiarella, A. M.; Pitarresi, J. R.; Rustgi, A. K. EMT, MET, Plasticity, and Tumor Metastasis. *Trends Cell Biol* **2020**, *30* (10), 764–776. https://doi.org/10.1016/j.tcb.2020.07.003.

(78) Kalluri, R.; Weinberg, R. A. The Basics of Epithelial-Mesenchymal Transition. *Journal of Clinical Investigation* **2009**, *119* (6), 1420–1428. https://doi.org/10.1172/JCI39104.

(79) Heldin, C.-H.; Vanlandewijck, M.; Moustakas, A. Regulation of EMT by TGFβ in Cancer. *FEBS Lett* **2012**, *586* (14), 1959–1970. https://doi.org/10.1016/j.febslet.2012.02.037.

(80) Tobar, N.; Villar, V.; Santibanez, J. F. ROS-NFκB Mediates TGF-B1-Induced Expression of Urokinase-Type Plasminogen Activator, Matrix Metalloproteinase-9 and Cell Invasion. *Mol Cell Biochem* **2010**, *340* (1–2), 195–202. https://doi.org/10.1007/s11010-010-0418-5.

(81) Zhu, P.; Tan, M. J.; Huang, R.-L.; Tan, C. K.; Chong, H. C.; Pal, M.; Lam, C. R. I.; Boukamp, P.; Pan, J. Y.; Tan, S. H.; Kersten, S.; Li, H. Y.; Ding, J. L.; Tan, N. S. Angiopoietin-like 4 Protein Elevates the Prosurvival Intracellular O2−:H2O2 Ratio and Confers Anoikis Resistance to Tumors. *Cancer Cell* **2011**, *19* (3), 401–415. https://doi.org/10.1016/j.ccr.2011.01.018.

(82) Du, S.; Miao, J.; Zhu, Z.; Xu, E.; Shi, L.; Ai, S.; Wang, F.; Kang, X.; Chen, H.; Lu, X.; Guan, W.; Xia, X. NADPH Oxidase 4 Regulates Anoikis Resistance of Gastric Cancer Cells through the Generation of Reactive Oxygen Species and the Induction of EGFR. *Cell Death Dis* **2018**, *9* (10), 948. https://doi.org/10.1038/s41419-018-0953-7.

(83) Kim, H.; Sung, J. Y.; Park, E.-K.; Kho, S.; Koo, K. H.; Park, S.-Y.; Goh, S.-H.; Jeon, Y. K.; Oh, S.; Park, B.-K.; Jung, Y.-K.; Kim, Y.-N. Regulation of Anoikis Resistance by NADPH Oxidase 4 and Epidermal Growth Factor Receptor. *Br J Cancer* **2017**, *116* (3), 370–381. https://doi.org/10.1038/bjc.2016.440.

(84) Redza-Dutordoir, M.; Averill-Bates, D. A. Activation of Apoptosis Signalling Pathways by Reactive Oxygen Species. *Biochimica et Biophysica Acta (BBA) - Molecular Cell Research* **2016**, *1863* (12), 2977–2992. https://doi.org/10.1016/j.bbamcr.2016.09.012.

(85) Dixon, S. J.; Lemberg, K. M.; Lamprecht, M. R.; Skouta, R.; Zaitsev, E. M.; Gleason, C. E.; Patel, D. N.; Bauer, A. J.; Cantley, A. M.; Yang, W. S.; Morrison, B.; Stockwell, B. R. Ferroptosis: An Iron-Dependent Form of Nonapoptotic Cell Death. *Cell* **2012**, *149* (5), 1060–1072. https://doi.org/10.1016/j.cell.2012.03.042.

(86) Green, D. R.; Llambi, F. Cell Death Signaling. *Cold Spring Harb Perspect Biol* **2015**, *7* (12), a006080. https://doi.org/10.1101/cshperspect.a006080.

(87) Ferri, K. F.; Kroemer, G. Organelle-Specific Initiation of Cell Death Pathways. *Nat Cell Biol* **2001**, *3* (11), E255–E263. https://doi.org/10.1038/ncb1101-e255.

(88) Jin, Z.; El-Deiry, W. S. Overview of Cell Death Signaling Pathways. *Cancer Biol Ther* **2005**, *4* (2), 147–171. https://doi.org/10.4161/cbt.4.2.1508.

(89) Scherz-Shouval, R.; Elazar, Z. Regulation of Autophagy by ROS: Physiology and Pathology. *Trends Biochem Sci* **2011**, *36* (1), 30–38. https://doi.org/10.1016/j.tibs.2010.07.007.

(90) Li, L.; Tan, J.; Miao, Y.; Lei, P.; Zhang, Q. ROS and Autophagy: Interactions and Molecular Regulatory Mechanisms. *Cell Mol Neurobiol* **2015**, *35* (5), 615–621. https://doi.org/10.1007/s10571-015-0166-x.

(91) Orrenius, S.; Nicotera, P.; Zhivotovsky, B. Cell Death Mechanisms and Their Implications in Toxicology. *Toxicological Sciences* **2011**, *119* (1), 3–19. https://doi.org/10.1093/toxsci/kfq268.

(92) Vanden Berghe, T.; Kaiser, W. J.; Bertrand, M. J.; Vandenabeele, P. Molecular Crosstalk between Apoptosis, Necroptosis, and Survival Signaling. *Mol Cell Oncol* **2015**, *2* (4), e975093. https://doi.org/10.4161/23723556.2014.975093.

(93) Hanson, B. Necroptosis: A New Way of Dying? *Cancer Biol Ther* **2016**, *17* (9), 899–910. https://doi.org/10.1080/15384047.2016.1210732.

(94) Wu, W.; Liu, P.; Li, J. Necroptosis: An Emerging Form of Programmed Cell Death. *Crit Rev Oncol Hematol* **2012**, *82* (3), 249–258. https://doi.org/10.1016/j.critrevonc.2011.08.004.

(95) Frisch, S.; Francis, H. Disruption of Epithelial Cell-Matrix Interactions Induces Apoptosis. *J Cell Biol* **1994**, *124* (4), 619–626. https://doi.org/10.1083/jcb.124.4.619.

(96) Buchheit, C. L.; Rayavarapu, R. R.; Schafer, Z. T. The Regulation of Cancer Cell Death and Metabolism by Extracellular Matrix Attachment. *Semin Cell Dev Biol* **2012**, *23* (4), 402–411. https://doi.org/10.1016/j.semcdb.2012.04.007.

(97) Li, J.; Cao, F.; Yin, H.; Huang, Z.; Lin, Z.; Mao, N.; Sun, B.; Wang, G. Ferroptosis: Past, Present and Future. *Cell Death Dis* **2020**, *11* (2), 88. https://doi.org/10.1038/s41419-020-2298-2.

(98) Xie, Y.; Hou, W.; Song, X.; Yu, Y.; Huang, J.; Sun, X.; Kang, R.; Tang, D. Ferroptosis: Process and Function. *Cell Death Differ* **2016**, *23* (3), 369–379. https://doi.org/10.1038/cdd.2015.158.

(99) Yang, W. S.; SriRamaratnam, R.; Welsch, M. E.; Shimada, K.; Skouta, R.; Viswanathan, V. S.; Cheah, J. H.; Clemons, P. A.; Shamji, A. F.; Clish, C. B.; Brown, L. M.; Girotti, A. W.; Cornish, V. W.; Schreiber, S. L.; Stockwell, B. R. Regulation of Ferroptotic Cancer Cell Death by GPX4. *Cell* **2014**, *156* (1–2), 317–331. https://doi.org/10.1016/j.cell.2013.12.010.

(100) Sato, H.; Tamba, M.; Ishii, T.; Bannai, S. Cloning and Expression of a Plasma Membrane Cystine/Glutamate Exchange Transporter Composed of Two Distinct Proteins. *Journal of Biological Chemistry* **1999**, *274* (17), 11455–11458. https://doi.org/10.1074/jbc.274.17.11455.

(101) Yang, W. S.; Stockwell, B. R. Synthetic Lethal Screening Identifies Compounds Activating Iron-Dependent, Nonapoptotic Cell Death in Oncogenic-RAS-Harboring Cancer Cells. *Chem Biol* **2008**, *15* (3), 234–245. https://doi.org/10.1016/j.chembiol.2008.02.010.

(102) Moosmayer, D.; Hilpmann, A.; Hoffmann, J.; Schnirch, L.; Zimmermann, K.; Badock, V.; Furst, L.; Eaton, J. K.; Viswanathan, V. S.; Schreiber, S. L.; Gradl, S.; Hillig, R. C. Crystal Structures of the Selenoprotein Glutathione Peroxidase 4 in Its Apo Form and in Complex with the Covalently Bound Inhibitor ML162. *Acta Crystallogr D Struct Biol* **2021**, *77* (2), 237–248. https://doi.org/10.1107/S2059798320016125.

(103) Ayala, A.; Muñoz, M. F.; Argüelles, S. Lipid Peroxidation: Production, Metabolism, and Signaling Mechanisms of Malondialdehyde and 4-Hydroxy-2-Nonenal. *Oxid Med Cell Longev* **2014**, *2014*, 1–31. https://doi.org/10.1155/2014/360438.

(104) Yang, W. S.; Kim, K. J.; Gaschler, M. M.; Patel, M.; Shchepinov, M. S.; Stockwell, B. R. Peroxidation of Polyunsaturated Fatty Acids by Lipoxygenases Drives Ferroptosis. *Proceedings of the National Academy of Sciences* **2016**, *113* (34). https://doi.org/10.1073/pnas.1603244113.

(105) Hassannia, B.; Vandenabeele, P.; Vanden Berghe, T. Targeting Ferroptosis to Iron Out Cancer. *Cancer Cell* **2019**, *35* (6), 830–849. https://doi.org/10.1016/j.ccell.2019.04.002.

(106) Shah, R.; Shchepinov, M. S.; Pratt, D. A. Resolving the Role of Lipoxygenases in the Initiation and Execution of Ferroptosis. *ACS Cent Sci* **2018**, *4* (3), 387–396. https://doi.org/10.1021/acscentsci.7b00589.

(107) Jin, X.; Tang, J.; Qiu, X.; Nie, X.; Ou, S.; Wu, G.; Zhang, R.; Zhu, J. Ferroptosis: Emerging Mechanisms, Biological Function, and Therapeutic Potential in Cancer and Inflammation. *Cell Death Discov* **2024**, *10* (1), 45. https://doi.org/10.1038/s41420-024-01825-7.

(108) Zou, Y.; Li, H.; Graham, E. T.; Deik, A. A.; Eaton, J. K.; Wang, W.; Sandoval-Gomez, G.; Clish, C. B.; Doench, J. G.; Schreiber, S. L. Cytochrome P450 Oxidoreductase Contributes to Phospholipid Peroxidation in Ferroptosis. *Nat Chem Biol* **2020**, *16* (3), 302–309. https://doi.org/10.1038/s41589-020-0472-6.

(109) Yan, B.; Ai, Y.; Sun, Q.; Ma, Y.; Cao, Y.; Wang, J.; Zhang, Z.; Wang, X. Membrane Damage during Ferroptosis Is Caused by Oxidation of Phospholipids Catalyzed by the Oxidoreductases POR and CYB5R1. *Mol Cell* **2021**, *81* (2), 355-369.e10. https://doi.org/10.1016/j.molcel.2020.11.024.

(110) Catalá, A.; Díaz, M. Editorial: Impact of Lipid Peroxidation on the Physiology and Pathophysiology of Cell Membranes. *Front Physiol* **2016**, *7*. https://doi.org/10.3389/fphys.2016.00423.

(111) Feng, H.; Stockwell, B. R. Unsolved Mysteries: How Does Lipid Peroxidation Cause Ferroptosis? *PLoS Biol* **2018**, *16* (5), e2006203. https://doi.org/10.1371/journal.pbio.2006203.

(112) Frazer, D. M.; Anderson, G. J. The Regulation of Iron Transport. *BioFactors* **2014**, *40* (2), 206–214. https://doi.org/10.1002/biof.1148.

(113) Zhou, L.; Zhao, B.; Zhang, L.; Wang, S.; Dong, D.; Lv, H.; Shang, P. Alterations in Cellular Iron Metabolism Provide More Therapeutic Opportunities for Cancer. *Int J Mol Sci* **2018**, *19* (5), 1545. https://doi.org/10.3390/ijms19051545.

(114) Fenton, H. J. H. LXXIII.—Oxidation of Tartaric Acid in Presence of Iron. *J. Chem. Soc., Trans.* **1894**, *65* (0), 899–910. https://doi.org/10.1039/CT8946500899.

(115) Yin, H.; Xu, L.; Porter, N. A. Free Radical Lipid Peroxidation: Mechanisms and Analysis. *Chem Rev* **2011**, *111* (10), 5944–5972. https://doi.org/10.1021/cr200084z.

(116) Mao, H.; Zhao, Y.; Li, H.; Lei, L. Ferroptosis as an Emerging Target in Inflammatory Diseases. *Prog Biophys Mol Biol* **2020**, *155*, 20–28. https://doi.org/10.1016/j.pbiomolbio.2020.04.001.

(117) Gnanapradeepan, K.; Basu, S.; Barnoud, T.; Budina-Kolomets, A.; Kung, C.-P.; Murphy, M. E. The P53 Tumor Suppressor in the Control of Metabolism and Ferroptosis. *Front Endocrinol (Lausanne)* **2018**, *9*. https://doi.org/10.3389/fendo.2018.00124.

(118) Bieging, K. T.; Mello, S. S.; Attardi, L. D. Unravelling Mechanisms of P53-Mediated Tumour Suppression. *Nat Rev Cancer* **2014**, *14* (5), 359–370. https://doi.org/10.1038/nrc3711.

(119) Kaiser, A. M.; Attardi, L. D. Deconstructing Networks of P53-Mediated Tumor Suppression in Vivo. *Cell Death Differ* **2018**, *25* (1), 93–103. https://doi.org/10.1038/cdd.2017.171.

(120) Jiang, L.; Kon, N.; Li, T.; Wang, S.-J.; Su, T.; Hibshoosh, H.; Baer, R.; Gu, W. Ferroptosis as a P53-Mediated Activity during Tumour Suppression. *Nature* **2015**, *520* (7545), 57–62. https://doi.org/10.1038/nature14344.

(121) Tarangelo, A.; Magtanong, L.; Bieging-Rolett, K. T.; Li, Y.; Ye, J.; Attardi, L. D.; Dixon, S. J. P53 Suppresses Metabolic Stress-Induced Ferroptosis in Cancer Cells. *Cell Rep* **2018**, *22* (3), 569–575. https://doi.org/10.1016/j.celrep.2017.12.077.

(122) Stockwell, B. R. Ferroptosis Turns 10: Emerging Mechanisms, Physiological Functions, and Therapeutic Applications. *Cell* **2022**, *185* (14), 2401–2421. https://doi.org/10.1016/j.cell.2022.06.003.

(123) Yin, L.; Liu, P.; Jin, Y.; Ning, Z.; Yang, Y.; Gao, H. Ferroptosis-Related Small-Molecule Compounds in Cancer Therapy: Strategies and Applications. *Eur J Med Chem* **2022**, *244*, 114861. https://doi.org/10.1016/j.ejmech.2022.114861.

(124) Seibt, T. M.; Proneth, B.; Conrad, M. Role of GPX4 in Ferroptosis and Its Pharmacological Implication. *Free Radic Biol Med* **2019**, *133*, 144–152. https://doi.org/10.1016/j.freeradbiomed.2018.09.014.

(125) Nishizawa, S.; Araki, H.; Ishikawa, Y.; Kitazawa, S.; Hata, A.; Soga, T.; Hara, T. Low Tumor Glutathione Level as a Sensitivity Marker for Glutamate-cysteine Ligase Inhibitors. *Oncol Lett* **2018**. https://doi.org/10.3892/ol.2018.8447.

(126) Ferrada, L.; Barahona, M. J.; Salazar, K.; Godoy, A. S.; Vera, M.; Nualart, F. Pharmacological Targets for the Induction of Ferroptosis: Focus on Neuroblastoma and Glioblastoma. *Front Oncol* **2022**, *12*. https://doi.org/10.3389/fonc.2022.858480.

(127) o W Griffith. Mechanism of Action, Metabolism, and Toxicity of Buthionine Sulfoximine and Its Higher Homologs, Potent Inhibitors of Glutathione Synthesis. *J. Biol Chem.* **1982**, 13704–13712.

(128) Eling, N.; Reuter, L.; Hazin, J.; Hamacher-Brady, A.; Brady, N. R. Identification of Artesunate as a Specific Activator of Ferroptosis in Pancreatic Cancer Cells. *Oncoscience* **2015**, *2* (5), 517–532. https://doi.org/10.18632/oncoscience.160.

(129) Liu, H.; Forouhar, F.; Lin, A. J.; Wang, Q.; Polychronidou, V.; Soni, R. K.; Xia, X.; Stockwell, B. R. Small-Molecule Allosteric Inhibitors of GPX4. *Cell Chem Biol* **2022**, *29* (12), 1680-1693.e9. https://doi.org/10.1016/j.chembiol.2022.11.003.

(130) Shimada, K.; Skouta, R.; Kaplan, A.; Yang, W. S.; Hayano, M.; Dixon, S. J.; Brown, L. M.; Valenzuela, C. A.; Wolpaw, A. J.; Stockwell, B. R. Global Survey of Cell Death Mechanisms Reveals Metabolic Regulation of Ferroptosis. *Nat Chem Biol* **2016**, *12* (7), 497–503. https://doi.org/10.1038/nchembio.2079.

(131) Gaschler, M. M.; Andia, A. A.; Liu, H.; Csuka, J. M.; Hurlocker, B.; Vaiana, C. A.; Heindel, D. W.; Zuckerman, D. S.; Bos, P. H.; Reznik, E.; Ye, L. F.; Tyurina, Y. Y.; Lin, A. J.; Shchepinov, M. S.; Chan, A. Y.; Peguero-Pereira, E.; Fomich, M. A.; Daniels, Jacob. D.; Bekish, A. V.; Shmanai, V. V.; Kagan, V. E.; Mahal, L. K.; Woerpel, K. A.; Stockwell, B. R. FINO2 Initiates Ferroptosis through GPX4 Inactivation and Iron Oxidation. *Nat Chem Biol* **2018**, *14* (5), 507–515. https://doi.org/10.1038/s41589-018-0031-6.

(132) Rahib, L.; Smith, B. D.; Aizenberg, R.; Rosenzweig, A. B.; Fleshman, J. M.; Matrisian, L. M. Projecting Cancer Incidence and Deaths to 2030: The Unexpected Burden of Thyroid, Liver, and Pancreas Cancers in the United States. *Cancer Res* **2014**, *74* (11), 2913–2921. https://doi.org/10.1158/0008-5472.CAN-14-0155.

(133) Mantovani, M. C.; Silva, I. B. B.; Lojudice, F. H.; Kossugue, P. M.; Sogayar, M. C. Pancreatic Stem Cells and Regenerative Medicine of Endocrine Pancreas. In *Resident Stem Cells and Regenerative Therapy*; Elsevier, 2024; pp 75–103. https://doi.org/10.1016/B978-0-443-15289-4.00013-5.

(134) Puri, S.; Folias, A. E.; Hebrok, M. Plasticity and Dedifferentiation within the Pancreas: Development, Homeostasis, and Disease. *Cell Stem Cell* **2015**, *16* (1), 18–31. https://doi.org/10.1016/j.stem.2014.11.001.

(135) Marstrand-Daucé, L.; Lorenzo, D.; Chassac, A.; Nicole, P.; Couvelard, A.; Haumaitre, C. Acinar-to-Ductal Metaplasia (ADM): On the Road to Pancreatic Intraepithelial Neoplasia (PanIN) and Pancreatic Cancer. *Int J Mol Sci* **2023**, *24* (12), 9946. https://doi.org/10.3390/ijms24129946.

(136) Murtaugh, L. C.; Keefe, M. D. Regeneration and Repair of the Exocrine Pancreas. *Annu Rev Physiol* **2015**, *77* (1), 229–249. https://doi.org/10.1146/annurev-physiol-021014-071727.

(137) Zhu, L.; Shi, G.; Schmidt, C. Max.; Hruban, R. H.; Konieczny, S. F. Acinar Cells Contribute to the Molecular Heterogeneity of Pancreatic Intraepithelial Neoplasia. *Am J Pathol* **2007**, *171* (1), 263–273. https://doi.org/10.2353/ajpath.2007.061176.

(138) Rhim, A. D.; Mirek, E. T.; Aiello, N. M.; Maitra, A.; Bailey, J. M.; McAllister, F.; Reichert, M.; Beatty, G. L.; Rustgi, A. K.; Vonderheide, R. H.; Leach, S. D.; Stanger, B. Z. EMT and Dissemination Precede Pancreatic Tumor Formation. *Cell* **2012**, *148* (1–2), 349–361. https://doi.org/10.1016/j.cell.2011.11.025.

(139) Basturk, O.; Hong, S.-M.; Wood, L. D.; Adsay, N. V.; Albores-Saavedra, J.; Biankin, A. V.; Brosens, L. A. A.; Fukushima, N.; Goggins, M.; Hruban, R. H.; Kato, Y.; Klimstra, D. S.; Klöppel, G.; Krasinskas, A.; Longnecker, D. S.; Matthaei, H.; Offerhaus, G. J. A.; Shimizu, M.; Takaori, K.; Terris, B.; Yachida, S.; Esposito, I.; Furukawa, T. A Revised Classification System and Recommendations From the Baltimore Consensus Meeting for Neoplastic Precursor Lesions in the Pancreas. *American Journal of Surgical Pathology* **2015**, *39* (12), 1730–1741. https://doi.org/10.1097/PAS.0000000000000533.

(140) Waddell, N.; Pajic, M.; Patch, A.-M.; Chang, D. K.; Kassahn, K. S.; Bailey, P.; Johns, A. L.; Miller, D.; Nones, K.; Quek, K.; Quinn, M. C. J.; Robertson, A. J.; Fadlullah, M. Z. H.; Bruxner, T. J. C.; Christ, A. N.; Harliwong, I.; Idrisoglu, S.; Manning, S.; Nourse, C.; Nourbakhsh, E.; Wani, S.; Wilson, P. J.; Markham, E.; Cloonan, N.; Anderson, M. J.; Fink, J. L.; Holmes, O.; Kazakoff, S. H.; Leonard, C.; Newell, F.; Poudel, B.; Song, S.; Taylor, D.; Waddell, N.; Wood, S.; Xu, Q.; Wu, J.; Pinese, M.; Cowley, M. J.; Lee, H. C.; Jones, M. D.; Nagrial, A. M.; Humphris, J.; Chantrill, L. A.; Chin, V.; Steinmann, A. M.; Mawson, A.; Humphrey, E. S.; Colvin, E. K.; Chou, A.; Scarlett, C. J.; Pinho, A. V.; Giry-Laterriere, M.; Rooman, I.; Samra, J. S.; Kench, J. G.; Pettitt, J. A.; Merrett, N. D.; Toon, C.; Epari, K.; Nguyen, N. Q.; Barbour, A.; Zeps, N.; Jamieson, N. B.; Graham, J. S.; Niclou, S. P.; Bjerkvig, R.; Grützmann, R.; Aust, D.; Hruban, R. H.; Maitra, A.; Iacobuzio-Donahue, C. A.; Wolfgang, C. L.; Morgan, R. A.; Lawlor, R. T.; Corbo, V.; Bassi, C.; Falconi, M.; Zamboni, G.; Tortora, G.; Tempero, M. A.; Gill, A. J.; Eshleman, J. R.; Pilarsky, C.; Scarpa, A.; Musgrove, E. A.; Pearson, J. V.; Biankin, A. V.; Grimmond, S. M. Whole Genomes Redefine the Mutational Landscape of Pancreatic Cancer. *Nature* **2015**, *518* (7540), 495–501. https://doi.org/10.1038/nature14169.

(141) Plass, C.; Pfister, S. M.; Lindroth, A. M.; Bogatyrova, O.; Claus, R.; Lichter, P. Mutations in Regulators of the Epigenome and Their Connections to Global Chromatin Patterns in Cancer. *Nat Rev Genet* **2013**, *14* (11), 765–780. https://doi.org/10.1038/nrg3554.

(142) Sausen, M.; Phallen, J.; Adleff, V.; Jones, S.; Leary, R. J.; Barrett, M. T.; Anagnostou, V.; Parpart-Li, S.; Murphy, D.; Kay Li, Q.; Hruban, C. A.; Scharpf, R.; White, J. R.; O'Dwyer, P. J.; Allen, P. J.; Eshleman, J. R.; Thompson, C. B.; Klimstra, D. S.; Linehan, D. C.; Maitra, A.; Hruban, R. H.; Diaz, L. A.; Von Hoff, D. D.; Johansen, J. S.; Drebin, J. A.; Velculescu, V. E. Clinical Implications of Genomic Alterations in the Tumour and Circulation of Pancreatic Cancer Patients. *Nat Commun* **2015**, *6* (1), 7686. https://doi.org/10.1038/ncomms8686.

(143) Morris, J. P.; Wang, S. C.; Hebrok, M. KRAS, Hedgehog, Wnt and the Twisted Developmental Biology of Pancreatic Ductal Adenocarcinoma. *Nat Rev Cancer* **2010**, *10* (10), 683–695. https://doi.org/10.1038/nrc2899.

(144) Ying, H.; Dey, P.; Yao, W.; Kimmelman, A. C.; Draetta, G. F.; Maitra, A.; DePinho, R. A. Genetics and Biology of Pancreatic Ductal Adenocarcinoma. *Genes Dev* **2016**, *30* (4), 355–385. https://doi.org/10.1101/gad.275776.115.

(145) Warburg, O. On the Origin of Cancer Cells. *Science (1979)* **1956**, *123* (3191), 309–314. https://doi.org/10.1126/science.123.3191.309.

(146) Li, J.-T.; Wang, Y.-P.; Yin, M.; Lei, Q.-Y. Metabolism Remodeling in Pancreatic Ductal Adenocarcinoma. *Cell Stress* **2019**, *3* (12), 361–368. https://doi.org/10.15698/cst2019.12.205.

(147) Ying, H.; Kimmelman, A. C.; Lyssiotis, C. A.; Hua, S.; Chu, G. C.; Fletcher-Sananikone, E.; Locasale, J. W.; Son, J.; Zhang, H.; Coloff, J. L.; Yan, H.; Wang, W.; Chen, S.; Viale, A.; Zheng, H.; Paik, J.; Lim, C.; Guimaraes, A. R.; Martin, E. S.; Chang, J.; Hezel, A. F.; Perry, S. R.; Hu, J.; Gan, B.; Xiao, Y.; Asara, J. M.; Weissleder, R.; Wang, Y. A.; Chin, L.; Cantley, L. C.; DePinho, R. A. Oncogenic Kras Maintains Pancreatic Tumors through Regulation of Anabolic Glucose Metabolism. *Cell* **2012**, *149* (3), 656–670. https://doi.org/10.1016/j.cell.2012.01.058.

(148) Orth, M.; Metzger, P.; Gerum, S.; Mayerle, J.; Schneider, G.; Belka, C.; Schnurr, M.; Lauber, K. Pancreatic Ductal Adenocarcinoma: Biological Hallmarks, Current Status, and Future Perspectives of Combined Modality Treatment Approaches. *Radiation Oncology* **2019**, *14* (1), 141. https://doi.org/10.1186/s13014-019-1345-6.

(149) Malka, D. Risk of Pancreatic Adenocarcinoma in Chronic Pancreatitis. *Gut* **2002**, *51* (6), 849–852. https://doi.org/10.1136/gut.51.6.849.

(150) Guerra, C.; Schuhmacher, A. J.; Cañamero, M.; Grippo, P. J.; Verdaguer, L.; Pérez-Gallego, L.; Dubus, P.; Sandgren, E. P.; Barbacid, M. Chronic Pancreatitis Is Essential for Induction of Pancreatic Ductal Adenocarcinoma by K-Ras Oncogenes in Adult Mice. *Cancer Cell* **2007**, *11* (3), 291–302. https://doi.org/10.1016/j.ccr.2007.01.012.

(151) Dardare, J.; Witz, A.; Merlin, J.-L.; Bochnakian, A.; Toussaint, P.; Gilson, P.; Harlé, A. Epithelial to Mesenchymal Transition in Patients with Pancreatic Ductal Adenocarcinoma: State-of-the-Art and Therapeutic Opportunities. *Pharmaceuticals* **2021**, *14* (8), 740. https://doi.org/10.3390/ph14080740.

(152) Marcucci, F.; Stassi, G.; De Maria, R. Epithelial–Mesenchymal Transition: A New Target in Anticancer Drug Discovery. *Nat Rev Drug Discov* **2016**, *15* (5), 311–325. https://doi.org/10.1038/nrd.2015.13.

(153) Hall, W. A.; Goodman, K. A. Radiation Therapy for Pancreatic Adenocarcinoma, a Treatment Option That Must Be Considered in the Management of a Devastating Malignancy. *Radiation Oncology* **2019**, *14* (1), 114. https://doi.org/10.1186/s13014-019-1277-1.

(154) Brix, N.; Tiefenthaller, A.; Anders, H.; Belka, C.; Lauber, K. Abscopal, Immunological Effects of Radiotherapy: Narrowing the Gap between Clinical and Preclinical Experiences. *Immunol Rev* **2017**, *280* (1), 249–279. https://doi.org/10.1111/imr.12573.

(155) Filatenkov, A.; Baker, J.; Mueller, A. M. S.; Kenkel, J.; Ahn, G.-O.; Dutt, S.; Zhang, N.; Kohrt, H.; Jensen, K.; Dejbakhsh-Jones, S.; Shizuru, J. A.; Negrin, R. N.; Engleman, E. G.; Strober, S. Ablative Tumor Radiation Can Change the Tumor Immune Cell Microenvironment to Induce Durable Complete Remissions. *Clinical Cancer Research* **2015**, *21* (16), 3727–3739. https://doi.org/10.1158/1078-0432.CCR-14-2824.

(156) Kolbeinsson, H. M.; Chandana, S.; Wright, G. P.; Chung, M. Pancreatic Cancer: A Review of Current Treatment and Novel Therapies. *Journal of Investigative Surgery* **2023**, *36* (1). https://doi.org/10.1080/08941939.2022.2129884.

(157) Holmström, K. M.; Finkel, T. Cellular Mechanisms and Physiological Consequences of Redox-Dependent Signalling. *Nat Rev Mol Cell Biol* **2014**, *15* (6), 411–421. https://doi.org/10.1038/nrm3801.

(158) Trachootham, D.; Alexandre, J.; Huang, P. Targeting Cancer Cells by ROS-Mediated Mechanisms: A Radical Therapeutic Approach? *Nat Rev Drug Discov* **2009**, *8* (7), 579–591. https://doi.org/10.1038/nrd2803.

(159) Pathania, D.; Sechi, M.; Palomba, M.; Sanna, V.; Berrettini, F.; Sias, A.; Taheri, L.; Neamati, N. Design and Discovery of Novel Quinazolinedione-Based Redox Modulators as Therapies for Pancreatic Cancer. *Biochimica et Biophysica Acta (BBA) - General Subjects* **2014**, *1840* (1), 332–343. https://doi.org/10.1016/j.bbagen.2013.08.005.

(160) Chang, L.; Karin, M. Mammalian MAP Kinase Signalling Cascades. *Nature* **2001**, *410* (6824), 37–40. https://doi.org/10.1038/35065000.

(161) Verheij, M.; Bose, R.; Hua Lin, X.; Yao, B.; Jarvis, W. D.; Grant, S.; Birrer, M. J.; Szabo, E.; Zon, L. I.; Kyriakis, J. M.; Haimovitz-Friedman, A.; Fuks, Z.; Kolesnick, R. N. Requirement for Ceramide-Initiated SAPK/JNK Signalling in Stress-Induced Apoptosis. *Nature* **1996**, *380* (6569), 75–79. https://doi.org/10.1038/380075a0.

(162) Cobb, M. H. MAP Kinase Pathways. *Prog Biophys Mol Biol* **1999**, *71* (3–4), 479–500. https://doi.org/10.1016/S0079-6107(98)00056-X.

(163) Tournier, C.; Hess, P.; Yang, D. D.; Xu, J.; Turner, T. K.; Nimnual, A.; Bar-Sagi, D.; Jones, S. N.; Flavell, R. A.; Davis, R. J. Requirement of JNK for Stress- Induced Activation of the Cytochrome c-Mediated Death Pathway. *Science (1979)* **2000**, *288* (5467), 870–874. https://doi.org/10.1126/science.288.5467.870.

(164) Davis, R. J. Signal Transduction by the JNK Group of MAP Kinases. *Cell* **2000**, *103* (2), 239–252. https://doi.org/10.1016/S0092-8674(00)00116-1.

(165) Pathania, D.; Kuang, Y.; Sechi, M.; Neamati, N. Mechanisms Underlying the Cytotoxicity of a Novel Quinazolinedione-based Redox Modulator, <scp>QD</Scp> 232, in Pancreatic Cancer Cells. *Br J Pharmacol* **2015**, *172* (1), 50–63. https://doi.org/10.1111/bph.12855.

(166) Nagaraj, N. S.; Smith, J. J.; Revetta, F.; Washington, M. K.; Merchant, N. B. Targeted Inhibition of Src Kinase Signaling Attenuates Pancreatic Tumorigenesis. *Mol Cancer Ther* **2010**, *9* (8), 2322–2332. https://doi.org/10.1158/1535-7163.MCT-09-1212.

(167) Byers, L. A.; Sen, B.; Saigal, B.; Diao, L.; Wang, J.; Nanjundan, M.; Cascone, T.; Mills, G. B.; Heymach, J. V.; Johnson, F. M. Reciprocal Regulation of C-Src and STAT3 in Non-Small Cell Lung Cancer. *Clinical Cancer Research* **2009**, *15* (22), 6852–6861. https://doi.org/10.1158/1078-0432.CCR-09-0767.

(168) Zhou, J.-H.; Cheng, H.-Y.; Yu, Z.-Q.; He, D.-W.; Pan, Z.; Yang, D.-T. Resveratrol Induces Apoptosis in Pancreatic Cancer Cells. *Chin Med J (Engl)* **2011**, *124* (11), 1695–1699.

(169) Sen, B.; Saigal, B.; Parikh, N.; Gallick, G.; Johnson, F. M. Sustained Src Inhibition Results in Signal Transducer and Activator of Transcription 3 (STAT3) Activation and Cancer Cell Survival via Altered Janus-Activated Kinase–STAT3 Binding. *Cancer Res* **2009**, *69* (5), 1958–1965. https://doi.org/10.1158/0008-5472.CAN-08-2944.

(170) Kuang, Y.; Sechi, M.; Nurra, S.; Ljungman, M.; Neamati, N. Design and Synthesis of Novel Reactive Oxygen Species Inducers for the Treatment of Pancreatic Ductal Adenocarcinoma. *J Med Chem* **2018**, *61* (4), 1576–1594. https://doi.org/10.1021/acs.jmedchem.7b01463.

(171) Hu, S.; Sechi, M.; Singh, P. K.; Dai, L.; McCann, S.; Sun, D.; Ljungman, M.; Neamati, N. A Novel Redox Modulator Induces a GPX4-Mediated Cell Death That Is Dependent on Iron and Reactive Oxygen Species. *J Med Chem* **2020**, *63* (17), 9838–9855. https://doi.org/10.1021/acs.jmedchem.0c01016.

(172) Faizan, M.; Kumar, R.; Mazumder, A.; Salahuddin; Kukreti, N.; Kumar, A.; Chaitanya, M. V. N. L. The Medicinal Chemistry of Piperazines: A Review. *Chem Biol Drug Des* **2024**, *103* (6). https://doi.org/10.1111/cbdd.14537.

(173) Sharma, A.; Wakode, S.; Fayaz, F.; Khasimbi, S.; Pottoo, F. H.; Kaur, A. An Overview of Piperazine Scaffold as Promising Nucleus for Different Therapeutic Targets. *Curr Pharm Des* **2020**, *26* (35), 4373–4385. https://doi.org/10.2174/1381612826666200417154810.

(174) Cao, D.; Liu, Z.; Verwilst, P.; Koo, S.; Jangjili, P.; Kim, J. S.; Lin, W. Coumarin-Based Small-Molecule Fluorescent Chemosensors. *Chem Rev* **2019**, *119* (18), 10403–10519. https://doi.org/10.1021/acs.chemrev.9b00145.

Chapter III Discovery and development of novel selective Carbonic Anhydrases Inhibitors

Chapter III - Discovery and development of novel selective Carbonic Anhydrases Inhibitors (CAIs)

1. Carbonic anhydrase inhibitors: a general view

Carbonic anhydrases (CAs, EC 4.2.1.1) are ubiquitous metalloenzymes, encoded by eight genetic families: the α-, β-, γ-, δ-, ζ-, η-Cas [1] and two recent θ- and ι-CAs.[2] The α -CAs are present in vertebrates, protozoa, algae, and cytoplasm of green plants and in some bacteria, the β- CAs are predominantly found in bacteria, algae and chloroplasts of both mono- as well as dicotyledons, in many fungi and some archaea. The γ -CAs were found in archaea, cyanobacteria, and most types of bacteria, the δ - and ζ -CAs seem to be present only in marine diatoms, the η -CAs in protozoa and θ- and ι-CAs in marine diatoms and bacteria.[1] These enzymes are involved in crucial physiological processes connected with respiration and transport of CO_2/bicarbonate, pH, and CO_2 homeostasis, electrolyte secretion in a variety of tissues/organs, biosynthetic reactions (e.g. gluconeogenesis, lipogenesis, and ureagenesis), bone resorption, calcification, tumorigenicity, and many other physiologic or pathologic processes (thoroughly studied in vertebrates).[1,3,4] All of them are metalloenzymes, but α-, β-, δ-, η- and θ- CAs use Zinc (II) ions in their active site, the γ -CAs are probably Fe(II) enzymes (but they are active also with bound Zn(II) or Co(II) ions), the ζ -class uses Cd(II) or Zn(II) whereas ι-CAs probably use Mn (II) to perform the physiologic reaction catalysis.[2]

1.1 Human carbonic anhydrases

All the human CA (*h*CA) isozymes are related to the α-CA family with different subcellular localization and tissue distribution.[5,6] There are five cytosolic forms (CA I, CA II, CA III, CA VII and CA XIII), five membrane bound isozymes (CA IV, CA IX, CA XII, CA XIV and CA XV), two mitochondrial forms (CA VA and CA VB), and a secreted CA isozyme (CA VI). Only three isoforms (VIII, X and XI), called CA-related proteins (CARPs) lack of catalytic activity and their function is not completely understood (**Figure 1**).

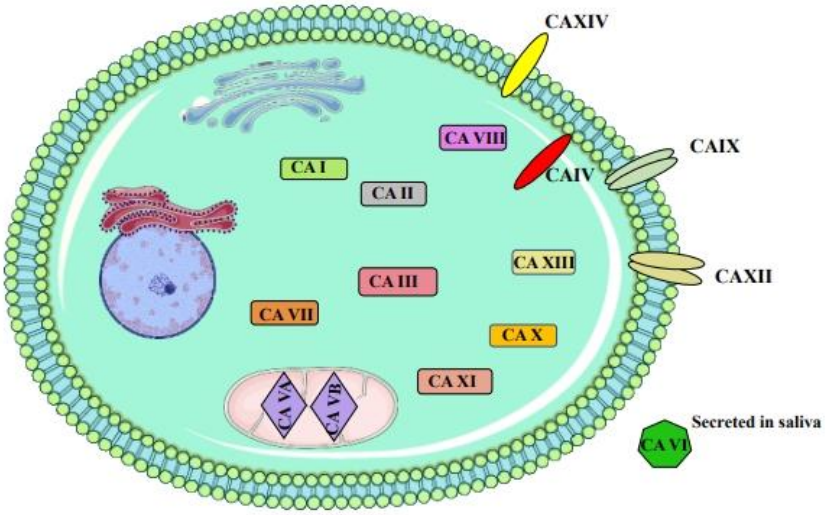


Figure 30. Subcellular localization of CAs. Source: [6]

Structural analysis revealed a high degree of sequence homology among these isoforms, regardless their subcellular location. Each isoform features a central twisted β-sheet surrounded by helical connections and additional β-strands. Despite the high structural homology, three isoforms - CA VI, IX and XII – exist in a dimeric form, each with distinct characteristics. However, the presence of a dimeric form does not appear to influence the catalytic properties of the enzyme. The observation of a dimeric arrangement suggests that the oligomeric arrangement of these isoforms responds to the necessity to perform specific functions in the tissues, where they are generally present.[7,8]

In general, the active site is located in a large, conical cavity with an approximately width of 12 Å and depth of 13 Å; the Zinc ion is located in the bottom, exhibiting a tetrahedral coordination with three histidine residues (His-94, His-96 and His-199) and a water molecule / hydroxide ion as a fourth ligand.[5,9] (**Figure 2**). The Zn^{2+} -bound water molecule/ hydroxide ion participates in a network of hydrogen bonds which helps to enhance its nucleophilicity. In particular, it is hydrogen bonded with the hydroxyl moiety of a conserved threonine residue (Thr199) and with two water molecules, located on two opposite sides: the first one, called the "*deep water*", is located in a hydrophobic cavity delimited by conserved residues (Val121, Val143, Leu198, and Trp209), while the second one is in a hydrophilic environment toward the entrance of the active site (Asn62, His64, Asn67 and Gln92). The active site cavity of all CAs is divided into these two very

different environments: an hydrophobic region is necessary to sequester the CO_2 substrate and orient the carbon atom for nucleophilic attack by the zinc-bound hydroxide, while the hydrophilic region creates a well ordered hydrogen-bonded network, which is necessary to allow the proton transfer reaction from the zinc-bound water molecule to the bulk solvent.[5]

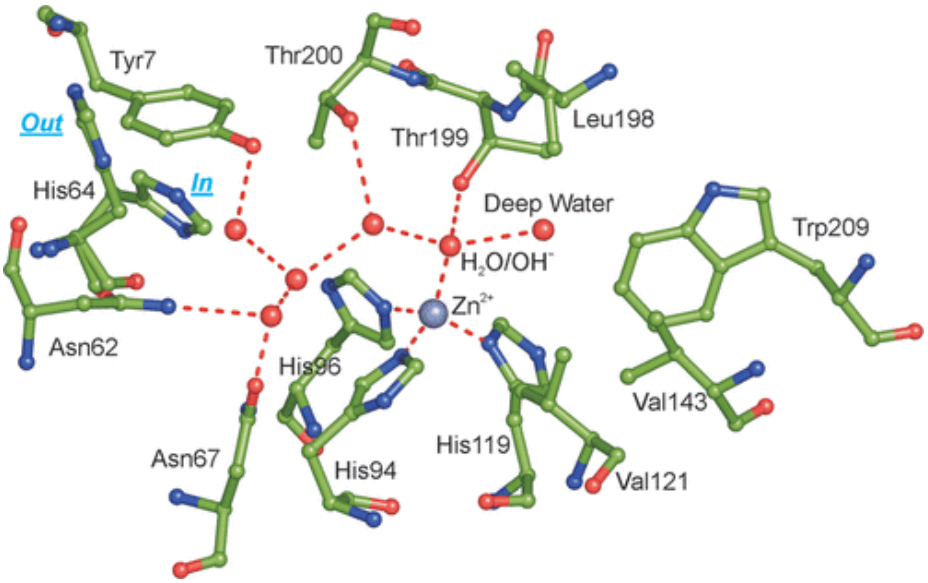


Figure 31. The active site of hCA II chosen as representative CA isoform. The Zn2+ is tetrahedrally coordinated by the three catalytic histidines and a water molecule/hydroxide ion, which is engaged in a well-defined network of hydrogen bonds. Water molecules are indicated as red circles. Source: [10]

1.1.1 Catalytic mechanism of hCAs

All these enzymes primarily catalizes the reversible hydration of carbon dioxide to bicarbonate ion and proton ($CO_2 + H_2O \leftrightarrows HCO_3^- + H^+$), although they partecipate in many other reactions (**Figure 3A**)[4]. The conversion of carbon dioxide to bicarbonate follows two step mechanism.[3] In the first step the Zn^{2+}-bound hydroxide attacks the CO_2 with consequent formation of HCO_3^-, which is then displaced from the active site by a water molecule that binds to the Zinc ion, inactivating the enzyme. The second step, which is rate limiting, regenerates the catalytically active Zn^{2+}-bound hydroxide ion through a proton transfer reaction from the Zn^{2+}-bound water molecule to an active site residue, generally the proton shuttle His64 to an exogenous proton acceptor (**Figure 3B**).[9]

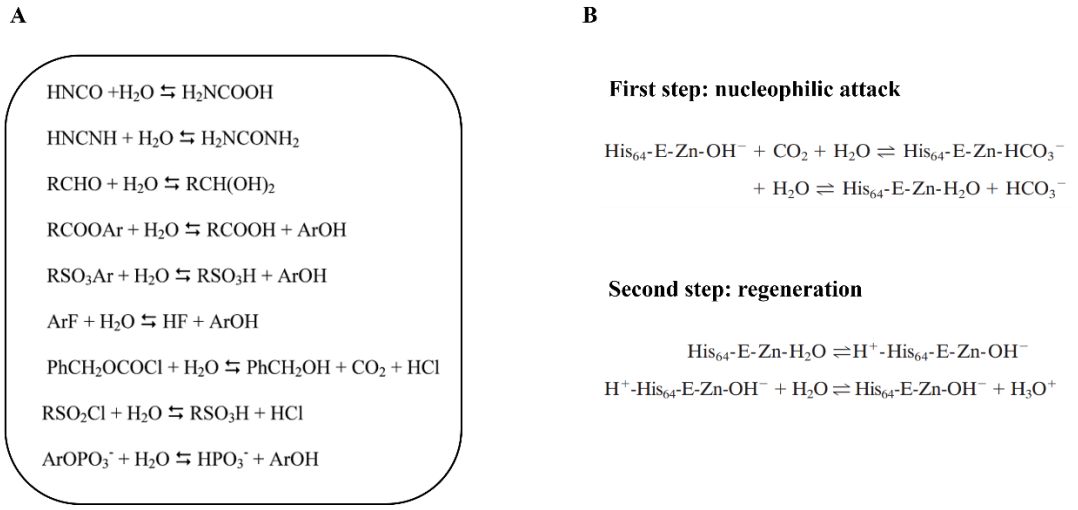


Figure 32. A) Reaction catalyzed by α-CAs. **B)** Schematic representation of the reversible reaction of hydration of carbon dioxide.

1.1.2 Physiological functions of hCA isozymes[10]

In humans, the *h*CA isoforms are involved in several physiological processes, some of which are not yet fully elucidated and remain under investigation. These enzymes play a central role in both transport and metabolic processes at the cellular level (**Table 1**). For example, CAI is expressed in the erythrocytes, and it is the most abundant non-hemoglobin protein in red blood cells as well as GI tract. CAII is the second most abundant isozyme and is present in nearly all cells. CAI, II, IV and XII functions range from gas exchange in erythrocytes, lungs and renal tubes, ion transport, reabsorption of bicarbonate and contribution to acid-base homeostasis, pH balance and metabolic acidosis. The CAV is present in the mitochondrial matrix and has a role in biosynthetic reactions and detoxification; the CAVA plays an important role in gluconeogenesis and ureagenesis showing intense signals in liver, pancreatic islets and beta cells, also distinguished in heart, lung, kidney, spleen, and intestine, while the other form CAVB shows distribution in various parts including pancreas, kidney, salivary glands, and spinal cord but not present in liver. CAVI is associated with secretions from glandular tissues, so this distinctive secretory isozyme is specifically expressed in the salivary glands of mammals, and other secretory glands like nasal and lacrimal. Its common roles are pH regulation in saliva with antireflux defense and protective effect in stomach. CAIX is present in GI tract and male genital ducts contributing to the acidification of testicular

fluid. CA related proteins- CAVIII, CAX, and CAXI show a broader expression profile in diverse tissues which suggest their importance in various unknown physiological roles and are noticed dominantly in central nervous system, brain and lungs.

Table 1. Organ/Tissue distribution, subcellular localization, CO_2 hydrase activity of the 15 Human α-CA isozymes. Source: [5]

	organ/tissue distribution	subcellular localization	catalytic activity (CO_2 hydration)
CA I	erythrocytes, gastrointestinal tract, eye	cytosol	low
CA II	erythrocytes, eye, gastrointestinal tract, bone osteoclasts, kidney, lung, testis, brain	cytosol	high
CA III	skeletal muscle, adipocytes	cytosol	very low
CA IV	kidney, lung, pancreas, brain capillaries, colon, heart muscle, eye	membrane-bound	medium
CA VA	liver	mitochondria	low
CA VB	heart and skeletal muscle, pancreas, kidney, spinal cord, gastrointestinal tract	mitochondria	high
CA VI	salivary and mammary glands	secreted into saliva and milk	low
CA VII	central nervous system	cytosol	high
CA VIII	central nervous system	cytosol	acatalytic
CA IX	tumours, gastrointestinal mucosa	transmembrane	high
CA X	central nervous system	cytosol	acatalytic
CA XI	central nervous system	cytosol	acatalytic
CA XII	kidney, intestine, reproductive epithelia, eye, tumors	transmembrane	low
CA XIII	kidney, brain, lung, gut, reproductive tract	cytosol	low
CA XIV	kidney, brain, liver, eye	transmembrane	low

[a]ND = not determined.

1.1.3 Pathological functions of the hCA isozymes

Several studies demonstrated the critical role of *h*CAs in variuos physiological processes and have shown that abnormal levels or activities of these enzymes have been often associated with different human diseases.[3,5]

CA activators may have pharmacological applications in pathologies in which learning and memory are impaired, such as Alzheimer's disease or aging.[10] On the other hand, CA inhibitors (CAIs) have been originally used as diuretics, antiglaucoma agents, antiepileptics, management of altitude sickness, antiobesity, antitumor drugs/diagnostic.[11]

Therefore, CA enzymes appeared to be important and attractive therapeutic targets, and their inhibitors as well as activators are currently used as drugs. For example CAI may play a role as an indicator to differentiate autoimmune hemolytic anemia from other types of anaemia,[12] the CAII disfunction is correlated with glaucoma, osteoporosis and edema[4,13] and CAIII deficiency is reported in myasthenia gravis and rheumatoid

arthritis.[14] Interestingly, CAIX is linked directly to tumors of ovary, endometrium, uterine cervix, and with CAXII, are markers for hypoxic tumors of breast, pancreatic cancer and other types.[15–17]

1.2 CA inhibitors and mechanisms of action

Over the past twenty years, numerous studies have explored the role of carbonic anhydrase in pathological issues and the mechanism of inhibition, leading to the identification of new classes of CA inhibitors (CAIs). Five different CA inhibition mechanisms are known, which are listed below[1]:

(i) Zinc binders
(ii) CAIs anchoring to the zinc-coordinated water/hydroxide ion
(iii) Inhibitors that occlude the active site cavity
(iv) Inhibitors which bind out of the active site
(v) Inhibitors with not known mechanism

Zinc binders[4]: sulfonamides and their derivatives (sulfamate and sulfamides) are the most important and oldest developed CAIs with at least 20 compounds in clinical use; they bind in deprotonated form, as anions, to the Zn (II) ion from the enzyme active site directly interacting with the metal ion (**Figure 4A**). This type of compounds possess three main portions: *a)* the pharmacophoric motif, also called zinc binding function (ZBG), which interacts with the metal ion and the residues of Thr199 and Glu106 in the neighborhood, *b)* the organic scaffold (aromatic or heterocyclic moiety) often absent in the new generation of derivatives, ensures the appropriate positioning of the ZBF in the active site and stabilizes the enzyme–inhibitor complex interacting with the hydrophobic/hydrophilic residues of the active site, and *c)* the tail which was absent in the first and second generation of sulfonamide CAIs, but which is extremely important for the last generation of derivatives able to interact with amino acid residues from the middle and edge of the active site cavity.

CAIs anchoring to the zinc-coordinated water/hydroxide ion[1]: phenol and spermine were the first compounds identified with this mechanism. The main difference between this class and the normal zinc binders is that these inhibitors are not in direct contact with the metal ion but establish hydrogen bonds between the H atom of the inhibitor and the

donor OH from the zinc hydroxide (**Figure 4B**); additionally, OH or other chemical functionalities make other hydrogen contacts with residues as Thr199, Thr200, Pro201 and Gln92.

CA Inhibitors that occlude the active site cavity[1]: these inhibitors bind away from the metal ion and appeared to interact with the protein at the entrance of the active site. They have a sticky group (SG) attached to an aromatic, heterocyclic or aliphatic scaffold and a tail which can extend in the external part of the cavity (**Figure 4C**). This inhibition mechanism has been evidenced for the first time for coumarins[18,19] but better in substituted coumarins, quinolines, lactones and thio-lactones. The most notable aspect of this inhibition mechanism is the fact that the inhibitors bind in an active site region which is the most variable between the various isoforms. This has important consequences for the drug design of CAIs, since compounds binding in that region should in principle interact differently with the various CAs and thus show isoform-selective inhibitory profiles.

CA inhibitors which bind out of the active site: this mechanism is relatively new and was studied after obtaining the co-crystal between CAII and the 2-(benzyl sulfonyl)-benzoic acid.[20] In this study the authors found that compound blocks the His64 which is important for the rate determining step of the entire catalytic cycle, impeding the proton transfer from the zinc- coordinated water molecule to the environment (**Figure 4D**).

Inhibitors with not known mechanism: this miscellanea of compounds have some molecular similarities with the other classes of inhibitors, but the mechanism of action is not well understood, probably being a consequence of the block of entrance of the active site or some allosteric interference in other portions of the enzymes.

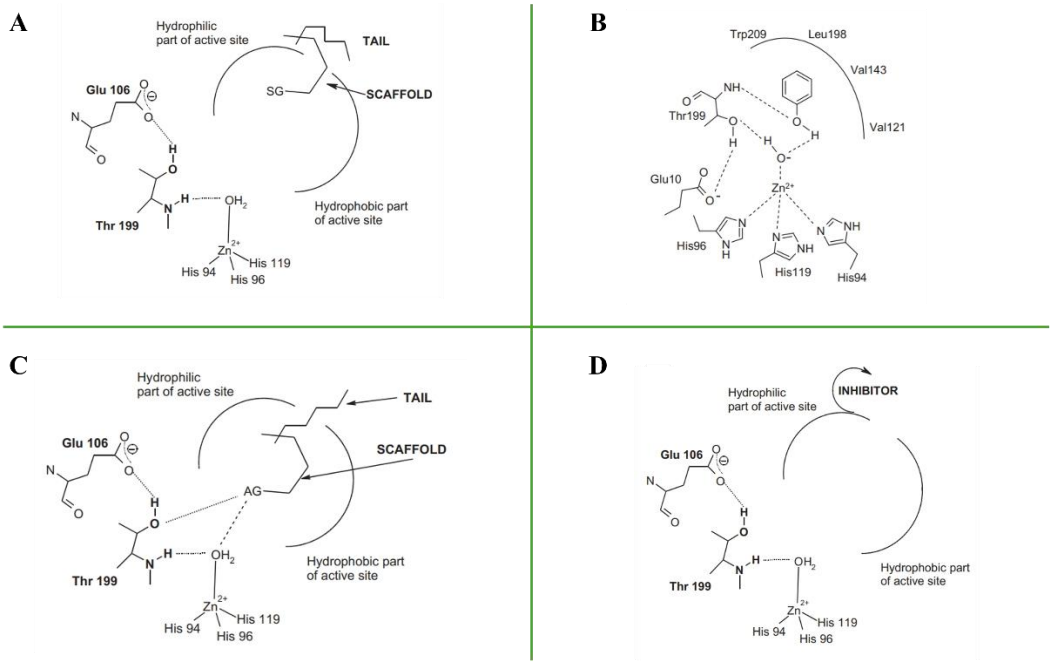


Figure 33. Representation of the CAIs mechanisms of action. A) Zinc binders, B) Zinc-coordinating water/hydroxide ion, C) Active site occluding, D) Outside binders. Source: image modified from [1]

Chapter IIIA- Development of a novel class of CAIs containing a trifluoro dihydroxy propanone pharmacophore

Chapter IIIA- Development of a novel class of CAIs containing a trifluoro dihydroxy propanone pharmacophore

1 State of art

In this context, significant efforts in CA drug design are directed in toward developing novel inhibitors that not only exhibit inhibitory activity and selectivity for specific isoforms, but also possess lower toxic compared to classical CAIs. One strategy involves optimizing the pharmacological properties of sulfonamide-CAIs by replacing the ZBG with alternative chemical structures featuring molecular diversities and original pharmacophores.

In a previous study by Sechi's group in collaboration with Prof. Supuran of the University of Florence, and Dr. Andrea Brancale of the Cardiff University, a combined ligand- and pharmacophore-based virtual screening approaches was employed to identify novel CAIs bearing an original pharmacophore.[21] The strategy used can be summarized in three key steps:

a) construction of an optimized pharmacophore model: a thorough analysis of several high-resolution X-ray crystallographic structures of CAII in complex with different sulfonamides led to the development of a four-point model incorporating a ZBG metal ligand, two H-bond acceptor functions and an aromatic hydrophobic region);
b) virtual screening of free database of more than 900000 of commercially available compounds was screened through multiple filtering, settings and preliminary docking procedures;
c) structural analysis of the identified hits with the CAII enzyme mode: the selected hits were evaluated based on their binding disposition within the CAII enzyme model.

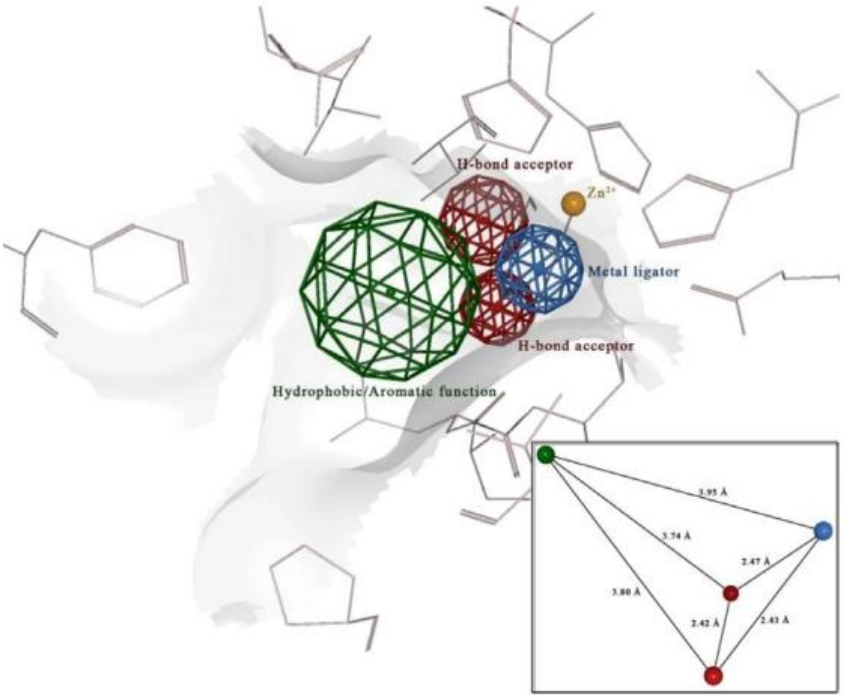


Figure 34. **Pharmacophore model represented into the active site. Schematic view and distance geometries of the pharmacophore functions (rectangular insert). Source:** [21]

Among the compounds identified through virtual screening, one structure featuring a trifluoro-dihydroxy-propanone moiety (**TDP, Figure 6**, compound **TDP1**) exhibited anti-CA II activity in the low micromolar concentration range (Ki CA II = 9 µM, **Table 2**). Notably, compound **TDP 1** (commercially available) was approximately 45-fold more active in inhibiting the human CA II isoform compared to CA I (K_i *h*CAII = 9 µM vs K_i *h*CA I = 410 µM), demonstrating a selectivity ratio comparable to that of reference compound acetazolamide (K_i ratios = 45 and 75, for **TDP1** and AZA, respectively). It has also been hypothesized that **TDP1** could interact with the Zn^{2+} ion through its dihydroxy system. This putative binding mode has been supported by preliminary docking studies, which suggested an accommodation within the CA active site similar to that of sulfonamide-containing compounds. Additionally, the electron-withdrawing trifluoromethyl group on the pharmacophore fragment may enhance the acidity of germinal diol, thereby improving its metal-chelating properties.

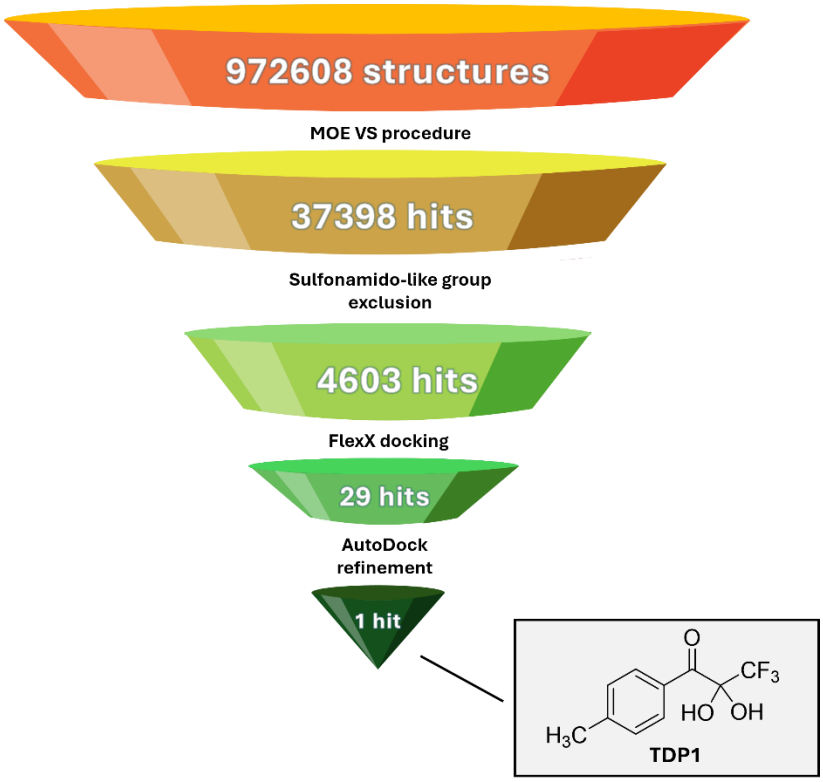


Figure 35. Schematization of the Virtual Screening workflow. Source: image modified from [21]

This compound was subsequently used as a lead structure for a further optimization n the PhD study of Dr. Roberta Cadoni, conducted under the supervision of Prof. Mario Sechi titled "*Synthesis of amides from aldehydes and amines via C-H bond activation and discovery and development of novel and selective carbonic anhydrase inhibitors*".

Similar to sulfonamide-based CA inhibitors, compound **TDP1** can be structurally represented by three main components: a) the ZBG (the trifluoro-dihydroxy-propanone moiety), b) an aromatic scaffold, and c) a tail consisting of a methyl group positioned in *para* of the core structure (**Figure 7**).

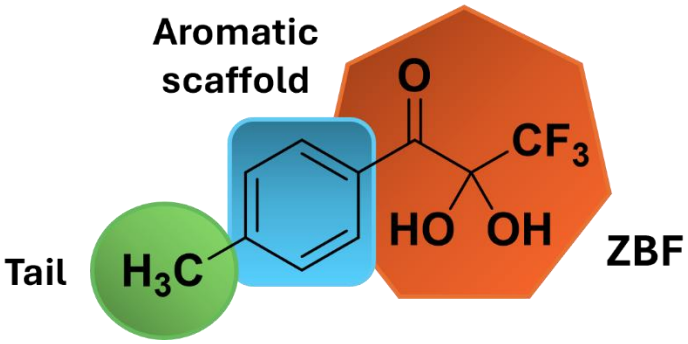


Figure 36. Schematic structure of hit compound **TDP1**

To enhance the inhibition activity of the *hit* compound **TDP1** against *h*CA IX and XII isoforms, the "tail optimization approach" was employed: *a)* increasing or decreasing the length of the aliphatic chain, *b)* modifying the steric bulk of alkyl substituents, *c)* inserting electron donating group on aromatic scaffold, *d)* deleting the tail. The *hit* compound **TDP1** and its derivatives (**Figure 8**) were tested for their ability to inhibit the catalytic activities of tumor associated *h*CA IX and XII isoforms (in addition to the cytosolic CA isoforms I and II) due to their overexpression in many cancer typologies, particularly in hypoxic tumors that are normally non-responsive to classical chemo- and radiotherapy.[16,17,22]

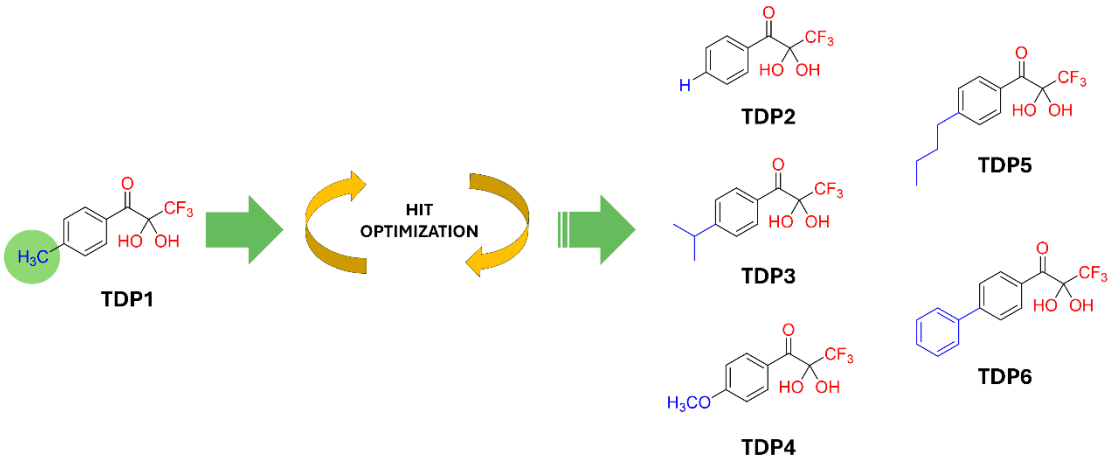


Figure 37. The new series of TDP compounds after hit optimization of TDP1.

The *hit* compound **TDP1** demonstrated an interesting inhibitory activity in submicromolar/high nanomolar range against *h*CA IX (Ki 0.84 μM), also showing

overlapping activity toward CA II and CA XII (K_is ~9 μM for both isozymes). As summarized in **Table 2**, with few exceptions (**TDP2** and **TDP6)**, all compounds selectively inhibited *h*CA IX, with K_i values ranging from 0.78 to 0.83 μM, regardless of the nature of substituent in the aromatic scaffold. Tail derivatization with various aliphatic moieties improved activity, whereas complete removal of the substituents (in **TDP2**) or insertion of bulkier group (in **TDP6**) appeared to be detrimental.

Table 2. Inhibition of hCA isoforms I, II, IX and XII with compounds of the **TDPs** by a stopped-flow CO_2 hydrase assay. Aetazolamide (AAZ; 5-acetamido-1,3,4-thiadiazole-2-sulfonamide) was used as standard,.

Compound		**K_I (μM)***			
		***h*CA I**	***h*CA II**	***h*CA IX**	***h*CA XII**
TDP1 (hit)	4-Me-C_6H_4	410	9.0	0.84	9.05
TDP2	Ph	54.3	63.5	4.51	6.86
TDP3	4-iPr-C_6H_4	86.0	>100	0.80	5.87
TDP4	4-MeO-C_6H_4	520	3.2	0.83	24.3
TDP5	4-nBu-C_6H_4	17.3	4.7	0.78	19.7
TDP6	4-Ph-C_6H_4	65.7	2.5	5.60	7.21
AAZ	-	0.25	0.012	0.025	0.006

*** Errors in the range of ± 5-10 % of the reported value from 3 different assays.**

2 Molecular modelling

A preliminary molecular modeling study was conducted in order to simulate the binding mode of compounds belonging to this new class of inhibitors within the active site of *h*CA IX (**Figure 9**). Interactions between *h*CA IX and the *hit* compound **TDP1**, as well as all members of series **TDP** (**TDP 2-6)** were predicted through docking experiments using an *h*CA IX-mimic protein (PDB code: 3IAI). The docking results showed that all derivatives are positioned within the catalytic pocket of *h*CA IX, where the first oxygen of the diol group forms an H-bond with Thr199, while the second oxygen interacts with the zinc ion. These results corroborate the hypothesis that the trifluoromethyl-dihydroxy propanone group could serve be a suitable bioisostere of the sulfonamide group.

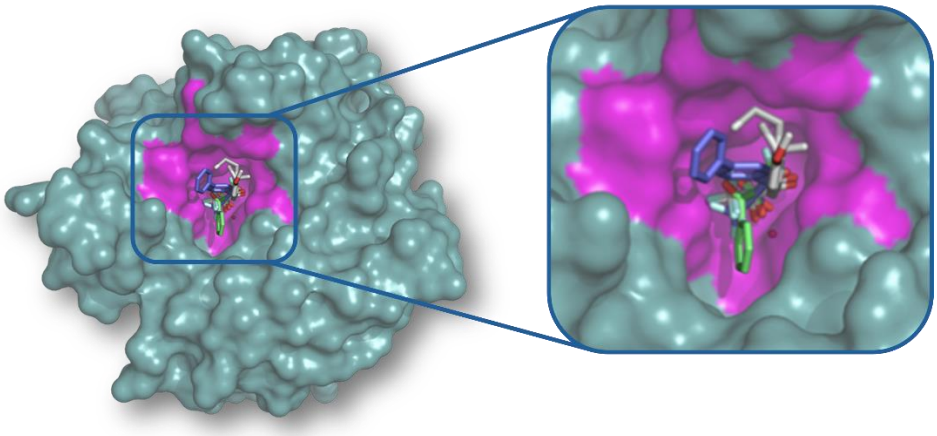


Figure 9. **Representation of the docking of the TDP compounds with hCAIX (PDB: 3IAI). On the left, zoom-in of the active site of hCAIX showing the superposition of docked TDP compounds.**

3 Rational of the PhD work

In the context of CA inhibitors and the role of certain isoforms in the cancer development, recent studies established new connections between CAIX and some cancer types as PDAC[23–25] and its potential involvement in the ferroptosis.[26–28] In particular, previous studies have identified a link between hypoxia induced CAIX activity and the suppression of ferroptosis mediated cell death in breast cancer cells and that the inhibition of CAIX renders tumor cells more vulnerable to ferroptosis inducers.[26] More specifically, components involved in iron-sulfur biogenesis, such as cysteine desulfurase (NFS1) and the cystine-glutamate antiporter xCT, have been identified as key players in the susceptibility of CA IX inhibitors in the context of ferroptosis. A mechanistic explanation points to the increased intracellular acidosis generated by the inhibition of CAIX, which is overexpressed in some hypoxic cancer cells. In this context, maintaining an appropriate pH is crucial not only for the enzymatic activity of the cancer cells but also for the detachment of primary tumor cells, a key step in metastasis formation.[29–31] The increased acidity resulted from the combination of CAIX inhibition and reduced of iron-sulfur clustering leads to increased intracellular ROS, lipid peroxidation and subsequent activation of ferroptosis mechanisms (**Figure 10**).

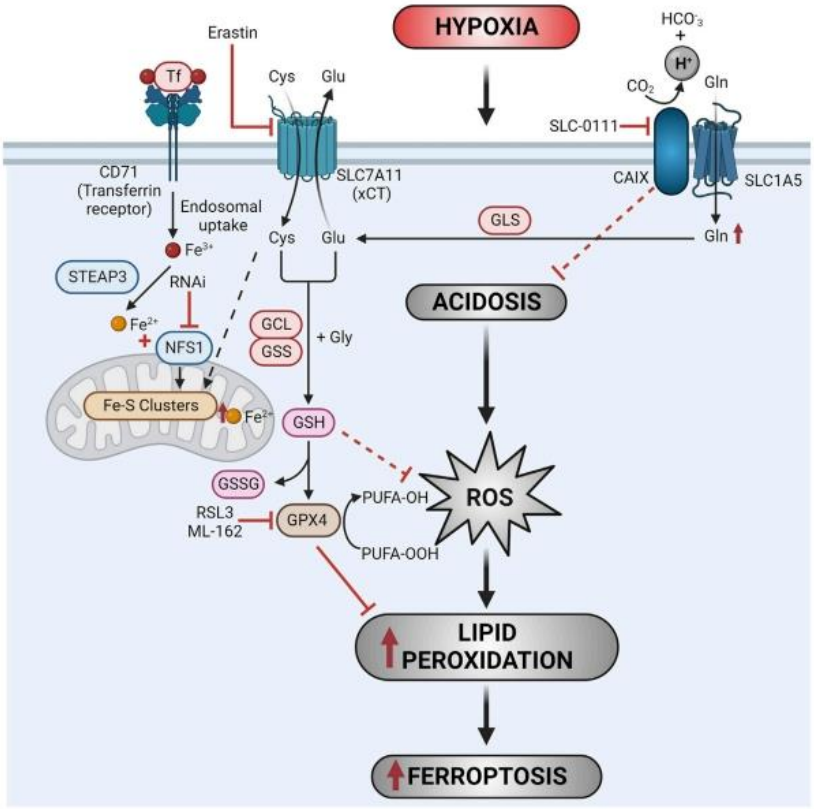


Figure 10. **Illustration of the series of events that lead to ferroptosis after pharmacological inhibition of CAIX and NFS1. Source:** [27]

Considering the possible interaction between PDAC and the overexpression of CAIX isoform, along with the promising selectivity demonstrated by the new class of derivatives carrying the trifluoro-hydroxy-propanone moiety in the inhibition for CAIX and XII isozymes, we planned to:

i) re-prepare the series of TDP derivatives to obtain additional experimental data;

ii) study the interaction of a representative compound with hCAII through X-ray crystallography.

iii) gather more information about the type of inhibition exhibited by the TDP series;

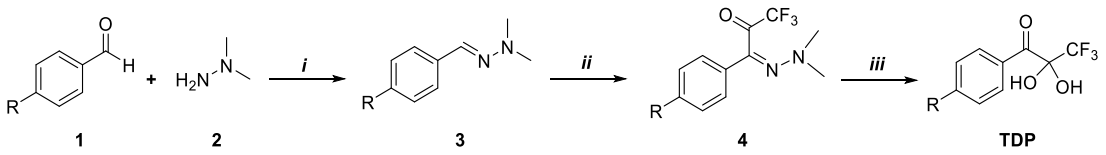
iv) evaluate the TDP for their antiproliferative activity on variuous human cancer cell lines including pancreatic tumor cells, both in normal and in simulated hypoxic conditions.

3.1 Repreparation of the novel class of trifluoro-hydroxy-propanone CA inhibitors

3.1.1 Chemistry

The synthesis of **TDP1** and its derivatives followed a previously optimized multistep procedure [32]. The geminal diols of the trifluoro-hydroxy-propanone pharmacophore arise from the electron-withdrawing group (i.e. CF_3), which stabilizes the carbonyl in the hydrated form.

Kamitori et all[33] first reported a method for obtaining **TDP**-based compounds in 1988 (**Figure 11, Experimental section**). This approach is based on the aforementioned observations. Initially, *p*-substituted aldehyde **1** react with *N-N'*-dimethyl hydrazine **2** in dichloromethane at room temperature to yield *p*-substituted-aldehyde-*N,N'*-dimethyl hydrazone **3**. Hydrazones, like enamines, act as 1,3-dipolar compounds with azomethine carbon serving as center of nucleophilic attack.[34] Subsequent electrophilic trifluoro-acylation of hydrazones, using 2,6-lutidine as base, generated the intermediate **4**. Hydrolysis with H_2SO_4 then yields TDP in good yields. (**Scheme 1**). The compound TDP1 and its derivatives 5-7 were fully characterized by multinuclear NMR spectroscopy. Data were consistent with the proposed structures.[35,36] Furthermore, mass spectrometry analysis confirmed the molecular formula of the compounds.



Scheme 1. Synthetic scheme for the preparation of the TDP derivatives. Reagents and conditions: *i*) DCM, r.t, 6 h; *ii*) TFAA, 2,6-lutidine, DCM, r.t, 6 h; *iii*) H_2SO_4 c., 2-24 h.

3.2 X-Ray crystallography

To obtain more information about the type of interaction of the new class of derivatives, the X-ray crystal structure of compound **TDP4** in complex with human carbonic anhydrase II (hCAII), used as model, was solved to a resolution of 1.9 Å (chemical structure **Figure 8**). From the obtained data **TDP4** mimics a typical zinc-binding compound (such as classic sulfonamide-based inhibitors). It binds directly to the

active site zinc through its diol moiety, causing displacement of the zinc-bound solvent (**Figure 12**). The inhibitor is also seen to partially displace water molecules of the ordered water network that aids in catalysis. The carbonyl oxygen adjacent of the diol group of **TDP4** is predicted to form a hydrogen bond with the hydroxyl of Thr 199 (bond distance = 2.7 Å). In addition, the same carbonyl of **TDP4** is also predicted to form hydrogen bonds with the backbone NH of Thr199 and Thr 200 (bond distance = 2.6 Å and 2.8 Å, respectively). The CF_3 group of **TDP4** is observed in a small hydrophobic pocket, making interactions with residues Val121, Leu141, Val143, and Val207. The methoxy group of the compound is predicted to be further stabilized by Van der Waals interactions with residues Pro201 and Gln92 (**Figure 12**). A surface view of the complex highlights that the **TDP4** compound interacts primarily with the hydrophobic region of the active site via its CF_3 group, with the carbonyl facing the hydrophilic region (**Figure 11**).

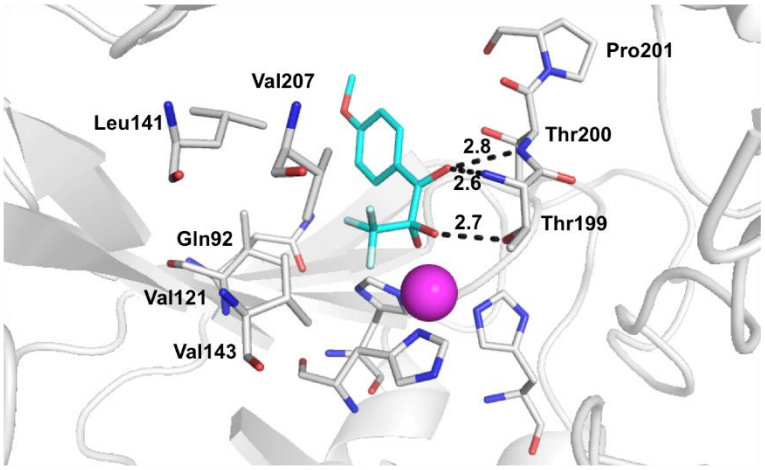


Figure 11. Frame representation of the compound TDP4 co-crystallized with hCAII.

3.3 Biological assays

The cytotoxicity of the most potent derivatives from the new TDP series (**TBP 1,4,5**) was tested against AsPC-1 adenocarcinoma cell line in normal conditions after 48 h, as well as in presence of $CoCl_2$ to induce hypoxia. Preliminary data indicated that all tested prototypes exhibited some cytotoxicity against this cell line.

More specifically, the prototype TBP4 demonstrated a significant antiproliferative effect at concentration of 10, 30, and 100 μM of compound treatment. It exhibited a dose-dependent inhibition of cell growth, achieving approximately ~25% antiproliferative effect at the highest concentration (**Figure 12A**). Better results were found when the compounds were tested on AsPC-1 cells in hypoxia-simulated conditions (**Figure 12B**). Hypoxia-simulated conditions significantly increased the susceptibility of the cells to the TDP treatment, with a ~25% reduction of cell viability for all TDP1 and TDP5 at a concentration of 30 μM, and ~40% cell growth inhibition for all TDPs at 100 μM.

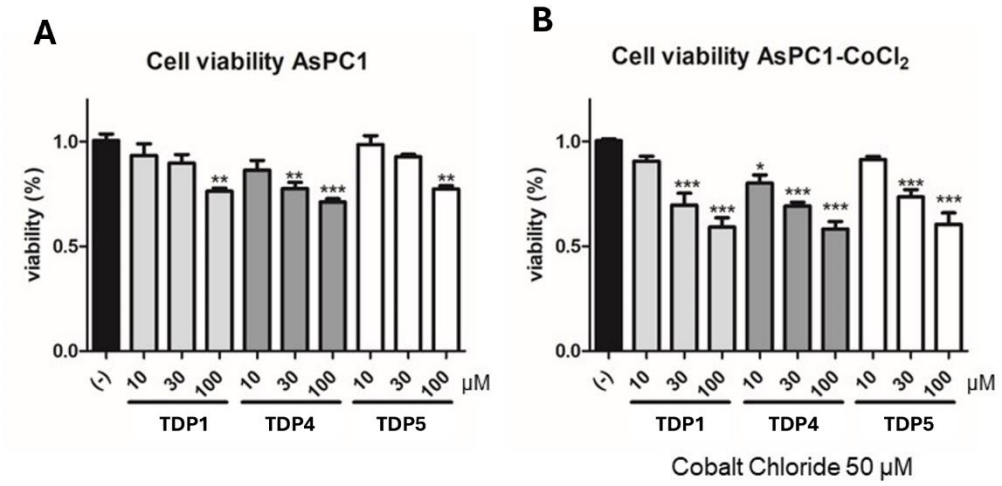


Figure 12. Cytotoxicity of TDP 1, 4 and 5 against the AsPC-1 cell line after 48 h treatment, in normal (A) and hypoxic simulated conditions (B).

3.5 Holotomography

Utilizing advanced holotomographic imaging techniques, a non-invasive method to investigate cellular and subcellular architecture, the ultrastructural modifications in HPAF-II and PL-45 pancreatic cancer cell lines treated with the model compounds TDP1 and TDP4, were characterized.

In HPAF-II cells, treatment with TDP1 and TDP4 elicited a notable rearrangement of intracellular components, primarily evidenced by the aggregation of intracellular vesicles adjacent to the plasma membrane, as indicated by blue arrows in the imaging data (**Figure 13**). A temporal analysis revealed a progressive increase in the vesicular content,

suggesting either an alteration in cellular trafficking mechanisms or a response to mitigate drug-induced stress.

Conversely, treatment of PL-45 cells with TDP1 and TDP4 exhibited a distinct response, characterized by the release of macrovesicles (red arrows, **Figure 13)** and the accumulation of intracellular vesicles (identified by green arrows, **Figure 13**), likely reflecting a variation in the cellular coping mechanisms to drug exposure. Additionally, significative alterations in nuclear morphology were observed, including nuclear shrinkage and the formation of perinuclear bubble-like spaces (yellow arrows, **Figure 13**). which may signal the initiation of apoptotic pathways.

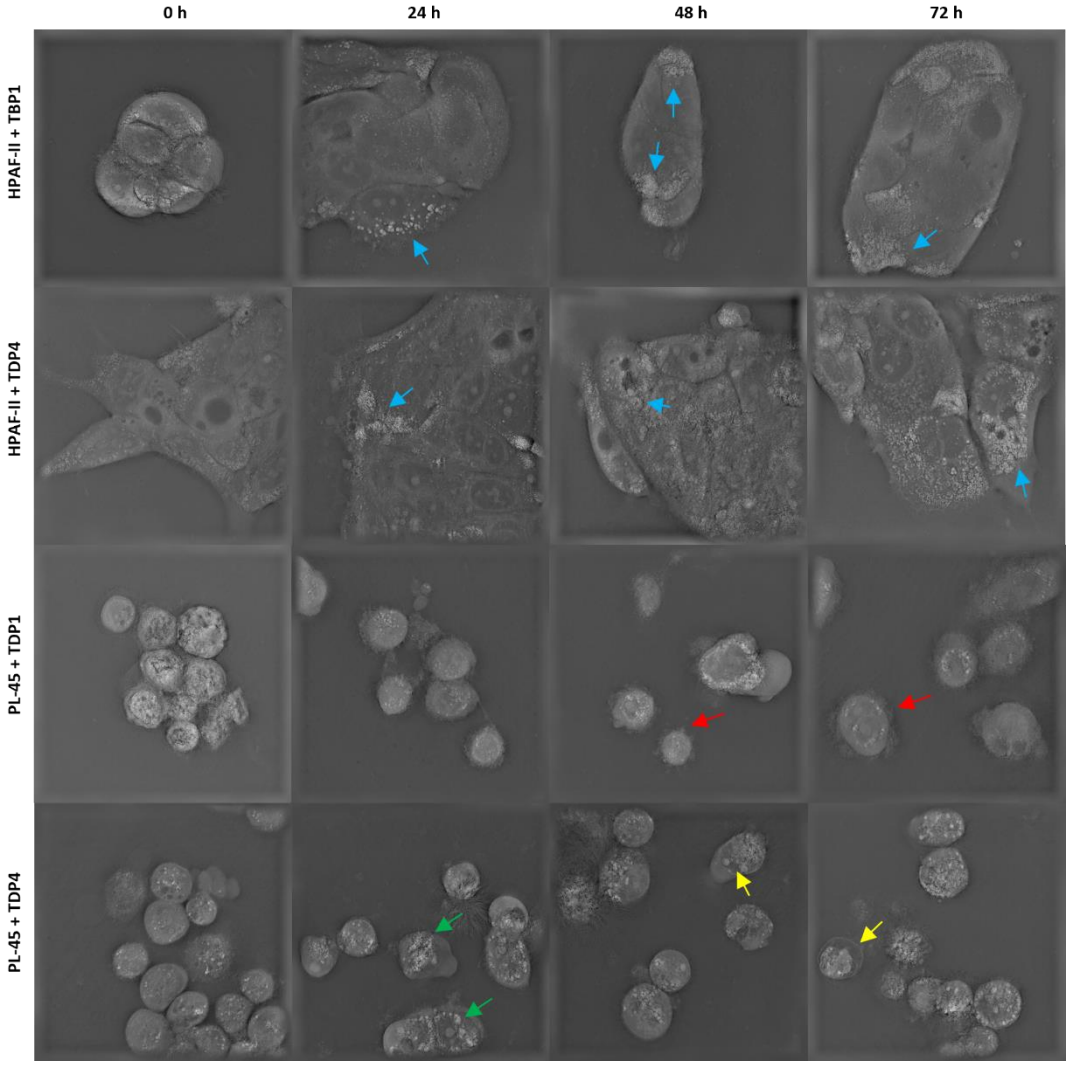


Figure 13. Holotomography images of pancreatic cancer cell lines (PL45 and HPAF-II) after exposure to TDP compounds (TDP1 and TDP4) at different times.

3.6 Fluorescence studies

To investigate the molecular effects of TDP1 and TDP4 on pancreatic cancer cells, advanced fluorescent microscopy analyses were conducted to examine the intracellular dynamics of Frataxin, a mitochondrial protein implicated in cellular iron homeostasis and antioxidant defense.

The fluorescent images revealed a notable accumulation of Frataxin in cells treated with TDP1 (**Figure 14A**), suggesting a significant interference with the mitochondrial function or iron metabolism. This observation may indicate a compensatory cellular response to oxidative stress and disruption in iron homeostasis induced by TDP1, potentially contributing to its antiproliferative effects on pancreatic cancer cells. In contrast, treatment with TDP4 did not appear to markedly affect Frataxin levels within the same cellular context (**Figure 14B**), implying a potential divergence in their mechanisms of action. Further studies are in progress to elucidate this behavior in more detail.

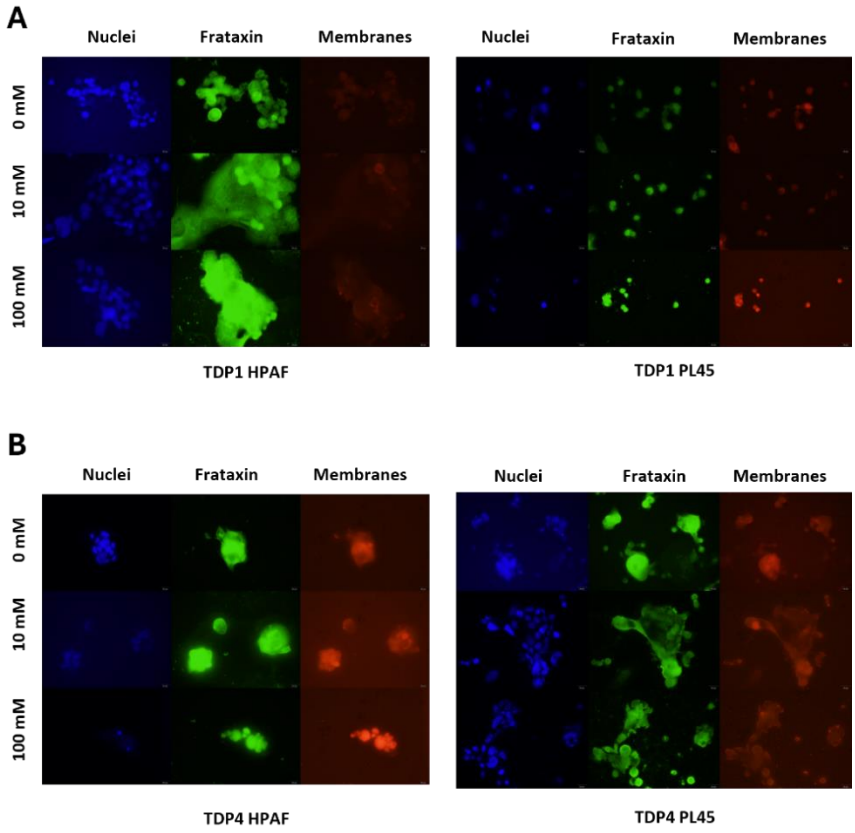


Figure 14. Image of fluorescence microscopy experiments on pancreatic cancer cell lines (PL45 and HPAF) treated with TBP compounds (TBP1 and TBP4) to examine Frataxin modification.

4 Conclusions

Results indicate that this novel TDP chemotype effectively inhibits human CAs, with selectivity towards hCAIX and hCAXII over other cytosolic isoforms. The most potent TDP compounds exhibited significant antiproliferative activity against representative hypoxic pancreatic tumor cell lines. Moreover, holotomographic imaging and fluorescence experiments provided insights into the cellular and subcellular architecture and intracellular dynamics, enabling a comprehensive analysis of drug-induced cytological effects. Additionally, X-ray crystallography data shed light about the CA inhibition mechanism, thus indicating that these compounds would behave similarly to other classical inhibitors.

These data would provide structural determinants for the development of a new class of novel and selective anticancer agents.

5. Experimental section

5.1 Chemistry

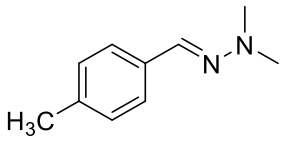
5.1.1 General methods

Unless otherwise noted, all solvents including anhydrous solvents and chemicals, were purchased from Aldrich Co. and/or Alfa Aesar, and used without further purification. All reactions involving air- or moisture-sensitive compounds were performed under a nitrogen atmosphere using oven-dried glassware and syringes to transfer solutions. Silica gel thin-layer chromatography (TLC) sheets from Merck silica gel F-254 plates (silica gel precoated aluminum sheets with fluorescent indicator at 254 nm) were used for TLC. Melting points (M.p.) were determined using an Electrothermal melting point or a Köfler apparatus and are uncorrected. Proton nuclear magnetic resonance (^{1}H NMR) spectra were recorded in $CDCl_3$ or DMSO-d_6 on 400 MHz Bruker Avance III nanobay. Chemical shifts (δ) are reported in parts per million (ppm) downfield from tetramethylsilane (TMS), used as an internal standard. Splitting patterns are designated as follows: broad singlet (bs), singlet (s), doublet (d), triplet (t), quartet (q), septet (sep), and multiplet (m). Mass spectra were obtained on a triple-quadrupole QqQ Varian 310-MS mass spectrometer, or a MALDI micro-MX (Waters, Micromass) equipped with a reflectron analyzer. Elemental analyses were performed on a Perkin-Elmer Elemental Analyzer 2400-CHN and were within ±0.4% of the theoretical values.

5.1.2 General procedure for the preparation of N,N-dimethyl arene aldehyde hydrazones (3a-f)[32]

To a well-stirred amount of the appropriate arene aldehyde **1a-f** (3.8 mmol, 1 equiv.), *N*,*N*-dimethylhydrazine (**2**, 4.2 mmol, 1.1. eq) was added dropwise. For liquid arene aldehydes the reaction was carried out without solvent, whilst CH_2Cl_2 (4 mL) was used in case of solid arene aldehydes. After being stirred for about 6 hours, CH_2Cl_2 (5 mL) was added to the mixture, then it was dried over Na_2SO_4, and the solvent was removed under reduced pressure to afford the product as a pale-yellow oil or white solid.

(*E*)-1,1-Dimethyl-2-(-methylbenzylidene)hydrazine (3a)



Pale yellow oil.

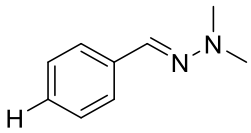
Yield: 98 %.

Rf: 0.66 (ethyl acetate / petroleum ether = 3:7).

^{1}H NMR 400 MHz ($CDCl_3$): δ 7.46 (d, *J* = 7.8 Hz, 2H, ArH), 7.25 (s. 1H, CH), 7.1 (d, *J* = 7.9 Hz, 2H, ArH), 2.94 (s, 6H, NCH_3), 2.33 (s, 3H, CH_3).

LC/MS: m/z 163.1 $[M+H]^+$.

(*E*)-2-Benzylidene-1,1-dimethylhydrazine (3b)



Pale yellow oil.

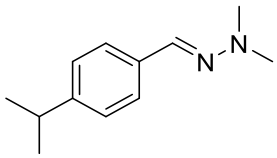
Yield: 98 %.

Rf: 0.74 (ethyl acetate / petroleum ether = 2:8).

^{1}H NMR 400 MHz (CDCl3): δ 7.56 (d, J = 7.6 Hz, 2H, ArH), 7.30 (t, J = 7.5 Hz, 2H, ArH), 7.23 (s, 1H, CH), 7.20 (m, 1H, ArH), 2.95 (s, 6H, NCH3).

LC/MS: m/z 149.1 $[M+H]^+$.

(*E*)-2-(4-Isopropylbenzylidene)-1,1-dimethylhydrazine (3c)



Pale yellow oil.

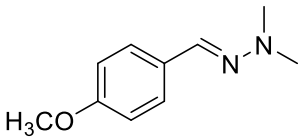
Yield: 96 %.

Rf: 0.73 (ethyl acetate / petroleum ether = 3:7).

^{1}H NMR 400 MHz (CDCl3): δ 7.49 (d, J =8.1 Hz, 2H, ArH), 7.26 (s, 1H, CH), 7.18 (d, J = 7.9 Hz, 2H, ArH), 2.94 (s, 6H, NCH3), 2.91-2.85 (m, 1H, CH), 1.24 (d, J = 6.9 Hz, 6H, CH3).

LC/MS: m/z 190.1 [M]+, 191.9 $[M+H]^{+}$.

(*E*)-2-(4-Methoxybenzylidene)-1,1-dimethylhydrazine2 (3d)



Pale yellow oil.

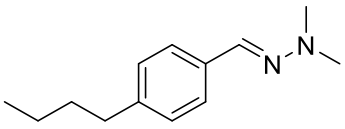
Yield: 83 %.

Rf: 0.59 (ethyl acetate / petroleum ether = 2:8).

^{1}H NMR 400 MHz (CDCl3): δ 7.51 (d, J = 9.0 Hz, 2H, ArH), 7.26 (s, 1H, CH), 6.87 (d, J = 8.8 Hz, 2H, ArH), 3.81 (s, 3H, CH3), 2.92 (s, 6H, NCH3).

LC/MS: m/z 179.1 $[M+H]^+$.

(*E*)-2-(4-Butylbenzylidene)-1,1-dimethylhydrazine (3e)



Pale yellow oil.

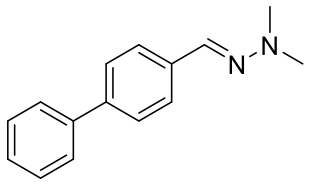
Yield: 97 %.

Rf: 0.71 (ethyl acetate / petroleum ether = 0.2:9.8).

^{1}H NMR 400 MHz (CDCl3): δ 7.47 (d, J = 8.1 Hz, 2H, ArH), 7.26 (s, 1H, CH), 7.13 (d, J = 7.9 Hz, 2H, ArH), 2.94 (s, 6H, NCH3), 2.59 (t, J =7.7 Hz, 2H, CH2), 1.59 (m, 2H, CH2), 1.35 (m, 2H, CH2), 0.92 (t, J = 7.2 Hz, 3H, CH3).

LC/MS: m/z 204.2 $[M]^{+}$, 226.8 $[M+Na]^{+}$.

(*E*)-2-(Biphenyl-4-ylmethylene)-1,1-dimethylhydrazine (3f)



White solid.

Yield: 93 %.

Rf: 0.77 (ethyl acetate / petroleum ether = 2:8).

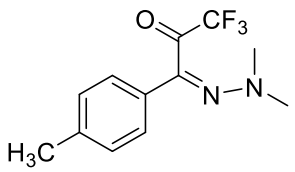
^{1}H NMR 400 MHz (CDCl3): δ 7.60 (overlapping, 6H, ArH), 7.43 (t, J = 7.4 Hz, 2H, ArH), 7.33 (t, J = 7.6 Hz, 1H, ArH), 7.28 (s, 1H, CH), 2.99 (s, 6H, NCH3).

LC/MS: m/z 225.0 $[M+H]^+$, 247.1 $[M+Na]^+$.

5.1.3 General procedure for the trifluoroacetylation of N,N-dimethyl-arene-aldehyde hydrazones (4a-f)

To an ice-cooled mixture of *N,N*-dimethyl arene aldehyde hydrazones **3a-f** (3.3 mmol, 1 equiv.) and 2,6-lutidine (2 equiv. for **3a,b** , 3 eq. for **3c-e**, 4 eq. for **3f**) in anhydrous dichloromethane (10 mL), a solution of trifluoroacetic anhydride (TFAA, 2 eq. for **3a,b**, 6 eq. for **3f** , 10 eq. for **3d**) in CH_2Cl_2 (3 mL) was added dropwise with continuous stirring. The mixture was than warmed to 20 °C and stirred for about 6 hours. The reaction mixture was diluted with dichloromethane (5 mL), washed sequentially with HCl 0.1N, H_2O and and $Na_2CO_{3(aq)}$. The organic layer was dried over anhydrous Na_2SO_4, and the solvent was removed under reduced pressure. The crude product was purified by trituration with a mixture of petroleum ether and diethyl ether.

(*Z*)-3-(2,2-Dimethylhydrazineylidene)-1,1,1-trifluoro-3-*p*-tolylpropan-2-one (4a)



White solid.

Yield: 50 %.

Rf: 0.31 (ethyl acetate / petroleum ether = 2:8).

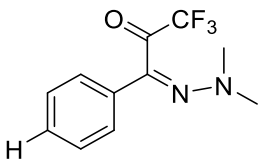
Mp: 113-115 °C.

^{1}H NMR 400 MHz ($CDCl_3$): δ 7.17 (d, *J* = 7.9 Hz, 2H, ArH), 7.10 (d, *J* = 7.9 Hz, 2H, ArH), 3.05 (s, 6 H, NCH_3), 2.37 (s, 3H, CH_3).

^{13}C NMR 400 MHz ($CDCl_3$): δ 178.0 (q, *J* = 29.9 Hz, CO), 138.5, 131.9 (s, C=N), 130.3, 129.9, 128.5, 117.8 (q, *J* = 292.2 Hz, CF_3), 47.1, 21.3.

^{19}F NMR 376 MHz ($CDCl_3$): δ -68.8 (s, 3F, CF_3).

(*Z*)-3-(2,2- Dimethylhydrazineylidene)-1,1,1-trifluoro-3-phenyl propan-2-one (4b)



Pale yellow solid.

Yield: 63 %.

Rf: 0.27 (ethyl acetate / petroleum ether = 1:9).

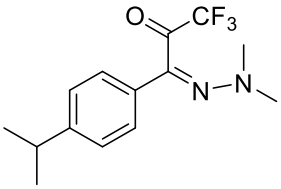
MP: 71 °C.

^{1}H NMR 400 MHz ($CDCl_3$): δ 7.36 (overlapping, 3H, ArH), 7.21 (overlapping, 2H, ArH), 3.05 (s, 6H, NCH_3).

^{13}C NMR 400 MHz ($CDCl_3$): δ 177.9 (q, *J* = 30.3 Hz, CO), 133.0 (s, C=N), 130.5, 128.6, 127.7, 125.9, 118.0 (q, *J* = 292.3 Hz, CF_3), 47.1.

^{19}F NMR 376 MHz ($CDCl_3$): δ -68.8 (s, 3F, CF_3).

(*Z*)-3-(2,2-Dimethylhydrazineylidene)-1,1,1-trifluoro-3-(4-isopropylphenyl)propan-2-one (4c)



White crystals.

Yield: 30 %.

Rf: 0.70 (ethyl acetate / petroleum ether = 2:8).

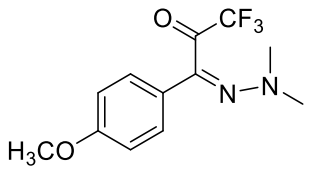
Mp: 86-88 °C.

^{1}H NMR 400 MHz ($CDCl_3$): δ 7.21 (d, *J* = 7.9 Hz, 2H, ArH), 7.12 (d, *J* = 7.9 Hz, 2H, ArH), 3.05 (s, 6 H, NCH_3), 2.95-2.88 (m, 1H, CH), 1.25 (d, *J* = 7.2 Hz, 6H, CH_3).

^{13}C NMR 400 MHz ($CDCl_3$): δ 176.2 (q, *J* = 32.1 Hz, CO), 149.9, 149.4, 140.0, 131.5 (s, C=N), 130.4, 126.5, 125.9, 122.9 (q, *J* = 286.6 Hz, CF_3), 41.2, 33.9, 23.7.

^{19}F NMR 376 MHz ($CDCl_3$): δ - 68.8 (s, 3F, CF_3).

(*Z*)-3-(2,2-Dimethylhydrazineylidene)-1,1,1-trifluoro-3-(4-methoxyphenyl)propan-2-one (4d).



Beige solid.

Yield: 35 %.

Rf: 0.30 (ethyl acetate / petroleum ether = 1.5:8.5).

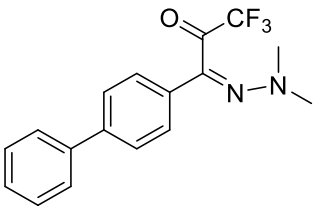
M.p: 85 °C.

^{1}H NMR 400 MHz ($CDCl_3$): δ 7.13 (d, *J* = 8.5 Hz, 2H, ArH), 6.89 (d, *J* = 8.5 Hz, 2H, ArH), 3.83 (s, 6 H, NCH_3), 3.06 (s, 3H, CH_3).

^{13}C NMR 400 MHz ($CDCl_3$): δ 190.8 (q, *J* =30.3 Hz, CO), 159.7, 131.7 (s, C=N), 127.4, 118.0 (q, *J* =292.2 Hz, CF_3), 113.8, 113.4, 52.2, 47.1.

^{19}F NMR 376 MHz ($CDCl_3$): δ -68.8 (s, 3F, CF_3).

(*Z*)-3-(4-Butylphenyl)-3(2,2-dimethylhydrazineylidene)-1,1,1-trifluoropropan-2-one (4e)



White crystals.

Yield: 65 %.

Rf: 0.48 (ethyl acetate / petroleum ether = 1:9).

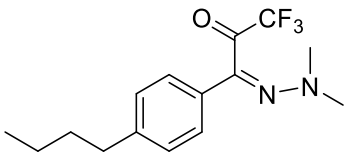
M.p: 86-88 °C.

^{1}H NMR 400 MHz ($CDCl_3$): δ 7.17 (d, *J* = 8.0 Hz, 2H, ArH), 7.11 (d, *J* = 7.9 Hz, 2H, ArH), 3.05 (s, 6 H, NCH_3), 2.62 (t, *J* = 8 Hz, 2H, CH_2), 1.65-1.57 (m, 2H, CH_2) 1.41-1.32 (m, 2H, CH_2), 0.93 (t, *J* = 7.4 Hz, 3H, CH_3).

^{13}C NMR 101 MHz ($CDCl_3$): δ 175.2 (q, *J* = 31.1 Hz, CO), 143.5, 130.3 (s, C=N), 127.9, 118.0 (q, *J* = 292.3 Hz, CF_3), 47.1, 35.5, 33.4, 22.4, 13.4.

^{19}F NMR 376 MHz ($CDCl_3$): δ -68.8 (s, 3F, CF_3).

(*Z*)-3-(Biphenyl-4-yl)-3(2,2-dimethylhydrazineylidene)-1,1,1-trifluoropropan-2-one (4f)



White solid.

Yield: 89 %.

Rf: 0.25 (ethyl acetate / petroleum ether = 2:9).

Mp: 145 °C.

^{1}H NMR 400 MHz ($CDCl_3$): δ 7.62-7.59 (overlapping, 4H, ArH), 7.45 (t, *J* = 7.8 Hz, 2H, ArH), 7.36 (t, *J* = 7.1 Hz, 1H, ArH), 7.29 (d, *J* = 7.3 Hz, 2H, ArH), 3.10 (s, 6 H, NCH_3).

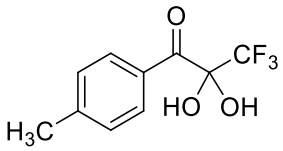
^{13}C NMR 400 MHz ($CDCl_3$): δ 178.0 (q, *J* = 32.4 Hz, CO), 141.4, 140.3, 131.9 (s, C=N), 130.9, 128.9, 127.1, 127.1, 126.5, 122.4, 118.0 (q, *J* = 292.6 Hz, CF_3), 47.3.

^{19}F NMR 376 MHz ($CDCl_3$): δ -68.8 (s, 3F, CF_3).

5.1.4 General procedure for the hydrolysis of trifluoroacetylated N,N-dimethyl hydrazones (TDP 1-6)

The appropriate trifluoroacetylated hydrazone 4a-f was dissolved in 5N H_2SO_4 and the solution was stirred for 24 hours for compounds **4a,b**, 2.5 hours for **4c** and 1 hour for **4e** at room temperature (for **4d and 4f** the reaction mixture was heated at 60°C for 24 hours). Then, the product was extracted with diethyl ether and the organic layers were dried over Na_2SO_4. The solvent was then removed under reduced pressure. Finally, the product was then purified by trituration with a mixture of petroleum ether and diethyl ether.

3,3,3-Trifluoro-2,2-dihydroxy-1-(p-tolyl)propan-1-one (TBP1)



White crystals.

Yield: 60 %.

Rf: 0.51 (ethyl acetate / petroleum ether = 2:8).

Mp: 84-86 °C.

^{1}H NMR 400 MHz ($CDCl_3$): δ 8.23 (d, *J* = 8.6 Hz, 2H, ArH), 7.30 (d, *J* = 8.6 Hz, 2H, ArH), 4.79 (s, 2 H, OH), 2.45 (s, 3H, CH_3).

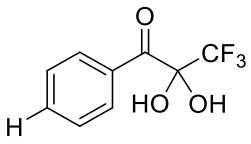
^{13}C NMR 101 MHz ($CDCl_3$): δ 191.4 (s, CO), 146.7, 132.0, 129.3, 128.9, 121 (q, *J* = 289.1 Hz, CF_3), 93 (q, *J* = 32.5 Hz, COH), 21.9.

^{19}F NMR 376 MHz ($CDCl_3$): δ -81.2 (s, 3F, CF_3).

ESI: m/z 231.0 $[M-2]^+$

Elemental analysis: $C_{10}H_9F_3O_3$. **Calculated**: C 51.29, H 3.87. **Found:** C 51.43, H 3.78.

3,3,3-Trifluoro-2,2-dihydroxy-1-phenylpropan-1-one (TBP2)



White crystals.

Yield: 60 %.

Rf: 0.47 (ethyl acetate / petroleum ether = 2:8)

M.p: 83 °C.

^{1}H NMR 400 MHz ($CDCl_3$): δ 8.33 (d, *J* = 8.1 Hz, 2H, ArH), 7.68 (t, *J* = 7.1 Hz, 1H, ArH), 7.51 (t, *J* = 7.8 Hz, 2H, ArH), 4.77 (s, 2 H, OH).

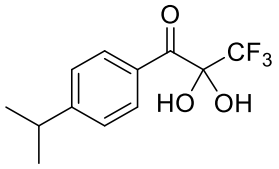
^{13}C NMR 400 MHz ($CDCl_3$): δ 191.2 (s, CO), 135.2, 131.8, 131.6, 128.5, 121.0 (q, *J* = 286.8 Hz, CF_3), 93.8 (q, *J* = 35.6 Hz, COH).

^{19}F NMR 376 MHz ($CDCl_3$): δ -81.1 (s, 3F, CF_3).

ESI: m/z 257.0 $[M+K-2]^+$.

Elemental analysis: $C_9H_7F_3O_3$. **Calculated**: C 49.10, H 3.20. **Found:** C 49.07, H 3.32.

3,3,3-Trifluoro-2,2-dihydroxy-1-(4-isopropylphenyl)propan-1-one (TBP3)



Yellow oil.

Yield: 82 %.

Rf: 0.25 (ethyl acetate / petroleum ether = 1:9).

^{1}H NMR 400 MHz ($CDCl_3$): δ 8.27 (d, *J* = 8.2 Hz, 2H, ArH), 8.35 (t, *J* = 8.6 Hz, 2H, ArH), 4.72 (s, 2 H, OH), 2.99 (m, 1H, CH), 1.29 (d, *J* = 7.0 Hz, 6H, CH_3).

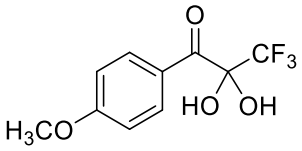
^{13}C NMR 400 MHz ($CDCl_3$): δ 191.3 (s, CO), 157.2, 132.2, 129.2, 126.7, 121.5 (q, *J* = 286.1 Hz, CF_3), 93.8 (q, *J* = 35.4 Hz, COH), 34.4, 23.5.

^{19}F NMR 376 MHz ($CDCl_3$): δ -81.2 (s, 3F, CF_3).

ESI: m/z 244.0 $[M\text{-}H_2O]^+$.

Elemental analysis: $C_{12}H_{13}F_3O_3$. **Calculated**: C 54.96, H 5.00. **Found:** C 54.67, H 5.34.

3,3,3-Trifluoro-2,2-dihydroxy-1-(4-methoxyphenyl)propan-1-one (TBP4)



White crystals.

Yield: 59 %.

Rf: 0.54 (ethyl acetate / petroleum ether = 3:7).

M.p: 81°C.

^{1}H NMR 400 MHz ($CDCl_3$): δ 8.34 (d, *J* = 9.2 Hz, 2H, ArH), 6.97 (d, *J* = 9.2 Hz, 2H, ArH), 4.82 (s, 2 H, OH), 3.92 (s, 3H, CH_3).

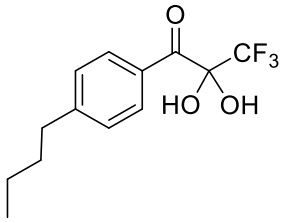
^{13}C NMR 400 MHz ($CDCl_3$): δ 189.8 (s, CO), 165.2, 134.7, 132.9, 121.0 (q, *J* =289.9 Hz, CF_3), 113.9, 93.7 (q, *J* = 34.1 Hz, COH), 55.7.

^{19}F NMR 376 MHz ($CDCl_3$): δ -81.4 (s, 3F, CF_3).

ESI: m/z 249 $[M-1]^+$.

Elemental analysis: $C_{10}H_9F_3O_4$. **Calculated**: C 48.01, H 3.63**. Found:** C 48.20, H 3.42.

3,3,3-Trifluoro-2,2-dihydroxy-1-(4-butylphenyl)-propan-1-one (TBP5)



Yellow oil.

Yield: 74 %.

Rf: 0.58 (ethyl acetate / petroleum ether = 2:8).

^{1}H NMR 400 MHz ($CDCl_3$): δ 8.25 (d, *J* = 8.3 Hz, 2H, ArH), 7.30 (d, *J* = 8.3 Hz, 2H, ArH), 4.86 (s, 2 H, OH), 2.69 (t, *J* = 7.7 Hz, 2H, CH_2), 1.63 (m, 2H, CH_2), 1.37 (m, 2H, CH_2), 0.94 (t, *J* = 7.4 Hz, 3H, CH_3).

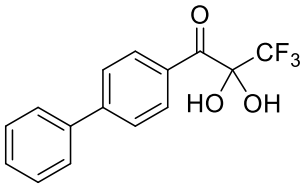
^{13}C NMR 400 MHz ($CDCl_3$): δ 191.5 (s, CO), 151.4, 132.1, 129.1, 128.6, 121.0 (q, *J* = 288.1 Hz, CF_3), 94,1 (q, *J* = 38.4 Hz, COH), 35.9, 32.9, 22.4, 13.9.

^{19}F NMR 376 MHz ($CDCl_3$): δ -81.2 (s, 3F, CF_3).

ESI: m/z 313.0 $[M+K-2]^+$.

Elemental analysis: $C_{13}H_{15}F_3O_3$. **Calculated**: C 56.52, H 5.47. **Found:** C 56.83, H 5.31.

3,3,3-Trifluoro-2,2-dihydroxy-1-(biphenyl-4-yl)-propan-1-one (TBP6)



White crystals.

Yield: 85 %.

Rf: 0.31 (ethyl acetate / petroleum ether = 2:8).

Mp: 87-88 °C.

^{1}H NMR 400 MHz ($CDCl_3$): δ 8.41 (d, *J* = 8.8 Hz, 2H, ArH), 7.73 (d, *J* = 7.2 Hz, 2H, ArH), 7.64 (d, *J* =8.2 Hz, 2H, ArH), 7.51-7.43 (overlapping, 3H, ArH), 4.81 (s, 2 H, OH).

^{13}C NMR 101 MHz ($CDCl_3$): δ 191.3 (s, CO), 147.8, 139.4, 132.5, 130.2, 129.0, 128.7, 127.4, 127.1, 121.5 (q, *J* = 289.6 Hz, CF_3), 93.8 (q, *J* = 37.3 Hz, COH).

^{19}F NMR 376 MHz ($CDCl_3$): δ -81.2 (s, 3F, CF_3).

ESI: m/z 333 $[M+K-2]^+$.

Elemental analysis: $C_{15}H_{11}F_3O_3$. **Calculated:** C 60.82, H 3.74. **Found:** C 60.64, H 3.42.

5.2 X-Ray crystallography of hCA II in complex with TBP4

5.2.1 Materials and methods

Expression and purification of hCAII was performed as previously described.[3] Crystals of hCAII were grown using the sitting drop vaporization method with a precipitant solution of 1.6 M Na-Citrate, 50 mM Tris, pH 7.8. Crystals were observed after 5 days. A 50 mM (~40% DMSO) stock solution of compound TBP4 was diluted in the precipitant solution of the well and used to soak the crystal 24 hours prior to data collection.

Diffraction data was then collected "in-house" with an RU-H3R rotating Cu anode (λ=1.5418 Å) operating at 50 kV and 22 mA. An R-Axis IV^{++} image plate detector (Rigaku, USA) was utilized with a crystal to detect distance of 100 mm, oscillation angle of 1°, and exposure time of 5 min per image for a total of 245 images. Data was indexed, integrated, and scaled with the program *HKL 2000*[4]. The data was scaled to the $P2_1$ space group to a resolution of 1.9 Å (summarized in Table 1). Molecular replacement was performed with the program *Phenix*[5] to determine the phases using search model PDB: 3KS3[6]. *Phenix*[5] was also used for structure refinements. *Coot*[7] was utilized to modify the model between refinements and analyze the interactions between the active site and TBP4. All figures were produced in *PyMol*[8].

Table S1. X-ray crystallography statistics for hCA II_TBP4 refinement

Sample	**hCA II_TBP4**
Space Group **Cell Dimensions (Å;°)**	*$P2_1$* a = 42.4, b = 41.1, c = 71.9; β= 104.3
Resolution (Å)	19.9 – 1.88 (1.98 – 1.88)
Total Reflections	19252
Rsym[a] (%)	4.60 (33.3)
I/Iσ	30.9 (4.03)
Redundancy	3.3 (3.4)
Completeness (%)	97.6 (98.5)
Rcryst[b] (%)	16.3 (17.6)
Rfree[c] (%)	20.7 (25.0)
Residue Nos. (Chain A, B)	4-261
# of Protein Atoms	2049
# of Water Molecules	123
# of Ligand Atoms	17
Ramachandran stats (%): Favored, allowed, generously allowed	96.8, 3.2, 0.0
Avg. B factors (Å2): Main-chain, Side-chain, Ligand	24.4, 30.0, 36.0
rmsd for bond lengths, angles (Å,°)	0.008, 1.21

5.3 Biological assay

5.3.1 CA inhibition assay

An Applied Photophysics stopped-flow instrument has been used for assaying the CA catalysed CO_2 hydration activity.[9] Phenol red (at a concentration of 0.2 mM) has been used as indicator, working at the absorbance maximum of 557 nm, with 20 mM Hepes (pH 7.4) and 20 mM $NaBF_4$ (for maintaining constant the ionic strength), following the initial rates of the CA-catalyzed CO_2 hydration reaction for a period of 10-100 s. The CO_2 concentrations ranged from 1.7 to 17 mM for the determination of the kinetic parameters and inhibition constants. For each inhibitor, at least six traces of the initial 5-10% of the reaction have been used for determining the initial velocity. The uncatalyzed rates were determined in the same manner and subtracted from the total observed rates. Stock solutions of inhibitor (10 mM) were prepared in distilled-deionized water and dilutions up to 0.01 nM were done thereafter with distilled-deionized water. Inhibitor and enzyme solutions were preincubated together for 15 min at RT prior to assay, to allow for the formation of the E-I complex. The inhibition constants were obtained by non-linear least-squares methods using PRISM 3, whereas the kinetic parameters for the uninhibited enzymes from Lineweaver-Burk plots, as reported earlier[10], and represent the mean from at least three different determinations. All CAs were recombinant proteins obtained as reported earlier by these groups.[11]

Table S2. Inhibition of hCA isoforms I, II, IX and XII with TDPs by a stopped-flow CO_2 hydrase assay. Acetazolamide (AAZ; 5-acetamido-1,3,4-thiadiazole-2-sulfonamide) was used as standard.

Compound		**K_I (μM)***			
		***h*CA I**	***h*CA II**	***h*CA IX**	***h*CA XII**
TDP1 (hit)	4-Me-C_6H_4	410	9.0	0.84	9.05
TDP2	Ph	54.3	63.5	4.51	6.86
TDP3	4-iPr-C_6H_4	86.0	>100	0.80	5.87
TDP4	4-MeO-C_6H_4	520	3.2	0.83	24.3
TDP5	4-nBu-C_6H_4	17.3	4.7	0.78	19.7
TDP6	4-Ph-C_6H_4	65.7	2.5	5.60	7.21
AAZ	-	0.25	0.012	0.025	0.006

*** Errors in the range of ± 5-10 % of the reported value from 3 different assays.**

Bibliography

(1) Supuran, C. T. How Many Carbonic Anhydrase Inhibition Mechanisms Exist? *J Enzyme Inhib Med Chem* **2016**, *31* (3), 345–360. https://doi.org/10.3109/14756366.2015.1122001.

(2) Akocak, S.; Supuran, C. T. Activation of α-, β-, γ- δ-, ζ- and η- Class of Carbonic Anhydrases with Amines and Amino Acids: A Review. *J Enzyme Inhib Med Chem* **2019**, *34* (1), 1652–1659. https://doi.org/10.1080/14756366.2019.1664501.

(3) Supuran, C. T. Carbonic Anhydrases: Novel Therapeutic Applications for Inhibitors and Activators. *Nat Rev Drug Discov* **2008**, *7* (2), 168–181. https://doi.org/10.1038/nrd2467.

(4) Pastorekova, S.; Parkkila, S.; Pastorek, J.; Supuran, C. T. Carbonic Anhydrases: Current State of the Art, Therapeutic and Future Prospects. *J Enzyme Inhib Med Chem* **2004**, *19* (3), 199–229. https://doi.org/10.1080/14756360410001689540.

(5) Alterio, V.; Di Fiore, A.; D'Ambrosio, K.; Supuran, C. T.; De Simone, G. Multiple Binding Modes of Inhibitors to Carbonic Anhydrases: How to Design Specific Drugs Targeting 15 Different Isoforms? *Chem Rev* **2012**, *112* (8), 4421–4468. https://doi.org/10.1021/cr200176r.

(6) Singh, S.; Lomelino, C.; Mboge, M.; Frost, S.; McKenna, R. Cancer Drug Development of Carbonic Anhydrase Inhibitors beyond the Active Site. *Molecules* **2018**, *23* (5), 1045. https://doi.org/10.3390/molecules23051045.

(7) Alterio, V.; Hilvo, M.; Di Fiore, A.; Supuran, C. T.; Pan, P.; Parkkila, S.; Scaloni, A.; Pastorek, J.; Pastorekova, S.; Pedone, C.; Scozzafava, A.; Monti, S. M.; De Simone, G. Crystal Structure of the Catalytic Domain of the Tumor-Associated Human Carbonic Anhydrase IX. *Proceedings of the National Academy of Sciences* **2009**, *106* (38), 16233–16238. https://doi.org/10.1073/pnas.0908301106.

(8) Whittington, D. A.; Waheed, A.; Ulmasov, B.; Shah, G. N.; Grubb, J. H.; Sly, W. S.; Christianson, D. W. Crystal Structure of the Dimeric Extracellular Domain of Human Carbonic Anhydrase XII, a Bitopic Membrane Protein Overexpressed in Certain Cancer Tumor Cells. *Proceedings of the National Academy of Sciences* **2001**, *98* (17), 9545–9550. https://doi.org/10.1073/pnas.161301298.

(9) Sjöblom, B.; Polentarutti, M.; Djinović-Carugo, K. Structural Study of X-Ray Induced Activation of Carbonic Anhydrase. *Proceedings of the National Academy of Sciences* **2009**, *106* (26), 10609–10613. https://doi.org/10.1073/pnas.0904184106.

(10) Imtaiyaz Hassan, Md.; Shajee, B.; Waheed, A.; Ahmad, F.; Sly, W. S. Structure, Function and Applications of Carbonic Anhydrase Isozymes. *Bioorg Med Chem* **2013**, *21* (6), 1570–1582. https://doi.org/10.1016/j.bmc.2012.04.044.

(11) Supuran, C. T. Carbonic Anhydrase Inhibitors. *Bioorg Med Chem Lett* **2010**, *20* (12), 3467–3474. https://doi.org/10.1016/j.bmcl.2010.05.009.

(12) Kuo, W.-H.; Yang, S.-F.; Hsieh, Y.-S.; Tsai, C.-S.; Hwang, W.-L.; Chu, S.-C. Differential Expression of Carbonic Anhydrase Isoenzymes in Various Types of Anemia. *Clinica Chimica Acta* **2005**, *351* (1–2), 79–86. https://doi.org/10.1016/j.cccn.2004.07.009.

(13) Masereel, B.; Thiry, A.; Dogne, J.-M.; Supuran, C. Anticonvulsant Sulfonamides/Sulfamates/Sulfamides with Carbonic Anhydrase Inhibitory Activity: Drug Design and Mechanism of Action. *Curr Pharm Des* **2008**, *14* (7), 661–671. https://doi.org/10.2174/138161208783877956.

(14) Du, A.-L.; Du, A.-L.; Ren, H.-M.; Du, A.-L.; Ren, H.-M.; Lu, C.-Z.; Tu, J.-L.; Xu, C.-F.; Sun, Y.-A. Carbonic Anhydrase III Is Insufficient in Muscles of Myasthenia Gravis Patients. *Autoimmunity* **2009**, *42* (3), 209–215. https://doi.org/10.1080/08916930802668610.

(15) Lou, Y.; McDonald, P. C.; Oloumi, A.; Chia, S.; Ostlund, C.; Ahmadi, A.; Kyle, A.; auf dem Keller, U.; Leung, S.; Huntsman, D.; Clarke, B.; Sutherland, B. W.; Waterhouse, D.; Bally, M.; Roskelley, C.; Overall, C. M.; Minchinton, A.; Pacchiano, F.; Carta, F.; Scozzafava, A.; Touisni, N.; Winum, J.-Y.; Supuran, C. T.; Dedhar, S. Targeting Tumor Hypoxia: Suppression of Breast Tumor Growth and Metastasis by Novel Carbonic Anhydrase IX Inhibitors. *Cancer Res* **2011**, *71* (9), 3364–3376. https://doi.org/10.1158/0008-5472.CAN-10-4261.

(16) Guler, O.; Simone, G.; Supuran, C. Drug Design Studies of the Novel Antitumor Targets Carbonic Anhydrase IX and XII. *Curr Med Chem* **2010**, *17* (15), 1516–1526. https://doi.org/10.2174/092986710790979999.

(17) Winum, J.; Rami, M.; Scozzafava, A.; Montero, J.; Supuran, C. Carbonic Anhydrase IX: A New Druggable Target for the Design of Antitumor Agents. *Med Res Rev* **2008**, *28* (3), 445–463. https://doi.org/10.1002/med.20112.

(18) Maresca, A.; Temperini, C.; Vu, H.; Pham, N. B.; Poulsen, S.-A.; Scozzafava, A.; Quinn, R. J.; Supuran, C. T. Non-Zinc Mediated Inhibition of Carbonic Anhydrases: Coumarins Are a New Class of Suicide Inhibitors. *J Am Chem Soc* **2009**, *131* (8), 3057–3062. https://doi.org/10.1021/ja809683v.

(19) Maresca, A.; Temperini, C.; Pochet, L.; Masereel, B.; Scozzafava, A.; Supuran, C. T. Deciphering the Mechanism of Carbonic Anhydrase Inhibition with Coumarins and Thiocoumarins. *J Med Chem* **2010**, *53* (1), 335–344. https://doi.org/10.1021/jm901287j.

(20) D'Ambrosio, K.; Carradori, S.; Monti, S. M.; Buonanno, M.; Secci, D.; Vullo, D.; Supuran, C. T.; De Simone, G. Out of the Active Site Binding Pocket for Carbonic Anhydrase Inhibitors. *Chemical Communications* **2015**, *51* (2), 302–305. https://doi.org/10.1039/C4CC07320G.

(21) Pala, N.; Dallocchio, R.; Dessì, A.; Brancale, A.; Carta, F.; Ihm, S.; Maresca, A.; Sechi, M.; Supuran, C. T. Virtual Screening-Driven Identification of Human Carbonic Anhydrase Inhibitors Incorporating an Original, New Pharmacophore. *Bioorg Med Chem Lett* **2011**, *21* (8), 2515–2520. https://doi.org/10.1016/j.bmcl.2011.02.059.

(22) Supuran, C. T. Inhibition of Carbonic Anhydrase IX as a Novel Anticancer Mechanism. *World J Clin Oncol* **2012**, *3* (7), 98. https://doi.org/10.5306/wjco.v3.i7.98.

(23) Li, Y.; Dong, M.; Sheng, W.; Huang, L. Roles of Carbonic Anhydrase IX in Development of Pancreatic Cancer. *Pathology & Oncology Research* **2016**, *22* (2), 277–286. https://doi.org/10.1007/s12253-015-9935-6.

(24) Pore, N.; Jalla, S.; Liu, Z.; Higgs, B.; Sorio, C.; Scarpa, A.; Hollingsworth, R.; Tice, D. A.; Michelotti, E. In Vivo Loss of Function Screening Reveals Carbonic Anhydrase IX as a Key Modulator of Tumor Initiating Potential in Primary Pancreatic Tumors. *Neoplasia* **2015**, *17* (6), 473–480. https://doi.org/10.1016/j.neo.2015.05.001.

(25) Couvelard, A.; O'Toole, D.; Leek, R.; Turley, H.; Sauvanet, A.; Degott, C.; Ruszniewski, P.; Belghiti, J.; Harris, A. L.; Gatter, K.; Pezzella, F. Expression of Hypoxia-inducible Factors Is Correlated with the Presence of a Fibrotic Focus and Angiogenesis in Pancreatic Ductal Adenocarcinomas. *Histopathology* **2005**, *46* (6), 668–676. https://doi.org/10.1111/j.1365-2559.2005.02160.x.

(26) Chafe, S. C.; Vizeacoumar, F. S.; Venkateswaran, G.; Nemirovsky, O.; Awrey, S.; Brown, W. S.; McDonald, P. C.; Carta, F.; Metcalfe, A.; Karasinska, J. M.; Huang, L.; Muthuswamy, S. K.; Schaeffer, D. F.; Renouf, D. J.; Supuran, C. T.; Vizeacoumar, F. J.; Dedhar, S. Genome-Wide Synthetic Lethal Screen Unveils Novel CAIX-NFS1/XCT Axis as a Targetable Vulnerability in Hypoxic Solid Tumors. *Sci Adv* **2021**, *7* (35). https://doi.org/10.1126/sciadv.abj0364.

(27) McDonald, P. C.; Dedhar, S. Co-Vulnerabilities of Inhibiting Carbonic Anhydrase IX in Ferroptosis-Mediated Tumor Cell Death. *Front Mol Biosci* **2023**, *10*. https://doi.org/10.3389/fmolb.2023.1327310.

(28) McDonald, P. C.; Chafe, S. C.; Supuran, C. T.; Dedhar, S. Cancer Therapeutic Targeting of Hypoxia Induced Carbonic Anhydrase IX: From Bench to Bedside. *Cancers (Basel)* **2022**, *14* (14), 3297. https://doi.org/10.3390/cancers14143297.

(29) Oosterwijk-Wakka, J.; Boerman, O.; Mulders, P.; Oosterwijk, E. Application of Monoclonal Antibody G250 Recognizing Carbonic Anhydrase IX in Renal Cell Carcinoma. *Int J Mol Sci* **2013**, *14* (6), 11402–11423. https://doi.org/10.3390/ijms140611402.

(30) Robey, I. F.; Baggett, B. K.; Kirkpatrick, N. D.; Roe, D. J.; Dosescu, J.; Sloane, B. F.; Hashim, A. I.; Morse, D. L.; Raghunand, N.; Gatenby, R. A.; Gillies, R. J. Bicarbonate Increases Tumor PH and Inhibits Spontaneous Metastases. *Cancer Res* **2009**, *69* (6), 2260–2268. https://doi.org/10.1158/0008-5472.CAN-07-5575.

(31) Hashim, A. A. I.; Abrahams, D.; Xu, L.; Centeno, B.; Sunassee, E.; Abddelgader, R.; Dubois, L.; Lambin, P.; Gatenby, R. A.; Gillies, R. J. Abstract 5932: Targeting Tumor Acidity with the LDHA Inhibitor (FX11) and CAIX Inhibitor (DH348) Overcomes Resistance to PD-1 Blockade and Inhibits Metastasis in a Pancreatic Cancer Model. *Cancer Res* **2017**, *77* (13_Supplement), 5932–5932. https://doi.org/10.1158/1538-7445.AM2017-5932.

(32) Cadoni, R. Synthesis of Amides from Aldehydes and Amines via C-H Bond Activation and Discovery and Development of Novel and Selective Carbonic Anhydrase Inhibitors, University of Sassari, Sassari, 2014.

(33) Kamitori, Y.; Hojo, M.; Masuda, R.; Fujitani, T.; Ohara, S.; Yokoyama, T. Electrophilic Substitution at Azomethine Carbon Atoms. Reaction of Aromatic Aldehyde Hydrazones with Trifluoroacetic Anhydride. *American Chemical Society* **1988**, *53*, 135–139.

(34) Snider, B. B.; Conn, R. S. E.; Sealfon, S. Reactions of Phenylhydrazones with Electron-Deficient Alkenes. *J Org Chem* **1979**, *44* (2), 218–221. https://doi.org/10.1021/jo01316a012.

CHAPTER IIIB

MULTIVALENT CARBONIC ANHYDRASE INHIBITORS

Chapter IIIB - Multivalent carbonic anhydrase inhibitors

1. General view

Considering the numerous human carbonic anhydrase (*h*CA) isoforms and their involvement in many physiopathological activities, the development of selective carbonic anhydrase inhibitors (CAIs) and/or activators (CAAs) constitutes one major challenge. This evidence can be related to two main factors such as a) the diffuse localization of all the isoforms in many tissues and organs which makes it difficult to target a specific CA isoform implicated in a particular disease, and b) the structural homology among of many CA isoforms, which hinders to design specific and selective drugs. However, advances in protein sequencing and crystallographic analysis of the CA isozymes along with the extensive synthesis of molecules aimed at identifying new and more effective CAIs.[1–5]

Significant efforts have been made to rationalize and identify distinct features that characterize the molecular heterogeneity of CAs, to be used in drug design. However, valuable information derived from numerous reports can be extrapolated. For example, despite the strict molecular homology of the active site of almost all the *h*CAs, there are important differences in the amino acid residues located in the middle and outer part of the active site cavity, [1,6–8] which have been considered for orienting drug design, as the "tail approach". This successful strategy, which emerged almost 25 years ago, [9] consists of appending one or more 'tails' to an aromatic/heteroaromatic scaffold that incorporates a zinc binding function (ZBG). This structural model can interact with the residues of the middle-outer part of the active site of CAs.[5,10] Another important advancement in the design of CA-selective inhibitors has been made considering the cellular localization of the different isozymes, particularly for the CAIX and XII isoforms, which are located in the cellular membrane. In this case, the development of cell-membrane impermeable molecular prototypes has led to the identification of new selective CAIX/XII inhibitors [1,4,11–13]

2. The multivalence inhibition approach

Despite the enormous effort dedicated to obtaining new and more selective CAI, the path remains long and challenging. The small-molecule approach, including classic medicinal chemistry and rational drug design, is anyway the subject of intense research efforts.[5,14] More recently, the multivalency strategy has emerged as a promising way to achieve more selective and potent biomolecular recognition through the combination of multiple non-covalent interactions.[15] Multivalence recognition is a well-known biological process, for example in cell adhesion and cell-virus interaction.[16,17] This supramolecular behavior was extensively studied in glycobiology where the carbohydrate-protein interaction is an important biological phenomena, involving the information transfer between cells[18,19]. In the context of enzyme inhibition, the study of glycosidases and the extensive work in the exploration of multivalence effect has provided insights into the multivalency interaction.[20] Multivalency involves a complex, multifactorial combination of characteristics such as valency effect, ligand structure, topology on the enzyme inhibition and the related thermodynamic and entropic variations that make complicate the deciphering and validation of this effect.[19,21] In general, the main outcome to achieve, particularly in the context of enzyme inhibition, is the increasing of overall binding affinity of weak ligands, which is possible to pursue considering the relative affinity of a ligand (relative potency per binding unit *rp/n*).[15,20] A positive multivalence effect is achieved when the relative potency of the ligands is higher in the multivalence system compared to the monovalent one, generally with rp/n > 1.

As mentioned above, multiple phenomena contribute to the multivalence effect, but four main modes of action are typically defined[15,16,22]:

a) *the chelation/coordination effect*, firstly proposed for carbohydrate-protein interaction[23], occurs when multivalent ligands bind oligomeric receptors by occupying multiple binding sites (**Figure 1A**);
b) *the subsite binding*, when at least a primary and a secondary binding site are present on the target (**Figure 1B**);
c) *the clustering effect*, when the multivalent ligand causes the clustering of multiple receptors, which can then be occupied (**Figure 1C**);

d) *the statistical rebinding effect*, resulting from the intrinsic multiple valency binding characteristic of the ligand which can result in higher apparent affinity (**Figure 1D**).

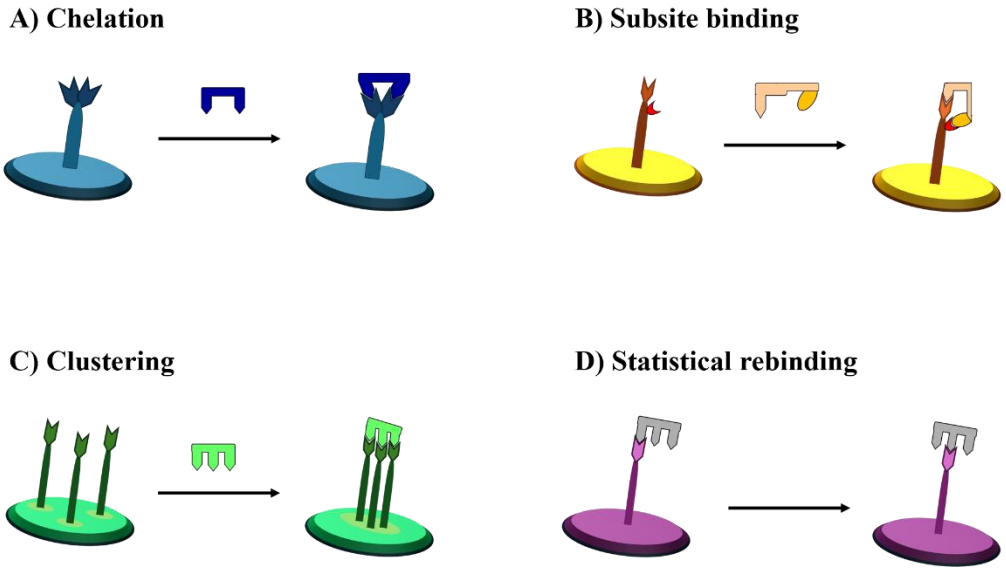


Figure 1. Representation of the four main multivalence mechanisms of action.

3. Multivalent carbonic anhydrase inhibition

Multimeric enzyme inhibition is challenging to achieve because attaching multiple inhibitors to a molecular platform does not necessarily lead to an effective multivalent system. Several factors, such as topology, structure, and valency of the platform, length and rigidity of the ligation system, must be refined in order to observe the multivalent effect. Nevertheless, where this effect is achievable, it can be an opportunity to explore new drug design approaches.

In the field of CA inhibition, owing to the advances in bioconjugation techniques[24], the multivalent approach opened up the possibility of creating a variety of innovative and selective prototypes using several (bio)molecular scaffolds as nanoparticles (gold and silica nanoparticles), nanorods, dendrimers, polyols, fullerenes and cyclopeptides.[25] Meanwhile, the classical medicinal chemistry approach has obtained attractive results for example in the case of bis-sulfamate CAI which show increased and more selective activity against CAII, IX and XII compared to the monosulfamate,[26,27] as well as the

results obtained with bivalent compounds against CAIX[28,29]. However, the preparation of multivalent structures has been a challenging task due to the difficulty of performing multiple one-pot reactions by covalently linking together a controlled number of bioactive ligands. For this reason, multiple chemical approaches aimed to obtain fast and efficient covalent conjugations have been implemented in this area, and in particular the click-type chemistry is playing an important role in CAI drug design.[30–32]

4. Rational of the PhD work

The dysregulation of some CA isoforms, particularly the *h*CAIX and XII, in the progress of many cancer typologies, specifically in resistant and hypoxic tumors, is currently the focal point to develop new anticancer treatments.[13,33,34]

In the course of 6-months research at the ChemBioNAC group at the 'Institute of Biomolecules Max Mousseron' in Montpellier (France), I worked under the supervision of Prof. Jean-Yves Winum in the development of new multivalent CAI prototypes. The ChemBioNAC group has a consolidated expertise on the chemical biology of nucleic acids and relies on the design, synthesis and analysis of natural or modified oligonucleotides for diagnostic and therapeutic purposes, extending the use of nucleic acids as functional systems in the interface between biology and synthetic chemistry.

The PhD project was a logical continuation of previous research undertaken by the Doctor Justine Mansot[35] under the supervision of Prof. Michael Smietana, in which they proposed the application of oligonucleotide strands as platform for the insertion of CAI molecules to pursue a multivalence strategy. The multivalent approach for CAI was already used in the past[25] and, by analogy, the use of oligonucleotides, previously utilized for multitargeting,[36,37] emerged as a promising option, due to their structural versatility, ability for biological recognition and potential multiple chemical manipulation. Specifically, the use of oligonucleotide was considered to target the transmembrane *h*CAIX and XII isoforms, implicated in many hypoxic cancer types[33], owing to their massive negative charge. This negative charge reduces the absorption of the putative oligo-linked CAIs through the cell membrane, thus selectively exposing the linked CAI uniquely to these two *h*CA isozymes.

4.1 Chemistry

For this purpose, we chose two well known bioactive compounds in the context of CA inhibition, i.e. 4-(2-aminoethyl)benzensulfonamide (**1, Figure 3)** and 7-hydroxy-3-methyl-coumarin (4-methylumbelliferone) (**3, Figure 3)**, which were conjugated to a single 12-mer oligonucleotide strand in specific position by a CuAAC click-type conjugation[38]. The necessary azido-derivatives to be used for the subsequent click reaction were prepared through classical synthetic chemistry, while the oligo strands were prepared separately using a synthetic automatic approach.

We achieved the conjugation through the "post-synthetic route" (**Figure 2**) which involved the incorporation of a synthon bearing a chemical function that can react with the azide functionality carried by the molecule to be introduced. This conjugation can occur either in a supported manner[39] (before the solid support detachment step) or in solution[40] (after the solid support detachment step).

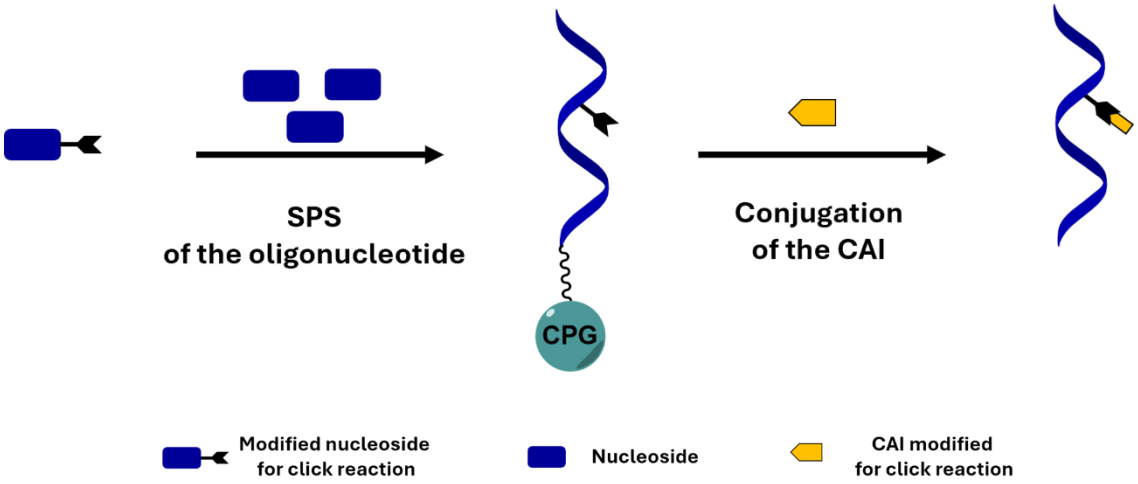


Figure 2. Illustration of the "post-synthetic route" for the oligo-inhibitors derivatives synthesis. Firstly, the oligonucleotide was obtained by multistep automatic synthesis, introducing a functionalized nucleoside in the desired positions. Secondly, the modified inhibitor structures react with the modified nucleoside forming a new linker bridge.

To connect the oligonucleotide with the CAI by click reaction, we chose a uridine phosphoramidite synthon bearing a propargyl group (**7, Figure 3)**, which was automatically incorporated in the desired position of the oligo-strand using the automatic synthetic approach To prevent hydrolysis of the lactone nucleus, we used the CPG-free

oligonucleotide for the subsequent click reaction with the coumarin. For the sulfonamide derivative, we employed both reaction type, depending on the difficulty of achieving homogeneous click reactions with good yields.

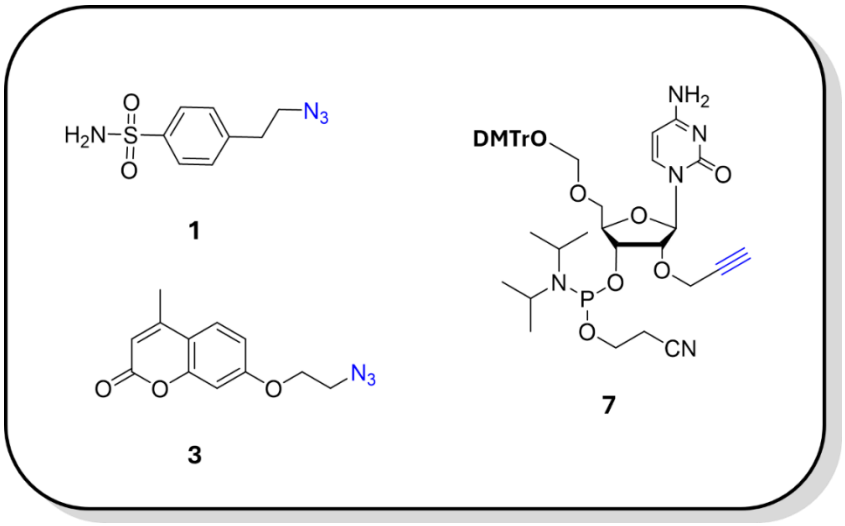
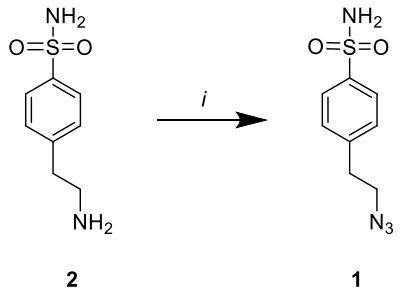


Figure 3. CAIs and the uridine phosphoramidite synthons used for the synthetic procedures.

4.1.1 Preparation of the azido-modified carbonic anhydrase inhibitors

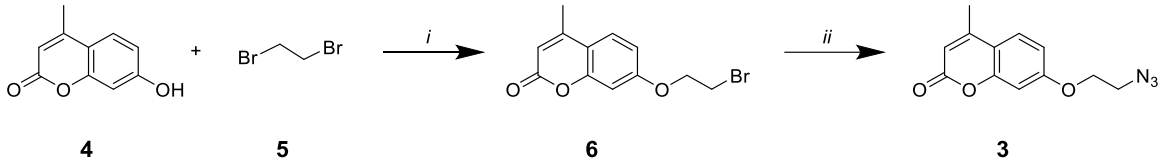
The azido-sulfonamide derivative **1** was synthesized starting from the commercially available benzenesulfonamide **2**, which was treated with $CuSO_4$ and a solution of NaN_3/Tf_2O complex overnight yielding **1** in good yield (**Scheme 1**).



Scheme 1. Reagents and conditions: *i*) NaN_3 in H_20/Toluene, Tf_2O, $CuSO_4$, MetOH/H_2O, r.t overnight.

The azido-coumarin derivative **3** was synthesized in a two-step reaction. First, hydroxy-coumarine **4** was coupled with dibromoethane **5** in ACN in the presence of K_2CO_3 at

reflux overnight. The bromoethoxy-coumarin **6** was obtained after filtration was then converted to the azido-derivative **3** using H_2O/NaN_3 and acetone at reflux for 8 hours (**Scheme 2**).



4 **5** **6** **3**

Scheme 2. Reagents and conditions: *i*) K_2CO_3, ACN, reflux, overnight. *ii*) NaN_3/H_2O, Acetone, reflux, 8 h.

4.1.2 Preparation of the single strand 12mer oligonucleotide

The multivalent bio-platform was prepared using an efficient method developed in the 1980s for chemical synthesis of single-stranded DNA (and RNA) on solid supports.[41] In the case of DNA synthesis, this methodology involves the assembly of molecular building blocks: nucleosides that are *a*) functionalized at the 3'-hydroxyl position with a phosphoramidite group containing a labile O-cyanoethyl (CNE) group and N-diisopropyl group, and *b*) protected at the 5'-hydroxyl position by a 4,4'-dimethoxytrityl (DMTr) acid-labile group (**Figure 4B**). The nucleobases, which contain exocyclic amine functions, are also protected by labile groups (benzoyl for A and C, and isobutyryl for G) (**Figure 4A**). All synthons derived from natural nucleosides are commercially available.

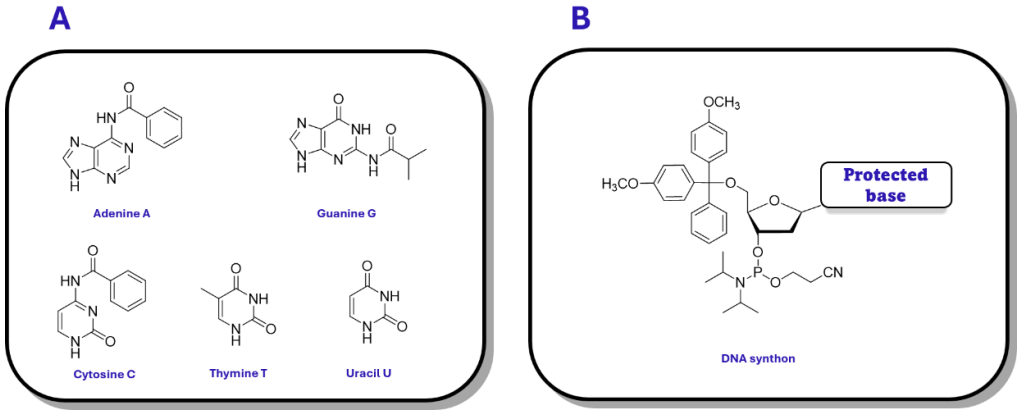


Figure 4. A) Protected purines and pyrimidines used for the oligo synthesis. B) General representation of the functionalized and protected form of the bases.

The synthesis of single-stranded DNA (and RNA) was performed in a supported manner. It involves the use of a first nucleoside attached at the 3' position via an ester function linked by a succinyl group to porous glass beads (CPG) and protected at the 5' position by a DMTr group. The successive incorporation of the different protected phosphoramidite synthons dA, dC, dG, dT (and A, C, G and U for RNA) occurs from the 3' to the 5' end. A supported synthetic cycle has been developed, yielding excellent results for the iterative incorporation of these phosphoramidite synthons. This cycle consists of four steps, which are repeated as many times as necessary (**Figure 5**)

Step 1 (Detritylation): the first step of this cycle involves deprotecting the 5'-hydroxyl group of the supported nucleoside through acidic treatment with a 3% solution of trichloroacetic acid (TCA) in dichloromethane. The release of the cationic DMTr species is quantified by UV spectroscopy (498 nm) and conductivity measurements at each deprotection step, allowing for the determination of the coupling yields.

Step 2 (Coupling): at this stage, the free alcohol group on the support reacts with with the phosphoramidite group of the synthon to be incorporated. This coupling step requires an activator such as tetrazole, to facilitate the formation of a triester phosphite bond that links the supported nucleoside to the desired synthon. The activator used in our case is 5-(benzylthio)-1H-tetrazole (BMT).

Step 3 (Capping): since coupling is never complete, this step is used to "cap" the unreacted hydroxyl groups that did not react with the phosphoramidite group of the synthon. For this, a solution of "CAP A," composed of THF/pyridine/acetic anhydride (8:1:1), and a solution of "CAP B," containing N-methylimidazole (NMI, 10% in THF), are used to protect the free 5'-OH group with an acetyl group. This crucial step prevents the formation of deletion sequences.

Step 4 (Oxidation): the final step involves oxidizing the phosphorus of the triester phosphite group from oxidation state (III) to oxidation state (V), resulting in the formation of a triester phosphate. This oxidation is carried out using a 0.1 M iodine solution in THF pyridine: water (78:20:2).

Elongation: these four steps were then repeated iteratively until the desired DNA sequence was synthesized by incorporating the appropriate synthons.

Elimination of support and deprotection

The DNA is then detached from the solid support through an ammoniacal treatment (other milder basic treatments can also be used, depending on the sensitivity of the synthons). In this process, the ester function that linked the first nucleoside to the solid support is replaced by a free hydroxyl group at the 3' position. The labile protections on the amines present in the nucleobases are also removed.

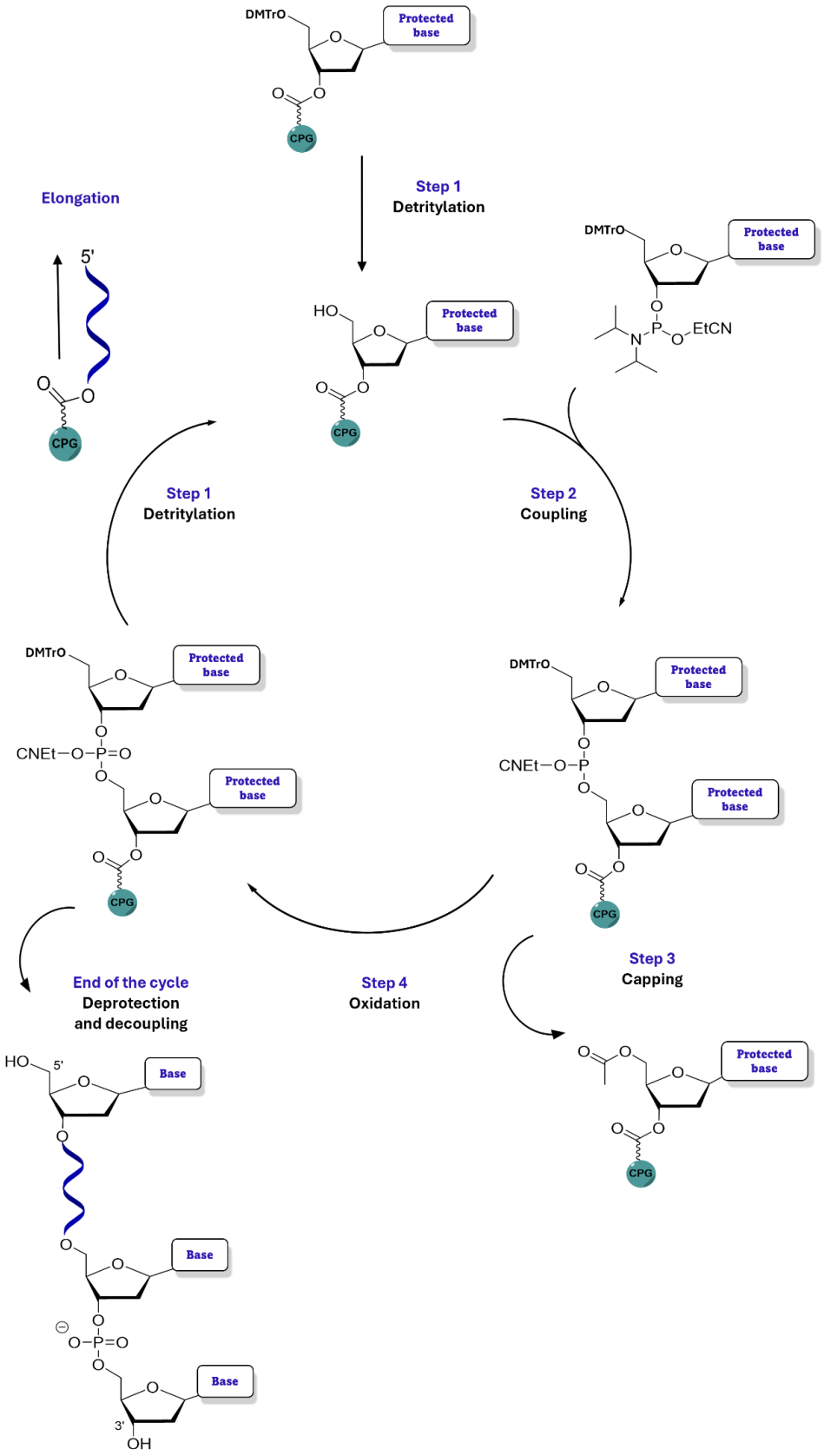
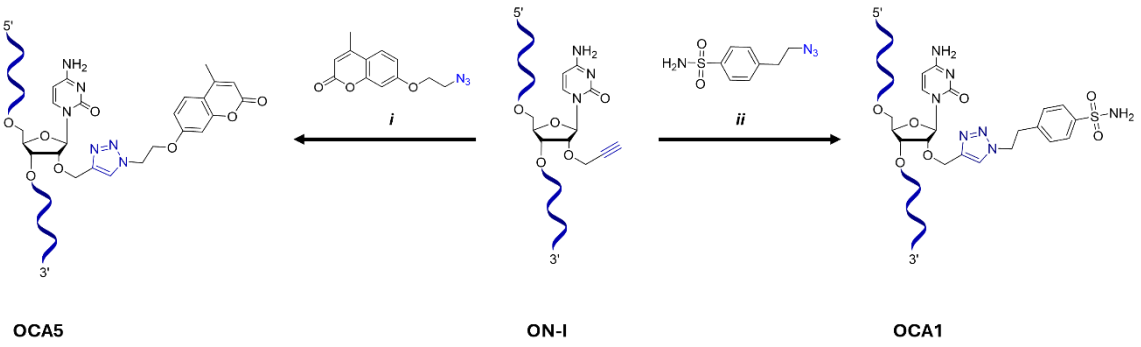


Figure 5. Representation of the elongation cycle used for the synthesis of the DNA oligonucletide.

4.1.3 Incorporation of the CA inhibitors in the DNA oligonucleotide

The incorporation of CAIs into the oligonucleotides was achiev aed through click reaction using a microwave reactor, where all the necessary reactants were added together into a glass vessel and kept under controlled temperature with stirring for the necessary time (**Scheme 3** and **Experimental section**)



Scheme 3. General representation for the incorporation of the azido CAIs 1 and 3 into the oligonucleotide with one reactive site ON-I (the monovalent derivatives OCA1 and OCA5 are represented in the scheme). Reagents and conditions: *i* and *ii*) $CuSO_4$, Sodium Ascorbate, THPTA, milliQ H_2O, 60°, 1-2 hr, microwave**.**

To evaluate the multivalency effect we designed and synthesized two sets of oligo-CAIs incorporating one to four CAIs inside the oligonucleotide platforms. These were prepared by introducing from one to four click-reactive sites (ON-I to ON-IV, as described in the experimental section), and subsequently tested for the enzymatic inhibition. The oligo-CAIs obtained are divided into sulfonamide-like CAIs (**Figure 6**, OCA1 to 4) and coumarin-like CAIs (**Figure 6**, OCA5 to 8).

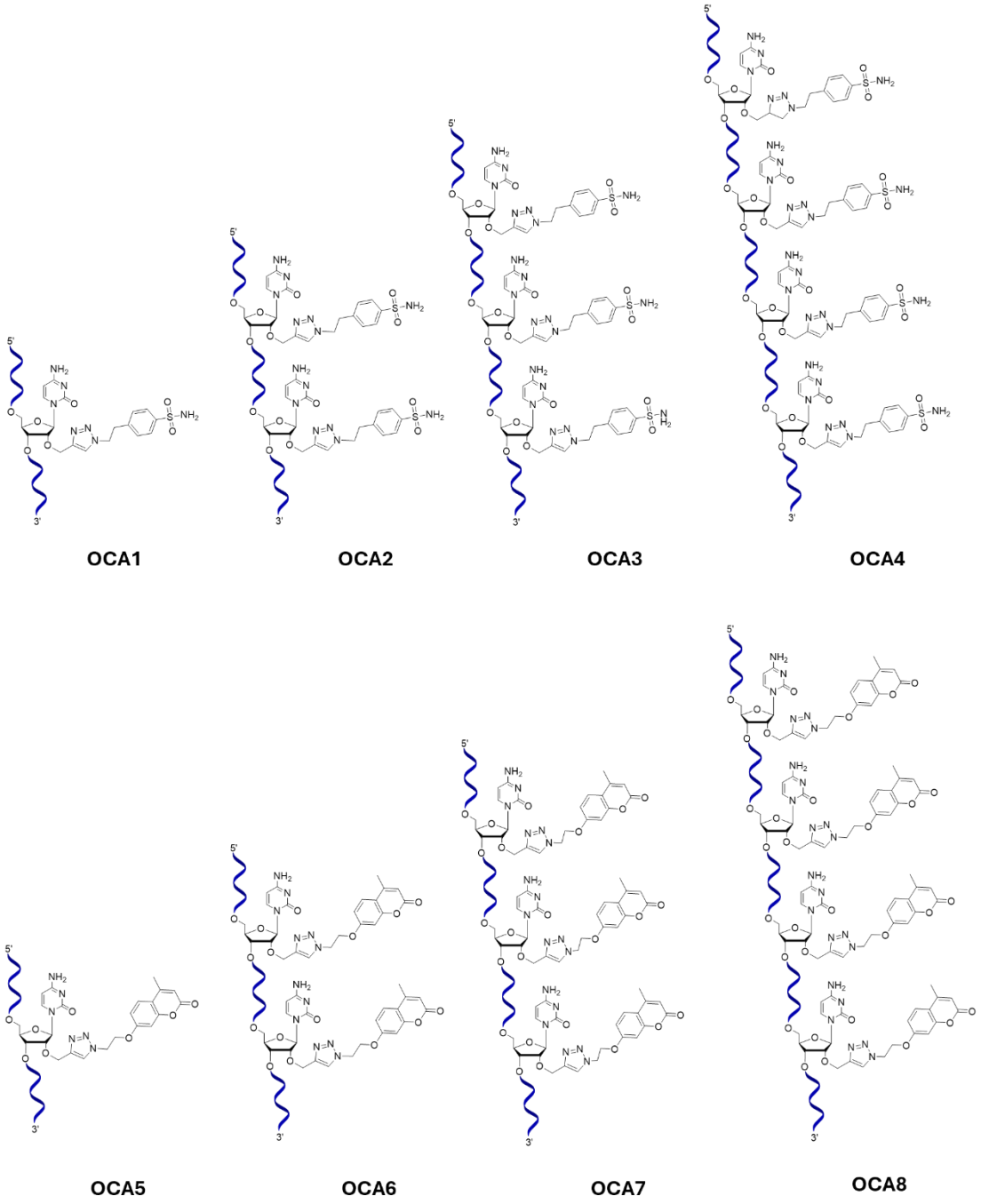


Figure 6. Illustration of the two sets of compounds obtained after the CAIs incorporation: sulfonamide derivatives OCA1-4 and coumarin derivatives OCA 5-8.

4.2 Enzymatic inhibition assay

The enzymatic inhibition activity of the two sets of compounds was tested by the stop-flow technique, against the cytosolic *h*CA isoforms I and II and the transmembrane isoforms IV, IX and XII, with acetazolamide (AZA) used as standard (**Table 1**).

Table 1. Inhibition of *h*CA isoforms I, II, IV, IX and XII with compounds of the series **OCA**, and acetazolamide (AAZ; 5-acetamido-1,3,4-thiadiazole-2-sulfonamide), used as standard, by a stopped-flow CO_2 hydrase assay. The sites of insertion of the CAIs are uridines (**U_1** for sulfonamides and **U_3** for coumarins).

		K_I (nM)*				
ID	**Sequence**	**CAI**	**CAII**	**CAIV**	**CAIX**	**CAXII**
OCA1	5′-GCC AGC **U_1**GA CCG -3′	762	386	894	99.7	129
OCA2	5′-GC**U_1** AGC **U_1**GA CCG -3′	554	243	1650	124	78.2
OCA3	5′-GC**U_1** AGC **U_1**GA **U_1**CG -3′	1560	498	1980	84.0	141
OCA4	5′-GC**U_1** A**U_1**C **U_1**GA **U_1**CG -3′	1740	310	1430	148	103
OCA5	5′-GCC AGC **U_3**GA CCG -3′	>10 μM	>10 μM	>10 μM	682	3420
OCA6	5′-GC**U_3** AGC **U_3**GA CCG -3′	>10 μM	>10 μM	>10 μM	731	2230
OCA7	5′-GC**U_3** AGC **U_3**GA **U_3**CG -3′	>10 μM	>10 μM	>10 μM	1450	1880
OCA8	5′-GC**U_3** A**U_3**C **U_3**GA **U_3**CG -3′	>10 μM	>10 μM	>10 μM	2210	1300
AZA		250	12	74	25	5.7

Comparison of inhibition constant values (Ki) recorded for each isoform in the presence of the derivatives suggests that the conjugation of both sulfonamide- and coumarin-type CA inhibitors directly and positively influenced the selectivity for the transmembrane CA IX and XII isoforms. Collectively, with Ki_s in the range 78-148 nanomolar against IX and XII isoforms, the sulfonamide-based oligonucleotide OCA2 and OCA3 demonstrated the most potent inhibition activities. However, almost all the derivatives have specificity for the isoforms CA IX and XII as evidenced by the ratio of the inhibition constants between the intracellular and transmembrane *h*CA isoforms (CA I-II vs IX-XII). This ratio highlights the specificity to inhibit the isoforms CA IX and CA XII compared to the isoforms I and II (**Table 2**).

Table 2. Ratio of the inhibition constants (Ki) of OCA compounds againsts the isoforms I - II and the isoforms XI and XII.

ID	I / IX	II / IX	I / XII	II / XII
OCA1	7,6	3,9	5,9	3,0
OCA2	4,5	2,0	7,1	3,1
OCA3	18,6	5,9	11,1	3,5
OCA4	11,8	2,1	16,9	3,0
OCA5	14,7	14,7	2,9	2,9
OCA6	13,7	13,7	4,5	4,5
OCA7	6,9	6,9	5,3	5,3
OCA8	4,5	4,5	7,7	7,7

To evaluate the impact of enzyme inhibition by multivalent prototypes compared to the monovalent counterparts, the relative inhibition potency "Pr" of the monovalent and multivalent systems should be considered. "Pr" indicates the ratio "Ki monovalent / Ki multivalent" for a given isoform (**Table 3**). An improvement in the inhibition potency of the multivalent system is observed for the enzyme isoforms when the Pr is greater than 1. Our results showed different increments in the Pr values when the Ki of the monovalent derivatives OCA1 and OCA5 were compared to their multivalent counterparts reflecting an increase in potency of some derivatives as the platform incorporate more linked inhibitors, as expected.

Table 3. Relative inhibition potency (Pr) of the monovalent system (OCA 1 and OCA5) compared with the other multivalent systems.

PR	CAI	CAII	CAIV	CAIX	CAXII
OCA 1 / 2	1,4	1,6	0,5	0,8	1,6
OCA 1 / 3	0,5	0,8	0,5	1,2	0,9
OCA 1 / 4	0,4	1,2	0,6	0,7	1,3
OCA 5 / 6	1,0	1,0	1,0	0,9	1,5
OCA 5 / 7	1,0	1,0	1,0	0,5	1,8
OCA 5 / 8	1,0	1,0	1,0	0,3	2,6

Although this parameter seems useful for comparing multivalent and monovalent entities, there are several aspects that need to be considered. Specifically, the comparison between two multivalent systems, which therefore have a different number of bound inhibitors, does not accurately reflect a possible increase in the potency directly attributable to the multivalence effect, because the increased potency is more logically related to the higher number of inhibitors linked to the platform, unless there is a clearly evident, substantial variation in the inhibition constants (more than proportional).

Indeed, to avoid this question, an important parameter to be considered is the relative inhibition potency "Pr" normalized for the ratio between the number “n” of linked inhibitors of the considered systems. When this value (Pr/n) is greater than 1 it is plausible to define a positive multivalence effect. This concept is observable in the case of the oligo-coumarin derivatives OCA5-8 against the CAXII isoform, where if we consider only the relative potency Pr between the Ki of the monovalent OCA5 and the Ki of the other multivalent compounds of the set, we observe an increase in the Pr value (**Table 3**) undoubtedly favorable as regards the increased inhibition activity. Conversely, when we normalize the relative potency by the number of bound inhibitors (Pr/n), we observe a reduction of the value, always < 1, which confirm the lack of the multivalence effect (**Table 4**)

Table 4. Relative inhibition potency normalized for the number of binded inhibitors ratio (Pr/n) of the monovalent system (OCA 1 and OCA5) compared with the other multivalent systems.

PR/N	CAI	CAII	CAIV	CAIX	CAXII
OCA 1 / 2	0,7	0,8	0,3	0,4	0,8
OCA 1 / 3	0,2	0,3	0,2	0,4	0,3
OCA 1 / 4	0,1	0,3	0,2	0,2	0,3
OCA 5 / 6	0,5	0,5	0,5	0,5	0,8
OCA 5 / 7	0,3	0,3	0,3	0,2	0,6
OCA 5 / 8	0,3	0,3	0,3	0,1	0,7

There are several considerations to consider rationalize these results. Firstly, factors contributing to the lack of multivalency may relate to the type of platform used. Despite the increased selectivity towards the transmembrane isoforms CAIX and CAXII, the spatial distribution of the inhibitors may not be arranged in parallel, thus preventing interactions with the protein via the various mechanisms outlined earlier. Although this negative factor may be counterbalanced by thermodynamic binding factors, in the case of an oligonucleotide-based platform with numerous intermolecular interactions, this could become a limiting factor. Secondly, the nucleotide sequence also plays a crucial role in the topology of the platform, as well as the distance between the functionalized bases that are necessary for the inhibitors linking. Another factor could involve the extreme hydrosolubility conferred by the oligonucleotide portion of the molecule, which increases the energy required to bring the inhibitory structures into contact with the protein. On the other hand, the ability of the inhibitors to arrange themselves in an ideal configuration to interact with the enzyme is crucial for the biological interaction. Consequently, the inhibitor-platform linker is also of significant importance, particularly in terms of its length and freedom of rotation.

5. Conclusions

In the context of CA inhibition, which has long faced the challenge of identifying molecules capable of selectively targeting specific isoforms, the multivalent targeting has recently provided new perspectives for developing more potent and selective inhibitors. In this project, aimed at obtaining novel multivalent CA inhibitors targeting different isoforms, an original oligonucleotide-based platform containing two types of CAIs – i.e sulfonamide- and coumarin-based derivatives – was developed. Two sets of oligonucleotide prototypes were obtained, each conjugated with an increasing number of bound inhibitors, which were tested against various *h*CA isoforms.

The results showed significant inhibition and selectivity towards the CAIX and CAXII isoforms, which are implicated in several pathologies, especially various types of cancer. Despite the interesting selectivity and potency demonstrated by some oligo-prototypes, a consistent multivalent effect was not observed at this stage, and this can be attributed to various physicochemical factors. However, the design of certain modifications to apply

to the oligonucleotide platform is currently under evaluation to obtain new insights and a potential multivalent effect.

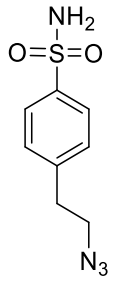
6. Experimental part

6.1 General methods

Unless otherwise noted, all solvents, including anhydrous solvents and chemicals, were purchased from Aldrich Co. and/or Alfa Aesar, and used without further purification. All reactions involving air- or moisture-sensitive compounds were performed under an argon atmosphere using oven-dried glassware and syringes to transfer solutions. Silica gel thin-layer chromatography (TLC) sheets for Merck silica gel F-254 plates (silica gel precoated aluminum sheets with fluorescent indicator at 254 nm) were used for TLC. Proton nuclear magnetic resonance (^{1}H NMR) spectra were recorded in $CDCl_3$ or DMSO-d_6 on 400 MHz Bruker Avance III nanobay. Chemical shifts (δ) are reported in parts per million (ppm) downfield from tetramethylsilane (TMS), used as internal standard. Splitting patterns are designated as follows: broad singlet (bs), singlet (s), doublet (d), triplet (t), quartet (q), septet (sep), and multiplet (m). Mass spectra were obtained on micrOTOF-Q mass spectrometer, or a Axima MALDI-TOF equipped with a reflector analyser. Purifications were performed using ThermoFisher UHPLC Ultimate 3000. Microwave reactions were performed using Anton Paar microwave synthesis system.

6.2 Synthesis and characterization of the CA inhibitors

Synthesis of 4-(2-azidoethyl) benzenesulfonamide [1]



Solution A: NaN_3 (0.83 g, 12.75 mmol, 10.2 eq) was solubilized in 50/50 water-toluene (4mL) and Tf_2O (0.74 g, 2.63 mmol, 2.1 eq) was added dropwise in 5 minutes at 0°C and stirred at that temperature for 1 hr.

Solution B: 4-(2-aminoethyl) benzenesulfonamide (**2**, 0.250 g, 1.25 mmol) was solubilized in water (4mL) and methanol (8mL) and $CuSO_4$ (0.028 g, 0.175 mmol, 0.14 eq) was added.

Solution A was added dropwise to solution B at 0°C, let warm to rt and stirred overnight. The solvent was evaporated and the solid solubilized in ethyl acetate, washed with water and brine, dried with Na_2SO_4 and reduced to obtain a white solid

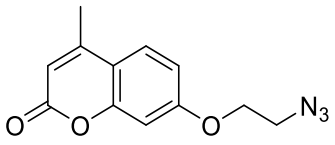
Yield: 81.5%.
Rf: 0.6 (DCM / MeOH = 9.5:0.5)

^{1}H-NMR 400MHz (DMSO d_6): δ 7.76 (d, 2H), 7.47 (d, 2H), 7.30 (s, 2H), 3.61 (t, 2H), 2.92 (t, 2H)

^{13}C 400MHz (DMSO d_6): δ 143.12, 142.86, 129.76, 126.20, 51.57, 34.59

MS: m/z 225 [M-H]

Synthesis of 7-(2-azidoethoxy)-4-methyl-2H-chromen-2-one [3]



To a solution of 7-(2-bromoethoxy)-4-methyl-2H-chromen-2-one (**6**, 0.5 g, 1.77 mmol) in acetone (20 mL), NaN_3 (0.230 g, 3.53, 2eq) in water (5 mL) was added dropwise and the mixture was stirred for 8 hr at reflux. After the evaporation of the solvent, the residue was solubilized in ethyl acetate and washed with water and brine. The organic phase was dried with Na_2SO_4, filtered and evaporated to obtain a white solid that was purified with flash chromatography (CH_3Cl / Et. Ac = 7:3)

Yield: 61.7%.

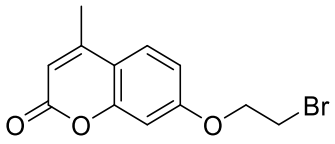
Rf: 0.73 (CH_3Cl / Et. Ac = 7:3)

^{1}H-NMR 400MHz ($CDCl_3$): δ 7.55 (d, 1H), 6.93 (dd, 1H), 6.85 (d, 1H), 6.19 (s, 1H), 4.24 (t, 2H), 3.69 (t, 2H), 2.44 (s, 3H)

^{13}C 400MHz ($CDCl_3$): δ 161.15, 155.20, 152.46, 125.75, 114.14, 112.68, 112.37, 101.48, 67.42, 49.96, 18.71.

MS: m/z calc 245, found: 280 [M+Cl]

Synthesis of 7-(2-bromoethoxy)-4-methyl-2H-chromen-2-one [6]



To a solution of 7-hydroxy-4-methyl-2H-chromen-2-one (**4**, 2 g, 11.35 mmol) and K_2CO_3 (9.4 g, 204.34) mmol) in acetonitrile (100 mL), 1,2-dibromoethane (**5**, 6.4 g, 51.08 mmol) was added dropwise and the solution was stirred for 2 hr at reflux. Subsequently, the mixture was filtered and the solvent evaporated. The solid residue obtained was solubilized in DCM, the organic phase washed with brine and dried with Na_2SO_4, filtered and evaporated to obtain a white solid that was purified with flash chromatography (CH_3Cl / Ethyl Acetate = 9:1).

Yield: 43.7%.
Rf: 0.81 (CH_3Cl / ethyl acetate = 9:1).

^{1}H-NMR 400MHz ($CDCl_3$): δ 7.50 (d, 1H), 6.89(d, 1H), 6.87 (d, 1H), 6.14 (s, 1H), 4.35 (t, 2H), 3.67 (t, 2H), 2.39 (s, 3H)

^{13}C 400MHz ($CDCl_3$): δ 161.22, 161.02, 155.18, 152.43, 125.76, 114.15, 112.53, 112.37, 101.71, 68.18, 28.49, 18.69.

MS: m/z 283 [M+H]

6.3 Synthesis of oligonucleotide strands

6.3.1 General procedure A for solid supported synthesis

Oligonucleotide synthesis was performed on solid support (CPG beads 1000 A) Commercially available phosphoramidite synthons dA, dG, dC, and 2'-O-Propargyl Uridine CED phosphoramidite were incorporated with a 1.30 min time coupling (0.1 M in anhydrous acetonitrile), to afford the corresponding desired 12-mer sequences (ON-I II-III-IV). After the supported synthesis, CPG beads were washed with anhydrous acetonitrile and then dried under vacuum.

6.3.2 General procedure B for oligonucleotide supports cleavage and deprotection

Ammonia (33% in H_2O, 1 mL/µmol oligonucleotide) was added to the solid-supported oligonucleotide to cleave the support and all basolabiles protection, (cyanoethyl and base protection) at 40 °C overnight, followed by a filtration of the beads. The solution containing oligonucleotide and ammonia was evaporated.

6.3.3 Synthesis of modified sequences (ON-I-II-III-IV)

All sequences were synthetized following general procedure A, and deprotected following general procedure B concerning. The resulting oligo strands were purified on reverse flash chromatography (Gradient: 1% acetonitrile to 24% acetonitrile 25 mM TEAAc in 20 min). The oligo strand used for three and four incorporations of the sulfonamide **1** (ON3 and ON4) were deprotected and purified following the same method after the post-synthetic supported CuAAC click reaction. All sequences were characterized by chromatography HPLC-C18 and mass spectrometry MALDI-TOF.

Table S1. Sequences of the oligonucleotide strands

Oligo name	Structure sequences
ON-I	5'-GCC AGC **U**GA CCG-3'
ON-II	5'-GC**U** AGC **U**GA CCG-3'
ON-III	5'-GC**U** AGC **U**GA **U**CG-3'
ON-IV	5'-GC**U** A**U**C UGA **U**CG-3'

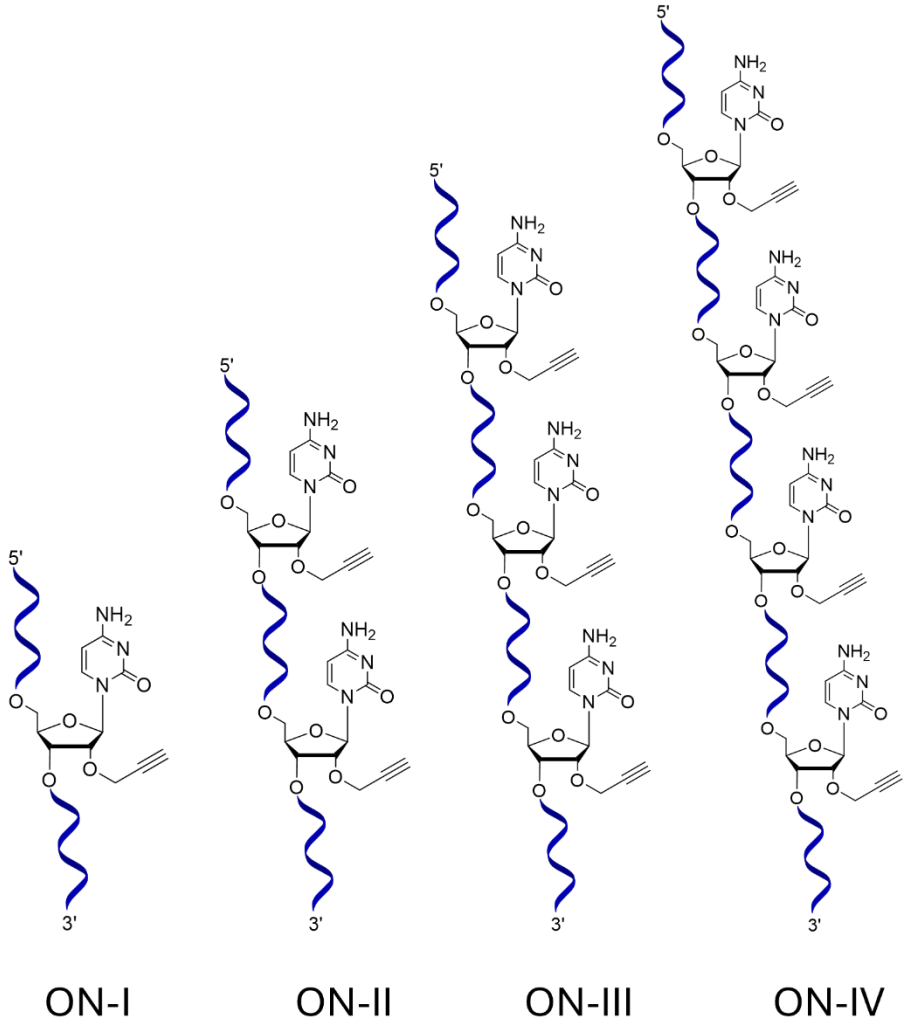


Figure S1. Oligonucleotide strands used for coupling reactions with the carbonic anhydrase inhibitors

6.4 Synthesis of the final compounds (OCA1-8)

6.4.1 Preparation of the sulfonamide multivalent inhibitors

Synthesis of the monovalent sulfonamide-oligonucleotide [OCA1]

To a microwave sealed vessel the oligonucleotide **ON-I** in degassed milliQ water (0.164 µmol in 100 µL) was added. A solution of the corresponding sulfonamide **1** was added (3 eq, 0.492 µmol, 5 µL of a 0.1 M solution in degassed dioxane), followed by a freshly prepared $CuSO_4$ solution (1 eq, 0.164 µmol, 3.28 µL of a 0.5 M solution in degassed H_2O), sodium ascorbate (5 eq, 0.820 µmol, 4 µL of a 0.2 M solution in degassed H_2O) and THPTA (3 eq, 0.492 µmol, 5 µL of a 0.1 M solution in degassed H_2O). The resulting preparation was submitted to microwave for 1h30 at 60 °C. After this time, saturated EDTA acid solution was added in the same reaction volume of water and then purified and lyophilized.

Synthesis of the bivalent sulfonamide-oligonucleotide [OCA2]

To a microwave sealed vessel the oligonucleotide **ON-II** in degassed milliQ water (0.137 µmol in 70 µL) was added. A solution of the corresponding sulfonamide **1** was added (6 eq, 0.822 µmol, 8.2 µL of a 0.1 M solution in degassed dioxane), followed by a freshly prepared $CuSO_4$ solution (1 eq, 0.137 µmol, 2.8 µL of a 0.5 M solution in degassed H_2O), sodium ascorbate (5 eq, 0.685 µmol, 3.5 µL of a 0.2 M solution in degassed H_2O) and THPTA (3 eq, 0.411 µmol,4.1 µL of a 0.1 M solution in degassed H_2O). The resulting preparation was submitted to microwave for 2h at 60 °C. After this time, saturated EDTA acid solution was added in the same reaction volume of water and then purified and lyophilized.

Synthesis of the trivalent sulfonamide-oligonucleotide on solid support [OCA3]

To a microwave sealed vessel with 1 µmol of the solid-supported oligonucleotide **ON-III** a solution of the corresponding sulfonamide **1** was added (8 eq, 8 µmol, 80 µL of a 0.1 M solution in degassed dioxane), followed by a freshly prepared $CuSO_4$ solution (1 eq, 1 µmol, 20 µL of a 0.5 M solution in degassed H_2O), sodium ascorbate (5 eq, 5 µmol, 25 µL of a 0.2 M solution in degassed H2O), THPTA (3 eq, 3 µmol, 30 µL of a 0.1 M solution in degassed H_2O) and TEAC tampon (15 µL). The resulting preparation was submitted to microwave for 1h30 at 60°C. After this time, CPG beads were filtered and washed with dioxane (3 x 5 mL), water (3 x 5 mL), saturated EDTA acid solution (3 x 5 mL), water (3 x 5 mL) and acetonitrile (3 x 5 mL). After that, the compound was deprotected from CPG using general procedure B and then purified, desalted, and lyophilized.

Synthesis of the tetravalent sulfonamide-oligonucleotide on solid support [OCA4]

To a microwave sealed vessel with 1 µmol of the solid-supported oligonucleotide **ON-IV**, a solution of the corresponding sulfonamide **1** was added (10 eq, 10 µmol, 100 µL of a 0.1 M solution in degassed dioxane), followed by a freshly prepared $CuSO_4$ solution (1 eq, 1 µmol, 20 µL of a 0.5 M solution in degassed H_2O), sodium ascorbate (5 eq, 5 µmol, 25 µL of a 0.2 M solution in degassed H2O), THPTA (3 eq, 3 µmol, 30 µL of a 0.1 M solution in degassed H_2O) and TEAC tampon (35 µL). The resulting preparation was submitted to microwave for 2h at 60°C. After this time, CPG beads were filtered and washed with dioxane (3 x 5 mL), water (3 x 5 mL), saturated EDTA acid solution (3 x 5 mL), water (3 x 5 mL) and acetonitrile (3 x 5 mL). After that, the compound was deprotected from CPG using general procedure B and then purified, desalted, and lyophilized.

6.4.2 Preparation of the coumarin multivalent inhibitors

Synthesis of the monovalent coumarin-oligonucleotide [OCA5]

To a microwave sealed vessel the oligonucleotide **ON-I** in degassed milliQ water (0.2 µmol in 790 µL) was added. A solution of the corresponding coumarin **3** was added (3 eq, 0.6 µmol, 6 µL of a 0.1 M solution in degassed dioxane), followed by a freshly prepared $CuSO_4$ solution (1 eq, 0.2 µmol, 4 µL of a 0.5 M solution in degassed H_2O), sodium ascorbate (5 eq, 1 µmol, 5 µL of a 0.2 M solution in degassed H_2O) and THPTA (3 eq, 0.6 µmol, 6 µL of a 0.1 M solution in degassed H2O). The resulting preparation was submitted to microwave for 1h at 60 °C. After this time, saturated EDTA acid solution was added in the same reaction volume of water and then purified and lyophilized.

Synthesis of the bivalent coumarin-oligonucleotide [OCA6]

To a microwave sealed vessel the oligonucleotide **ON-II** in degassed milliQ water (0.342 µmol in 790 µL) was added. A solution of the corresponding coumarin **3** was added (4 eq, 1.37 µmol, 14 µL of a 0.1 M solution in degassed dioxane), followed by a freshly prepared $CuSO_4$ solution (1 eq, 0.342 µmol, 6.8 µL of a 0.5 M solution in degassed H_2O), sodium ascorbate (5 eq, 1.71 µmol, 8.6 µL of a 0.2 M solution in degassed H_2O) and THPTA (3 eq, 1.03 µmol, 10 µL of a 0.1 M solution in degassed H2O). The resulting preparation was submitted to microwave for 2h at 60 °C. After this time, saturated EDTA acid solution was added in the same reaction volume of water and then purified and lyophilized.

Synthesis of the trivalent coumarin-oligonucleotide [OCA7]

To a microwave sealed vessel the oligonucleotide **ON-III** in degassed milliQ water (0.328 µmol in 165 µL) was added. A solution of the corresponding coumarin **3** was added (9 eq, 2.96 µmol, 29.6 µL of a 0.1 M solution in degassed dioxane), followed by a freshly prepared $CuSO_4$ solution (1 eq, 0.328 µmol, 6.6 µL of a 0.5 M solution in degassed H_2O), sodium ascorbate (5 eq, 1.64 µmol, 8.2 µL of a 0.2 M solution in degassed H_2O) and THPTA (3 eq, 0.984 µmol, 9.8 µL of a 0.1 M solution in degassed H2O). The resulting preparation was submitted to microwave for 1h at 60 °C. After this time, saturated EDTA acid solution was added in the same reaction volume of water and then purified and lyophilized.

Synthesis of the tetravalent coumarin-oligonucleotide [OCA8]

To a microwave sealed vessel the oligonucleotide **ON-IV** in degassed milliQ water (0.426 µmol in 200 µL) was added. A solution of the corresponding coumarin **3** was added (12 eq, 5.112 µmol, 51.12 µL of a 0.1 M solution in degassed dioxane), followed by a freshly prepared $CuSO_4$ solution (1 eq, 0.426 µmol, 8.52 µL of a 0.5 M solution in degassed H_2O), sodium ascorbate (5 eq, 2.13 µmol, 10.7 µL of a 0.2 M solution in degassed H_2O) and THPTA (3 eq, 1.278 µmol, 12.8 µL of a 0.1 M solution in degassed H_2O). The resulting preparation was submitted to microwave for 30 min at 60 °C. After this time, saturated EDTA acid solution was added in the same reaction volume of water and then purified and lyophilized.

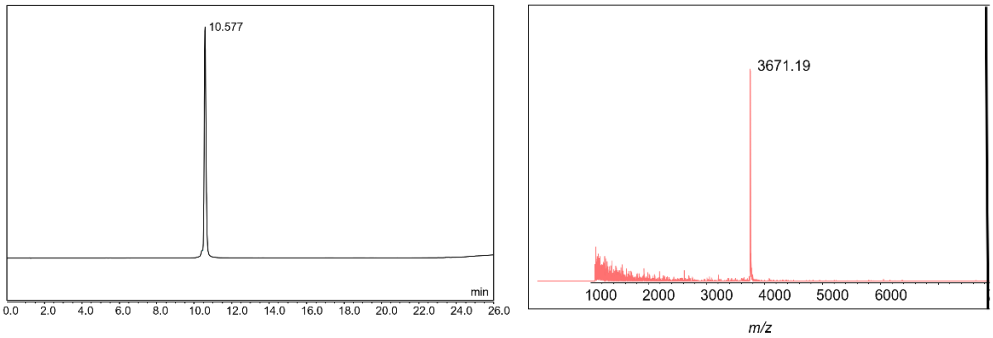
6.5 Characterizations

6.5.1 Oligonucleotide strands

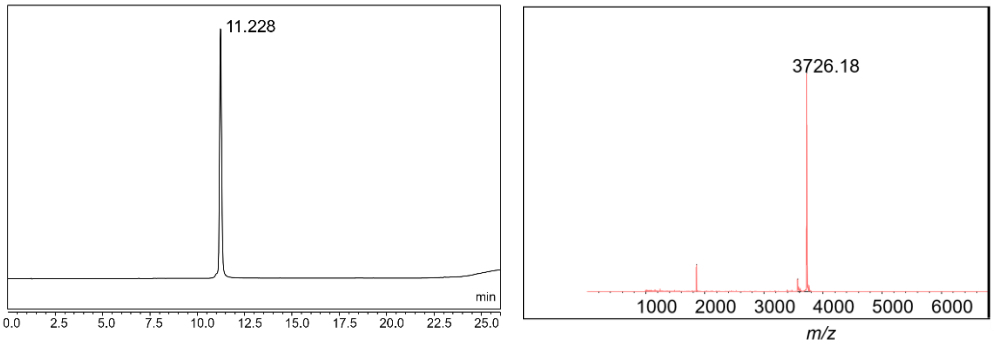
Table S2. Calculated mass values of the oligonucleotide strands, using the negative method of MALDI detenction and measured negative charge (Z) of 1

	Mass/Z neg			
z	ON-I	ON-II	ON-III	ON-IV
1	3670,42	3725,45	3780,48	3795,49

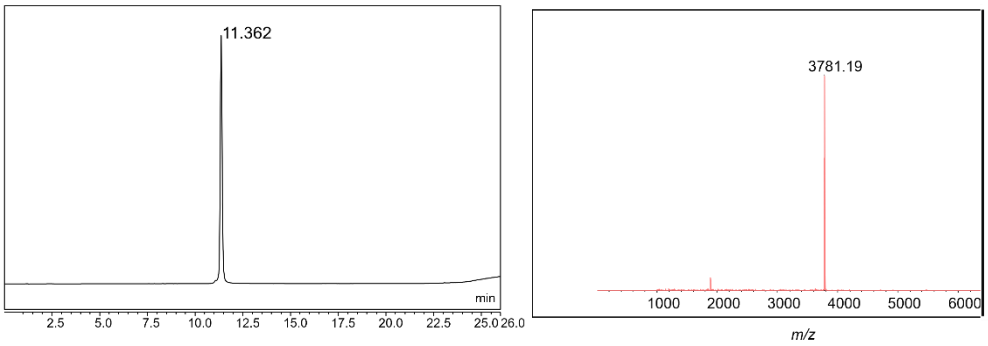
HPLC and MALDI-TOF (ON-I)



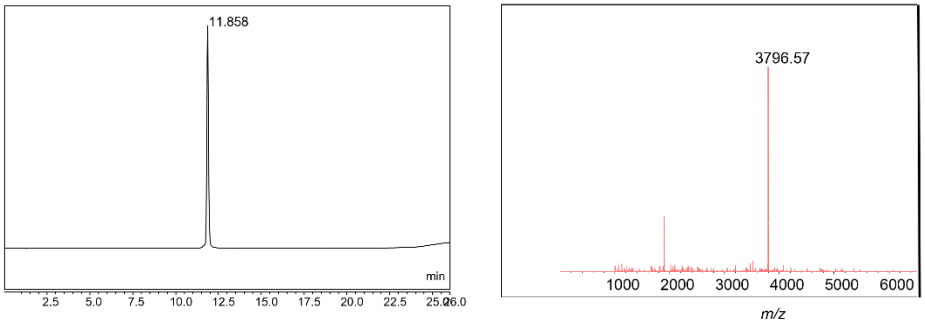
HPLC and MALDI-TOF (ON-II)



HPLC and MALDI-TOF (ON-III)



HPLC and MALDI-TOF (ON-IV)

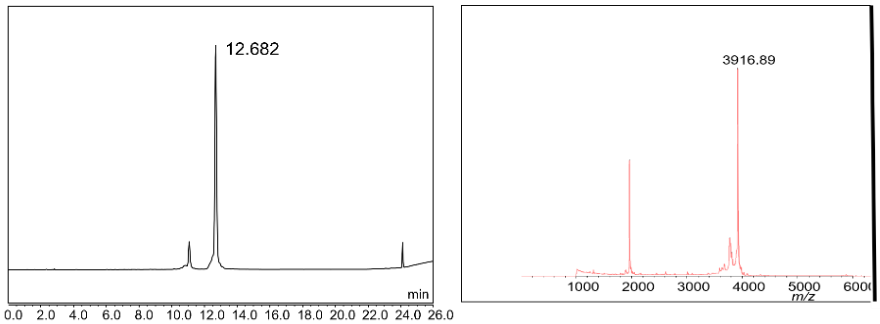


6.5.2 Final compounds

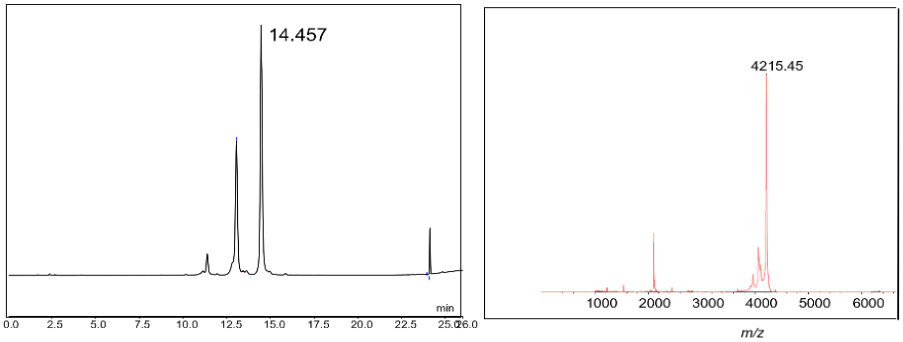
Table S2. Calculated mass values of the final compounds, using the negative method of MALDI detenction and measured negative charge (Z) of 1

	Mass/Z neg							
z	OCA1	OCA2	OCA3	OCA4	OCA5	OCA6	OCA7	OCA8
1	3896,67	4177,96	4459	4700	3915	4215	4516,19	4776,41

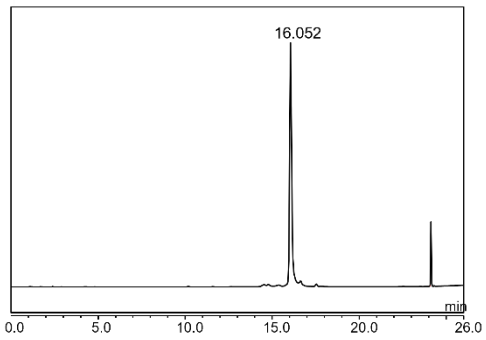
HPLC and MALDI-TOF (OCA-1)

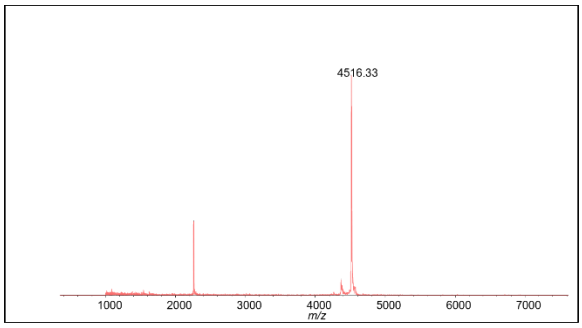


HPLC and MALDI-TOF (OCA-2)

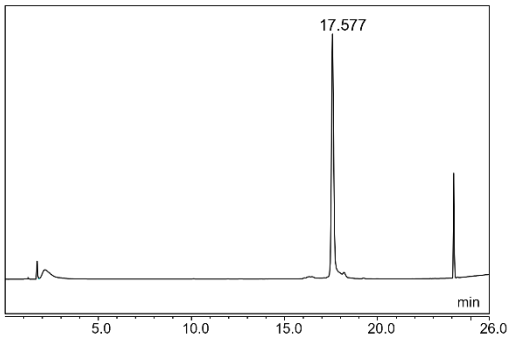


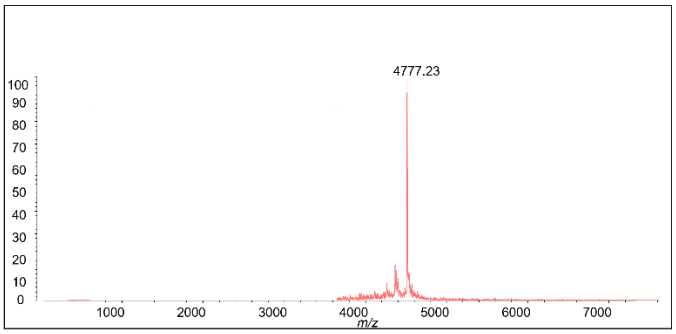
HPLC and MALDI-TOF (OCA-3)



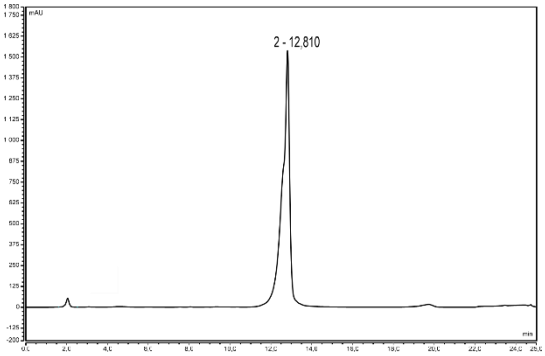


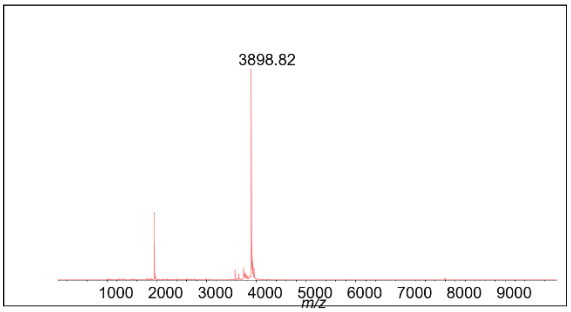
HPLC and MALDI-TOF (OCA-4)



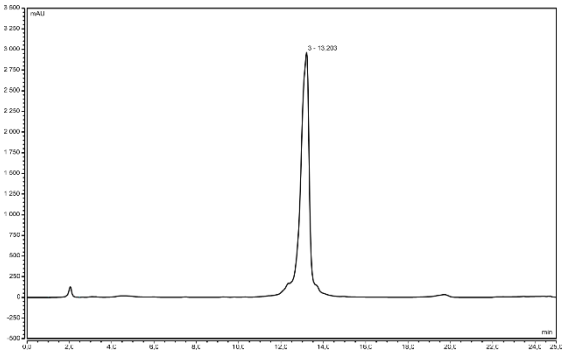


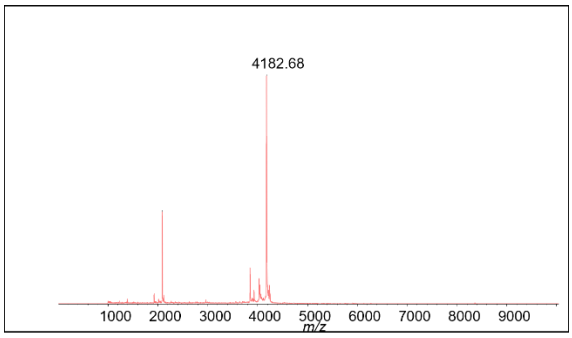
HPLC and MALDI-TOF (OCA-5)



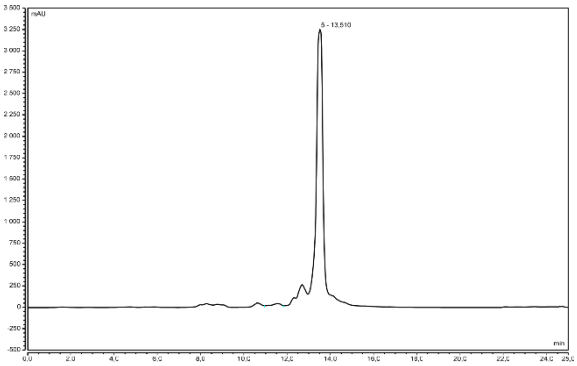


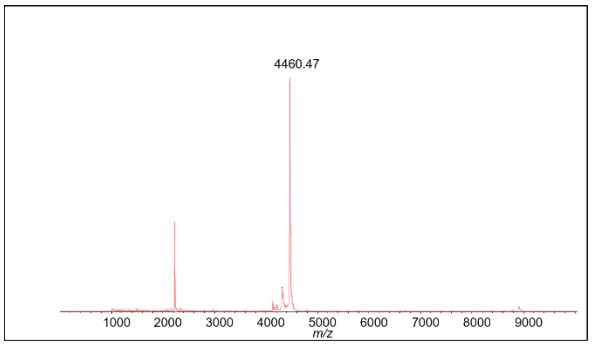
HPLC and MALDI-TOF (OCA-6)



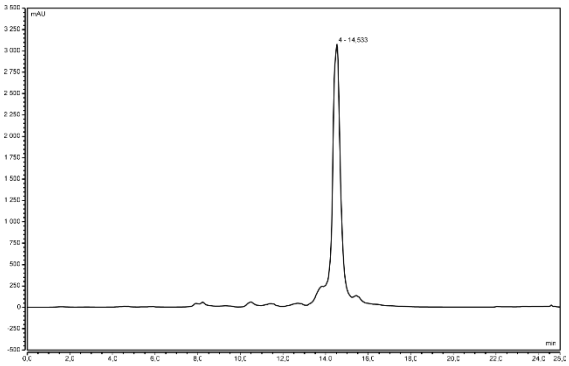


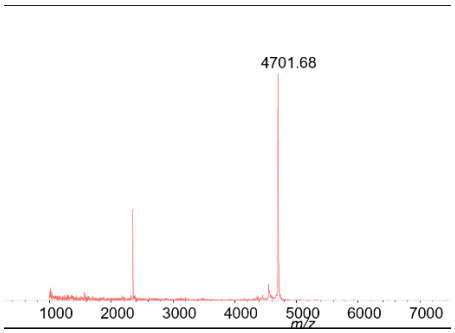
HPLC and MALDI-TOF (OCA-7)





HPLC and MALDI-TOF (OCA-8)





Bibliography

(1) Alterio, V.; Di Fiore, A.; D'Ambrosio, K.; Supuran, C. T.; De Simone, G. Multiple Binding Modes of Inhibitors to Carbonic Anhydrases: How to Design Specific Drugs Targeting 15 Different Isoforms? *Chem Rev* **2012**, *112* (8), 4421–4468. https://doi.org/10.1021/cr200176r.

(2) Alterio, V.; Di Fiore, A.; D'Ambrosio, K.; Supuran, C. T.; De Simone, G. *Drug Design of Zinc-Enzyme Inhibitors: Functional, Structural, and Disease Applications*, Wiley : Hoboken.; Supuran, C. T., Winum, J. Y., Eds.; 2009.

(3) Imtaiyaz Hassan, Md.; Shajee, B.; Waheed, A.; Ahmad, F.; Sly, W. S. Structure, Function and Applications of Carbonic Anhydrase Isozymes. *Bioorg Med Chem* **2013**, *21* (6), 1570–1582. https://doi.org/10.1016/j.bmc.2012.04.044.

(4) Supuran, C. T. Carbonic Anhydrases: Novel Therapeutic Applications for Inhibitors and Activators. *Nat Rev Drug Discov* **2008**, *7* (2), 168–181. https://doi.org/10.1038/nrd2467.

(5) Supuran, C. T. Advances in Structure-Based Drug Discovery of Carbonic Anhydrase Inhibitors. *Expert Opin Drug Discov* **2017**, *12* (1), 61–88. https://doi.org/10.1080/17460441.2017.1253677.

(6) Ivanova, J.; Leitans, J.; Tanc, M.; Kazaks, A.; Zalubovskis, R.; Supuran, C. T.; Tars, K. X-Ray Crystallography-Promoted Drug Design of Carbonic Anhydrase Inhibitors. *Chemical Communications* **2015**, *51* (33), 7108–7111. https://doi.org/10.1039/C5CC01854D.

(7) Supuran, C. T. How Many Carbonic Anhydrase Inhibition Mechanisms Exist? *J Enzyme Inhib Med Chem* **2016**, *31* (3), 345–360. https://doi.org/10.3109/14756366.2015.1122001.

(8) De Simone, G.; Alterio, V.; Supuran, C. T. Exploiting the Hydrophobic and Hydrophilic Binding Sites for Designing Carbonic Anhydrase Inhibitors. *Expert Opin Drug Discov* **2013**, *8* (7), 793–810. https://doi.org/10.1517/17460441.2013.795145.

(9) Scozzafava, A.; Menabuoni, L.; Mincione, F.; Briganti, F.; Mincione, G.; Supuran, C. T. Carbonic Anhydrase Inhibitors. Synthesis of Water-Soluble, Topically Effective, Intraocular Pressure-Lowering Aromatic/Heterocyclic Sulfonamides Containing Cationic or Anionic Moieties: Is the Tail More Important than the Ring? *J Med Chem* **1999**, *42* (14), 2641–2650. https://doi.org/10.1021/jm9900523.

(10) Kumar, A.; Siwach, K.; Supuran, C. T.; Sharma, P. K. A Decade of Tail-Approach Based Design of Selective as Well as Potent Tumor Associated Carbonic Anhydrase Inhibitors. *Bioorg Chem* **2022**, *126*, 105920. https://doi.org/10.1016/j.bioorg.2022.105920.

(11) Pastorekova, S.; Casini, A.; Scozzafava, A.; Vullo, D.; Pastorek, J.; Supuran, C. T. Carbonic Anhydrase Inhibitors: The First Selective, Membrane-Impermeant Inhibitors Targeting the Tumor-Associated Isozyme IX. *Bioorg Med Chem Lett* **2004**, *14* (4), 869–873. https://doi.org/10.1016/j.bmcl.2003.12.029.

(12) Scozzafava, A.; Briganti, F.; Ilies, Marc. A.; Supuran, C. T. Carbonic Anhydrase Inhibitors: Synthesis of Membrane-Impermeant Low Molecular Weight Sulfonamides Possessing in Vivo Selectivity for the Membrane-Bound versus Cytosolic Isozymes. *J Med Chem* **2000**, *43* (2), 292–300. https://doi.org/10.1021/jm990479.

(13) Supuran, C. T.; Alterio, V.; Di Fiore, A.; D' Ambrosio, K.; Carta, F.; Monti, S. M.; De Simone, G. Inhibition of Carbonic Anhydrase IX Targets Primary Tumors, Metastases, and Cancer Stem Cells: Three for the Price of One. *Med Res Rev* **2018**, *38* (6), 1799–1836. https://doi.org/10.1002/med.21497.

(14) Pastorekova, S.; Parkkila, S.; Pastorek, J.; Supuran, C. T. Carbonic Anhydrases: Current State of the Art, Therapeutic and Future Prospects. *J Enzyme Inhib Med Chem* **2004**, *19* (3), 199–229. https://doi.org/10.1080/14756360410001689540.

(15) Kanfar, N.; Bartolami, E.; Zelli, R.; Marra, A.; Winum, J.-Y.; Ulrich, S.; Dumy, P. Emerging Trends in Enzyme Inhibition by Multivalent Nanoconstructs. *Org Biomol Chem* **2015**, *13* (39), 9894–9906. https://doi.org/10.1039/C5OB01405K.

(16) Kiessling, L. L.; Gestwicki, J. E.; Strong, L. E. Synthetic Multivalent Ligands as Probes of Signal Transduction. *Angewandte Chemie International Edition* **2006**, *45* (15), 2348–2368. https://doi.org/10.1002/anie.200502794.

(17) Fasting, C.; Schalley, C. A.; Weber, M.; Seitz, O.; Hecht, S.; Koksch, B.; Dernedde, J.; Graf, C.; Knapp, E.; Haag, R. Multivalency as a Chemical Organization and Action Principle. *Angewandte Chemie International Edition* **2012**, *51* (42), 10472–10498. https://doi.org/10.1002/anie.201201114.

(18) Lee, Y. C.; Lee, R. T. Carbohydrate-Protein Interactions: Basis of Glycobiology. *Acc Chem Res* **1995**, *28* (8), 321–327. https://doi.org/10.1021/ar00056a001.

(19) Lundquist, J. J.; Toone, E. J. The Cluster Glycoside Effect. *Chem Rev* **2002**, *102* (2), 555–578. https://doi.org/10.1021/cr000418f.

(20) Compain, P. Multivalent Effect in Glycosidase Inhibition: The End of the Beginning. *The Chemical Record* **2020**, *20* (1), 10–22. https://doi.org/10.1002/tcr.201900004.

(21) Mammen, M.; Choi, S.-K.; Whitesides, G. M. Polyvalent Interactions in Biological Systems: Implications for Design and Use of Multivalent Ligands and Inhibitors. *Angewandte Chemie International Edition* **1998**, *37* (20), 2754–2794. https://doi.org/10.1002/(SICI)1521-3773(19981102)37:20<2754::AID-ANIE2754>3.0.CO;2-3.

(22) Kiessling, L. Synthetic Multivalent Ligands in the Exploration of Cell-Surface Interactions. *Curr Opin Chem Biol* **2000**, *4* (6), 696–703. https://doi.org/10.1016/S1367-5931(00)00153-8.

(23) Wittmann, V.; Pieters, R. J. Bridging Lectin Binding Sites by Multivalent Carbohydrates. *Chem Soc Rev* **2013**, *42* (10), 4492. https://doi.org/10.1039/c3cs60089k.

(24) Hermanson, G. T. *Bioconjugate Tecnhiques*, Third.; Audet, J., Preap, M., Eds.; Academic Press, 2013.

(25) Carta, F.; Dumy, P.; Supuran, C. T.; Winum, J.-Y. Multivalent Carbonic Anhydrases Inhibitors. *Int J Mol Sci* **2019**, *20* (21), 5352. https://doi.org/10.3390/ijms20215352.

(26) Vitale, R. M.; Alterio, V.; Innocenti, A.; Winum, J.-Y.; Monti, S. M.; De Simone, G.; Supuran, C. T. Carbonic Anhydrase Inhibitors. Comparison of Aliphatic Sulfamate/Bis-Sulfamate Adducts with Isozymes II and IX as a Platform for Designing Tight-Binding, More Isoform-Selective Inhibitors. *J Med Chem* **2009**, *52* (19), 5990–5998. https://doi.org/10.1021/jm900641r.

(27) D'Ambrosio, K.; Smaine, F.-Z.; Carta, F.; De Simone, G.; Winum, J.-Y.; Supuran, C. T. Development of Potent Carbonic Anhydrase Inhibitors Incorporating Both Sulfonamide and Sulfamide Groups. *J Med Chem* **2012**, *55* (15), 6776–6783. https://doi.org/10.1021/jm300818k.

(28) Krall, N.; Pretto, F.; Decurtins, W.; Bernardes, G. J. L.; Supuran, C. T.; Neri, D. A Small-Molecule Drug Conjugate for the Treatment of Carbonic Anhydrase IX Expressing Tumors. *Angewandte Chemie International Edition* **2014**, *53* (16), 4231–4235. https://doi.org/10.1002/anie.201310709.

(29) Krall, N.; Pretto, F.; Neri, D. A Bivalent Small Molecule-Drug Conjugate Directed against Carbonic Anhydrase IX Can Elicit Complete Tumour Regression in Mice. *Chem Sci* **2014**, *5* (9), 3640. https://doi.org/10.1039/C4SC00685B.

(30) Wilkinson, B. L.; Innocenti, A.; Vullo, D.; Supuran, C. T.; Poulsen, S.-A. Inhibition of Carbonic Anhydrases with Glycosyltriazole Benzene Sulfonamides. *J Med Chem* **2008**, *51* (6), 1945–1953. https://doi.org/10.1021/jm701426t.

(31) Morris, J. C.; Chiche, J.; Grellier, C.; Lopez, M.; Bornaghi, L. F.; Maresca, A.; Supuran, C. T.; Pouysségur, J.; Poulsen, S.-A. Targeting Hypoxic Tumor Cell Viability with Carbohydrate-Based Carbonic Anhydrase IX and XII Inhibitors. *J Med Chem* **2011**, *54* (19), 6905–6918. https://doi.org/10.1021/jm200892s.

(32) El-Gazzar, M. G.; Nafie, N. H.; Nocentini, A.; Ghorab, M. M.; Heiba, H. I.; Supuran, C. T. Carbonic Anhydrase Inhibition with a Series of Novel Benzenesulfonamide-Triazole Conjugates. *J Enzyme Inhib Med Chem* **2018**, *33* (1), 1565–1574. https://doi.org/10.1080/14756366.2018.1513927.

(33) Supuran, C. T. Inhibition of Carbonic Anhydrase IX as a Novel Anticancer Mechanism. *World J Clin Oncol* **2012**, *3* (7), 98. https://doi.org/10.5306/wjco.v3.i7.98.

(34) Guler, O.; Simone, G.; Supuran, C. Drug Design Studies of the Novel Antitumor Targets Carbonic Anhydrase IX and XII. *Curr Med Chem* **2010**, *17* (15), 1516–1526. https://doi.org/10.2174/092986710790979999.

(35) Justine Mansot. Développement de Nouvelles Stratégies Pour Le Domaine de La Catalyse Asymétrique à Base d'ADN. Thèse en Ingéniere Biomoléculaire, École doctorale Sciences Chimiques Balard - Unité de recherche IBMM UMR 5247 UM, CNRS, ENSCM, Montpellier, 2020.

(36) Zatsepin, T. S.; Stetsenko, D. A.; Gait, M. J.; Oretskaya, T. S. Use of Carbonyl Group Addition−Elimination Reactions for Synthesis of Nucleic Acid Conjugates. *Bioconjug Chem* **2005**, *16* (3), 471–489. https://doi.org/10.1021/bc049712v.

(37) Sadhu, K. K.; Röthlingshöfer, M.; Winssinger, N. DNA as a Platform to Program Assemblies with Emerging Functions in Chemical Biology. *Isr J Chem* **2013**, *53* (1–2), 75–86. https://doi.org/10.1002/ijch.201200100.

(38) Fantoni, N. Z.; El-Sagheer, A. H.; Brown, T. A Hitchhiker's Guide to Click-Chemistry with Nucleic Acids. *Chem Rev* **2021**, *121* (12), 7122–7154. https://doi.org/10.1021/acs.chemrev.0c00928.

(39) Bouillon, C.; Meyer, A.; Vidal, S.; Jochum, A.; Chevolot, Y.; Cloarec, J.-P.; Praly, J.-P.; Vasseur, J.-J.; Morvan, F. Microwave Assisted “Click” Chemistry for the Synthesis of Multiple Labeled-Carbohydrate Oligonucleotides on Solid Support. *J Org Chem* **2006**, *71* (12), 4700–4702. https://doi.org/10.1021/jo060572n.

(40) Weisbrod, S. H.; Marx, A. Novel Strategies for the Site-Specific Covalent Labelling of Nucleic Acids. *Chemical Communications* **2008**, No. 44, 5675. https://doi.org/10.1039/b809528k.

(41) Matteucci, M. D.; Caruthers, M. H. Synthesis of Deoxyoligonucleotides on a Polymer Support. *J Am Chem Soc* **1981**, *103* (11), 3185–3191. https://doi.org/10.1021/ja00401a041.